The eternal variety
Of the ion society
Is dancing its way
Recombining their play
'Cause never do they stay
In their so called sobriety

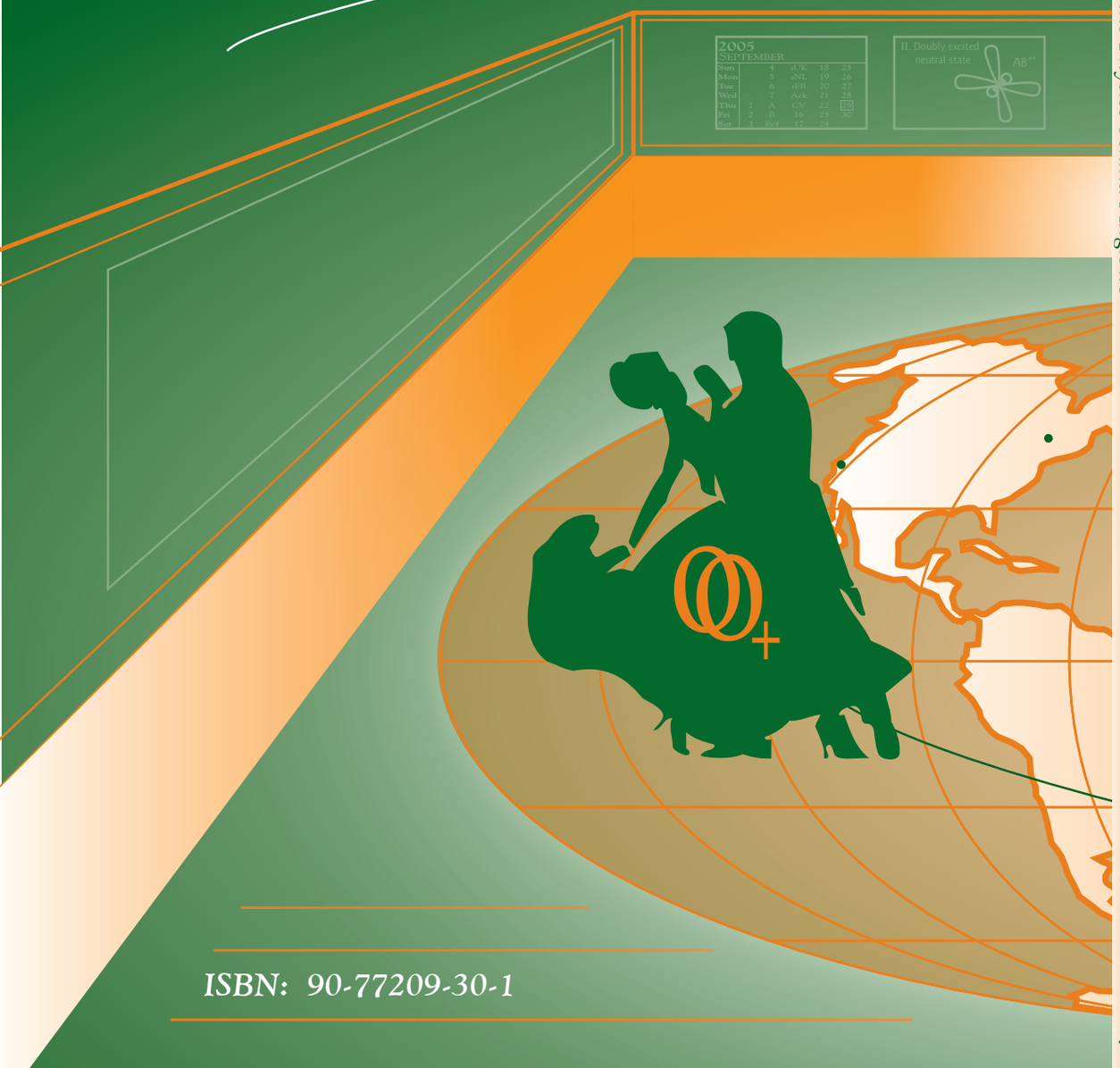

ISBN: 90-77209-30-1

Dissociative Recombination of Atmospheric Ions
Towards Unravelling the Physics behind Airglows
Annemieke Petrignani
2005

Dissociative Recombination of Atmospheric Ions

Towards Unravelling the Physics behind Airglows

Annemieke Petrignani

Dissociative Recombination of Atmospheric Ions

Towards Unravelling the Physics behind Airglows

Design by Werner G. L. Taube-Petrignani
ISBN: 90-77209-30-1

Dissociative Recombination of Atmospheric Ions

Towards Unravelling the Physics behind Airglows

EEN WETENSCHAPPELIJKE PROEVE OP HET GEBIED VAN
DE NATUURWETENSCHAPPEN, WISKUNDE EN INFORMATICA

PROEFSCHRIFT

ter verkrijging van de graad van doctor
aan de Radboud Universiteit Nijmegen
op gezag van de Rector Magnificus prof. dr. C.W.P.M. Blom,
volgens besluit van het College van Decanen
in het openbaar te verdedigen op donderdag 29 September 2005
des ochtends om 10.30 uur precies
door

Annemieke Petrignani

geboren op 1 December 1975
te Middelburg, Nederland

Promotors	Prof. dr. W. J. van der Zande Prof. dr. M. Larsson (Stockholms Universitet)
Manuscript commissie	Prof. dr. D. H. Parker (voorzitter) Prof. dr. X. Urbain (Université Catholique de Louvain) Dr. J. L. Herek (FOM Instituut voor Atoom- en Molecuulfysica)

The work described in this PhD thesis has been performed at:

FOM Instituut voor Atoom- en Molecuulfysica
Kruislaan 407
1098 SJ Amsterdam, Nederland
www.amolf.nl

Instituut voor Moleculen en Materialen
Radboud Universiteit Nijmegen
Toernooiveld 1
6525 ED Nijmegen, Nederland
www.mlf.science.ru.nl

SRI International
333 Ravenswood Ave
Menlo Park, CA 94025, United States
www.sri.com

Manne Siegbahn Laboratoriet
Frescativägen 24
S-104 05, Stockholm, Sverige
www.msi.se

This work is part of the research program of the "Stichting voor Fundamenteel Onderzoek der Materie (FOM)", which is financially supported by the "Nederlandse organisatie voor Wetenschappelijk Onderzoek (NWO)". It has been partially supported by the NASA Planetary Atmospheres Program under grant NAG5-11173 to SRI International. Support has also been given by the EU research-training network Electron Transfer Reactions (ETR) under contract HPRN-CT-2000-00142 and by the Swedish Research Council.

Pour Werner

The simple solid sound

The eternal variety
Of the ion society
Is dancing its way
Recombining their play
'Cause never do they stay
In their so called sobriety

Of lyrics rushing round

The atomic variety
Of the ion society
Is strolling astray
In this dissociative play
Forever enlightened as they may
Be in war and peace so quietly

by Mariska Petrignani

List of publications covered in this thesis

Chapter 4

A. Petrignani, P. C. Cosby, F. Hellberg, R. D. Thomas, M. Larsson and W. J. van der Zande, *Electron Energy Dependence of the Branching in Dissociative Recombination of* O_2^+, J. Chem. Phys. **122**, 234311, 2005

A. Petrignani, P. C. Cosby, F. Hellberg, R. D. Thomas, M. Larsson and W. J. van der Zande, *Vibrationally Resolved Rate Coefficients and Branching Fractions in the Dissociative Recombination of* O_2^+, J. Chem. Phys. **122**, 014302, 2005

A. Petrignani, F. Hellberg, R. D. Thomas, P. C. Cosby, M. Larsson and W. J. van der Zande, *Vibrational Dependence in the Dissociative Recombination of* O_2^+, in "Dissociative Recombination: Theory, Experiment and Applications VI" edited by A. Wolf and L. Lammich and P. Schmelcher (2005) pages 182–186

Chapter 5

F. Hellberg, A. Petrignani, W. J. van der Zande, S. Rosén, R. D. Thomas, A. Neau and M. Larsson, *Dissociative recombination of* NO^+*: Dynamics of the* $X\,^1\Sigma^+$ *and* $a\,^3\Sigma^+$ *Electronic States*, J. Chem. Phys. **118**, 6250–6259, 2003

Chapter 6

A. Petrignani, P. U. Andersson, J. B. C. Pettersson, R. D. Thomas, F. Hellberg, A. Ehlerding, M. Larsson and W. J. van der Zande, *Dissociative Recombination of the Weakly-Bound NO-Dimer Cation: Cross Sections and Three-Body Dynamics*, submitted to J. Chem. Phys. in May 2005

Chapter 7

A. Petrignani, M. C. G. N. van Vroonhoven, G. C. Groenenboom, W. J. van der Zande, *The Effect of Rydberg-Valence Couplings on Dissociative Recombination Cross Sections*, in preparation

Other Publications

R. D. Thomas, F. Hellberg, A. Neau, S. Rosén, M. Larsson, C. R. Vane, M. E. Bannister, S. Datz, A. Petrignani, W. J. van der Zande, *Three-Body Fragmentation Dynamics of Amidogen and Methylene Radicals via Dissociative Recombination*, Phys. Rev. A **71**, 032711, 2005

R. D. Thomas, A. Ehlerding, W. Geppert, F. Hellberg, M. Larsson, V. Chaunerchyk, E. Bahati, M. E. Bannister, C. R. Vane, A. Petrignani, W. J. van der Zande, P. Andersson and J. B. C. Pettersson, *The Effect of Bonding on the Fragmentation of Small Systems*, in "Dissociative Recombination: Theory, Experiment and Applications VI" edited by A. Wolf and L. Lammich and P. Schmelcher (2005) pages 187–190

F. Österdahl, S. Rosén, V. Bednarska, A. Petrignani, M. Larsson and W. J. van der Zande, *Position- and Time-Sensitive Coincident Detection of Fragments from the Dissociative Recombination of* O_2^+ *using a Single Hexanode Delay-Line Detector*, in "Dissociative Recombination: Theory, Experiment and Applications VI" edited by A. Wolf and L. Lammich and P. Schmelcher (2005) pages 286–289

R. D. Thomas, F. Hellberg, A. Ehlerding, M. Larsson, A. Petrignani, W. J. van der Zande, P. U. Andersson, and J. B. C. Pettersson, *Dissociative Recombination of the Strongly-Bound* $(D_2O)_2.D^+$ *Cation: Cross Sections and Three-Body Dynamics*, in preparation

Contents

2005
SEPTEMBER

Sun		4	sUK	18	25
Mon		5	sNL	19	26
Tue		6	sFR	20	27
Wed		7	Ack	21	28
Thu	1	A	CV	22	29
Fri	2	B	16	23	30
Sat	3	Ref	17	24	

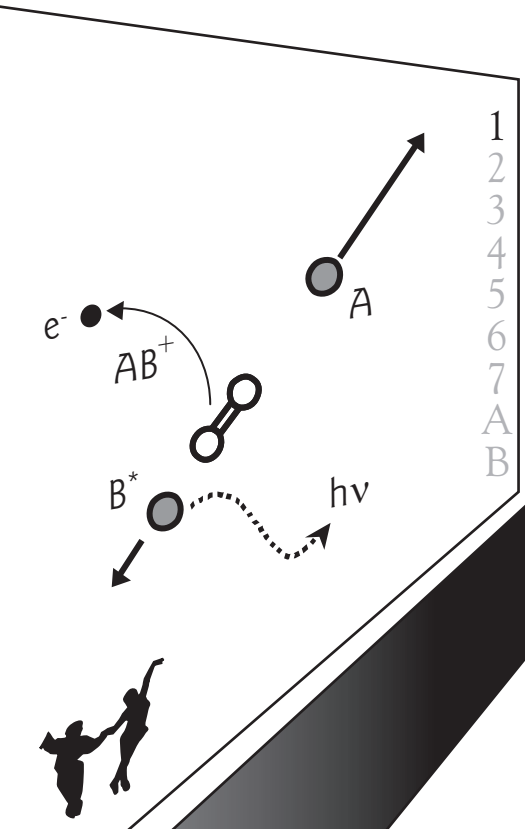

1
2
3
4
5
6
7
A
B

Physics is...
focused energy that goes everywhere

– husband of –

Annemieke

Chapter 1

On Airglows and Dissociative Recombination

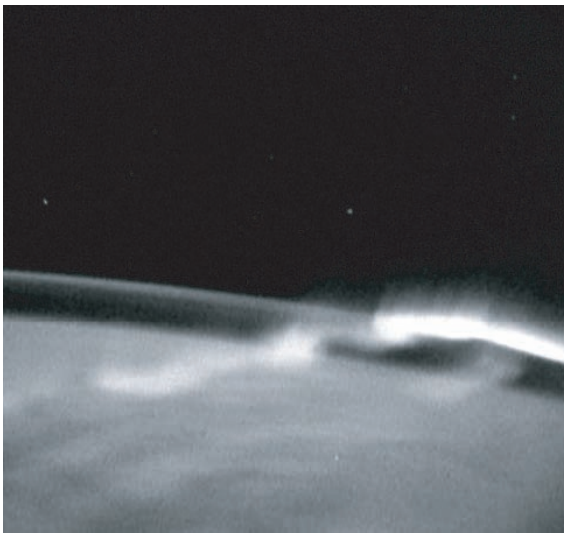

Figure 1.1: Aurora and airglow of the Earth. The aurora is the bright light that is highly structured and is limited to high latitudes. The airglow is the faint arc of uniform light extending to the left and is found at all latitudes.

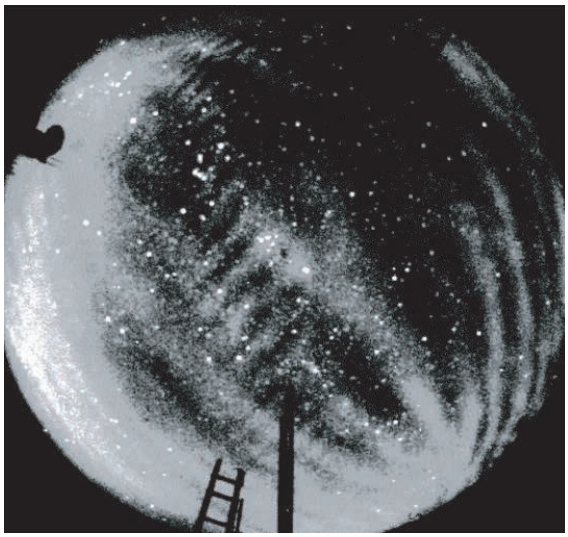

Figure 1.2: All-sky photograph of the oxygen green-line emission at 577.7 nm taken from Ref. [1].

1.1 Introduction

Colourful displays of light in the sky have intrigued observers for many years. Throughout history the Earth's aurorae have been feared and admired, as they are impressive displays of light, appearing and disappearing, and violent in their presence. In earlier times they were thought to be messages from the gods and it was not until last century that it was discovered, with fierce opposition, that particles originating from the sun were responsible for these outbursts of light. Besides aurorae, there is another intriguing and beautiful light phenomena: the airglow. High in the sky the air is glowing with an intensity that can even be observed from the ground by the aided eye. This airglow is a peaceful glow that is uniform and continuously present illuminating the entire planet as a corona of light. From space, this corona can be observed glowing over the night side of a planet (see Fig. 1.1). Besides their beauty, aurorae and airglows are valuable sources of information on the terrestrial and other planetary atmospheres as well as on our sun. They constitute an important diagnostic tool revealing information about atmospheric regions which are otherwise difficult to study. Aurorae and airglows complement each other as information sources due to their different origins. Airglows are driven by solar and galactic radiation and are continuously and globally present. Aurorae are driven by energetic solar particles, generally more intense than airglows, and irregular in shape and occurrence. In the presence of a planetary magnetic field, like on Earth, the solar particles are guided to the polar regions, separating the aurorae from the airglow. The chemistry and physics behind airglows and aurorae incorporate a variety of processes involving atomic, molecular, neutral, and ionic atmospheric species. One of the major reactions behind airglows is dissociative recombination.

The research presented in this thesis concerns the dissociative recombination reaction in the context of planetary atmospheres and airglows. It aims at improving our understanding of the dissociative recombination reaction as an airglow source as well as a fundamental

physical process by addressing some of the mysteries and unknowns in the dissociative recombination of the two major atmospheric molecular ions, O_2^+ and NO^+, and of the dimer ion, $(NO)_2^+$. This chapter provides a short introduction to atmospheres, airglows, and the dissociative recombination reaction. First, planetary atmospheres are discussed, illustrating the diagnostic value of airglows and discussing their potential as indicators in the search for life. The discussion then moves to the Earth's upper atmosphere and its airglows, specifically the atomic oxygen green- and red-line emissions. The reader is further referred to references [2], [3], and [4] for general reviews on atmospheres and airglows. Subsequently, a short history of the dissociative recombination reaction as an atmospheric process is discussed, illustrating its relevance to the Earth's upper atmosphere and to the green-line emission in particular. This is followed by an introduction to the physics of the dissociative recombination reaction, presenting the principles behind the process and the dependencies relevant to atmospheric modelling. Finally, an overview of the present research together with a short description and motivation is given.

1.2 Planetary Atmospheres

Airglows and aurorae are a feature of most planetary atmospheres. The information they provide about an atmosphere enhances with the knowledge that is already available. For unknown atmospheres, airglows and aurorae can provide information on the basic atmospheric structure and the interaction with the sun. As the available knowledge about the atmosphere grows, the nature of their diagnostic value changes and more detailed information may be obtained, such as data on trace species, temporal and spatial variability, and even specific information on physical states of molecular precursors. These detailed investigations, however, require knowledge on the behaviour and dependencies of the underlying chemical and physical processes. Laboratory studies as well as atmospheric observations are essential tools in acquiring the necessary insight. In the absence of detailed knowledge, atmospheric models are required to include assumptions, which may later prove to be incorrect.

Of special importance to the diagnostic value of airglows is their possible use in the search for extraterrestrial life. On Earth, O_2 molecules are both directly and indirectly responsible for the green-line emission of atomic oxygen in the Earth's airglow (see Fig. 1.2) and it has been suggested that this green airglow may be an atmospheric diagnostic suitable for detecting O_2-rich atmospheres [5]. A recent important discovery has, however, changed the conception of the production of green airglow and its diagnostic implications [6]. This discovery involves the observation of the green airglow in the Venusian atmosphere, which demonstrates that green-line production is not limited to planets with Earth-like atmospheres. Although the green airglow may still be a useful diagnostic tool, its role in the search for the possible presence of O_2 is unclear.

The green-line emission is a good example where detailed investigations are hindered by insufficient knowledge. Observations of the Earth's atmosphere show that the green-airglow intensity at high altitudes rises steeply with increasing altitude. The underlying process for this green airglow is believed to be the dissociative recombination of O_2^+ (see §1.4). However, the steep increase cannot be correctly modelled using the currently available knowledge. Two issues hinder the interpretation of the *in situ* observations. First, knowledge is absent on the vibrational dependence of the dissociative recombination reaction and second, the exact

vibrational population of O_2^+ ions on Earth is not known. A major goal of the research presented in this thesis was to unravel the vibrational dependency and other potential influences in the dissociative recombination reaction relevant to these airglow observations. If the vibrational dependence proves to be important, the diagnostic implications will be far reaching, considering the presence of the O_2^+ ions in planetary atmospheres. The O_2^+ ion is not only one of the main molecular ions on Earth, it is also the main molecular ion on Mars and Venus. This was a surprise as the Venusian and Martian atmospheres consist mainly (95%) of carbon dioxide. Interestingly, the ion densities in the ionospheres, which is the high altitude region where airglows are found, are comparable for all three planets. An important difference is that the O_2^+ vibrational distribution on Earth is colder than those on Venus and Mars. The terrestrial O_2^+ ions are primary ions where solar radiation ionises O_2 molecules, which also quench the produced O_2^+ ions effectively. The O_2^+ ions on Venus and Mars are secondary ions formed by collisions between the primary ions, CO_2^+, and atomic oxygen, giving rise to vibrationally excited O_2^+, which remain excited in the absence of their neutral counterparts. In fact, the vibrational and translational temperatures on these planets show an interesting contrast: the kinetic temperature in the ionospheres of Mars and Venus is lower than that on Earth, whereas the vibrational temperature is higher than on Earth. Although CO_2 does not quench vibrationally excited states easily, it does function as a very efficient remover of heat through infrared radiation processes; hence greenhouse gases can also cause cooling at the proper place. An illustration of the differences and similarities between the three planets is given in Fig. 1.3. Specific for the Venusian atmosphere is the combination of an extremely slow rotation (243 Earth days), an absence of a magnetic field, and pressure gradients that drive plasma from the day side to the night side; these features result in a highly complex night-side ionosphere. The Venusian airglow in this night-side ionosphere reflects the chemistry of minor atmospheric species. For Mars, dissociative recombination is not only a source for airglow, but also for O atoms that have sufficient kinetic energy to escape the gravitational forces of the planet [7, 8]. It is interesting to note that the Venusian and Martian upper atmospheres are comparable in temperature and pressure as well as in ionic densities, profiles, and species.

1.3 The Earth's Atmosphere

Airglows are found high in the atmosphere, where the low pressures allow for excited atmospheric species to radiatively decay rather than react completely with other species. Two major defining features lie at the basis of the chemistry and physics of the upper atmosphere: gravitational separation of the atmospheric constituents and ionisation and excitation due to solar and galactic radiation. This combination gives rise to airglows that are often well-separated in altitude. The regions of gravitational separation and ionisation are called the thermosphere and ionosphere. These two regions largely overlap and are defined based on two different profiles: the temperature and electron-density profile. This section covers some of the characteristics of the Earth's thermosphere and ionosphere, followed by a description of airglow emissions that are related to the dissociative recombination reaction.

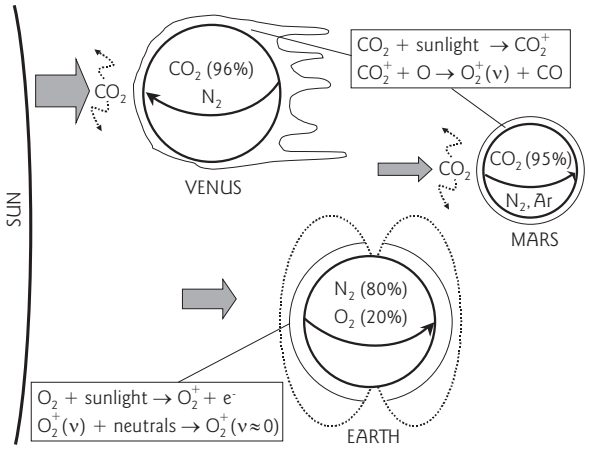

Figure 1.3: Illustration of similarities and differences between the planets Venus, Earth, and Mars. The thin solid curves around the planets are the respective ionospheres, where airglows are found. The curved arrows indicate the revolution direction. The dotted curves illustrate the Earth's magnetic field, which separates the aurora and the airglow. The O_2^+ ions are formed differently on Earth than on Venus and Mars. The upper atmospheres of Venus and Mars are relatively cold due to energy dissipation through CO_2 cooling. Some specifications are listed in the table. The values are relative to the Earth's values unless otherwise specified.

	Venus	Earth	Mars
Distance from the sun	0.72	1	1.52
Diameter	0.95	1	0.5
Mass	0.8	1	0.1
Duration of a day	243	1	1.03
Pressure	90	1	7e-3
$T_{surface}$ (K)	740	300	220
T_{upper} (K)	100–300	700–1000	150–300
Escape velocity (km s^{-1})	10	11	5

1.3.1 The Thermosphere

The Earth's atmosphere is commonly divided into different altitude regions based on its temperature profile (see Fig. 1.4). The temperature on Earth does not decrease monotonically with increasing altitude. In fact, the temperature rises twice, first in the stratosphere and then in the thermosphere. The ozone layer, located at around 40 km, is responsible for the heating in the stratosphere. The increase in the thermosphere, where the temperature rises strongly, is a consequence of the low pressure and the absence of an effective energy-loss mechanism. Here, the temperature no longer relates to an equilibrium between the available degrees of freedom. Due to the low pressures, diffusion processes dominate over chemical processes and subsequently gravitational separation arises. Below the thermosphere, chemical processes dominate and the air is essentially a constant mixture of N_2 (80%) and O_2 (20%). Above the thermosphere, i.e., in the exosphere, collisions are no longer important and gravitational escape becomes possible, provided that the escaping particles have sufficient initial velocity.

1.3.2 The Ionosphere

Solar and galactic radiation as well as precipitating solar particles (although mainly restricted to the polar regions) are responsible for the ionisation and excitation of the atmospheric constituents in the upper atmosphere. The ionosphere describes the altitude region of the atmosphere where the concentrations of free electrons and ions are appreciable. The atmospheric ionisation together with the gravitational separation mainly determine the ion-density profiles as shown in Fig. 1.5. Both processes favour atomic ions above molecular ions at high altitudes. The large mean free paths at these very high altitudes enforce this

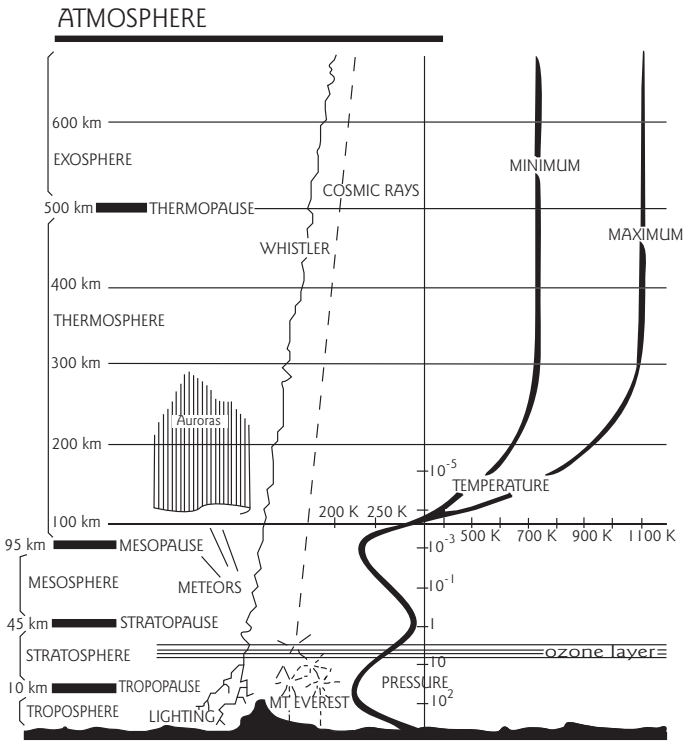

Figure 1.4: The Earth's atmosphere divided into altitude regions based on the temperature profile taken from Ref. [4]. The coldest temperature is found in the mesosphere, which can be as low as 180 K. The hottest temperatures are found in the thermosphere, however, there is no question of an equilibrium between the available degrees of freedom. The *pause* regions denote the borders where the temperature profile changes. The altitude and temperature ranges differ in place and time. The temperature is higher at solar maximum than at solar minimum, which is shown in the figure for the upper atmosphere, where the effect is the largest. Diurnal and seasonal variations are also found.

preference as the much greater number of intramolecular loss processes (dissociation, photon emission) generate many more decay pathways for complex molecular ions than for atomic ions. Chemical processes start to gain in importance towards lower altitudes, resulting in increasing secondary-ion densities. It is noted that the ion-density profiles shown in Fig. 1.5 display strong diurnal, seasonal, and solar activity variations due to the high solar dependency.

The ionosphere is typically split into different regions based on the electron-density profile (see Fig. 1.6), which is connected to the ion-density profiles. Usually, the following regions are defined, the *D*, *E*, and *F* regions, where each region has its specific constituents and processes (see Table 1.1 and text below). The nomenclature is historically defined. The *E* region was the first reflective (electrical) layer to be discovered and was called the Heaviside Layer, after its discoverer. The *F* layer was discovered by Appleton, who suggested to use the symbols *E* and *F* for both layers and thus accommodate other possible layers by using neighbouring letters of the alphabet.

The *F* region

The *F* region is characterised by atomic species, relatively simple chemistry, and transport processes. The overall maximum in the O^+ and electron density occurs as a result of a balance between the plasma transport and chemical loss processes, where the plasma transport processes dominate above this maximum value. Collisions between charged particles and between charged and neutral particles play an important role. The chemistry centres on the conversion of O^+, formed as primary ion, to the secondary ions, O_2^+ and NO^+, through collision with O_2 and N_2, respectively. These molecular ions can recombine with electrons and dissociate. The excitation energy in the dissociative recombination reactions is carried off kinetically or through electronic excitation of the products, giving rise to airglows. The dissociative recombination reactions are the only route to neutralisation. By day, the NO^+

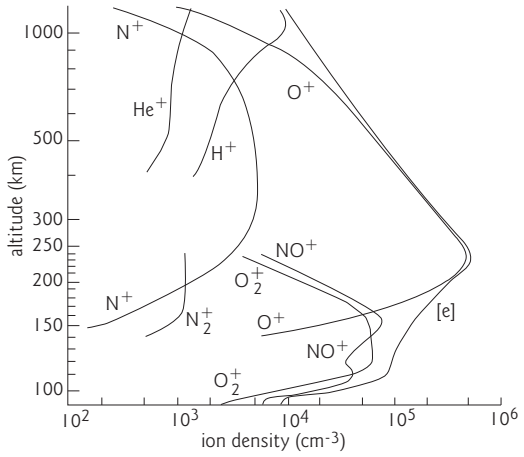

Figure 1.5: The Earth's ion density profiles taken from Ref. [2]. These profiles are mainly determined by the gravitational separation and ionisation processes. Chemical processes become increasingly influential towards the lower altitudes.

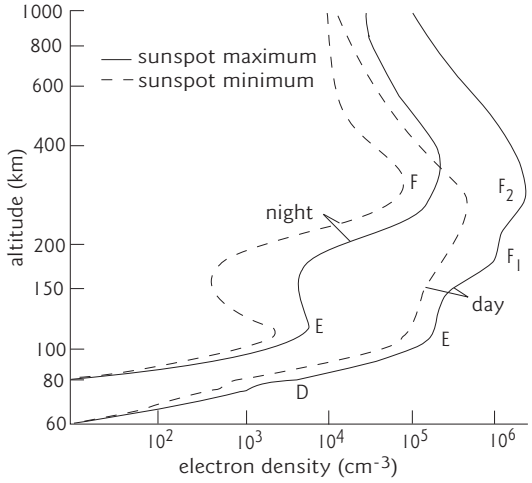

Figure 1.6: The ionospheric *D*, *E*, and *F* regions and the electron density profile taken from Ref. [2]. The borders of the regions are at rapidly increasing electron densities. The solar dependency gives rise to a high temporal behaviour. The F_1 region exists only by day and the electron densities in the *D* region below 80 km go down to zero at night.

route is the most important, because most of the O_2 is photodissociated and hence less O_2^+ is formed.

The *E* region

The *E* region is characterised by molecular ions and chemical processes. The atmosphere is less ionised than in the *F* region and reactions between charged particles are unimportant. The molecular ions N_2^+ and O_2^+ are the primary ionisation products. However, most of the N_2^+ ions are lost in rapid secondary reactions with atomic and molecular oxygen. As a result, O_2^+ and NO^+ are the main molecular ions. Most O_2^+ ions react with N_2 to form NO and NO^+, rather than dissociatively recombine with electrons, because the N_2 density is orders of magnitude higher. As a consequence, the NO^+ route to neutralisation is again the most important one.

The *D* region

The *D* region is characterised by chemical complexity, cluster ions, and negative ions. Around 82–85 km a boundary is observed in the ion profiles, where water-cluster ions dominate below the boundary and the molecular NO^+ and O_2^+ ions dominate above it. The low temperatures, relatively high pressures, and wide range of minor trace reactants permit a multitude of chemical reactions. Three-body chemical reactions (e.g. anion formation) also play an important role, giving rise to strong altitude dependencies as their rates depend on the square of the concentration of the neutral constituents. The atmosphere at these low altitudes is only weakly ionised due to the considerable reduction of photoionisation. The steep decrease in electron density is caused by the reduced photoionisation rate as well as

Table 1.1: Characteristics of the *D*, *E*, and *F* regions of the Earth's ionosphere. The listed values are rough estimates for daytime and high solar activity conditions. There is a division in altitude in the *D* region concerning the main ions. Below roughly 82 km water-cluster ions become dominant over the diatomic ions.

	D		*E*	*F*
altitude (km)	60−100		100−150	150−500
T (K)	200−300		300−700	700−1100
pressure (mBar)	10^{-1}−10^{-4}		10^{-4}−10^{-6}	10^{-6}−10^{-10}
mean free path	cm−0.1 m		0.1 m−100 m	100 m−100 km
collision time	μs−ms		ms−s	s−hrs
defining features	chemical complexity anions, clusters		chemistry dominant molecular ions	simple chemistry atomic ions
defining chemistry	neutral-neutral 3-body reactions		neutral-neutral neutral-ion	neutral-ion ion-ion
main neutrals (%)	N_2 (80), O_2 (20)		N_2 (↓60), O (↑35) O_2 (↓5) [a]	O (↑90), N_2 (↓10) O_2 (↓0) [a]
	<82 km	>82 km		
main ions	$(H_2O)_n.H^+$	NO^+, O_2^+	O_2^+, NO^+, O^+	O^+, NO^+, O_2^+
n[neutral] (cm^{-3})	10^{14}	10^{13}	10^{11}	10^8
n[ion] (cm^{-3})	10^3	10^4	10^5	10^6

[a] The ↓ and ↑ arrows indicate that the given values decrease and increase with altitude, respectively.

by increased loss rates such as anion formation. The dissociative recombination of water-cluster ions also reduce the electron density and additionally act as loss process for the cluster ions themselves. The production rate of the water-cluster ions is dependent on the rate of dimer-ion formation, like $O_2.O_2^+$, which is a three-body process. The rate of O_4^+ formation is highly dependent on altitude, not only due to the pressure dependence, but also due to the destruction by O atoms, the density of which increases sharply with altitude, and due to the negative temperature dependence of formation of weakly bound clusters. The strong dependencies give rise to even stronger temporal variations than in the higher regions.

1.3.3 Airglow Emissions

The energy that is deposited in the Earth's upper atmosphere by the solar and galactic radiation is dissipated mainly through radiative decay processes, giving rise to the airglow. The energy dissipation is, however, slow as the dominant constituents of the terrestrial atmosphere are the symmetric diatomic species O_2 and N_2, which do not radiate in the infrared (in contrast to CO_2 on Mars and Venus). Although the airglow is strongest during the day, the overwhelming scattering of the sunlight hinders ground observations. During the night, airglow emissions can be observed from the ground and if not for its largest contribution in the infrared, the airglow could be seen by the naked eye. The airglow at daytime is called the dayglow and is mainly driven by direct absorption of sunlight (photoexcitation and photodissociation). The airglow at nighttime is called the nightglow and is mainly driven by collisional processes involving particles that have retained the solar energy. The

energy reservoir at night incorporates primarily neutrals at lower altitudes and ions at higher altitudes.

The main airglow contribution originates from electronic transitions of internally excited oxygen and nitrogen, be it atomic or molecular. The strongest dayglow feature on Earth is the *first infrared atmospheric band* due to the transition from the first excited $a\,^1\Delta_g$ state to the ground $X\,^3\Sigma_g^-$ state of O_2. Other atmospheric bands originate from, e.g., N_2, NO, and OH (vibrational) transitions. The excitation of the molecules and molecular ions may be due to direct photoexcitation. Excited atomic species, however, mainly originate from photodissociation or collisional processes, such as the dissociative recombination reaction, rather than direct excitation of the ground state atom. Excitation of the H atom does occur, which leads to the Lyman α atomic-line emissions. Interestingly, many airglows arise from transitions involving long-lived metastable states. This is important as the long radiative lifetimes allow for longer travel distances, which give rise to significant non-local effects, and the metastable species can participate in otherwise endothermic reactions.

The Green- and Red-Line Emissions

Two major atomic-line transitions related to the dissociative recombination reaction are the so-called auroral green- and red-line emissions. The auroral green line of atomic oxygen at 557.7 nm is especially pronounced in the Earth's atmosphere and was the first component of the airglow to be identified with a specific atomic or molecular event. This green airglow arises from the $O(^1S) \rightarrow O(^1D)$ transition, where $O(^1S)$ has a radiative lifetime of 0.71 s [see Fig. 1.7(a)]. The green-line emission is often accompanied by red-line emissions from the $O(^1D) \rightarrow O(^3P)$ transition. This transition actually produces two red lines at 630.0 and 636.4 nm. The radiative lifetime of the $O(^1D)$ state is considerably longer at 108 s. The collision time in the upper *F* region of the ionosphere is, however, sufficiently long that the $O(^1D)$ atoms also radiate their energy away.

Both the green-line and the red-doublet emissions arise in two different altitude regions of the atmosphere. The green and red airglow at lower altitudes (90–100 km, $D-E$ region) are the strongest. Here, the neutral species are the main source of the airglows. By day, the $O(^1D)$ is mainly produced by photodissociation of O_2. Maximum solar energy absorption occurs at 80–110 km producing a maximum in $O(^1D)$ emission. $O(^1D)$ is also formed at

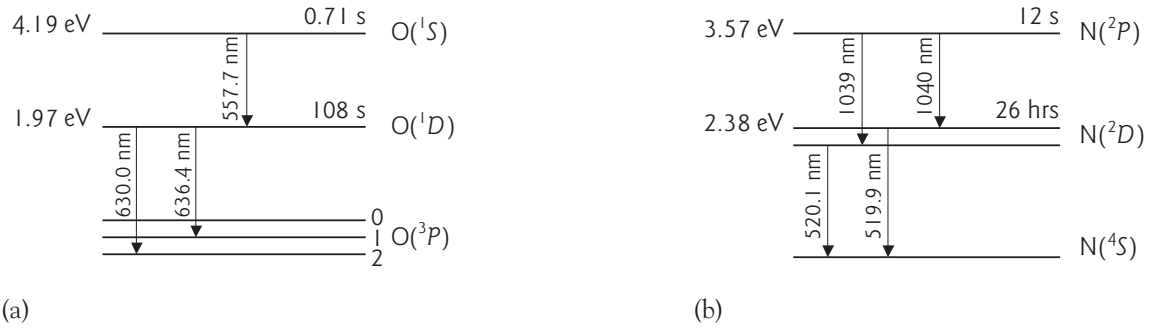

Figure 1.7: Level structure of atomic (a) oxygen and (b) nitrogen, showing the lifetimes, transitions, and emissions of the excited states. The zero-point energy is set at the ground state. Both the $O(^1S)$ and $O(^1D)$ can be formed in the dissociative recombination of O_2^+ with low-energy electrons. The NO^+ route produces predominantly $N(^2D)$ atoms. The excited $N(^2P)$ is energetically not reachable at low-energy electron collisions.

even lower altitudes through photodissociation of ozone (~ 40 km). However, quenching of $O(^1D)$ by N_2 and O_2 is efficient, and at 40 km the collisional lifetime is less than 1 μs, so that radiation is very improbable. By night, the ground state $O(^3P)$ atoms act as energetic reservoir and form $O(^1S)$ atoms in the so-called two-step Barth process; the $O(^3P)$ atoms collide with each other to form excited O_2, which collides with another $O(^3P)$ to form $O(^1S)$. The emission at higher altitudes is in the *F* region. Here, the excitation process comes from photodissociation of O_2 and dissociation recombination of O_2^+ and NO^+. By night, the dissociative recombination reaction is the dominant airglow source, however, galactic radiation is still present. As the present research shows, the NO^+ route cannot yield $O(^1D)$, but predominantly produces $N(^2D)$ which, because of its excessively long radiative lifetime, is not a strong airglow source [see Fig. 1.7(b)]. The O_2^+ route on the other hand yields both $O(^1D)$ and $O(^1S)$, making the O_2^+ ion the only known source behind the green airglow in the *F* region at night.

1.4 Dissociative Recombination

The dissociative recombination (DR) reaction is not only a driving force behind airglows, it is also the cause of planetary escape, neutralisation, radical formation and even of energy production in combustion engines. It is ubiquitous, highly energetic and a fundamentally challenging process to be unravelled. The first quantitative measurements were presented in 1949 and theoretical models on the physics started in 1950. However, even to this day, the reaction still holds its mysteries. The knowledge of the reaction that has so far been attained is insufficient to make the necessary predictions for detailed airglow research and thus laboratory studies remain essential. It is surprising that atmospheric observations were needed to provide information on the physics of the DR reaction rather than laboratory data allowing atmospheric observations to be of diagnostic value. Some of the milestones in the history of the DR reaction concerning the ionosphere and specifically the auroral green-line emission are listed in Table 1.2 and discussed in the next section.

1.4.1 Dissociative Recombination in the Ionosphere

The DR reaction was suggested to be an airglow source in the terrestrial atmosphere as early as 1931, when Kaplan proposed that the DR of O_2^+ might be behind the auroral green-line emission that is observed in aurorae as well as airglow. At the time, it was not known that DR constituted an important process in the ionosphere and it was still thought that the higher atmospheric regions consisted of hydrogen that was very cold and still. In fact, it was not until 1936 that Martyn and Pulley [9] predicted a hot and oxygen-containing upper atmosphere and not until 1947 that Bates and Massey [10] suggested that DR reactions may be responsible for the recombination in the atmosphere (instead of radiative recombination). It took the following two decades to gather enough information to conclusively show DR is indeed the process behind atmospheric recombination [11–16]. A first attempt in predicting the magnitude of the DR rate was made in 1950 by Bates [17]. Bates presented a model including electron capture, autoionisation, and a survival factor for dissociation and concluded that "*in certain by no means exceptional cases dissociative recombination can be extremely rapid*", thereby supporting experimental determinations that the rate is sufficiently high for DR to be the possible recombination process in the ionosphere. A first determination of the validity of the

Table 1.2: Milestones in the history of the dissociative recombination (DR) reaction regarding the ionosphere and specifically the auroral green-line emission.

year	author(s)	description
1931	Kaplan	DR of O_2^+ is proposed as source of the auroral green-line emission
1936	Martyn & Pulley	Prediction of hot upper atmosphere containing oxygen and nitrogen
1947	Bates & Massy	Reactions like DR are proposed as recombination processes in the ionosphere
1949	Biondi & Brown	First quantitative measurements on recombination rates
1950	Bates	DR of molecular ions is suggested process behind these measured rates
1950	Bates	First model to calculate the DR rate yielding 10^{-7} cm^3 s^{-1}
1953	Nicolet	$O(^1S)$ atoms are predicted to be energetically allowed in the DR of O_2^+
1957	Bates & McDowell	Atmospheric DR rate of O_2^+ is required to be $10^{-7/8}$ cm^3 s^{-1}
1961	Kasner, Rogers, & Biondi	Experimentally determined DR rates of O_2^+ and N_2^+
1964	Biondi	DR shown to be important to the mid altitudes of the ionosphere
1966	Warke	Semiclassical theory for the determination of the DR rate
1970	Bardsley & Biondi	Direct and indirect mechanisms in the DR reaction
1979	Guberman	Quantum-mechanical calculation of vibration specific rates in the DR of O_2^+
1986-88	Guberman	Product-state predictions that include direct DR confer no significant $O(^1S)$ production
1990	Bates	Indirect DR mechanism suggested to be important in the DR of O_2^+
1991	Guberman & Giusti-Suzor	Inclusion of indirect DR still predicts no significant $O(^1S)$ production
1997	Guberman	Inclusion of spin-orbit coupling yields finite $O(^1S)$ production

DR of O_2^+ being a source for the auroral green line was presented in 1954 by Nicolet [18]. In his paper the production of $O(^1S)$ was discussed using solely energetic arguments as there was no theory available to predict the specific atomic states of the DR products. He argued that energetically even two $O(^1S)$ atoms could be found in a recombination reaction. In 1966, Warke presented a semiclassical theory to predict the DR rate using quantum mechanics to describe the electrons and classical theory to describe the heavy particles [19]. It took another 30 years before the production of $O(^1S)$ atoms in the DR of O_2^+ could be quantified. Disagreements between theory and experiment stimulated a number of attempts in both fields. At present, no quantitative models exists that can predict the outcome of the DR reaction or its behaviour upon varying conditions with sufficient accuracy to make laboratory experiments superfluous.

As mentioned before (see §1.2), the interpretation of terrestrial green-line observations are hindered by the lack of knowledge on the vibrational dependence of DR reaction. The inability to model this airglow behaviour raises questions as to the role of DR as the sole source for the production of $O(^1S)$ in the *F* region at nighttime. As a consequence, the amount of vibrational excitation of the O_2^+ ions in the Earth's ionosphere is subject to debate. Assuming the DR process is the only source of nighttime green airglow, the atmospheric observations indicate that the vibrational excitation of the O_2^+ ions might be higher than expected, with the amount of excitation increasing upon altitude [20–22]. The quenching processes for the O_2^+ ions are, however, rather efficient indicating that the O_2^+ ions are only weakly excited [20, 23, 24]. Laboratory studies may provide answers on the issue. Ironically, the interpretation of the laboratory research has also been hindered for a long time by the absence of detailed information on the vibrational states of the O_2^+ ions under investigation.

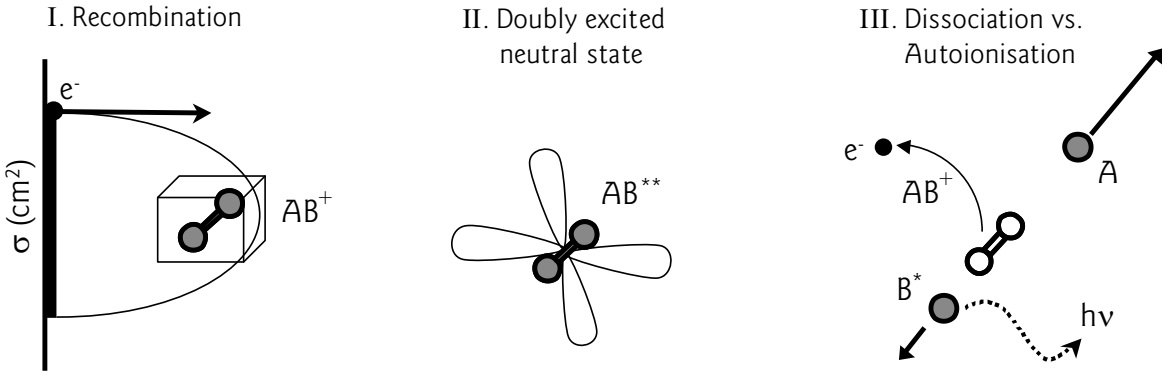

Figure 1.8: Illustration of the dissociative recombination of a diatomic ion. First electron capture occurs. The parabolic (comet-like) trajectory due to the $\frac{1}{r}$ Coulomb interaction is sketched (I). Upon collision and capture the electron loses energy by (generally) exciting a second electron (II). The doubly excited neutral (white) can subsequently dissociate into neutral fragments (grey) or re-emit the electron in an autoionisation process (arrow) (III).

1.4.2 Physics of the Dissociative Recombination Reaction

The DR reaction can be viewed as a two-step process: recombination and dissociation. The general mechanism behind the reaction is called *direct dissociation*, illustrated in Fig. 1.8. First, the molecular ion recombines with an electron (I). The cross section, σ, is indicative of the effective size of the molecular ion, which can be much larger than the geometric size as a result of the long-range Coulomb attraction. Upon recombination, the captured electron loses energy by exciting a second electron and an intermediate neutral is formed, which is doubly excited and unstable (II). A repulsive inter-nuclear force arises that drives the nuclei apart towards dissociation. However, before the nuclei are sufficiently separated such that dissociation is irreversible, the electron may be emitted via an autoionisation process (III). The rate of the DR reaction is determined by the electron-capture possibility and the survival factor after recombination, which defines the probability that the molecule will subsequently dissociate. The energies involved in the reaction are even larger than the ionisation energy of the molecule, since the intermediate neutral state is embedded in the molecular ionic continuum. Upon dissociation, this large energy is given to the fragments as internal excitation or kinetic activation. When internally excited, the product fragments may radiatively relax, giving rise to the airglow. These excited fragments are also highly reactive and chemically important. The ground-state fragments possess the maximum amount of kinetic energy and play a role in atmospheric heating and planetary escape. The DR rate is expressed as rate coefficient ($cm^3\ s^{-1}$) or cross section, σ (cm^2). The rate coefficient is either expressed as function of temperature, $\alpha(T)$, or in terms of collision energy, $k(E_c)$. The thermal rate coefficient is the convolution of the energy-dependent rate coefficient over the Maxwell-Boltzmann distribution of collision energies present at each temperature.

There are often multiple combinations of internal product states possible, which is referred to as the *physical* branching. Each combination of internal states is a *physical* dissociation limit or branching channel. The branching is expressed in either branching fractions or quantum yields. The *physical* branching fraction, B_β, denotes the percentage of the total reactivity going into a specific *physical* dissociation limit, β. The quantum yield is the number of atoms produced in a specific state in an average DR event. For a diatomic molecular ion,

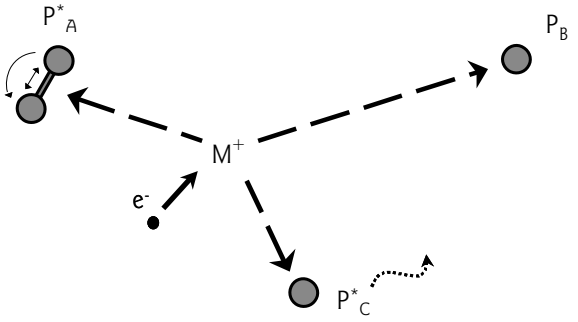

Figure 1.9: Illustration of the dissociative recombination of a polyatomic ion. The fragments produced can be atoms as well as molecules, where the molecular products may also be rovibrationally excited. In polyatomic systems, not only the internal states of the product fragments may vary, but also multiple *chemical* fragmentation pathways may be possible.

the quantum yields add up to two and the branching can be expressed by

$$\begin{aligned} AB^+(\mathrm{n}, v, J) + e^-(E_c) \quad &\rightarrow A(\mathrm{n_A}) + B(\mathrm{n_B}) \ + \mathrm{KER} \\ &\rightarrow \ldots \text{ branching to channel } \beta \ \text{ for } B_\beta\,\% \end{aligned} \tag{1.1}$$

where the molecular ion AB^+ can be in any rovibronic internal state, (n, v, J), and the electron that recombines with the ion can bring any amount of kinetic energy along into the reaction. This energy is called the collision energy, E_c, and is the translational energy of the electron in the molecular frame. The internal energy of the parent ion along with the collision energy determines the total energy available. The neutral product atoms A and B formed in the reaction may be in a ground or electronically excited state, represented by $\mathrm{n_A}$ and $\mathrm{n_B}$. The kinetic energy release (KER) of the reaction is the difference between the initial energy and the total internal energies of the product atoms.

The DR reaction of a polyatomic ion is more complicated (see Fig. 1.9). First, the product fragments may be atoms as well molecules and these may also be rovibrationally excited. The number of possible *physical* branching channels is therefore very large. Second, the break-up of a polyatomic ion can lead to different combinations of atomic and molecular fragments irrespective of their internal state. This chemical break-up is described in terms of *chemical* branching or fragmentation and can be expressed by

$$\begin{aligned} \mathrm{M}^+ + e^- \quad &\rightarrow P_A \ + P_B \ (+P_\mathrm{C}) + \mathrm{KER} \\ &\rightarrow \ldots \text{ fragmenting to channel } f \ \text{ for } F_f\,\% \end{aligned} \tag{1.2}$$

where M^+ is the polyatomic ion and P_A, P_B, and/or P_C are the product atoms or molecules. For each fragmentation channel, the fragments and/or the number of fragments that are produced may differ. The *chemical* branching fraction, F_f, denotes the percentage of the total reactivity going into a specific fragmentation channel, f. Each *chemical* fragmentation limit groups together a number of *physical* branching limits.

Dissociative Excitation

A second reaction process investigated in this thesis is the dissociative excitation (DE) reaction, which is closely related to the DR reaction. When sufficient energy is available to the dissociation reaction, one of the product fragments may be an ion. Hence, the electron is not permanently captured in the DE reaction. The DE reaction is an endothermic reaction,

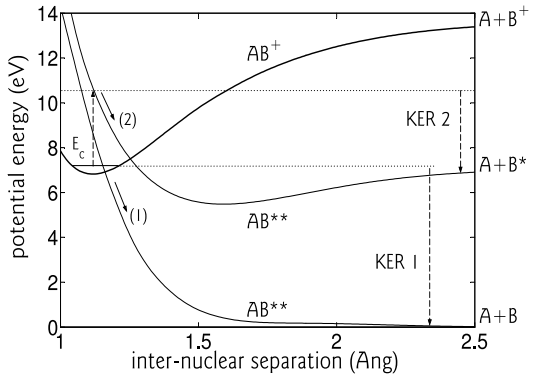

Figure 1.10: The direct dissociation mechanism in the DR reaction. The electron is captured, producing a doubly excited neutral repulsive state, giving rise to dissociation. At 0-eV collisions, the neutral repulsive state leading towards ground-state atoms is accessible (1). The neutral state dissociating towards $A+B^*$ becomes accessible when additional energy is added into the reaction (2). The kinetic energy release (KER) of the respective pathways are indicated. Note that path (1) is also accessible at higher collision energies and the electron may be captured in either state.

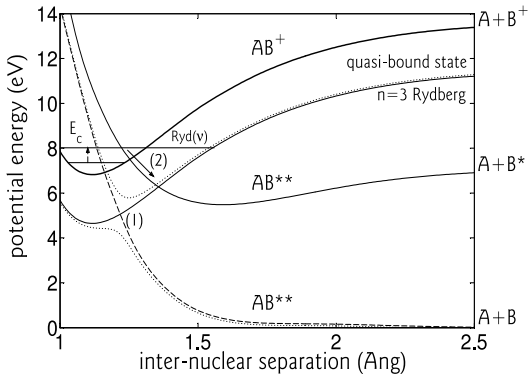

Figure 1.11: The indirect dissociation mechanism in the DR reaction. At the small arrow a quasi-bound rovibrationally excited state is formed in the Rydberg state, which is subsequently (pre)dissociated by a doubly excited valence state (1). Alternatively, the elongation of the molecular bond in the vibrationally excited Rydberg state may open a (pre)dissociation pathway by a doubly excited state that would otherwise not be open (2).

which will only become energetically possible above the dissociation energy of the molecular ion, and can be expressed by

$$\mathrm{M}^+(\mathrm{n}, v, J) + e^-(E_c) \rightarrow P_A \; + P_B^+ + e^- \; - E_t \tag{1.3}$$

where the energy, E_t, is the energy required to break a bond. This energy can be supplied by internal excitation of the parent ion or by the electron as collision energy.

Direct and Indirect Dissociation Mechanism

The quantum-chemical picture of the process of *direct dissociation* is illustrated via the potential curves shown in Fig. 1.10. The initial state is the rovibronic state of the AB^+ ion. Direct capture means that the electron is directly captured into a doubly excited neutral state. The repulsive neutral state must either cross the initial ionic state (path 1) or enough collision energy must be provided to access the repulsive state around the inter-nuclear distances of the initial ionic state (path 2). The shown doubly excited neutral states, AB^{**}, lead to the asymptotic limits, $A+B$ and $A+B^*$, where the star denotes excitation. Although the excited limit $A+B^*$ is energetically allowed at 0-eV collisions, the pathway towards it is only accessible at high collision energies (or excited ionic states). Typically, multiple repulsive neutral states are involved that may lead to the same or more dissociation limits. Autoionisation is possible in the region where the inter-nuclear separation does not exceed that of the bound ionic state.

A second important mechanism for DR is the *indirect dissociation* process, which involves Rydberg states of the neutral molecule with principal quantum numbers of 3 to 10. This mechanism is illustrated in Fig. 1.11, which shows the same dissociation limits as in Fig. 1.10

along with some of the complications involved in the DR process. The initial capture may take place at discrete energies in a rovibrationally excited level in the Rydberg state, indicated by Ryd(v). Through (pre)dissociation of this Rydberg state, the capture process results in the formation of the fragments. In the shown pathway (2), the Rydberg state allows for elongation of the inter-nuclear separation such that electron capture may occur although the repulsive valence state itself is not directly accessible. Hence, coupling between the Rydberg and the valence state may result in dissociation to otherwise inaccessible limits. The Rydberg states affect the dissociation via already accessible valence states as well. An example of a strong Rydberg-valence coupling is illustrated in the so-called adiabatic representation of the potential curves (1). Instead of the original repulsive valence state, a quasi-bound and a perturbed dissociating state are formed, both possessing a mixed valence and Rydberg character. Capture may thus take place in the rovibrational levels of this quasi-bound state. The Rydberg-valence coupling results in (pre)dissociation. The indirect process may both enhance or decrease the direct DR rate. The quantum-chemical picture shows us that the dissociation behaviour may be very complicated and small changes may result in entirely different outcomes.

More complications may play a role in the dissociation behaviour, such as spin-orbit coupling between valence states of different symmetries. In fact, spin-orbit coupling is extremely important to the O(^{1}S) production in the DR of O_2^+ (see Chapter 4). Spin-orbit coupling in the DR reaction is usually of minor importance as the dissociation occurs on a fast time scale of fs, as does autoionisation. This time scale is much faster than the time required for a spin flip. Interestingly, dissociation is also faster than the rotational times (ps) of the intermediate neutral molecule. This may result into an additional effect in the DR reaction, which is an angular dependence on the orientation of incoming electron with respect to the molecular axis. The aspect of angular dependence is investigated in the DR of O_2^+ as well as NO^+ (see Chapters 4 and 5).

Statistical Model

In contrast to the complex quantum-chemical picture of the DR reaction, the reaction may also be approached from a statistical point of view [25]. The branching fractions of the dissociation limits may be modelled through the orbital angular momentum degeneracy and the spin multiplicity, giving the number of possible molecular states connected to a certain dissociation limit. For example, the number of molecular states connected to $A(^1D) + B(^1D)$ and $A(^3P) + B(^3P)$ is $1 \cdot 5 \cdot 1 \cdot 5 = 25$ and $3 \cdot 3 \cdot 3 \cdot 3 = 81$, respectively. Thus the respective branching fractions are 25/106 = 24% and 81/106 = 76%. In addition, the spin-forbidden pathways may be excluded from the model as it is known that generally only spin-allowed transitions play a role in the DR reaction. For example, when both the parent ion and the electron have spin half, initial neutral symmetries may be formed of both singlet and triplet character. As the possible molecular states connected to the $A(^3P) + B(^3P)$ symmetry also include quintet states, these have to be excluded from the number of states that are taken into account, leaving only 36 of the 81 states, thus changing the branching fractions into 25/61 = 41% and 36/61 = 59%. Although the statistical model does not include Rydberg-valence couplings nor explains any dependence such as on the vibrational level of the parent ion, the mere fact that it often agrees with observation is very surprising, as will be shown in Chapter 5. This statistical behaviour of the DR of diatomic ions stands in contrast to the complex

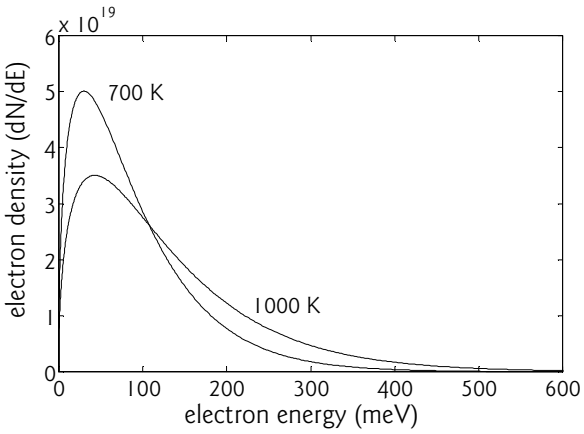

Figure 1.12: The electron-energy distributions at 700 and 1000 K based on the Boltzmann distribution. For dissociative recombination reactions in the atmosphere, these electron energies are representative for the collision energies between the electrons and molecular ions.

quantum-chemical aspects underlying the DR reaction. It is noted here that this relatively 'simple' DR behaviour extends to largely comparable DR rates for molecular ions of similar size. This apparent simplicity in spite of the complex underlying mechanisms illustrates the challenge of unravelling the DR reaction as a fundamental process.

Some Atmospheric Numbers

In the *F* region, the major ions are O_2^+ and NO^+, the pressure is very low at 10^{-5} to 10^{-7} mbar, and the temperature is roughly between 700 and 1000 K. At night the electron and the molecular ion density are on the order of 10^5 and 10^4 cm^{-3}, respectively, whereas the density of neutral species is a few orders of magnitude higher at 10^8 cm^{-3}. The DR rate and the product states are dependent on the internal states of the parent ions and the electron temperature, which gives rise to altitude dependent products and emission intensities in the atmosphere. Figure 1.12 shows the electron energies based on Boltzmann distributions at 700 and 1000 K. These electron energies are representative of the collision energy between the electrons and O_2^+ and NO^+ ions. As can be observed, the collision energies are mostly below 300 meV. This sets the necessary energy range for performing the laboratory experiments. However, it is noted that at high altitudes (> 200 km) the electron temperatures may well be significantly higher than the ion and neutral temperature.

1.5 My Thesis

The research presented in this thesis studies the DR reaction of the two main molecular ions on Earth, O_2^+ and NO^+, as well as the $(NO)_2^+$ dimer ion, both for their atmospheric importance as well as for their fundamental relevance in understanding of DR mechanisms. Additionally, a computational study has been carried out to increase the understanding on the mechanisms involved in the DR reaction. A major challenge in the DR of O_2^+ was to develop a means of creating, characterising, and reproducing vibrational populations that we could subsequently study. Extreme conditions of control during the experiment were necessary in order to investigate the finer details of the DR reaction. The capabilities of the detection techniques and the limited amount of time available for experiments also proved to be challenging. A summary of all the presented studies and their aims is given below. An overview of all the measurements that were carried out in the four laboratory studies is given

in Appendix A. In the next two chapters the experimental setups and data analysis used in these laboratory studies are described. After discussing the apparatus and data analysis, each of the four subsequent chapters presents the data and results obtained from the experimental and computational studies.

- **Chapter 4: Dissociative Recombination of O_2^+**
  Experimental investigation of the potential influences in the DR of O_2^+, divided into two parts. The first part covers the electron-energy dependence of the dynamics in the DR of O_2^+ relevant for temperature dependent branching in the atmosphere (up to $\sim$1000 K). This study reports the energy-dependent branching fractions as well as quantum yields and addresses the aspect of anisotropy in the DR reaction. The second part covers the vibrational-state dependence of the rate and dynamics in the DR of O_2^+ relevant to the green-line emission. This study reports total rate coefficients of vibrational populations and partial cross sections and branching fractions of the individual vibrational levels. It includes the development of an ion source to create and control vibrational populations of O_2^+ ions as well as the characterisation of these populations. This examination additionally addresses super elastic collisions between the electrons and the O_2^+ ions, which give rise to vibrational quenching of the ions.

- **Chapter 5: Dissociative Recombination of NO^+**
  Experimental investigation of the branching of the ground state of NO^+ at 0, 1 and 5 eV collision energy and the first metastable $a\,^3\Sigma^+$ state of NO^+ at 0 eV collision energy. This study revolves around the possible productions of the highly reactive $N(^2D)$, the red-airglow emitter $O(^1D)$, and highly energetic ground-state fragments, which may escape gravitational forces. The aspects of statistical behaviour, the spin-forbidden channels, and anisotropy in the DR reaction are addressed. The so-called toroidal effect relevant to storage-ring experiments is included for the first time in the analysis of DR dynamics data. Also, the DR reaction is implemented for the first time as measure of radiative lifetime, namely of the metastable $a\,^3\Sigma^+$ state.

- **Chapter 6: Super-Dissociative Recombination of $(NO)_2^+$**
  Experimental investigation of the rate, fragmentation, and dynamics in the DR of a weakly-bound dimer ion. This study is mostly qualitative and focuses on the issues of the enhanced DR cross section often observed in the DR of dimer ions, the break-up mechanisms involved in the DR of a weakly-bound system, and the degree of similarity of the $(NO)_2^+$ dynamics to the monomer ion. Additionally, experimental difficulties such as fragment identification are addressed.

- **Chapter 7: Computational Study on Dissociative Recombination**
  Computational study of the quantum-chemical aspects relevant to the DR reaction: direct and indirect dissociation, autoionisation, electron-capture widths, and couplings effects. The computations are implemented for the DR of O_2^+ and empirically based on previously determined and optimised O_2^+ potential curves, coupling strengths, and electron-capture widths.

.

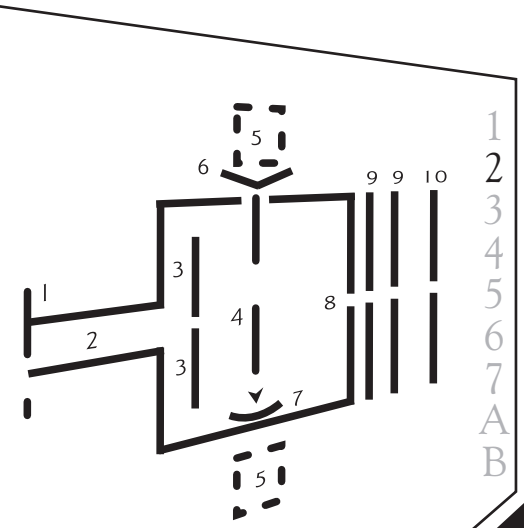

Physics is...

trying to explain my sister how to spin the bal

– eldest sister of –

Annemieke

Chapter 2

Experimental Descriptions

The central goal of the laboratory research was to obtain reliable data on the effect of the internal state of the parent ion on the dissociative recombination (DR) reaction. In order to produce different vibrational distributions, an ion source had to be developed and characterised and a DR experiment had to be performed in which these distributions were preserved. The central instrument used in the laboratory studies is the CRYRING *heavy-ion storage ring. An important technique for the ion source development is translational spectroscopy. The combination of different techniques and instruments generated the possibility for state selected DR studies. This chapter describes the heavy-ion storage ring,* CRYRING*, located at the Manne Siegbahn Laboratory in Stockholm and the fast-beam translational spectroscopy apparatus located at SRI International, Menlo Park, California. First, a general description of the heavy-ion storage ring is given, followed by detailed descriptions of the electron cooler and the ion sources and detectors used. Special attention is given to the new ion source, which was developed for these experiments and then tested and characterised using the fast-beam translational spectroscopy technique that is discussed at the end of this chapter.*

2.1 The Heavy-Ion Storage Ring CRYRING

The heavy-ion storage ring, CRYRING, is an electromagnetic storage-ring facility used for research in atomic, nuclear, and molecular physics. CRYRING stands for CRYsis-synchrotron-RING, where CRYSIS stands for CRY*ogenic* S*tockholm* I*on* S*ource* [26]. This is the special ion source dedicated for the production of highly charged ions. The ring has been operational since 1990. The first test ion beam, consisting of H_2^+ ions, made one turn in the ring at the end of 1990, followed by storage for seconds in 1992. A beam-cooling device, called the electron cooler (see §2.1.2), was installed in May 1992 [27]. The DR experiments started the year after with research on H_3^+ [28], preceded by a feasibility study of the suitability of storage rings for DR [29]. Many researchers have investigated and performed experiments on a diverse collection of atomic, molecular, singly-, and multiply-charged cations, and even anions, ever since, both using electron collisions or laser excitation tools. CRYRING is a complex, versatile and large facility. The ring alone has a total circumference of 51.6 m. The number of parameters to be handled by the control system goes up to 300 of which 50 can vary in time requiring autonomous function generators [30]. The pressure inside the ring approaches an interstellar vacuum of 10^{-11} mbar, providing storage times up to tens of seconds. Furthermore, superconducting magnets were installed in 1997 that could produce the necessary high magnetic fields near the electron cooler [31] for the production of near mono-energetic beams (see §2.1.2). CRYRING is particularly powerful for studies of ion-electron reactions, among which is the DR reaction, because of its ability to merge a cold electron beam with the stored ion beam at collision energies tuned to a nominal 0 eV.

A photograph and schematic picture of the ring is shown in Fig. 2.1. The path the ions follow starts at the top right of the schematic, then goes to the left towards the ring, and then continues counterclockwise around the ring. Along this path, the ions are created (I), extracted, mass-selected (II), pre-accelerated (III), injected (IV), and further accelerated (V) to finally form a continuous, energetically well-defined, stored ion beam. Neutral products that are created in the electron cooler (VI) exit the ring without deflection into a zero-degree arm (VII). The ring section consists of twelve straight sections connected by twelve main

dipole magnets that together define the orbit of the ion beam in the ring. Six of the twelve sections contain quadrupoles and sextupoles, which function as focusing devices for the ion beam. The other six sections contain equipment for injection, acceleration, diagnostics, and experimental equipment like the electron cooler. The main source of ion-beam destruction in the ring comes from collisions of the ions with rest-gas molecules. The rest gas mainly consists of H_2 molecules (90%). However, it is the remaining 10% (e.g. CH_4, CO, CO_2, Ar) that determines the ion-beam lifetime [32]. The long storage times that can be achieved provide time for molecular ions with a permanent dipole moment to cool vibrationally through radiative decay. The storage times are generally not sufficient for considerable rotational cooling. The rotational temperature of the ions is mainly determined by the temperature at their production [33]. For the ions described in this thesis, storage times of seconds are easily achieved. It is noted that for H_2^+, which can be stored at much higher beam energies, storage can be as long as a minute.

2.1.1 CRYRING as Dissociative Recombination Experiment

An experimental study at the CRYRING is typically performed within one beam week of beam time, during which one or more measurements are carried out. A summary of the measurements described in this thesis can be found in Appendix A. The description of a typical DR measurement follows here. An appropriate ion source is chosen and installed on the ion-source platform (I). The voltage of the platform is raised to 40 kV, providing the means for pre-acceleration towards the ring. All ions created inside the source are electrostatically extracted, while an analysing magnet located just after the ion source takes care of mass selection (II) ($\frac{\Delta m}{m} \approx \frac{1}{200}$). Generally, ion sources operate in a continuous mode and fill the ring only during injection. A number of ion sources can be operated in a pulsed mode and are synchronised with the injection and detection cycle of the ring. The ion beam is pre-accelerated (III) to the 40 keV platform-energy before injection into the storage ring (IV). A radio frequency quadrupole (RFQ) linear acceleration is available, however its use is limited to light ions ($m/q \leq 4$) [34]. Once in the ring, the ion beam is further accelerated (V) up to a maximum beam energy of $90/m$ MeV with m the mass in atomic units. The upper limit is due to the use of magnetic deflection. The time it takes to accelerate the ions to the full beam energy depends on the ion mass and is about a second for the ions described in this thesis. Shorter acceleration times (150−200 ms) are possible, but require a more complicated acceleration procedure [35]. Acceleration of the ion beam results in narrowing and stabilisation of the ion beam. In fact, the period of the ions is highly stable and is known to six significant digits, determined with the so-called Schottky spectrum using a non-destructive pick-up device in the ring. The ion beam is shaped further in the electron cooler (VI), where a cold electron beam is merged with the ion beam (see §2.1.2). Throughout storage, the ion beam continuously circulates around the ring undergoing electron-ion reactions in the electron cooler, such as the DR reaction. All neutral products from these reactions fly straight into a zero-degree arm (VII) following the electron cooler. This zero-degree arm functions as detection region (see §2.1.4). The arm is opened to the ring by a shutter only during actual measurements. This is mostly for protection of the detectors. At the start of the measuring process, the shutter opens and, when required, the detection systems are triggered. The time window during which the measurement takes place is called the measuring gate. From injection to the start of the

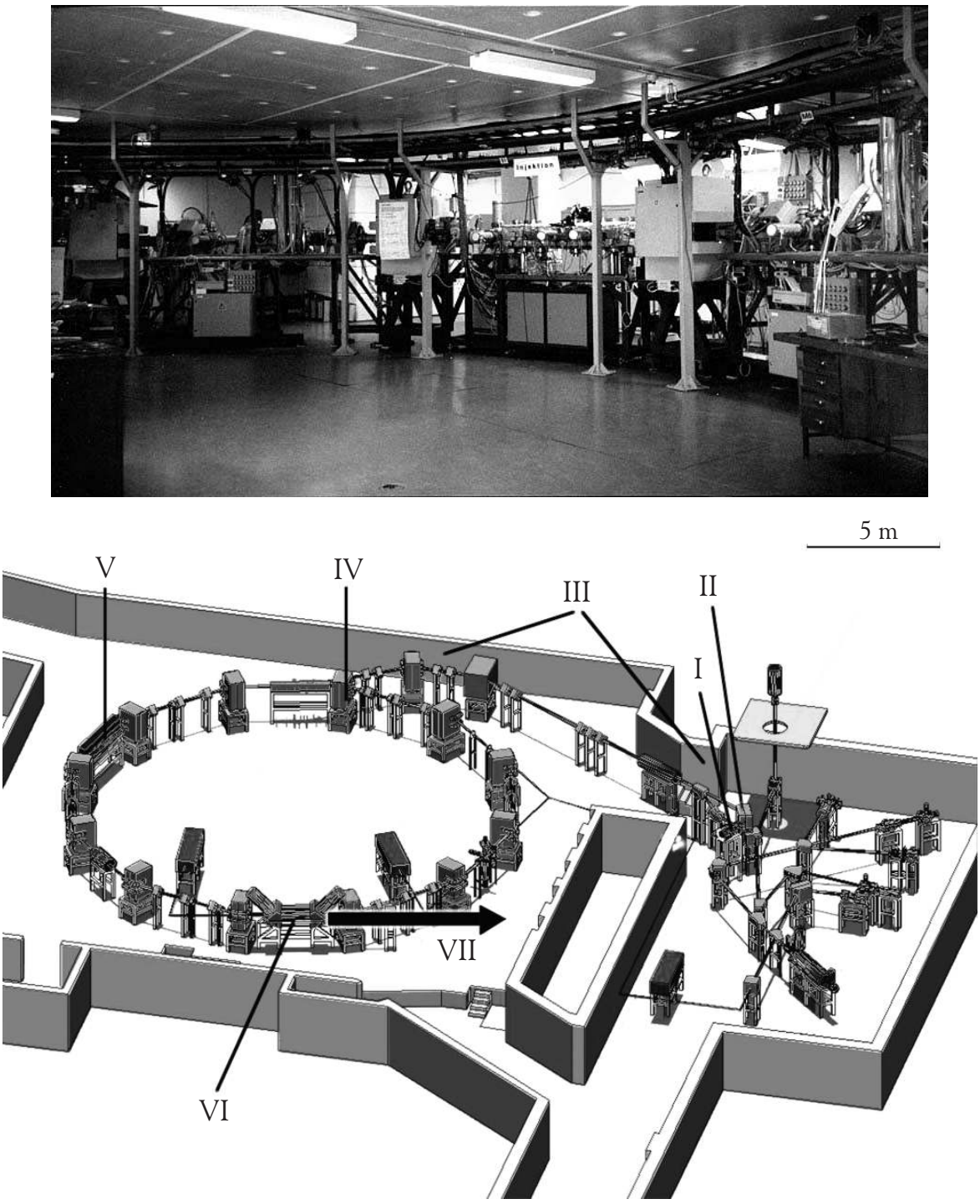

Figure 2.1: The heavy-ion storage ring CRYRING. In all experiments, the ions follow the path starting at the right, going to the left towards the ring, and then continuing counterclockwise around the ring, while the neutral DR-reaction products leave the ring on the bottom to the right. Along this path, the ions are created (I), extracted, mass-selected (II), pre-accelerated (III), injected (IV), and further accelerated (V) to finally form a continuous, energetically well-defined, stored ion beam. The neutrals produced in and around the electron cooler (VI) exit the ring without deflection (VII). Throughout storage, the ion beam continues going around the ring, while interacting with the electrons and the rest gas and often travelling distances as large as the Earth-Moon distance at velocities of 1% of the speed of light. The photograph is taken from inside the ring facing the injection point (IV).

measuring gate, the electron beam can be set to match the ion velocity to ensure so-called phase-space cooling of the ion beam (see §2.1.2). Each full storage time from injection to the moment the ion-beam is destroyed (the ion beam is dumped after a set time) is referred to as a beam cycle. After each cycle, the ion beam is refreshed by a new pulse from the ion source. Each newly stored ion beam equals the previous one, unless experimental conditions are changed (such as the ion-source conditions). A complete measurement consists of data integrated over many beam cycles.

Throughout storage, the ions collide with the rest-gas molecules everywhere in the ring, giving rise to charge-transfer (CT) reactions,

$$M^+ + R \rightarrow M + R^+ \tag{2.1}$$

and collision-induced dissociation (CID) reactions,

$$M^+ \xrightarrow{R} P_A^+ + P_B \tag{2.2}$$

where M^+ is a molecular ion, R is a rest-gas molecule, and the product fragments in the CID reaction are charged and neutral, represented by P_A^+ and P_B. CT reactions generate neutral products that give rise to a background signal at the same mass as the DR signal. CID reactions generate neutral and charged products as also occurs in dissociative excitation (DE). Hence, the background collisions occurring in and around the electron cooler give rise to a background contribution both in the DR and the DE signals. The destruction rate is usually constant over the storage time, giving rise to a mono-exponential decrease in the ion-beam intensity. When DR or DE reactions start playing a role in the beam destruction, the ion-beam lifetime becomes more complicated as the DR and DE rates are dependent on the electron energy and the ionic states. By monitoring background signal in other regions of the ring than the electron cooler, a measure of the ion-beam intensity is obtained, which makes it possible to measure the beam lifetime. The fact that the DR reaction, which only takes place over 0.85 m of the total circumference of 51.6 m, can affect the beam lifetime is an indication of the enormous DR cross section, because, despite the ultra-high vacuum, the density of background gas is still similar or larger than the electron density achieved. One has to keep in mind though, that the energy difference between the ions and the electrons is small (even down to 0 eV), which increases the efficiency of the collisions, whereas between the rest-gas molecules and the ions it is on the order of MeV energy, resulting in very small destruction cross sections.

2.1.2 The Electron Cooler

The electron cooler has two functions. The first function is implied by its name; electron cooling of the ion beam. The second function is to act as reaction region for the DR or DE studies. The electron cooler generates a nearly mono-energetic electron beam, which can be merged with the stored ion beam over a distance of nearly one metre [31, 36].

The Electron Beam

The electron-cooler is shown in Fig. 2.2. As can be seen from the photograph, it is quite an imposing piece of equipment. The electrons are produced at a cathode of 4 mm diameter (top-left of the schematic) at a temperature around 1200 K, corresponding to an electron-energy

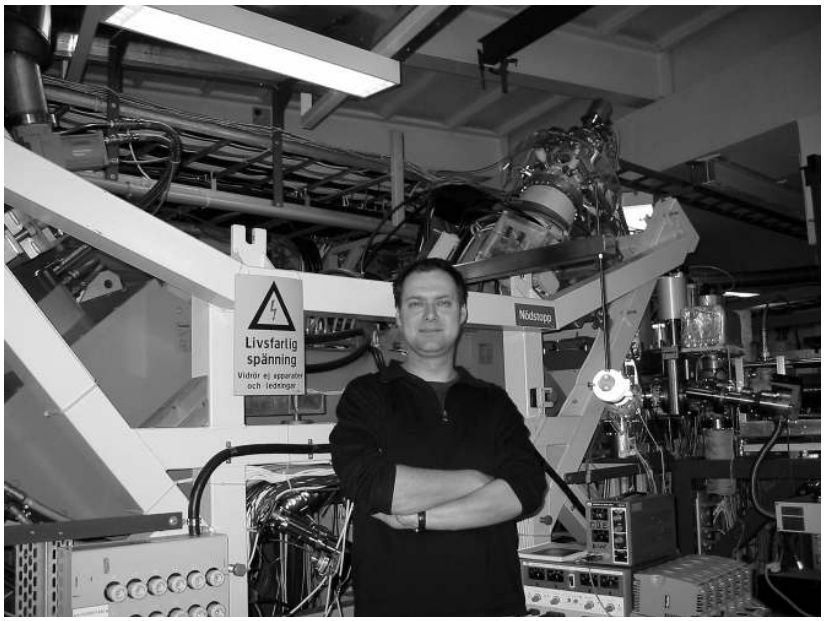

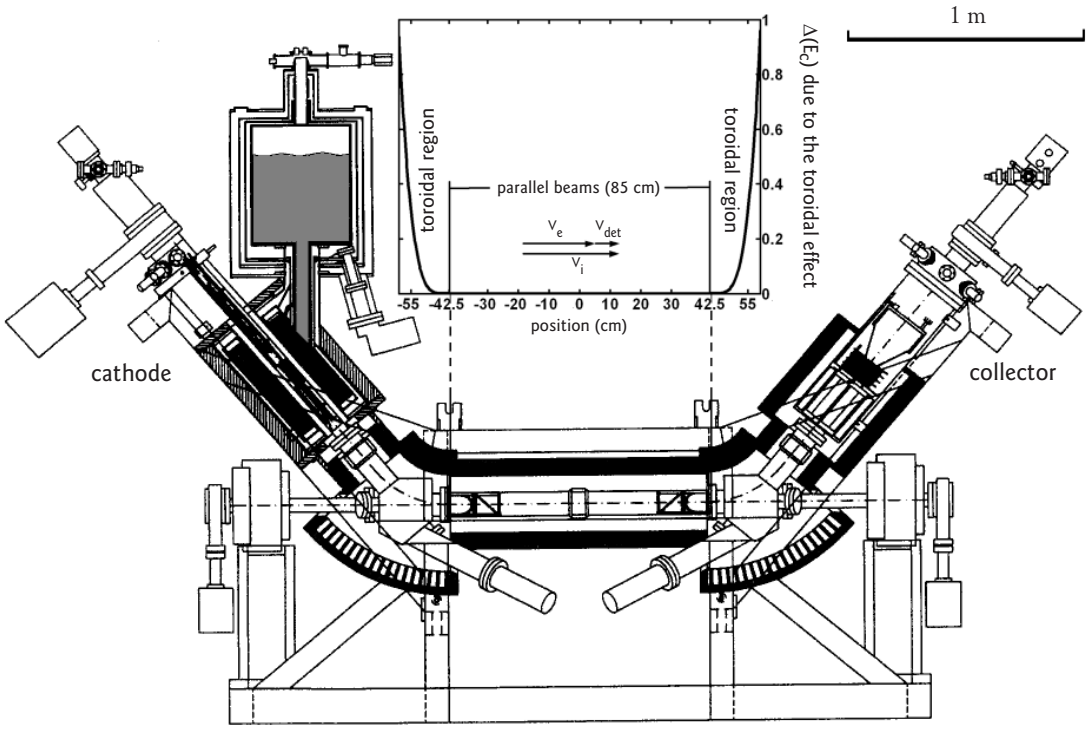

Figure 2.2: The electron cooler of the CRYRING, which acts as beam cooling device as well as interaction region. It is capable of producing very cold electron beams with transversal and longitudinal temperature of 1−2 and 0.1 meV, respectively. The electrons are produced at the cathode, then expanded and accelerated down to the ion beam, where the electron beam is merged over a finite length with the ion beam and then deflected up to the collector. The photograph gives an impression of the size of the electron cooler. Standing in front of the device is my husband, who is 1.85 m tall.

spread of 100 meV. The electrons are then adiabatically expanded (by a factor of 100) and accelerated to match the velocity of the stored ion beam. This process of first parallelisation followed by acceleration reduces the velocity-spread considerably. The resulting velocity spread of the electron beam can be described by the anisotropic bi-Maxwellian distribution,

$$f(\mathrm{v}_e) = \frac{m_e}{2\pi \mathrm{k} \mathrm{T}_{e_\perp}} \sqrt{\frac{m_e}{2\pi \mathrm{k} \mathrm{T}_{e_\parallel}}}\, exp\left(-\frac{m_e \mathrm{v}_{e_\perp}^2}{2\mathrm{k}\mathrm{T}_{e_\perp}} - \frac{m_e(\mathrm{v}_{e_\parallel} - \overline{\mathrm{v}}_{e_\parallel})^2}{2\mathrm{k}\mathrm{T}_{e_\parallel}} \right) \tag{2.3}$$

where m_e is the electron mass (kg), k is the Boltzmann constant (J K^{-1}), $\mathrm{T}_{e_\perp}$ and $\mathrm{T}_{e_\parallel}$ are the transversal and longitudinal electron temperatures (K), respectively, $\mathrm{v}_{e_\parallel}$ and $\mathrm{v}_{e_\perp}$ are the longitudinal and transversal electron velocities (m s^{-1}), respectively, and $\overline{\mathrm{v}}_{e_\parallel}$ is the mean longitudinal velocity of the electron beam (m s^{-1}). The mean transversal velocity is not included as it is zero. The expansion and acceleration employed at the CRYRING reduces the transversal and longitudinal electron-energy spread to $\mathrm{k}\mathrm{T}_{e_\parallel} \approx 0.1$ meV and $\mathrm{k}\mathrm{T}_{e_\perp} \approx 1{-}2$ meV, respectively. The transversal spread is solely determined by the expansion. However, the longitudinal spread is determined by a combination of the initial spread, the amount of acceleration, and the electron density (electron-electron interactions). The amount of acceleration depends on the ion-beam energy and the desired electron energy during the experiment. For example, for O_2^+ the desired electron energy is around 54 eV, whereas for $(NO)_2^+$ it is merely around 16 eV. After expansion and acceleration, the electron beam is merged with the ion beam over a distance of 0.85 m distance (central region of the cooler). The electron beam is then deflected and decelerated back to an energy close to the cathode potential and dumped in a collector (top-right of the cooler).

The electron-beam energy is determined by the acceleration, $E_e = q_e U_{cath}$, where q_e is the electron charge (C) and U_{cath} is the cathode potential (V), i.e., minus the contact-potential drop (Fermi potential) that arises due to the transition of the electrons from the metal to the vacuum. An important correction on the electron energy comes from the self-induced space charge of the beam. The space charge gives rise to a drop in energy towards the centre of the beam, creating a well in the electron-beam potential. The space charge energy can be expressed as,

$$E_{sp} = \frac{I_e\, r_c\, m_e\, c^2}{q_e\, \mathrm{v}_e} \left(1 + 2ln\left(\frac{b}{a}\right)\right) \tag{2.4}$$

where E_{sp} is the self-induced space charge energy (J), I_e is the electron current (A), r_c is the classical radius of the electron (m), m_e is the electron mass (kg), c is the speed of light (m s^{-1}), v_e is the longitudinal electron velocity (m s^{-1}), and a and b are the diameters of the vacuum tube and the electron beam, respectively. The vacuum tube is the reference of the ground potential and its diameter is 10 cm. The electron-beam size is typically ~ 4 cm in diameter and may be changed, for example, in experiments that require a high electron density. A high density is achieved at the cost of electron-energy resolution. It is noted that the space-charge correction may additionally be affected by the generation of positive ions in the electron beam due to electron collisions on rest gas, which modifies Eq. (2.4) slightly [see Eq. (2.9)].

Electron Cooling

When the cold electron beam is merged with the ion beam, heat is transferred from the ions to the electrons, decreasing the velocity spread of the ion beam. This does not affect the internal degrees of freedom of the ions. In recent years it has been discovered that the interactions between the 'cold' electrons and the ions may also give rise to internal cooling [see Eq. (2.8)]. These interactions have become an active field of research in the last few years and also form part of the investigations presented in this thesis (see §4.9.1). The cold electron beam is continuously renewed, allowing for continuous cooling of the ion beam and achieving a well-defined beam energy. The cooling process further reduces the emittance of the ion beam and results in a measurable decrease of the ion-beam size. At the high beam energies of an H_2^+ experiment, the final beam size can be as small as 1 mm. In our experiments with O_2^+ at 3 MeV, the beam size is around 6 mm.

Electron-Ion Collisions

The electron cooler is the interaction region for the DR and DE reactions [see Eqs. (1.1)−(1.3)]. The electron cooler can be split into three sections (see Fig. 2.2). In the central part, which is 0.85 m long, the electron and ion beam are co-axial, giving rise to very low-energy collisions. In this region, the collision energy is determined by the detuning velocity,

$$\mathrm{v}_{det} = \mathrm{v}_i - \mathrm{v}_e \tag{2.5}$$

where v_i and v_e are the longitudinal ion and electron velocities in the lab-frame, respectively (see Fig. 2.2). On either side of the centre section there is a so-called toroidal region, where the electron beam is merged into and deflected out of the ion beam. Here, the collision energy increases steeply as the angle between the two beams increases (indicated in the inset of Fig. 2.2). The toroidal regions are each about 12.5 cm long. The correction for the toroidal effect is described in the next chapter (see Chapter 3). It is noted that, unless otherwise specified, the term collision energy as used in the experimental studies refers to the relative energy in the central section of the cooler as determined by the detuning velocity,

$$E_c = \frac{1}{2}\,\mu\,\mathrm{v}_{det}^2 \tag{2.6}$$

where μ is the reduced mass and $\mu = \frac{m_i\, m_e}{m_i + m_e} \approx m_e$ since $m_i >> m_e$ for all molecules. At 0 eV collision energy, the electron velocity is tuned accurately to the ion velocity. The associated electron-beam energy is referred to as the cooling energy, because the electron-cooling effect is optimal at the velocity-matched condition. Using $\mathrm{v}_e = \mathrm{v}_i$ at cooling and $\mu = m_e$, the collision energy can be expressed as,

$$E_c = (\sqrt{E_{cool}} - \sqrt{E_e})^2 \tag{2.7}$$

where $E_{cool} = \frac{1}{2} m_e \mathrm{v}_i^2$ is the electron energy at cooling and $E_e = \frac{1}{2} m_e \mathrm{v}_e^2 \approx q_e U_{cath}$ is the electron energy determined by the set cathode potential. Due to the high MeV ion-beam energies and the cold electron beam, the collision energy can be accurately set over a large dynamic range. The absolute resolution that can be attained at the CRYRING is approximately 2 meV at $E_c = 0$ eV. The resolution is limited by the transverse velocity spread of the electron

beam. The resolution decreases upon increasing collision energy and at $E_c = 200$ meV it is about 5 meV [37]. The collision energy may be set to a static value or may be varied continuously during a single beam cycle. In the latter case the electrons are typically first accelerated to a velocity larger than that of the ion beam and then smoothly decelerated to below the ion velocity to ensure passing through 0 eV collision energy. This process is referred to as ramping (of the energy). The storage time interval during which the collision energy is varied is referred to as the ramp.

The electron-ion collisions mentioned so far are phase-space cooling and the central reactions in this thesis, the DR and DE reactions. However, the interactions are not limited to these two reactions. A third reaction that is also subject to investigation in one of the studies presented in this thesis (see §4.9.1), is the super elastic collision (SEC) reaction that may rovibrationally cool the ions,

$$\mathrm{M}^+(v) + e^- \rightarrow \mathrm{M}^+(v - \mathrm{n}) + e^- \tag{2.8}$$

where M^+ stands for a molecular ion. If the molecular ion has a permanent dipole moment, the effect of SECs will add to the vibrational cooling through radiative decay. In the absence of a permanent dipole moment, SECs will be the sole cause of vibrational cooling. Other electron-ion collisions not treated in this thesis are dissociative ionisation (DI) and resonant ion-pair (RIP) formation. These two reactions are endothermic for low-energy collisions and weakly-excited parent ions and produce only charged products.

Electron-Rest Gas Collisions

The interaction of the electron beam with the rest gas inside the electron cooler gives rise to electron-impact ionisation of rest-gas molecules. These ionised molecules are subsequently trapped in the electron-energy-well created by the self-induced space-charge potential [see Eq. (2.4)]. These positive charges in their turn partly compensate for the negative space-charge effect and Eq. (2.4) is modified to the following empirical formula,

$$E_{sp} = \frac{I_e\, r_c\, m_e\, c^2}{q_e\, \mathrm{v}_e} \left(1 + 2ln\left(\frac{b}{a}\right)\right) \cdot \left(1 - \frac{\xi(E_e)}{\mathrm{v}_{cool}}\right) \tag{2.9}$$

where $\xi(E_e)$ is some positive-ion-trapping function that depends on the electron energy through the electron-impact ionisation efficiency and v_{cool} acts as normalisation factor. The electron-beam energy is often higher than the ionisation energies of all the rest-gas molecules (15.8, 15.4, 14.0, 13.8, and 12.6 eV for Ar, H_2, CO, CO_2, and CH_4, respectively) [38]. However, for heavy ions like $(NO)_2^+$, electron energies as low as 16 eV have to be used. Since 90% of the rest gas consists of H_2 molecules, the positive-ion trapping effect mostly concerns H_2^+. At low electron energies, the other rest-gas molecules will play a increasingly larger role. The data-analysis procedure for the space-charge correction at low and high electron energies is described in the next chapter (see Chapter 3).

2.1.3 Ion Sources

Creation of ions is an important aspect of all DR experiments. Although the storage in CRYRING allows ions to cool internally, in practice, many aspects of the ion beam are determined in the ion source. Generally, the ions sources use amongst other electron-impact

ionisation to produce the ions. Electron-impact ionisation is a sudden process, in many ways comparable to photoionisation. In this process vibrationally excited species are easily formed. Vibrational excitation depends on the change in molecular geometry upon ionisation. Rotational excitation is much less likely. One can say that the ion-beam rotational temperature reflects the neutral gas temperature of the ion source. In an ion source one can optimise the collisional processes occurring between ionisation and extraction of the ions. These collisions can give rise to, for example, dimer ion formation and, more importantly, reduction of the vibrational temperature.

Three different ion sources were used in the laboratory studies presented in this thesis. Each of these ion sources has distinct properties, which determines the suitability to the experiment in question (see also Appendix A). Here, short descriptions and relevant features of the ion sources, JIMIS and MINIS, are given. The ion source, PHILIS, is described in more detail as we developed this ion source specifically for our DR research. It is noted that many more ion sources of interest to DR research are used at the CRYRING, such as super-sonic expansion sources. The interested reader is referred to literature [34, 35, 39].

MINIS

MINIS is a hot filament Penning discharge source [34, 39]. It is the most frequently used source at the CRYRING. It has produced many of the at CRYRING investigated ions, ranging from small diatomic molecular to large polyatomic ions like hydrocarbons. It is known to produce hot ions, especially rotationally ($\sim$ 1000 K) [33], and ion-beam currents up to mA. The filament is located inside the source, which heats the gas and puts constraints on the operational lifetime. The source can be operated in a pulsed-mode, which conserves gas, increases the lifetime, and increases the output current. It is a brute-force ion source, which offers little control over the conditions and the vibrational distribution of the ions is unknown and not constant. A schematic of the ions source can be found elsewhere [35].

JIMIS

JIMIS is a cold hollow cathode ion source, operating at high pressures and if desired, in a pulsed mode [34, 39]. The ion source creates a plasma from the gas(es) present through electrical discharge. The high pressure in the source allows collisional quenching to cool the ions before extraction and this is known to produce vibrationally cold ions, which is especially important for ions without a permanent dipole moment as they cannot radiatively decay. The low temperature and high pressure also makes the source well-suited for the production of cluster and dimer ions. The source is water-cooled, uses little power (2 W), and generally produces ions with a rotational temperature around 300 K. The currents produced in the case of cluster ions are usually somewhat low (10-100 nA). A schematic of the ions source can be found elsewhere [35].

PHILIS

PHILIS is a Nier type electron-impact ion source that has been constructed at SRI International and the FOM institute AMOLF specifically for our research. The design offers a high level of control over the ion-source settings, which are used to regulate the vibrational population

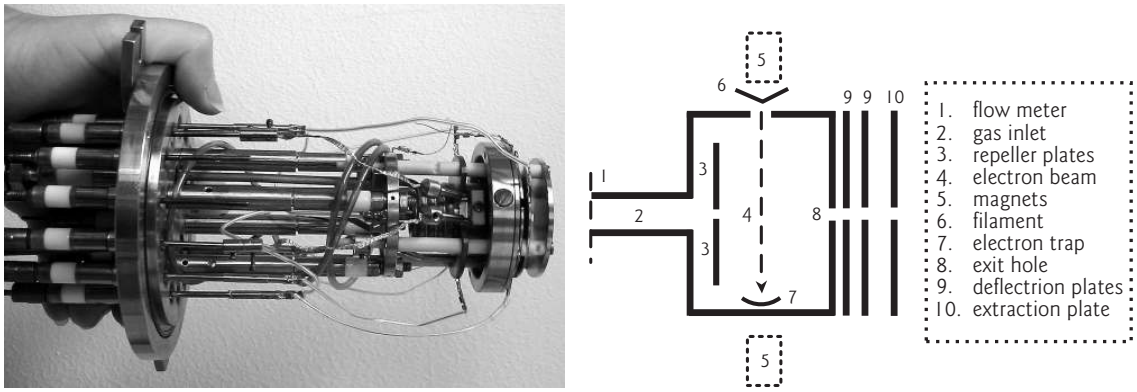

Figure 2.3: On the left a photograph and on the right a schematic diagram of the electron-impact ion source, PHILIS, designed to control the creation of different vibrational populations of O_2^+ ions.

of the ions. The ion source produces low currents (nA), which presents difficulties for the storage process of the ions [35]. Again, the source can be operated in a pulsed-mode.

The design of PHILIS has been based on a similar source used in previous research [40–42] and is shown in Fig. 2.3. Oxygen gas enters through the gas inlet, where the flow rate is monitored to accurately control the pressure inside the source. The electron filament is external to the source to reduce the heat load on the gas and increase the operational lifetime. The ion source is additionally water-cooled and the rotational temperature is estimated to be around 300 K. A magnetic guiding field is used to direct the electrons emitted by the filament towards the electron trap. The voltage difference between the filament and the trap determines the electron-impact energy. Two repeller plates located inside the source are used to steer the ions towards the exit aperture and thus influence their residence time inside the source. Finally, the deflection and extraction plates are used to guide and accelerate the ion beam.

The vibrational population of the ions leaving the ion source is regulated by varying the electron-impact energy, the pressure, and the voltage on the repeller plates. The electron-impact energy affects the excitation upon formation of the ions and the pressure and repeller-plate potentials affect the amount of collisional quenching of the ions. Each combination of these variables creates a specific vibrational population. Consequently, a certain vibrational population can be reproduced by switching to its corresponding ion-source setting. The ion source has been characterised at SRI International using the fast-beam translational spectroscopy apparatus that is described at the end of this chapter.

2.1.4 Detection Systems

We made use of three detection systems/techniques in the laboratory studies presented in this thesis which required the use of two different kinds of detectors (see also Appendix A). The detection systems were set up to detect the neutral products entering the zero-degree arm. Each detection technique measured a different quantity of the neutrals. Figure 2.4 shows the location of the detectors. The detectors cannot be used simultaneously, since each detector obstructs the one further downstream. As has been noted earlier, the zero-degree arm is closed to the ring by a shutter. The ion-beam intensity is often very high at the start of a beam cycle and the detectors are protected from this high intensity. The trigger to open

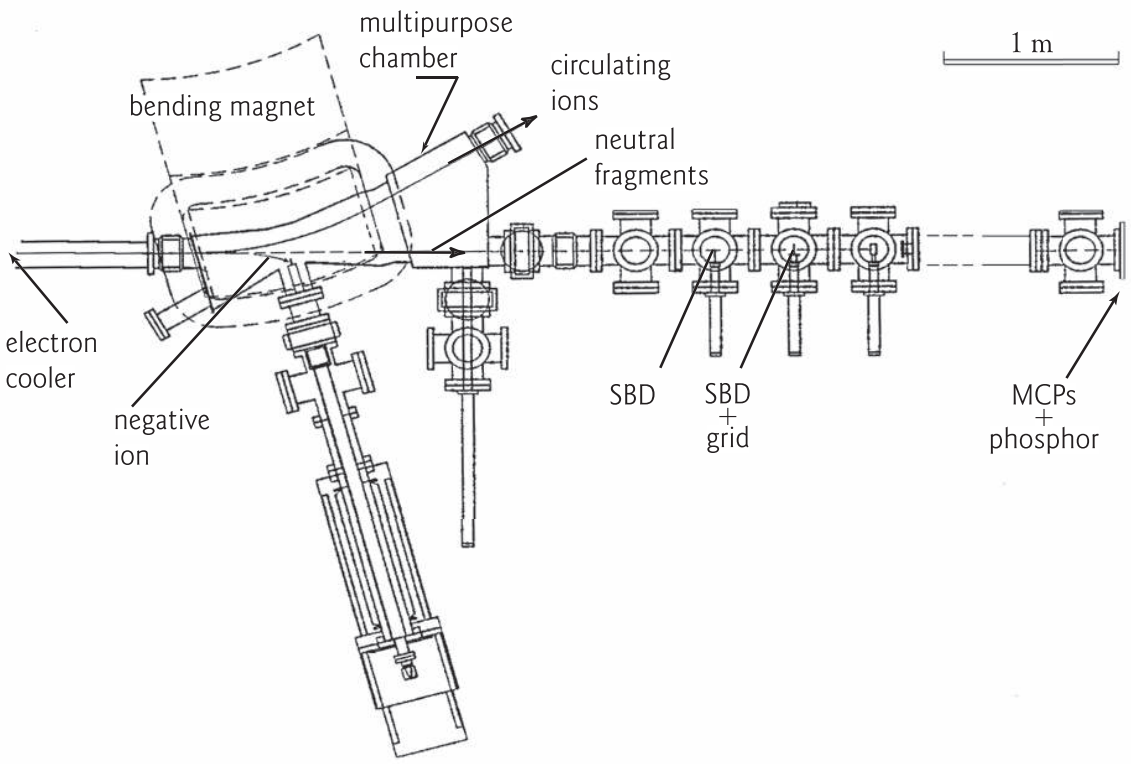

Figure 2.4: Schematic showing the zero-degree detection arm of the ring and the locations of the detection systems. The horizontal arrow indicates the trajectory of the neutral products and the inclined arrow the trajectory of the parent ions. Each of the surface barrier detectors (SBDs) as well as the grid that are located inside the zero-degree arm may be extracted without endangering the vacuum to free the way to the detector further downstream. The micro-channel plates (MCPs) and the phosphor at the far end are part of the imaging system. The imaging system is located at distance of 6.3 m from the centre of the electron cooler and the SBDs are typically located at a distance between 3.5 and 4.5 m.

the shutter is connected to the trigger that starts the measurement. Thanks to the high pumping speed available in the zero-degree arm, the vacuum demands on our detectors can be matched. The typical operating pressure for the imaging detector is 10^{-8} mbar.

Surface Barrier Detector: Rate and Cross-Section Measurements

For rate-coefficient or cross-section measurements at CRYRING, an energy-sensitive silicon semiconductor device, the so-called surface barrier detector (SBD), is used to measure the neutral count rate of the reaction of interest (see Fig. 2.5). A small and a large SBD with active areas of 900 and 2800 mm^2, respectively, are mounted around 4 m from the centre of the electron cooler. The small SBD offers a high energy-resolution and, as such, a high mass resolution for the DR experiment. The large SBD is more suitable to use when all neutral products must be detected, as in the case of considerable kinetic energy releases. Other properties of the SBDs are more or less the same and the following description applies to both detectors.

At MeV energies, the incoming fragments deposit their energy in the active layer of the detector, creating electron-hole pairs that result in an output signal that is proportional to

Figure 2.5: A photograph of the small surface barrier detector (SBD). This detector is an energy-sensitive silicon semiconductor device used in storage-ring experiments to measure reaction rates or, in combination with a grid technique, the fragmentation products of the DR of a polyatomic ion. Its operation and features are described in the text.

the kinetic energy of the incoming fragments. A SBD cannot detect the neutral fragments in each dissociation event separately; the ns time-of-arrival difference between the fragments at MeV energy is shorter than the detector's integration time and thus undissociated and dissociated molecules with only neutral fragments give equal signals. DR events therefore always give rise to an output-signal height that is characteristic of the full beam energy. DE events, however, give rise to an output-signal height that is characteristic to a fraction of the beam energy, determined by the neutral-mass fraction (of the parent ion) produced in the DE reaction under investigation. A constant fraction discriminator (CFD) is used to select the DR or DE signal, which are relayed to multi-channel scalers (MCSs). The MCS records the events as function of storage time (in 2 or 5 ms bins). During the measurement, the counts are integrated over all beam cycles. The energy dependence of the count rate can be measured by ramping (varying during storage time) the electron energy for each cycle (see §3.1). The background signals that are present in the DR and DE rate measurements are the CT and CID signals, respectively [see Eqs. (2.1) and (2.2)]. The CT reactions produce single neutral particles of full beam energy and the CIDs produce one or more neutral particles, which possess a fraction of the beam energy proportional to their mass fraction. The background (BG) signals are typically determined using the same SBD as the DR and DE signals. For a (brief) period during the measuring gate, the collision energy is turned up high (negligible DR signal) or down low (negligible DE signal). Alternatively, a separate BG measurement may be taken, either with a SBD or with other detectors at different locations in the ring [43]. In this case, the BG is typically recorded over a longer storage-time period than the measuring gate, referred to as the BG gate. The BG measurements are a direct measure of the ion-beam destruction and thus a measure for the lifetime of the ion beam. The efficiency of the SBD is close to unity, which makes it possible to perform absolute measurements. For absolute measurements, the ion-beam current needs to be determined [44]. The analysis of the (absolute) cross-section measurement is described in the next chapter.

Grid Technique: Chemical Branching Measurements

For a diatomic ion, the fragmentation process following DR is not interesting chemically; the identification of the fragments is obvious. In the case of triatomic and polyatomic species, the chemical identification yields new insights. A surprisingly simple, but not obvious, technique to measure the chemical fragmentation in the DR of a polyatomic ion, is to insert a metal grid with a known transmission in front of the SBD. Figure 2.6 shows a cartoon of a fragmentation measurement using the grid technique. The grid used at CRYRING has a transmission of

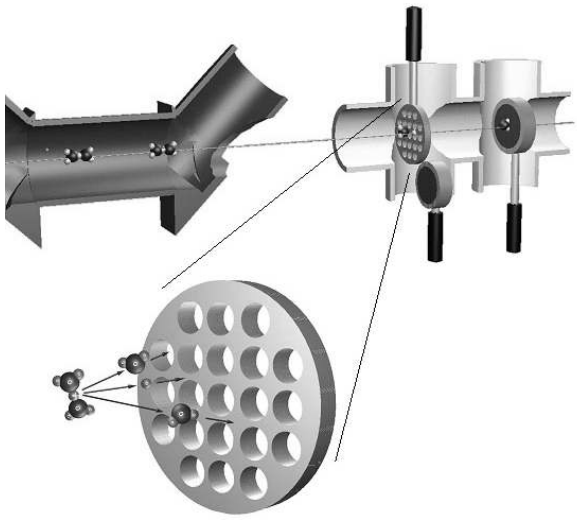

Figure 2.6: An illustration of the grid technique as used in the detection of the chemical fragmentation. A grid is inserted in front of a SBD, transmitting and stopping particles with a certain probability, which splits the DR signal into a series of lower-energy signals according to the mass of the transmitted particle(s).

$T = 0.297 \pm 0.015$ [45] and is thick enough to stop any of the neutral fragments that do not pass through the holes, irrespective of mass and size. In other words, the probability for a neutral fragment to pass through the grid is T, and the probability for the fragment to be stopped is $(1 - T)$. Since each neutral fragment carries a fraction of the total beam energy proportional to its mass and may pass while other fragment(s) are stopped, the total DR (and BG) signal is split into a series of peaks according to the beam-energy fraction arising from the different combinations of stopped/transmitted particles (see §3.2). The output signals of the SBD are relayed to a multi-channel analyser (MCA), which produces a histogram of the measured energies integrated over all measured cycles. The electron collision energy has to remain constant throughout the fragmentation measurement. The BG signals of interest in fragmentation measurements, are both the CT and CID signals [see Eqs. (2.1) and (2.2)]. In order to account for these contributions, the reaction rates are measured with the same SBD in 4 situations: electrons on and grid out (all signals), electrons on and grid in (all fragmented signals), electrons off and grid out (BG signals), and electrons off and grid in (fragmented BG signals). The analysis that follows, although fairly straightforward, is not intuitive, as will be shown in the next chapter.

Imaging Technique: Physical Branching Measurements

In DR and DE, one of the key questions is how the reaction energy is distributed over the various excited states and, for polyatomic ions, also the various product fragments. The description of this redistribution process requires detailed insight in the dynamics of the respective reaction. For studies of the DR dynamics at CRYRING, a position-sensitive imaging detection system is used [33, 46, 47]. Fig. 2.7 shows a schematic of the imaging system as used in the current studies. Each DR event occurring in the electron cooler gives rise to neutral product fragments that have the large velocity of the MeV beam towards the detector. The kinetic energy available in the dissociation process then adds a small velocity to the fragments. All fragments still move forward and can be intercepted with a detector of suitable size. The relative velocity of the dissociating fragments can be oriented in any direction with respect to the beam direction. Since the kinetic energy release (KER) is only on the order of a few eV, a long distance between the electron cooler and the imaging setup

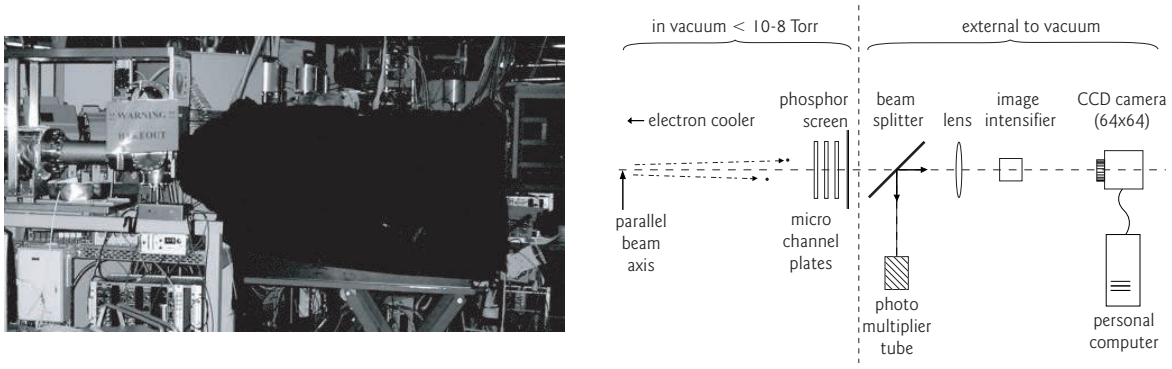

Figure 2.7: On the right, a schematic of the imaging detection system that was used to determine the relative transversal velocities of the DR products (see text for details). On the left, a photograph of the far end of the detection arm and the imaging system that is covered with a black absorbing cloth in order to prevent ambient light from producing false triggering. During experiments the lights are also turned off.

is required to allow the fragments to separate over a measurable distance.

The neutral products that enter the detection arm hit a stack of three micro-channel plates (MCPs) with a phosphor screen (60 mm diameter) at the far end of the detection arm. The light emitted from the phosphor screen is monitored by a photo-multiplier tube (PMT) and an image intensifier (II). The PMT signal triggers the II with a minimum delay of about 30 ns. Each trigger is related to an event arriving at the phosphor (DR, DE, BG, or noise event). The output of the II is focused onto a charge-coupled device (CCD) camera (64 x 64 pixels of 32 μm) and the output of the CCD camera is relayed to a computer. The MCPs and phosphor screen are the only devices of the detection system located inside the vacuum. The entire detection system is shielded from the ambient light to prevent false events.

The positions of all hits on the detector are recorded on an event-by-event basis, irrespective of the amount of particles (there is a maximum limit of 5−10 particles per event). A spot-finding software routine determines the positions of the hits in the CCD-frame. The limit of the separation that can be determined by this routine has a minimum of 2−3 mm separation on the phosphor. The difference in arrival time of the products in each reaction (ns) was not measured because of experimental difficulties [46, 48]. This means that only the projection of the inter-fragment distance was measured. An analytical model was used to relate the measured distances on the detector to the kinetic energy releases in the DR process (see Chapter 3). In a few of the measurements presented in this thesis (see Appendix A), each event was labelled with a time stamp relative to the start of the measuring gate in 50 ms accuracy in order to investigate the dynamics as function of storage time. For all measurements, all events were recorded irrespective of the amount of particles, saving the positions, intensities, and possible time stamps on an event-by-event basis.

The CID reactions [see Eq. (2.2)] are the only BG reactions of interest in the dynamics measurements. In this case, the dynamics rather than the rate of the BG signal is of interest. The BG dynamics are measured with the imaging system while turning the electron beam off. The DR and CID signals cannot be measured simultaneously (signals are time integrated) and need to be normalised to each other. The CID dynamics are often independent of the electron energy and the internal states of the ions and only need to be determined once. Whenever a dependency is suspected, such as in the case of changing ion-beam population, the dynamics should be measured for all investigated energies and ion populations used in the

DR measurement. The detection efficiency of the imaging system is about 50% per fragment and consequently no absolute measurements can be performed. More importantly, the data acquisition rate is quite low (300 Hz), whereas the count rates generated in the experiment are easily more than kHz. Long data acquisition times are therefore needed to attain enough statistics. The reaction dynamics are measured at one collision energy at the time. The DR signal is highest at 0 eV giving rise to the best signal-to-noise ratios at 0 eV collision energy. We have recently introduced and implemented an alternative imaging detector for the DR experiments at CRYRING, namely a hexanode delay-line detector (DLD) [49]. This DLD has a much higher data-acquisition rate of up to 5 kHz. Also, the DLD determines arrival-time differences with an accuracy of 1 ns. The main difficulty of this detector for use at the CRYRING, is the dead area (delay-line dead-time) surrounding the first hit. This dead area obstructs or hinders the detection of low-KER dissociation limits, such as, the for this thesis essential, $O(^1S)$ atoms.

2.2 Fast Beam Translational Spectroscopy

An important goal of the experiments presented in this thesis was to introduce measurements on internal states. It is known that source conditions may alter state distributions, hence a technique to probe the ions associated to an ion-source setting is necessary. In the O_2^+ experiment on the vibrational dependency of the DR reaction (see Chapter 4), we produced and characterised several vibrational populations of O_2^+ ions created with the PHILIS ion source, using dissociative charge transfer (DCT) reactions between O_2^+ and cesium. The DCT reactions and the characterisation of the populations are described in §4.7. Here, a compact description is given on the experimental properties of the setup viewed in respect to the storage-ring experiments. More detailed descriptions of the setup and its detection system can be found elsewhere [40].

The DCT experiment uses a fast-beam translation-spectroscopy apparatus and an imaging detection technique, the principles of which are similar to those of the storage-ring setup and detection technique used in the DR-dynamics experiments. Both types of experiments employ a fast ion beam combined with an imaging technique to determine the kinetic energy released in the respective reactions. Figure 2.8(a) sketches the DCT apparatus used in the

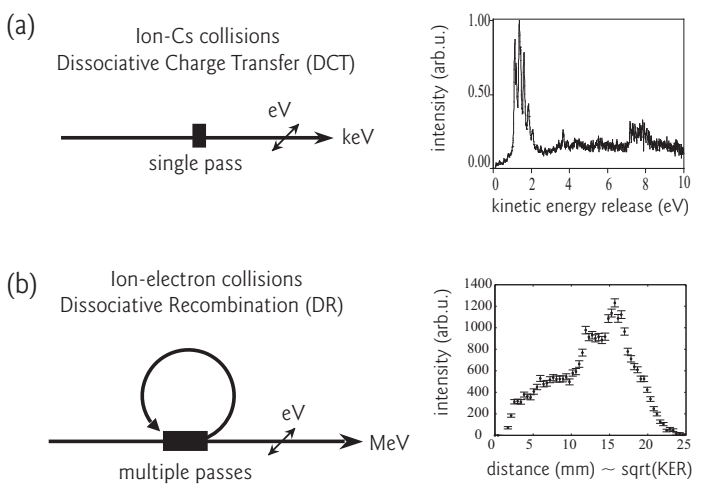

Figure 2.8: (a) Schematic of the experiment on the dissociative charge transfer (DCT) reactions employed to characterise the vibrational populations of O_2^+, which are used in the DR experiment at the CRYRING. (b) Schematic of the CRYRING, illustrating the main differences between the dissociative recombination (DR) and the DCT experiments.

characterisation of the vibrational populations. For comparison, Fig. 2.8(b) sketches the experimental arrangement employed in the DR study. The DCT studies are a single-pass experiment, in which the ion-beam energy is a few keV and the interaction region is small (a few mm) and extremely well defined. The DR experiments are conducted at MeV energies and, since the ions circulate in the storage ring, they pass through the 85 cm interaction region multiple times. The imaging technique in the DCT experiment involves the coincident detection of both oxygen fragments, recording their position and difference in arrival times (*3D*-detection). The vibrational population of the parent ions can be observed directly as the experimental spectrum of Fig. 2.8(a) shows; all peaks are individual vibrational levels of O_2^+ in contrast to the CRYRING imaging spectrum shown in Fig. 2.8(b), where only the electronic structure can be observed. The fast-beam technique at SRI International uses in fact rather slow keV beams. The associated smaller ion velocities make it possible to achieve the higher resolutions. Storage of ions is not possible, hence the ion-beam population is determined a few μs after their formation. As we will see, ion distributions may well change on time scales of ms, which is still short for the time scale of measurements at CRYRING, which typically start after 1 s.

$$d_{det} = \sqrt{\frac{KER}{E_{ion}}} \frac{m_1 + m_2}{\sqrt{m_1 m_2}} L \sin\theta = d_{lab} \sin\theta$$

1 2 3 4 5 6 7 A B

Wetenschap is...

van een mug een discussiepunt maken

Annemieke

Chapter 3

Data Analysis

This chapter describes the data processing and analysis of the CRYRING *experiments. In the following order, the analysis of the rate coefficients and cross sections, the chemical fragmentation (for polyatomic ions), the physical branching, and the extraction of a radiative lifetime are treated. The lifetime measurement is different from the other measurements in that it does not study the dissociative recombination reaction, but rather uses the reaction to determine the lifetime of an excited metastable state in NO^+ (see also §5.5). Details on the experiment and analysis of all measurements performed at* CRYRING *are summarised in Appendix A.*

3.1 Rate Coefficients and Cross Sections

The rate coefficients and cross sections of dissociative recombination (DR) and dissociative excitation (DE) are determined from the count rate measurements as recorded by the surface barrier detector (SBD) and multi-channel scaler (MCS) (see §2.1.4). In DR measurements, the full-beam-energy signal is recorded in time, whereas in DE measurements the partial-beam-energy signal corresponding to the selected DE channel is recorded in time. An example of a MCS spectrum from a DR measurement (solid grey curve) is shown in Fig. 3.1 and the associated electron-energy ramp (solid grey curve) in Fig. 3.2. Before t = 5 s and after t = 6.5 s, the electron-beam energy is set to the estimated cooling energy, where the collision energy should be zero and the DR rate should have a maximum. In between t = 5 s and t = 6.5 s, the electron collision energy is ramped, causing an enormous variation in the signal. In fact, the small signal near the start and the end of the ramp, where the collision energy is high, is dominated by background (BG) counts. The electrons are first accelerated to a velocity higher than that of the ions and then smoothly decelerated to a velocity lower than that of the ions to ensure passage through the true collision energy of 0 eV. The peak position of the MCS signal indicates the position of the true 0-eV crossing as the DR rate is maximum at 0-eV collisions. In practice, the exact cooling energy is determined from such MCS spectra; if a mono-exponential curve can be fitted through the MCS signal before the ramp, at peak maximum, and after the ramp, then the true cooling energy is found. The procedure to extract the (thermal) rate coefficient and/or cross section can roughly be divided into 4 parts.

3.1.1 Background Elimination and Normalisation

The BG contribution to the MCS signal that contains either the DR or the DE signal comes from charge-transfer (CT) signals or collision-induced dissociation (CID) signals, respectively [see Eqs. (2.1) and (2.2)]. This BG contribution is associated with the mono-exponentially decreasing ion-beam intensity, which can be observed in pure BG measurements (grey dots) and in the time dependence of the MCS signal before t = 5 s and after t = 6.5 s. The BG contribution can be subtracted from the MCS signal using the pure BG signal, which first needs to be normalised to the MCS spectrum. There are two typical ways of determining the necessary normalisation factor. First, the amount of beam cycles over which the MCS and the pure BG signals were taken can be used to determine the ratio between the intensities of the respective spectra. This is possible as the SBD has a detection efficiency that is close to unity. Second, the MCS spectrum often includes a brief period where the collision energy is

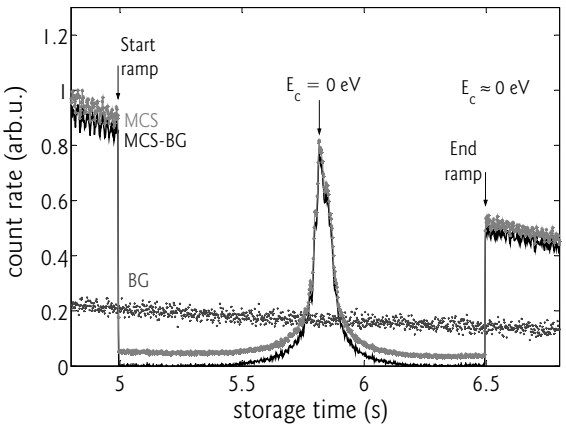

Figure 3.1: An example of an MCS spectrum (solid grey curve) as observed when the electron energy is ramped according to Fig. 3.2. The BG signal is measured separately (grey dots) and needs to be normalised to the MCS spectrum before subtraction. The DR rate is extracted from the MCS-BG (solid black curve) signal by normalising to the ion loss. The maximum in the MCS intensity is caused by the physical maximum in the DR rate at 0 eV collision energy. This maximum occurs at true cooling energy.

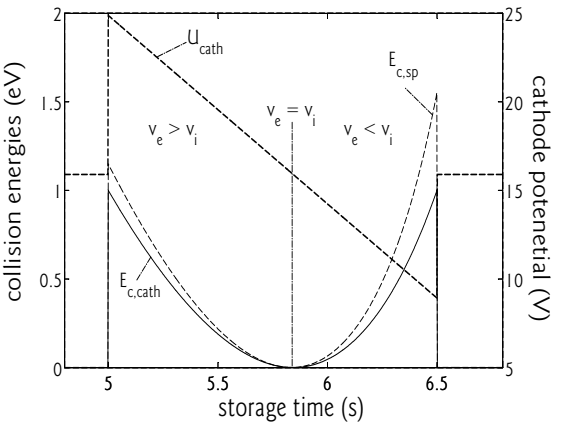

Figure 3.2: The cathode potential, U_{cath}, as function of time that gives rise to the MCS spectrum observed in Fig. 3.1. This cathode potential determines the collision energy. The solid black curve is the first approximation of the collision energy, $E_{c,cath}$, and the dashed black curve is the space-charge corrected energy, $E_{c,sp}$. At t $\approx$ 5.8 s, the ions and electrons are velocity-matched, $v_e = v_i$. Before and after this point, the electrons are faster and slower than the ions, respectively.

so high (or low) that the DR (or DE) signal is negligible and only BG signal remains. The pure BG spectrum (or its exponential fit) is then scaled to the intensity of the MCS signal at these energies and subsequently subtracted (solid black curve). The DR count rate is extracted after correcting for the ion-beam destruction, which typically involves dividing the background-subtracted MCS signal by the normalised BG signal. Extracting the reaction rate becomes more complicated when the electron-ion reactions start to contribute to the ion-beam destruction, i.e., when the pure BG signal is no longer a direct measure for the BG embedded in the MCS signal.

3.1.2 The Collision Energy and Space Charge Correction

The cathode potential, U_{cath}, that gives rise to the MCS spectrum as observed in Fig. 3.1 is shown in Fig. 3.2. The electrons are first accelerated and then smoothly decelerated to ensure passing the 0 eV collision energy. The collision energy related to this potential is determined with Eq. (2.7). In first approximation, this gives rise to the collision energy, $E_{c,cath}$ (solid black curve). In order to determine the real collision energy, the electron energy needs to corrected for the space-charge effect,

$$E_e = E_{cath} - E_{sp} \tag{3.1}$$

where $E_{cath} = q_e \cdot U_{cath}$ (solid black curve) is the first approximation of the electron energy in the lab frame and the space-charge energy, E_{sp}, depends on the electron-beam parameters and the positive ion trapping of ionised rest-gas molecules [see Eq. (2.9)]. At electron-beam energies much larger than the H_2 ionisation potential ($U_{cath} \gg 15.4$ V) the majority of the trapped positive ions are H_2^+ ions. In that case the positive-ion-trapping function $\xi(E_e)/v_{cool}$

is approximated by $A\sigma_{H_2}(E_e)$, where σ_{H_2} represents the ionisation cross section of H_2 and A is an empirical parameter. The space-charge correction is then expressed as,

$$E_{sp} = \frac{I_e\, r_c\, m_e\, c^2}{q_e\, \mathrm{v}_e} \left(1 + 2ln\left(\frac{b}{a}\right)\right) \cdot \left(1 - A\sigma_{H_2}(E_e)\right) \tag{3.2}$$

The parameter A is determined at cooling using $\mathrm{v}_e = \mathrm{v}_i$. Since the electron velocity is present on the right- and left-hand side of this expression, the space-charge correction is found iteratively. At electron-beam energies around and below the H_2 ionisation potential, more rest-gas molecules start playing a role. In this case the positive-ion-trapping function is approximated by a factor A', which again can be determined at cooling using $\mathrm{v}_e = \mathrm{v}_i$, now assuming that ionisation is independent of the electron energy,

$$E_{sp} = \frac{I_e\, r_c\, m_e\, c^2}{q_e\, \mathrm{v}_e} \left(1 + 2ln\left(\frac{b}{a}\right)\right) \cdot \left(1 - A'\right) \tag{3.3}$$

This latter space-charge correction has been applied to extract the $(NO)_2^+$ rate coefficient as low-energy electron beams around 16 eV were required to attain 0 eV collision energy. The magnitude of the corrections are larger than the energy-resolution in our experiment, however, the space charge gives rise to a systematic effect.

3.1.3 The Rate Coefficients and Toroidal Correction

The measured rate coefficient ($m^3\ s^{-1}$) is extracted from the reaction rate determined above,

$$k_{meas} = \frac{\mathrm{v}_i\, q_e}{n_e\, l_c} \cdot \frac{R_{meas}}{I_{ion}} \tag{3.4}$$

where R_{meas} is the reaction rate (s^{-1}), v_i is the ion velocity ($m\ s^{-1}$), q_e is the electron charge (C), n_e is the electron density (m^{-3}), and l_c is the central cooler length (0.85 m). The absolute measured rate coefficient can be determined provided ion-current measurements are taken. In that case, the rate is normalised to the ion current, I_{ion}. The measured cross section (m^2) is simply,

$$\sigma_{meas} = \frac{k_{meas}}{\mathrm{v}_{det}} \tag{3.5}$$

This cross section is not the 'true' cross section, since our electron beam is not mono-energetic [see Eq. (2.3)]. The 'true' energy-dependent cross section has to be derived from a deconvolution procedure taking into account the velocity distribution,

$$\sigma = \frac{\langle \sigma_{meas}(\mathrm{v})\, \mathrm{v} \rangle}{\mathrm{v}_{det}} \tag{3.6}$$

where $\langle \sigma_{meas}(\mathrm{v})\, \mathrm{v} \rangle$ stands for average measured rate coefficient and $\mathrm{v} = \sqrt{\mathrm{v}_{e_\perp}^2 + (\mathrm{v}_{det} + \mathrm{v}_{e_\parallel})^2}$. The convolution over the velocities is important at low collision energies. At high energies ($E_c \gg kT_e$), the 'true' cross section is very close to the measured rate divided by the detuning velocity.

However, the retrieved cross section still contains a contribution from the toroidal sections of the electron cooler (see §2.1.2). The toroidal correction of the cross section is numerically

implemented. The toroidal sections (see Fig. 2.2) are divided into small segments, Δx_{T} and for each segment the collision energy, $E_{\mathrm{c}}(x_{\mathrm{T}})$, is determined and the rate coefficient or cross section is toroidally corrected by,

$$\sigma_{\mathrm{tc}} = \sigma - \frac{2}{l_{\mathrm{c}}} \cdot \int_0^{x_{\max}} \sigma(E_{\mathrm{c}}(x_{\mathrm{T}}))\, dx_{\mathrm{T}} \tag{3.7}$$

where σ_{tc} is the toroidal-corrected cross section, x_{T} are the positions of the segments inside the toroidal region ($x_{\mathrm{T}} = 0 - 12.5$ cm), and $\sigma(E_{\mathrm{c}}(x_{\mathrm{T}}))$ is the cross section at the elevated toroidal collision energies, which is either known or extrapolated from the above derived cross section. This correction also requires an iteration procedure as the input is the cross section over the whole collision energy range.

3.1.4 The Thermal Rate Coefficient

The thermal rate coefficient, $\alpha(\mathrm{T})$ ($\mathrm{m}^3\ \mathrm{s}^{-1}$), can be expressed as a convolution of the rate coefficient or cross section over all collision energies present at a certain temperature T,

$$\alpha(\mathrm{T}_e) = \frac{8\pi\, m_e}{(2\pi\, m_e\, \mathrm{kT}_e)^{3/2}} \int_0^{\infty} E_{\mathrm{c}}\, \sigma(E_{\mathrm{c}}) e^{-E_{\mathrm{c}}/\mathrm{kT}_e} dE_{\mathrm{c}} \tag{3.8}$$

where m_e is the electron mass in kg, E_{c} is in Joule, and $\sigma(E_{\mathrm{c}})$ is in m^2. The thermal rate coefficient is often expressed as,

$$\alpha(\mathrm{T}_e) = \alpha_0 \left(\frac{300}{\mathrm{T}_e}\right)^{\gamma} \tag{3.9}$$

where α_0 is the thermal rate coefficient at 300 K and γ is a fit parameter for each reaction; $\gamma = 0.5$ for DR reactions where the direct dissociation mechanism is dominant [50].

3.2 Grid Technique: Analysis of the Chemical Branching

The chemical fragmentation or branching fractions are determined using the grid technique (see §2.1.4). Due to the use of the grid in combination with the SBD, the full-beam-energy DR signal is split into a series of peaks corresponding to beam-energy fractions determined by mass ratios. As an example, the fragmentation spectra for $(\mathrm{NO})_2^+$ as recorded with the MCA are shown in Fig. 3.3. The MCA spectrum with grid in and electrons on contains both DR and BG contributions. The BG contribution is determined from the spectra with the grid out (see Fig. 3.4). Without grid and with electrons on, the full-energy signal contains both DR and CT events, whereas the partial-energy signals come from CID reactions [see Eqs. (2.1) and (2.2)]. Without grid nor electrons, the full-energy signal contains only CT events. As the CID signal does not depend on the electrons, the ratio between the DR and CT contribution can be determined upon normalisation of both grid-out spectra to the CID peaks. This derived ratio can then be used to scale the fragmented BG signal and subtract it from the MCA spectrum with grid in and electrons on, thus extracting the DR fragmentation signal.

As is indicated in Fig. 3.3, an energy peak may consist of several contributions from particles with near-equal mass. The energy resolution of our SBD is not sufficient to separate

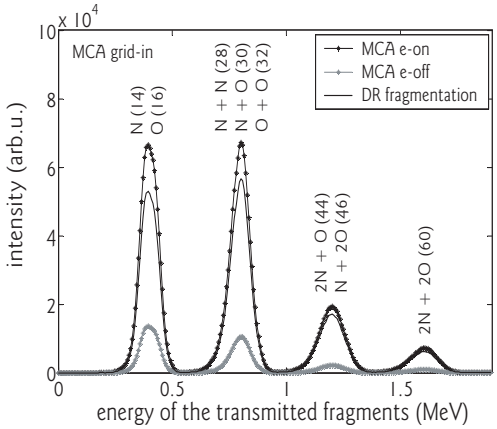

Figure 3.3: The MCA spectra for the study of the fragmentation of the $(NO)_2^+$ ion at 0 eV collision energy as measured using the SBD in combination with the grid. The curves with the stars are the measured spectra with electrons on (black) and electron off (grey) and the solid black curve is the extracted DR fragmentation signal. The four observed peak correspond to the kinetic energies as determined by the total mass of the transmitted fragment(s).

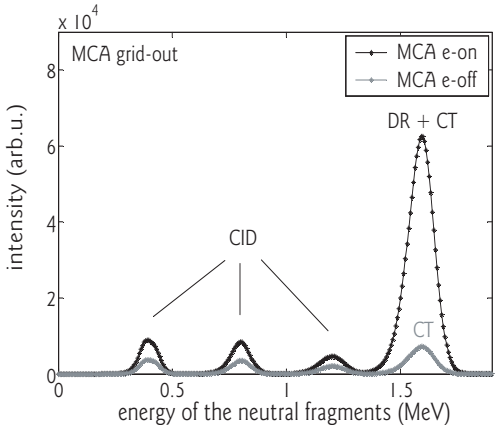

Figure 3.4: The MCA spectra for the study of the fragmentation of the $(NO)_2^+$ ion at 0 eV collision energy taken using the SBD without the grid. The curves with the stars are the measured spectra with the electrons on (black) and electrons off (grey). Without the grid, the first three peaks are related to collision-induced-dissociation (CID) events [see Eq. (2.2)], which are independent of the electrons. The full-beam energy peak is related to both DR and charge transfer (CT) events [see Eq. (2.1)] when the electron are on and only to CT events when the electrons are off. The CT contribution to the DR signal with the electrons on can be determined by normalising both spectra to the CID intensity.

these different masses at MeV energies. The individual mass contributions, M, are determined in a weighted least-squares fit with the local errors as weights and using Gaussian distributions for each mass with the width and intensity of each Gaussian as free parameters. Restrictions on the fit are often included, e.g., the Gaussian distributions can be restricted to equal widths for near-equal masses. For the $(NO)_2^+$ ion, one of the observed energy peaks has up to three mass-contributions (O_2, NO, and N_2). The shape and the width of the NO mass-30 distribution were therefore pre-determined through an additional measurement (see Chapter 6).

The chemical branching fractions are derived from the transmitted mass contributions, M. This procedure is described here taking the $(NO)_2^+$ ion as an example. As explained in the previous chapter, the probability for a neutral fragment to pass through the grid is T, and the probability for the fragment to be stopped is $(1-T)$. For instance, the product channel NO + NO has a chance of T^2 for both products to pass, resulting in a peak at full energy weighed by this probability. The chance that one NO will pass while the other NO is stopped is twice $T(1-T)$, resulting in a peak at half beam energy weighed by this probability. Each fragmentation channel [see Eqs. (6.1a)−(6.1g)] can be treated similarly, resulting in a set of linear equations that relate the number of counts in the different energy-fraction peaks, M, to the fragmentation number in the different product channels, N:

$$\begin{pmatrix} \mathrm{M(2N+2O)} \\ \mathrm{M(N+2O)} \\ \mathrm{M(2N+O)} \\ \mathrm{M(2O)} \\ \mathrm{M(N+O)} \\ \mathrm{M(2N)} \\ \mathrm{M(O)} \\ \mathrm{M(N)} \end{pmatrix} = \mathbf{T} \times \begin{pmatrix} N_{(a)} \\ N_{(b)} \\ N_{(c)} \\ N_{(d)} \\ N_{(e)} \\ N_{(f)} \\ N_{(g)} \end{pmatrix} \tag{3.10}$$

with **T** the transmission matrix:

$$\begin{pmatrix} 0 & 0 & 0 & 0 & T(1-T) & T(1-T)^2 & T^2(1-T) \\ T^2 & T^3 & T^2 & T^2 & T^2 & T^3 & T^3 \\ 0 & 0 & 0 & 0 & T(1-T) & T^2(1-T) & T(1-T)^2 \\ 0 & T(1\text{-}T)^2 & 0 & T(1-T) & 0 & 2T(1-T)^2 & 0 \\ 2T(1-T) & T(1-T)^2 + T^2(1-T) & 0 & 0 & 0 & 0 & 0 \\ 0 & T^2(1-T) & 0 & T(1-T) & 0 & 2T^2(1-T) & 0 \\ 0 & T^2(1-T) & T(1-T) & 0 & 0 & 0 & 2T^2(1-T) \\ 0 & T(1-T)^2 & T(1-T) & 0 & 0 & 0 & 2T(1-T)^2 \end{pmatrix}$$

where the subscripts $(a) - (g)$ refer to the dissociation limits given in Eqs. (6.1a)−(6.1g). The chemical branching fractions for each of these fragmentation channels, f, are obtained after normalisation to the total number of dissociations recorded,

$$F_f = \frac{N_{(f)}}{\sum_{i=a-g} N_{(f)}} \tag{3.11}$$

Hence, from eight observables (the signals of the different masses), six independent numbers, F_f, are extracted.

3.3 Imaging Technique: Analysis of the Physical Branching

The physical branching fractions are determined from the imaging measurements (see §2.1.4). The acquired data from the imaging measurement contains an event-by-event record of the positions of the particles on the detector for each event. The distances between these particle positions relate to the transverse velocities of the fragments in each event, which can be related to the total kinetic energy of the fragments and therefore to the branching limits.

Background Elimination

For a diatomic system, all 2-particle events are investigated, whereas for a polyatomic system, often the 3-particle events are investigated. The background contribution in the n-particle events is again first normalised to the imaging spectrum containing the DR signal and then subtracted. The normalisation factor is determined from events that are related to kinetic energy releases (KERs) that cannot come from real DR events.

Centre-of-Mass Distribution

The centre-of-mass distribution from dissociation events may cover a significant part of the detector's surface area. Depending on the ion, the ion beam is more or less effectively cooled. Moreover, the neutral beam travelling into the zero-degree arm is divergent and the imaging system is at the far end of the arm. The centre-of-mass beam-size is therefore analysed to check for possible missing events, i.e., events that fall outside the detection area. By plotting all detected positions of the neutrals, the profile of the neutral beam-size can be plotted. If possible missing events are suspected, it will affect the high KERs, i.e., large inter-fragment separations the most. This negative bias can be prevented, by ignoring all events with their centre-of-mass outside a maximum distance from the centre of the neutral beam, irrespective of the associated KER.

3.3.1 Analytical Model for a Diatomic Ion

In the case of a diatomic system, the total kinetic energy release is simply proportional to the square of the relative fragment momentum. Since no relative arrival-times were measured in any of the measurements reported in this thesis, only the measured distances on the detector are available, which are *2D* projections of the inter-fragment separations, d_{lab}. For a single event with a certain KER this is,

$$d_{det} = \sqrt{\frac{\mathrm{KER}}{E_{ion}}}\,\frac{m_1 + m_2}{\sqrt{m_1 m_2}}\,L \sin\theta = d_{lab}\,\sin\theta \tag{3.12}$$

where m_1 and m_2 are the masses of the two product atoms, L is the distance from the dissociation to the detector, E_{ion} is the ion-beam energy, and θ is the angle between the inter-nuclear axis of the dissociating molecule and the beam direction (see Fig. 3.5). There are two aspects to consider. First, the reaction region has a finite length of 85 cm, thus L is a range of distances. Second, the DR reaction may depend on the angle θ, as this angle is also the angle between the relative velocity vector of the electron and the orientation

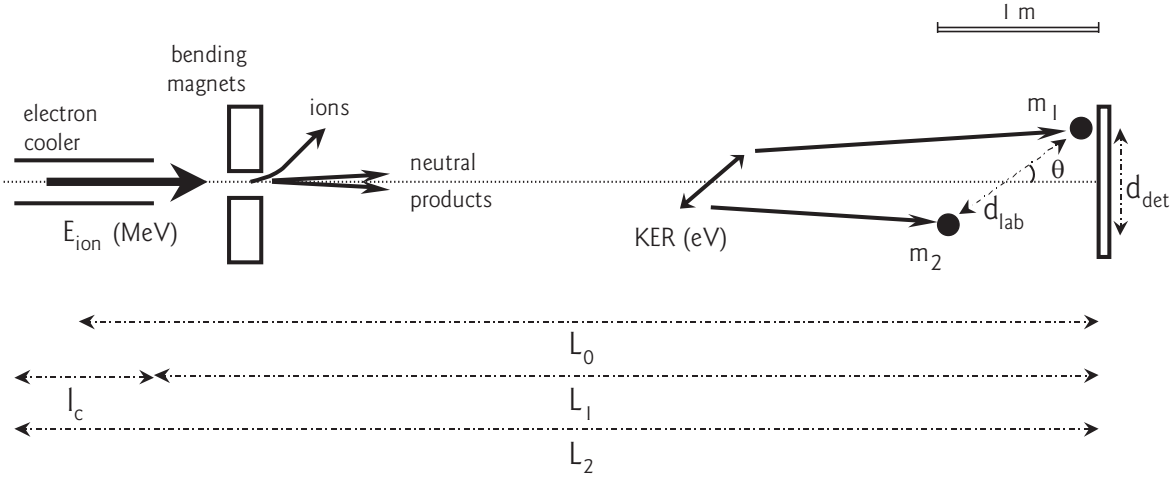

Figure 3.5: An illustration of the parameters that are used in the analytical *2D*-model of the imaging spectrum obtained from the DR of a diatomic ion at CRYRING. The parameters are explained in the text and in Appendix B.

of the molecular ion. An isotropic distribution means that all relative orientations of the low-energy electron velocity and the molecular axis are assumed to have equal DR cross section and therefore the angular distribution of $\sin\theta$ is uniform. The analytical form of the distance distribution of a molecular ion in state (v,J) dissociating isotropically into a single dissociation channel, β, including the effect of the cooler length, is given by [51],

$$D_{\beta,v,J}(d_{det}) = \frac{1}{C_0\, l_c}\left[\arctan\frac{K(L_2)}{d_{det}} - \arctan\frac{K(L_1)}{d_{det}}\right] \tag{3.13}$$

where $L_1 = L_0 - l_c/2$ and $L_2 = L_0 + l_c/2$, L_0 is the distance from the centre of the electron cooler to the imaging detector, l_c is the cooler length (0.85 m), C_0 is $d_{lab}(L_0)/L_0$, and $K(L_i) = Re\{\sqrt{(C_0 L_i)^2 - d_{det}^2}\}$ (see Fig. 3.5). Typical examples of anisotropy are that the DR cross section is larger for perpendicular or for parallel dissociations with respect to the beam direction [51]. The distance distributions for these dependencies as well as the isotropic distribution are shown in Fig. 3.6.

The spectrum observed on the imaging detector is a superposition of distance distributions, $D_{\beta,v,J}(d_{det})$, from each initial parent-state contribution dissociating into the possible branching channels. If it is assumed that the DR cross section has negligible rotational dependence and the rotational distribution is given by the Boltzmann distribution at a temperature T (K), the total distance distribution of the physical branching of a DR reaction can be modelled by,

$$D(d_{det}) = constant\ \sum_j (2j+1)e^{-j(j+1)B_r/kT} \times \sum_v \sum_\beta p(v)k(v)B(v,\beta)D_{\beta,v,J}(d_{det}) \tag{3.14}$$

where j are the rotational levels, B_r is the rotational constant of the molecular ion, $p(v)$ and $k(v)$ are the population and the rate coefficient of vibrational level v, and $B(v,\beta)$ is the branching fraction of the parent ions with vibrational level v dissociating into channel β. Figure 3.7 shows an example of an imaging spectrum with 3 isotropic distance distributions superimposed on each other. As can be seen, the distributions related to the lower KERs are superimposed on the tails of those related to the larger KERs. In the *2D* imaging spectra of isotropic DR reactions, electronic structure from the different excitations of the product atoms can usually be directly observed, whereas vibrational structure from possible multiple vibrational levels of the parent ions cannot be directly observed. Rather than observing separate vibrational peaks, the observed peak is broadened. The degree of structure that is visible is dependent on the KERs, the temperature, the demagnification factor between the phosphor and the CCD camera, and of course the spatial resolution of the camera.

The toroidal effect is included here in a similar manner as in the rate analysis. The toroidal sections are segmented and the collision energies in the segments are determined. For each collision energy, the branching fractions as well as the vibrational cross section may change and the number of dissociation channels may increase. For each toroidal collision energy, a model distance distribution ($D(d_{det})$) is produced, which is weighed by the total DR cross section at that energy. The toroidal correction includes experimentally determined values when possible and assumptions where necessary (e.g., branching fractions are assumed equal to those at 0 eV). All model distributions assume mono-energetic electron collisions.

In order to extract the desired branching fractions and possible vibrational cross sections, the analytical *2D*-model distance distributions are fit to the observed imaging spectrum using

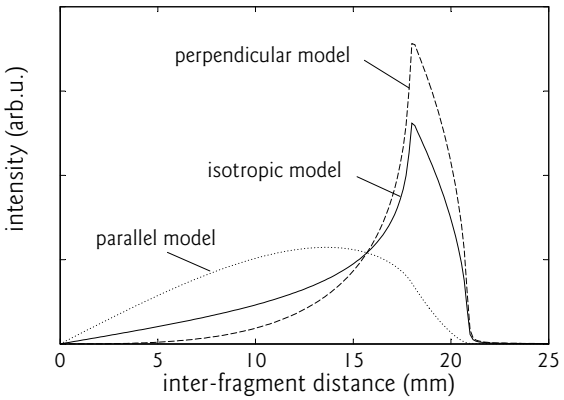

Figure 3.6: The shape of the *2D*-model distance distributions for a single dissociation limit as used in the fitting of imaging data from a storage-ring experiment; in the case of isotropic (solid curve), preferably perpendicular (dashed curve), and preferably parallel (dotted curve) dissociations. The perpendicular and parallel preferences are described in terms of $\cos^2\theta$ and $\sin^2\theta$, where θ is the angle between the orientation of the dissociation and the beam axis. The shown model distributions include a KER of 6.95 eV, a 300 K rotational temperature, a finite interaction region length of 85 cm, and the toroidal correction.

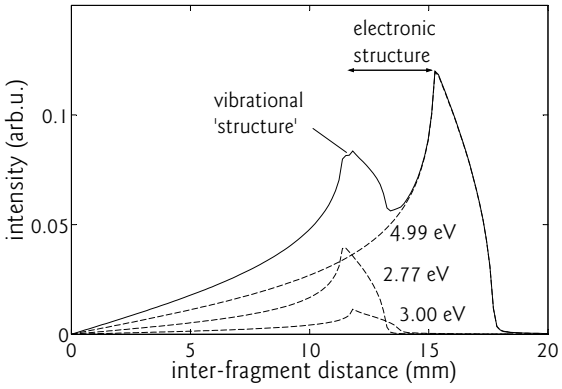

Figure 3.7: Three isotropic model distributions superimposed on each other as could be measured in an imaging experiment. Three example dissociation limits with two well-separated KERs (2.77 and 4.99 eV) and a not so well separated KER (3.00 eV) are chosen to illustrate the visibility of electronic and vibrational structures. The temperature used is 300 K and an arbitrary relative scaling of 1 : 0.3 : 4 between the channels is chosen.

a weighted least-squares fit with the local errors as weights. The inter-fragment separations that are below our spatial resolution are excluded from the fit. The resulting branching values are normalised to their total sum. The vibrational cross sections are normalised to an arbitrary value. No absolute values are derived due to the low efficiency of the imaging detection system. The rotational temperature of the ion beam and the demagnification factor of the optical system are optimised once for all spectra taken.

3.3.2 Forward Simulation for a Polyatomic Ion

In the case of a polyatomic system, the energy and linear momentum among the fragments must be conserved and the total kinetic energy is related to the so-called total displacement (TD) of the particles from the centre-of-mass (CM) of a dissociation (see also Fig. 1.9). The TD is analogous to the distance distribution described in the previous section. For a single KER value and one of the particles receiving no kinetic energy, i.e., it remains at the CM, the TD equals the inter-fragment distance of a diatomic dissociation. For 3-particle dissociations, the TD is defined as,

$$\mathrm{TD} = \sqrt{\frac{m_3 d_3^2 + m_2 d_2^2 + m_1 d_1^2}{\mu_{21}}} \tag{3.15}$$

where m_i are the masses of the particles, d_i are the distances of the particles to the CM as recorded on the detector, and μ_{21} is the reduced mass of the two particles furthest from the CM. An unambiguous determination of the TD values requires knowing the identities of the particles. The TD relates the observed 3-particle events to the branching channels. Fig.

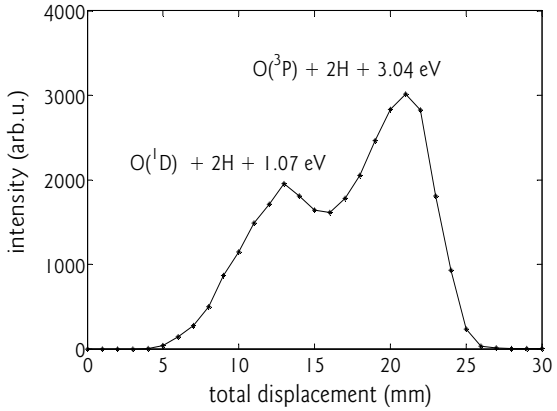

Figure 3.8: The TD distribution as measured in the DR of H_2O^+ fragmenting into O + H + H using the imaging technique [52]. This distribution provides information on the partitioning of the available energy over the total kinetic and internal energy and in this case even on the internal excitation of the individual O fragments.

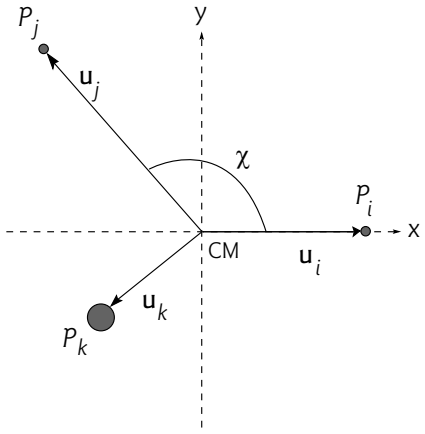

Figure 3.9: The displacement of the product fragments in the DR of a polyatomic ion fragmenting into three particles. The particles furthest from the centre-of-mass (CM) are P_i and P_j. The angle χ is the angle upon dissociation between these two particles and the CM. The vectors **u** are the momenta of the respective product fragments after dissociation.

3.8 shows the TD distribution for the DR of H_2O^+ fragmenting into O + H + H [52]. In this case, no molecular fragments are produced and the excitation of the O atom can be clearly observed. Excitation of the O atom gives rise to the peak at the lower TD values (less kinetic energy available) and the ground-state atoms give rise to the peak at higher TD values (maximum kinetic energy available). DR reactions producing molecular product fragments can give rise to very broad TD distributions with little structure due to the many possible rovibrational states. Other measured parameters can aid to investigate the dynamics of the reaction further. Typically, the projected angle on the detector, $\phi = \angle\,(P_i - \mathrm{CM} - P_j)$, is also determined, where P_i and P_j are the fragments furthest from the CM. These angles are related to the angles upon dissociation (see Chapter 6).

A forward simulation is used to analyse the polyatomic imaging spectrum, which is a Monte Carlo procedure producing dissociations on an event-by-event basis. Each dissociation is described by the following three variables, which can be fixed, varied within boundaries, varied randomly, or correlated (see Fig. 3.9). The total kinetic energy available in the dissociation is used as input. The free parameters are the intra-fragment angle upon dissociation, $\chi = \angle\,(P_i - \mathrm{CM} - P_j)$, in the molecular frame and the ratio between the fragment momenta of the particles P_i and P_j, $\rho = \mathbf{u}_j/\mathbf{u}_i$, which is defined such that $0 \leq \rho \leq 1$. The events are randomly distributed over the length of the electron cooler (toroidal section included), travel the same distances to the detector, and have the longitudinal velocity as in the experiment. The included KERs are the ones related to the physical branching channels [such as Eqs. (6.2a) – (6.2d) for $(NO)_2^+$], and if (ro)vibrational excited fragments are included, the total KER is reduced by the amount of excitation in energy increments based on, e.g., the vibrational spacing. The simulation described here is the one implemented for imaging studies of the three-body break-up of XH_2^+ ions in Stockholm and is explained in more detail in Refs. [52, 53]. The simulation best describing the measured data, is determined from a simultaneous weighted least-squares fit of all the used parameter distributions with the local

errors are weights.

3.4 Dissociative Recombination as Measure of Radiative Lifetime

The DR experiments at CRYRING often involve vibronic ground-state ions as the storage ring provides the time for molecular ions that possess a dipole moment to relax. The DR signal is therefore typically measured after several seconds of storage such that no temporal behaviour is hindering the measurement. It may, however, be desired to take advantage of the time-varying behaviour inside the ring to investigate the radiative lifetime of the ions. Ions in an excited metastable state, i.e., with a long radiative lifetime, give rise to signals over a sufficiently long time period to be able to investigate the temporal behaviour. The decay in the intensity of this DR signal provides a means to measure the lifetime of the metastable state. The procedure to record and extract the radiative lifetime is as follows. The measuring gate starts as soon as acceleration is completed (~ 1 s), such that most of the contribution from the decaying state can still be measured. Imaging spectra as described above (see Fig. 3.7) are acquired while labelling the recorded events with time stamps relative to the start of the measuring gate (50 ms accuracy). Distance distributions can then be derived at any selected time interval. The decrease in intensity of the time-varying DR signal can hence be extracted, giving us the lifetime (see also §5.5) .

There are two things to consider while extracting the time-varying signal. First, the spectra at the selected time intervals have to be normalised to each other; the low efficiency of the imaging detection system prevents absolute measurements. The signal from the vibronic ground-state ions provides the means for normalisation as it is constant in time, i.e., assuming the DR reaction has no influence on the population of the ion beam. In some cases the DR reactions can have a measurable effect on the destruction of the ion beam, such as in the DR of H_2^+. Second, there might be other temporal effects playing a role. This is why the temporal behaviour of the dynamics are studied instead of the rate. The metastable ionic state provides additional kinetic energy, giving rise to a contribution that is shifted towards somewhat higher inter-fragment separations. Predictions can be made on the possible dissociation limits and their KERs. The destruction of the ions is accounted for when normalising to the ground state signal. Contributions from other decaying states give rise to multiple lifetimes and therefore a multi-exponential decay curve.

3.5 Stochastic and Systematic Errors

The magnitude of the statistical errors are determined by the signal-integration time of both the DR signal and the BG signal. Due to the decreasing DR cross section upon increasing collision energy, longer signal-integration times are required for elevated energies. When the signal-to-noise ratio is small, long background-signal integration times are also desired. Besides the stochastic errors, there are a few systematic errors worth mentioning. In absolute rate measurements, systematic errors are introduced by the ion-current measurement. This current measurement is assumed to be accurate to about 20%. An experiment in which three storage rings were compared showed that the current measurement uncertainty may well be

smaller than 20% [44]. This uncertainty affects all measurements in a similar way; the relative cross-section determinations are more accurate. Systematic errors in the imaging measurement can be introduced by possible inhomogeneities of the detection system. However, the large centre-of-mass distribution (largely) compensates for this effect. In the least-squares fit of the model, systematic errors may arise from a possible presence of anisotropy in the DR reaction, contamination of vibrationally excited ions that are not taken into account, rotational DR dependence, and assumptions that are made for the toroidal corrections. In the imaging of polyatomic ions additional errors may arise from possible misidentification of the particles and the presence of events falsely attributed to the fragmentation channel under investigation. Errors in the analysis of the chemical fragmentation can originate from wrongly chosen Gaussian model distributions. Finally, all measurements can contain a bias due to missing events, however, this bias can be assessed using simulations and accounted for.

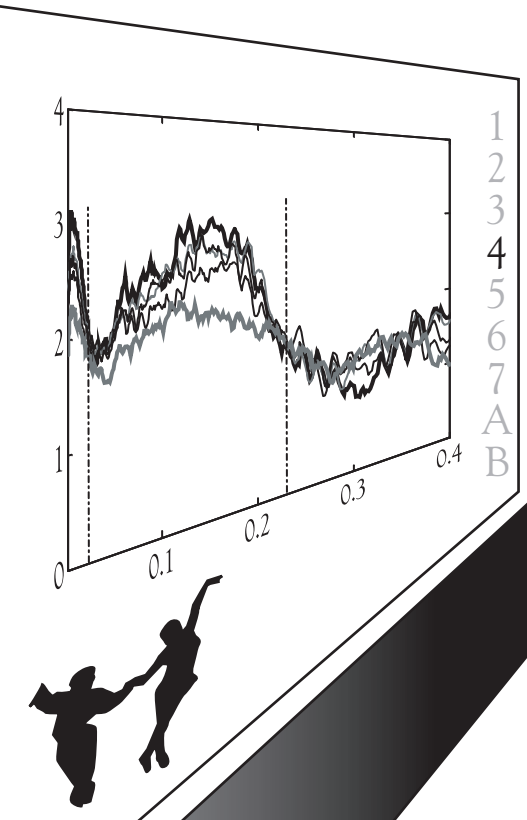

Physics is...

going on a conference to Australia

Annemieke

Chapter 4

Dissociative Recombination of Oxygen Ions

The motivation driving the present study was to provide new and improved laboratory answers to the question on the dependencies of the dissociative recombination (DR) of the molecular oxygen ion. This chapter covers the experimental studies of both the electron-energy as well as the vibrational-state dependence of the $O_2^+(X\,^2\Pi_g)$ electronic ground state. A general introduction to the current status and some of the physics of the DR reaction of O_2^+ is given first. The study of the electron-energy dependence is described in Part A of this chapter and covers the energy region of 0−300 meV using electronic and vibrational ground-state O_2^+ ions in order to determine the temperature-dependent branching relevant to atmospheric modelling (up to 1000 K). The branching results are presented as branching fractions as well as quantum yields and are discussed in the context of previous research and theoretical considerations. Attention is also given to the aspect of the angular dependence of the DR reaction. Part B covers the study of the effect of vibrational excitation in the DR reaction of $O_2^+(X\,^2\Pi_g)$. The methods used to control the vibrational populations of the parent oxygen ions, which are required to unravel the vibrational dependency, are presented first, followed by a description of five selected populations. For each of these vibrational populations, the total rate coefficient as a function of collision energy up to 0.4 eV is presented. This is followed by the product distributions at 0 eV collision energy of these same vibrational populations from which partial (vibrationally resolved) rate coefficients, quantum yields, and branching fractions for $O_2^+(X\,^2\Pi_g, v = 0-2)$ are derived. Next, the effects of the DR reactions and super elastic collisions (SECs) on the vibrational population of the ion beam are treated. The vibrational-state dependent results are discussed in the context of previous research on O_2^+ and similar systems as well as in the context of theory and atmospheric modelling.

4.1 On the Dissociative Recombination of O_2^+

4.1.1 The Current Status

DR of O_2^+ is one of the important reactions behind the green and red airglow in the Earth's atmosphere. It is even believed to be the only reaction responsible for the green airglow in the night time *F* region of the ionosphere (see §1.3). The $O(^1S)$ atoms formed in the DR reaction produce the green airglow at 557.7 nm when they relax radiatively to the $O(^1D)$ state, while the $O(^1D)$ atoms give rise to the red airglow at 630.0 nm when relaxing to the ground state. Both the $O(^1S)$ atoms, having a radiative lifetime of 0.71 s, and the $O(^1D)$ atoms, with a radiative lifetime of 108 s, are able to radiatively relax due to the long mean free paths. *In situ* atmospheric studies of the DR reaction of O_2^+ measure the green and/or the red airglow at 557.7 and 630.0 nm, respectively. The exothermicity of the reaction for ground-state oxygen ions and 0-eV electrons can be as large as 7 eV and plays a role in atmospheric heating as well as in gravitational escape on Mars [7, 8].

Terrestrial O_2^+ ions are expected to be weakly vibrationally excited. The amount of excitation increases with altitude due to the quickly decreasing particle densities. On Mars and Venus, the O_2^+ ions are more excited as no effective quenching mechanism exists. Surprisingly, the translational temperature of the electrons on Mars and Venus is only roughly 300 K at maximum, while on Earth, it can go up to about 1000 K. In order to interpret and quantify the green and red airglow observations and their ionospheric implications, the dependence of the DR reaction on the O_2^+ vibrational excitation and the electron

collision energy must be known. For terrestrial modelling, branching behaviour is required for the lowest vibrational levels and for collision energies up to roughly 300 meV. Although numerous atmospheric, laboratory, and theoretical studies of both the DR rate coefficients and branching of O_2^+ exist, this knowledge is still lacking. Previous research encompasses *in situ* studies employing ground-based and air-borne operations with satellite based instruments and space probes as well as laboratory research employing ion traps, stationary and flowing afterglows, and merged-beams techniques.

The thermal rate coefficient, $\alpha(O_2^+)$, is well established and reproduced in many experiments. The reported laboratory values [16, 23, 46, 54–61] range from $1.7 \cdot 10^{-7}$ to $2.4 \cdot 10^{-7}$ $cm^3\ s^{-1}$ at 300 K. The accepted value for ground state oxygen ions at 300 K is $1.95 \cdot 10^{-7}$ $cm^3\ s^{-1}$. In general, the temperature dependence of the thermal rate coefficient is reported to follow $\alpha(O_2^+) \sim T^{-0.7}$ with T pertaining mainly to the electron temperature. In merged-beam experiments it is the rate coefficient, k, in terms of the electron collision energy which is commonly reported and its dependence is found [46, 62–64] to be $k(O_2^+) \sim E_c^{-0.5}$. The agreement on the thermal rate coefficient is somewhat surprising in view of the fact that many of these experiments had unknown and certainly often different vibrational populations of the parent ions. The branching fractions and quantum yields of the product atoms for different vibrational levels are not well established and little is known on any vibrational dependence. In the case of the $O(^1S)$ quantum yield, experimental values have been found that range from almost 0.7% to 10% [22, 23, 42, 65–67]. Again, many of these experiments had different, and often unknown, vibrational populations of the parent ions. In the past decade, the rate coefficient and branching of specifically $O_2^+(X\,^2\Pi_g, v = 0)$ have been investigated using ion storage rings. At the ASTRID ion storage ring, a beam of an unknown vibrational composition of the mixed isotope $^{16}O^{18}O^+$ was used in the studies [67]. In earlier work of our group, the branching fractions at collision energies between 0 and 36 meV were established using an O_2^+ ion beam that consisted of $v = 0$ ions only [46]. This work included the theoretical prediction on the electron-energy dependence of the $O(^1S)$ quantum yield and showed good agreement between the two [22]. In an earlier paper [68] on a theoretical study of the DR of O_2^+, an $O(^1S)$ quantum yield of between 1.6% and 2.9% from the reaction of $v = 0$ ground state oxygen ions at 0 eV collision energy is predicted after introducing spin-orbit coupling into the model. The inclusion of spin-orbit coupling was a first for the modelling of a DR reaction. Though seemingly small, these predicted quantum yields are quite large; before the inclusion of the spin-orbit mechanism, a negligible $O(^1S)$ cross section for $O_2^+(v = 0)$ ions and small $O(^1S)$ cross sections from $v = 1$ and 2 ions were predicted [69]. Although theory is making considerable progress, to the best of our knowledge, no complete branching results have been reported for the DR of $O_2^+(v > 0)$.

In the case of atmospheric observations, many data are reported in which variations in the green airglow produced by de-excitation of $O(^1S)$ are linked to changes in the vibrational excitation of the parent O_2^+ ions. The change of 2% to 23% in the $O(^1S)$ quantum yield predicted from *in situ* measurements [21, 70–77] is much larger than that suggested from the laboratory experiments. From these *in situ* observations, it is believed that the $O(^1S)$ yield must be strongly dependent on the vibrational states of the parent O_2^+ ion [21, 76–78] with the vibrational excitation of the O_2^+ ions believed to increase with altitude and the largest $O(^1S)$ yields to come from the highest vibrational states. Studies of the production and quenching of $O_2^+(v)$ in the ionosphere, however, often report the vibrational deactivation at nighttime is fast, giving a source of confusion concerning the role of DR in the production

of $O(^1S)$ in the *F* region of our ionosphere [20, 23, 24, 79]. The role of DR in planetary atmospheres is also not well understood. For a long time it was believed that the green airglow could be a diagnostic tool for the detection of O_2-bearing atmospheres. However, in 2001, Slanger *et al.* reported the discovery of the oxygen green line in the Venus night glow [6], though Venus does not have an Earth-like atmosphere. The production of $O(^1S)$ responsible for the Venusian green-line emission is attributed to another reaction at lower altitudes. No vibrational dependent data on DR was available to include its possible influence.

4.1.2 The Physics Involved

The possible DR reaction pathways for ground-state $O_2^+(X\,^2\Pi_g, v = 0)$ ions and 0-eV electrons are shown in Eqs. (4.1a)–(4.1e). There are five dissociation limits energetically possible with KERs varying from 0.8 to 6.95 eV. The next dissociation limit is not reached until an additional 1.41 eV of energy is introduced, either through collision (E_c) or vibrational energy (E_v) [see Eq. (4.1f)]. In the latter case the necessary energy is not reached until $O_2^+(X\,^2\Pi_g, v = 8)$.

$$
\begin{aligned}
O_2^+(X\,^2\Pi_g, v) + e^-(E_c) \quad &\rightarrow O(^3P) + O(^3P) + (6.95 + E_v + E_c)\ \text{eV} && \text{(4.1a)}\\
&\rightarrow O(^3P) + O(^1D) + (4.99 + E_v + E_c)\ \text{eV} && \text{(4.1b)}\\
&\rightarrow O(^1D) + O(^1D) + (3.02 + E_v + E_c)\ \text{eV} && \text{(4.1c)}\\
&\rightarrow O(^3P) + O(^1S) + (2.77 + E_v + E_c)\ \text{eV} && \text{(4.1d)}\\
&\rightarrow O(^1D) + O(^1S) + (0.80 + E_v + E_c)\ \text{eV} && \text{(4.1e)}\\
&\rightarrow O(^1S) + O(^1S) - (1.41 + E_v + E_c)\ \text{eV} && \text{(4.1f)}
\end{aligned}
$$

Figure 4.1 shows a number of potential-energy curves relevant for the DR of O_2^+ at low energies. All of the valence states shown have a significant electron-capture matrix element as evaluated by Guberman [80]. The diabatic, doubly excited, repulsive, valence state curves that cross the ionic state near the equilibrium separation of the ion, ensure a finite Franck-Condon overlap. The dissociation limits connected to the valence states are shown on the right hand side. As can be observed, most dissociation limits are associated with only a single dominating diabatic state. Figure 4.2 shows most of the relevant potential curves in an adiabatic representation along with the metastable ionic curve $O_2^+(a\,^4\Pi_u)$. This adiabatic representation reveals some of the possible complications in assessing the outcome of the DR reaction in a simple way. Firstly, the avoided crossings between the different repulsive states and the low lying Rydberg states indicate large electronic couplings between the associated diabatic states, and those need to be taken into account when trying to predict the branching fractions and rate coefficients. Secondly, the production of the $O(^1S)$ products is complex. The $O(^1D) + O(^1S)$ dissociation limit [see Eq. (4.1e)] is assumed to be the only channel leading to $O(^1S)$ products, via the doubly excited $^1\Sigma_u^+$ state [69, 81]. For ground state O_2^+, this channel is neither accessible via the direct nor the indirect mechanisms, thus reducing the $O(^1S)$ yield [82]. The route to this channel is via formation of Rydberg states in the $^3\Sigma_u^-$ manifold followed by a radiationless transition involving spin-orbit coupling [68]. For higher vibrational levels the direct route to the $^1\Sigma_u^+$ state is open. Strong indications exist that the $O(^3P) + O(^1S)$ dissociation limit [see Eq. (4.1d)] does not play a role in the DR process. These indications are found both in experiments with vibrational ground state

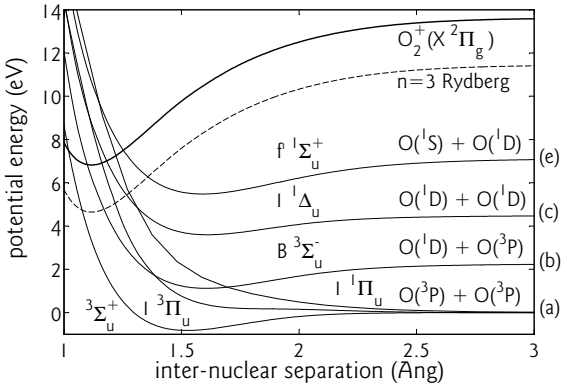

Figure 4.1: Diabatic representation of the potential curves relevant for the DR of O_2^+. The dissociation limits connected with each valence capture state are given on the right. The labels (a)−(c), and (e) refer to Eqs. (4.1a)−(4.1c), and (4.1e), respectively.

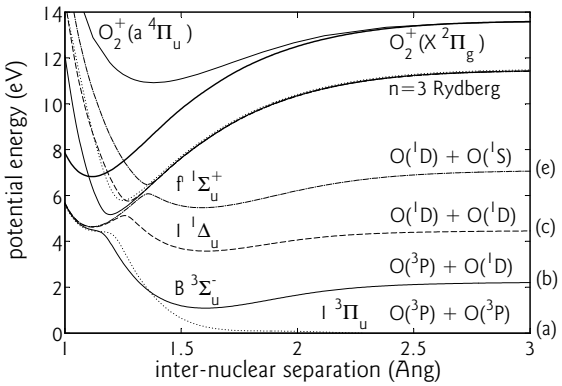

Figure 4.2: Adiabatic representation of the potential curves relevant for the DR process with O_2^+ together with the first ionic metastable state $a\ ^4\Pi_u$. The adiabatic neutral capture states show the consequences of the interaction with the n=3 Rydberg states. The dissociation limits connected with each unmixed valence capture state are given on the right. The labels (a)−(c), and (e) refer to Eqs. (4.1a)−(4.1c), and (4.1e), respectively.

O_2^+ ions and low-energy electrons [46, 83] as in an experiment [67] with the isotopomer $^{16}O^{18}O^+$. Additionally Helm *et al.* [42] did not observe any dissociation towards the $O(^3P)$ + $O(^1S)$ channel for all vibrations $v = 0 - 6$ in a process of field induced predissociation of high lying Rydberg states. This process has similarities with the DR process. Calculations indicate that the lowest lying repulsive state that dissociates to the $O(^3P)$ + $O(^1S)$ limit crosses the ionic ground state near the $v = 9$ level [69, 84].

A. Electron-Energy Dependence

4.2 Experimental Details

The experimental work for the study of electron-energy dependency of the DR process was conducted at the heavy-ion storage ring, CRYRING. This dependence has been studied through the product distributions using the imaging technique (see §2.1.4) at collision energies chosen between 0 and 300 meV. Longer data acquisition times were used to (partly) compensate for the loss in signal rate at the elevated energies. The O_2^+ ions were created with the JIMIS ion source, which is known to produce vibrationally cold ions (see §2.1.3). The ion beam was accelerated to 2.9 MeV in 1.1 s. The acquired imaging spectra in the present study are *2D* projections of the separations between the dissociating atoms, no arrival-time differences between the two O product atoms were measured. A summary of the experimental and analytical details is given in Appendix A.

4.3 Branching Fractions between 0 and 300 meV

The dissociation dynamics were studied at 13 different values of the collision energy. A selection of the acquired spectra is shown in Fig. 4.3. These spectra are the distance distributions at collision energies of 1, 10, 118, and 229 meV (space-charge corrected energies). The measured data (stars) exhibit a clear difference in branching behaviour for the different energies. At $E_c = 10$ meV the $O(^1D) + O(^1S)$ dissociation limit [peak (e)] is hardly visible. Previous research [46] revealed a disappearance of the $O(^1S)$ peak at 11 meV. Figure 4.3 also shows the fits corresponding to the different spectra (solid curves). They are determined by a weighted least-squares optimisation procedure for each E_c separately, while using isotropic model projections [67] for all five dissociation limits [see Eqs. (4.1a)−(4.1e)] and only their branching fractions as free parameters. The model used includes a rotational temperature of the molecular ions of 300 K and assumes only $v = 0$ parent ions; however, a small contribution of $O_2^+(X\,^2\Pi_g, v = 1)$ ions cannot be fully excluded from the fits. The demagnification of the optical system between the phosphor and the CCD camera is optimised once for all spectra. The discrepancy between the fit and the measured data near 0-mm separation is due to the inability of the data acquisition software to distinguish between two close/overlapping hits on the detector. The inter-fragment distances below 3 mm are therefore not included in the least-squares optimisation range. At low collision energies, a weak signal is observed at distances above 22 mm, pointing at higher KER values that cannot be fitted using $v = 0$ ions only nor using any other low vibrational level. The discrepancy between the fit and the data decreases upon increasing collision energy. Above 100 meV the fitted models can describe the entire measured spectrum.

The derived branching fractions for all investigated collision energies are listed in Table 4.1. The $O(^3P) + O(^1S)$ channel [see Eq. (4.1d)] is not listed; it was included in all the fits but turned out not to contribute to the acquired spectra with an uncertainty of about 1%. Its absence is predicted by quantum-chemical models and can also be inferred from other experimental information [42, 46, 67, 69, 84, 85]. All branching fractions are shown in Fig. 4.4. The corresponding errors have been estimated from repeating the optimisation using a large number of synthetic spectra modified with a Monte Carlo procedure in accord with their statistical error. The errors do not take into account the possibility of systematic errors due to, for example, inhomogeneities of the detection system, the possible presence of anisotropy in the DR reaction, or some contamination of vibrationally excited ions. As a reference, the reduced cross section, which is the DR cross section multiplied by the collision energy, is also presented [85]. The DR cross section due to the direct DR process decreases inversely proportional with the collision energy. Hence the product of cross section and collision energy is constant in the absence of any other process than the direct DR mechanism. The coarse structure that can be observed in Fig. 4.4 is indicative of resonant processes such as in the indirect DR mechanism, in which capture initially takes place into molecular Rydberg states. The reduced cross section shows minima near 30 and 250 meV, which may also be accompanied by changes in branching behaviour.

The observed branching behaviour shows the following properties. Branching to the $O(^1D) + O(^1S)$ limit [label (e)] starts at about 4% at 0 eV and goes down to 2% at 10 meV. Earlier research, which focused on the branching in the 0−40 meV region, shows a continuous decrease in the $O(^1S)$ yield down to zero between 0 and 11 meV, and a finite $O(^1S)$ yield up to 40 meV [46]. Above 40 meV, our results indicate that the $O(^1S)$ yield

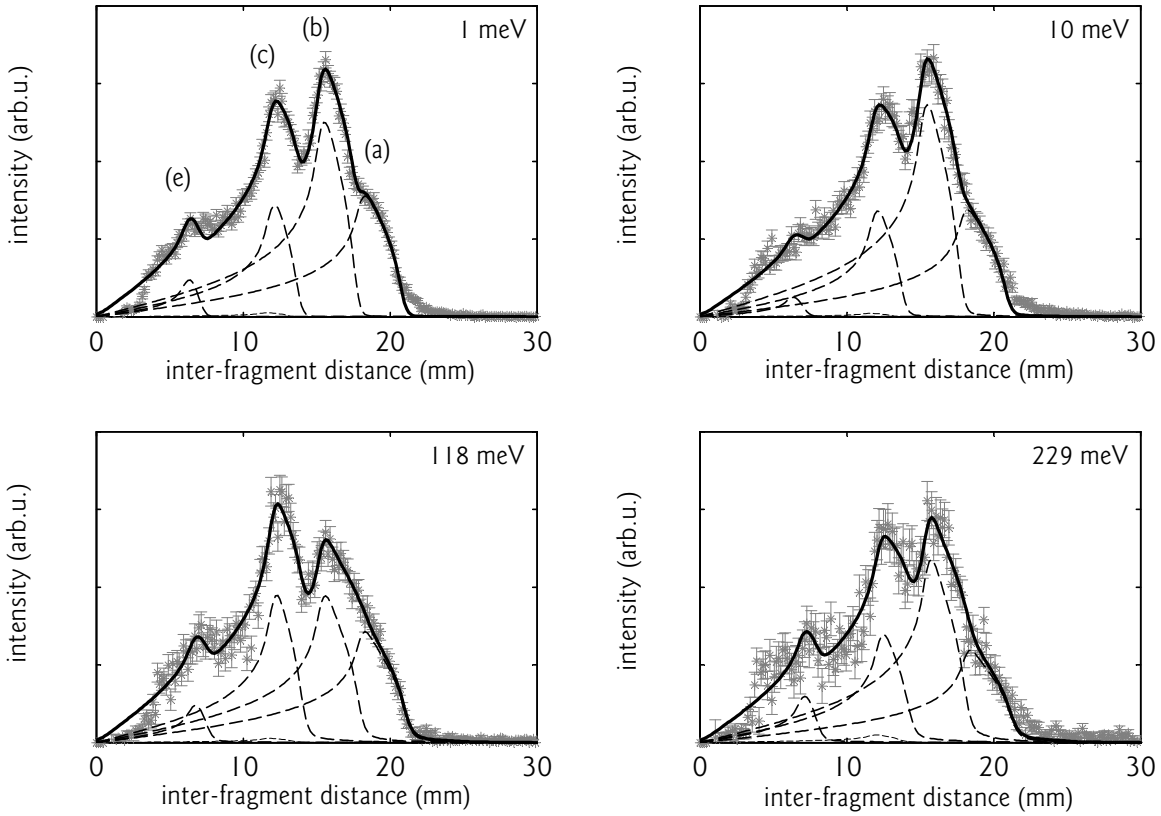

Figure 4.3: The distance distributions of the DR of O_2^+ at collision energies of 1, 10, 118, and 229 meV (space-charge corrected energies). The stars are the experimental data and the solid curves are the simulations based on isotropic distributions. The peaks corresponding to the dissociation limits given in Eqs. (4.1a)−(4.1c), and (4.1e) are indicated at 1 meV with the labels (a)−(c) and (e), respectively. The dashed curves show the contributions of the individual dissociation limits as results from the fits.

remains around a constant of 5%. Small, but significant oscillations can be observed that do not seem to be correlated with structures in the reduced cross section, nor clearly with the branching behaviour to the other limits. We do not observe any value that is significantly larger than 5% nor do we observe a strong increase with electron collision energy. As will be discussed later (see §4.4), the latter could have been expected. The branching to $O(^3P)$ + $O(^3P)$ [label (a)] and $O(^1D)$ + $O(^1D)$ [label (c)] behaves in an approximately similar fashion. Their absolute values are about the same but, more importantly, they show similar variations as a function of collision energy above 40 meV. Below 40 meV, they differ significantly. The behaviour above 40 meV could be suggestive of a single capture channel, which during the dissociation process distributes itself over these two dissociation limits. Below $E_c = 40$ meV, the relative importance of the $O(^3P)$ + $O(^3P)$ limit is higher than the $O(^1D)$ + $O(^1D)$ limit. For all energies, the most dominant dissociation limit is the mixed $O(^3P)$ + $O(^1D)$ limit [label (b)] with values up to 50%. In view of the fact that the total branching sums up to unity, the minimum in the dominant channel occurs at the energy where the two other channels show a maximum. The $O(^3P)$ + $O(^1S)$ channel [label (d)] is found to be consistently smaller than 2% and insignificant, an explicit experimental verification of the absence of this channel in the DR process. Figure 4.4 also shows the characteristic energy of the fine-structure splitting of the $O_2^+(X\,^2\Pi_g, v = 0)$ level at 24 meV as well as the branching fractions of the first excited

Table 4.1: The branching fractions and quantum yields for the different investigated collision energies. The $O(^3P)$ + $O(^1S)$ channel is not listed due to its insignificant contribution.

E_c (meV)	1	10	45	78	101	118	142	176	188	211	229	235	281
$O(^3P)$ + $O(^3P)$	[a] 32	29	24	29	33	32	31	25	22	28	27	26	29
$O(^3P)$ + $O(^1D)$	43	49	52	37	33	35	39	45	54	48	45	47	41
$O(^1D)$ + $O(^1D)$	20	20	20	29	27	28	26	23	19	17	22	21	24
$O(^1D)$ + $O(^1S)$	4	2	4	4	6	5	4	6	5	5	6	5	5
$O(^3P)$	[b] 1.07	1.06	0.99	0.94	0.98	0.97	1.00	0.93	0.96	1.03	0.97	0.97	0.97
$O(^1D)$	0.88	0.90	0.95	1.00	0.94	0.97	0.95	0.98	0.97	0.89	0.94	0.95	0.96
$O(^1S)$	0.04	0.02	0.04	0.04	0.06	0.05	0.04	0.06	0.05	0.05	0.06	0.05	0.05

[a] The branching fractions are rounded to the nearest integer value and may not add up to 100% due to rounding errors and the exclusion of the $O(^3P)$ + $O(^1S)$ channel

[b] The quantum yields may not add up to 2 due to the exclusion of the $O(^3P)$ + $O(^1S)$ channel

vibrational level at $\sim$ 232 meV, which have been determined in a recent study in our group on the vibrational dependence of the DR branching [85]. Both characteristic energies precede a resonance minimum in the DR cross section. The vibrational energy has a completely different effect from that of electron collision energy on the DR dynamics. More specifically, the $O(^1D)$ + $O(^1S)$ contribution of 14% for $v = 1$ is much higher than the $\sim$ 5% at 229 meV collision energy.

Earlier research in our group reported branching fractions for electron collision energies up to 36 meV in small energy increments (see Fig. 4.4) [22, 46]. The present $O(^1D)$ + $O(^1S)$ [label (e)] and the $O(^3P)$ + $O(^1D)$ [label (b)] dissociation limits agree well with these previous results. The $O(^1S)$ production drops significantly in both cases at an energy around 11−12 meV, whereas the $O(^3P)$ + $O(^1D)$ goes up. However, the present branching fractions to the $O(^3P)$ + $O(^3P)$ [label (a)] and $O(^1D)$ + $O(^1D)$ [label (c)] limits, at the two investigated energies in this region, are significantly different from the previous measurements. The dissociation limits are more or less reversed. This reversal in branching fractions to the $O(^3P)$ + $O(^3P)$ and the $O(^1D)$ + $O(^1D)$ limit will give rise to a change in the $O(^3P)$ and $O(^1D)$ quantum yields.

Figure 4.5 shows the quantum yields. The quantum yield is the number of atoms produced in a specific state for an average DR event. Hence, the quantum yields sum up to two in the case of the DR of a diatomic. The values of the quantum yields are listed in Table 4.1. As can be observed in Fig. 4.5, the $O(^1D)$ and $O(^3P)$ quantum yields are relatively insensitive to the collision energy and surprisingly similar. For practical purposes the $O(^1D)$ and $O(^3P)$ quantum yields could be assumed to have averages of 0.95 ± 0.04 and 0.99 ± 0.04, respectively, independent of collision energy. This nearly energy-independent behaviour is an intriguing result in view of the significant variations observed in the branching fractions. The $O(^3P)$ quantum yield is generally larger than the $O(^1D)$ quantum yield. At the investigated collision energy of 79 meV the quantum yields of $O(^1D)$ and $O(^3P)$ are nearly equal. This corresponds to the drop in branching towards the mixed $O(^3P)$ + $O(^1D)$ dissociation limit and precedes the similar behaviour of the two dissociation limits $O(^3P)$ + $O(^3P)$ and $O(^1D)$ + $O(^1D)$ (see Fig. 4.4). For reference purposes the quantum yields from our earlier collision energy-dependence research are shown [46]. The observed differences are directly related to

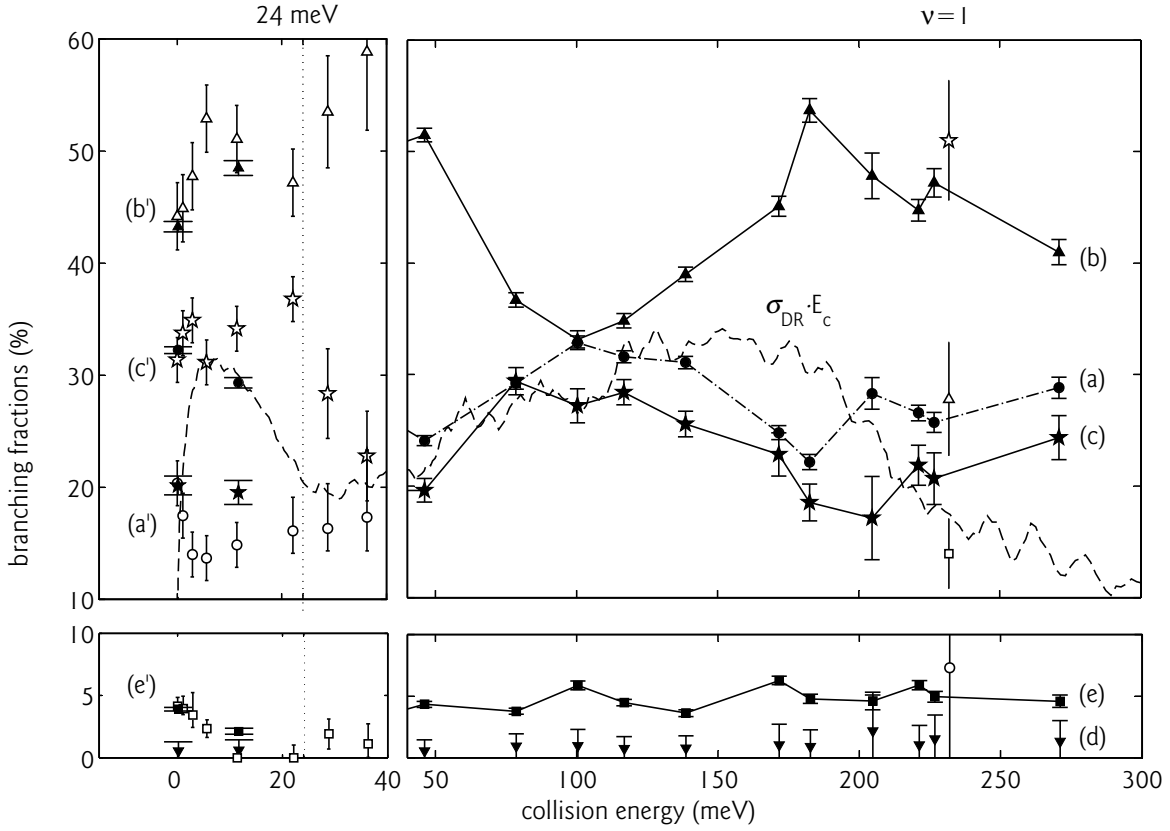

Figure 4.4: The branching fractions for the different dissociation limits at all investigated collision energies. The figure is cut into four adjacent and differently scaled regions. The left two regions show the present (filled symbols) and previous (unfilled symbols) [46] branching fractions for $E_c = 0 - 40$ meV as well as the energy position of the fine-structure splitting of the $O_2^+(X\,^2\Pi_g, v = 0)$ at 24 meV. The right two regions show the present results for $E_c > 40$ meV (filled symbols) and the branching fractions of $O_2^+(v = 1)$ at the energy position of 232 meV (unfilled symbols) [85]. The dissociation limits are as follows: $O(^3P) + O(^3P)$ (●), $O(^3P) + O(^1D)$ (▲), $O(^1D) + O(^1D)$ (★), $O(^3P) + O(^1S)$ (▼), and $O(^1D) + O(^1S)$ (■). For clarity, the limits are additionally labelled (a)−(e) and (a')−(e') for the present and previous [46] branching fractions, respectively, corresponding to Eqs. (4.1a)−(4.1e). In the top two regions the reduced cross section (arbitrarily scaled in intensity), $\sigma_{DR} \cdot E_c$, is also included (dashed curve) [85]. This curve indicates at what energies resonances in the cross section occur. The fine-structure splitting as well as the vibrational energy spacing proceed a cross-section resonance minimum.

the difference we observe in the branching. The $O(^1S)$ quantum yield equals the branching fraction of $O(^1D) + O(^1S)$. The small oscillations that can be observed do not seem to be correlated with the patterns in the quantum yields of $O(^1D)$ and $O(^3P)$ atoms.

4.3.1 Anisotropy Considerations

Isotropic distributions have been assumed for all dissociation limits and investigated collision energies; this means that all relative orientations of the low-energy electron and the molecular axis are assumed to have equal DR cross sections. However, possible anisotropies in the DR reaction can affect the shape of the *2D* distance distributions. In fact, the efficiency of collision reactions between electrons and molecular ions often depends on the relative orientation of the incoming electron and the molecular axis for reasons of symmetry. As it is believed that the

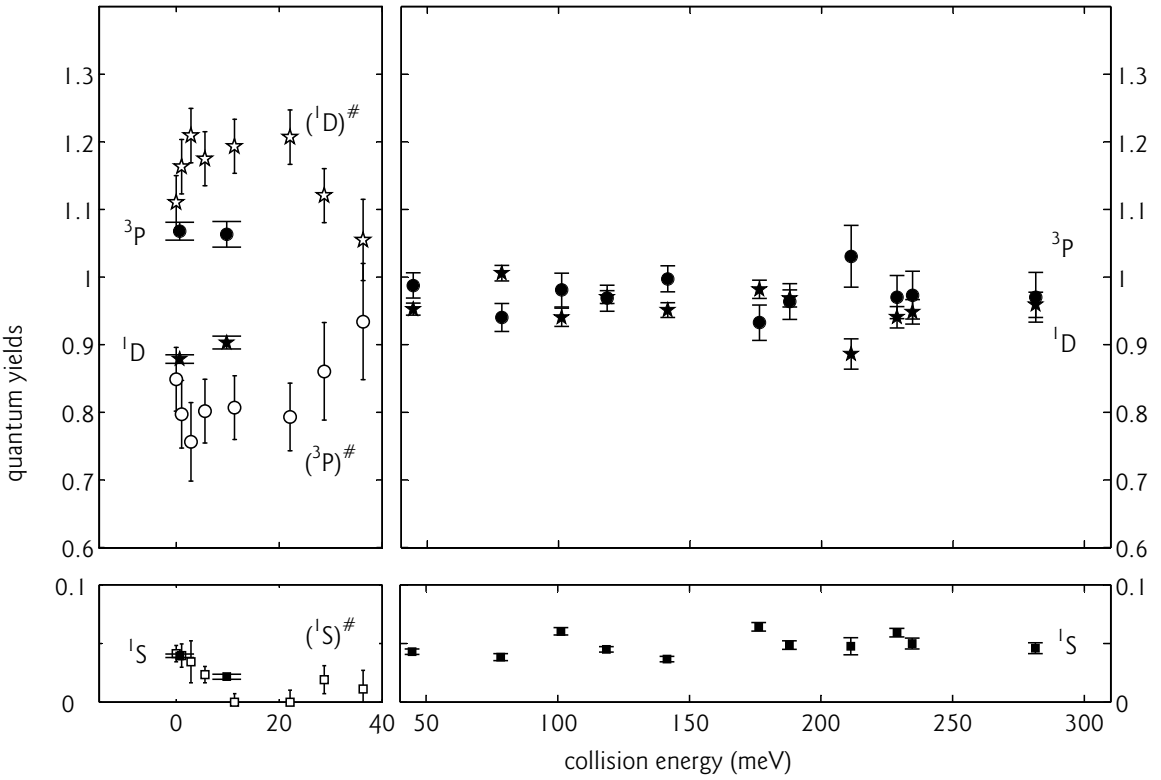

Figure 4.5: The quantum yields at the investigated collision energies (excluding the O(^3P) + O(^1S) channel). The figure is cut into four differently scaled regions. Note that the scale in the quantum yield jumps from 0.1 for the lower to 0.6 for the upper regions. The left two regions show the present (filled symbols) and previous (unfilled symbols) [46] quantum yields for $E_c = 0 - 40$ meV. The right two regions show the present results for $E_c > 40$ meV (filled symbols). The quantum yields are as follows: O(^3P) (●), O(^1D) (★), and O(^1S) (■). For clarity the yields are additionally labelled according to their excited state (the symbol # refers to the previously determined yields).

DR reaction is very fast on a rotational time scale, a preferred axis orientation will show up in the distance distribution. The model distance distributions corresponding to a single channel dissociating isotropically, with a perpendicular preference, and with a parallel preference are shown in Fig. 4.6. The preferences to perpendicular and parallel dissociations are described in terms of $\cos^2\theta$ and $\sin^2\theta$, respectively, where θ is the angle between the orientation of the dissociation and the beam axis. A strong preference for the ion to dissociate parallel to the beam velocity gives a distribution that is much less peaked at the maximum possible distance than in the case of a strong preference for the molecular orientation perpendicular to the beam velocity, which is parallel to the detector plane in our experiment. It has recently been reported that distributions in DR processes may be more complex [86]. These distributions, $I(\theta)$, may not be correctly described with only one parameter as in $I(\theta) \propto 1 + \beta P_2(\cos\theta)$, where β is the so-called anisotropy parameter and $P_2(\cos\theta)$ is the second-order Legendre polynomial. Higher-order Legendre polynomials may be necessary. Complex distributions may result when DR reactions at low collision energy are dominated by a single partial wave, $l\lambda$, with $l > 1$ and $\lambda > 0$. It is noted that, in principle, each dissociation channel may have a different anisotropy when a dissociation limit is connected to a specific molecular symmetry of the initial capture state.

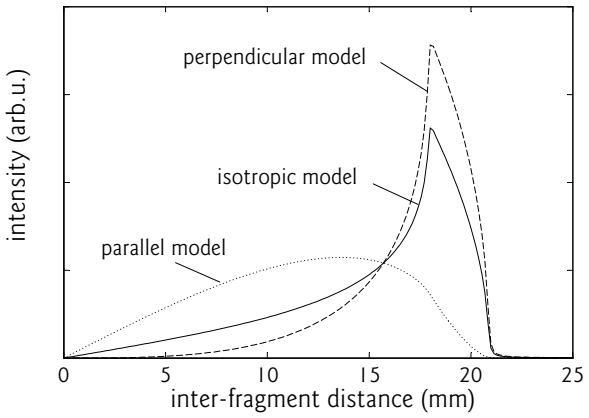

Figure 4.6: The shape of the *2D*-model distance distributions for a single dissociation limit as used to fit the imaging data from a storage-ring experiment; in the case of isotropic (solid curve), preferably perpendicular (dashed curve), and preferably parallel (dotted curve) dissociations. The perpendicular and parallel preferences are described in terms of $\cos^2\theta$ and $\sin^2\theta$, where θ is the angle between the orientation of the dissociation and the beam axis. The shown model distributions include a KER of 6.95 eV, a 300 K rotational temperature, a finite interaction region length of 85 cm, and the toroidal correction.

We investigated the possibility of anisotropy in the present observed distributions at all investigated energies. The nominal 0-eV distribution is included as well, although no preferred relative velocity is present at 0-eV collisions. However, it is sometimes argued that an intrinsically present anisotropy in the merged-beam experiment can still be detected because of the anisotropy of the velocity distribution of the electrons in the reaction region; the velocity spread parallel to the ion-beam velocity is smaller than the velocity spread perpendicular. To the best of our knowledge, no anisotropy has ever been observed at 0 eV. It has been observed for higher energies, such as in the DR of NO^+, where a perpendicular preference was found for one of the dissociation channels at 1 eV collision energy [51, 87].

Figure 4.7 shows the fits for the present distributions at $E_c = 1$, 10, 118, and 229 meV collision energies based on predicted angular distributions for the different dissociation limits in the DR of O_2^+ [86]. This prediction states that the $O(^3P)$ + $O(^3P)$ ground-state limit is related to a preference towards parallel dissociation and the other four limits are related to a preference towards perpendicular dissociation. All fits result in roughly 70% dissociating into the ground-state limit. As can be observed, the large $O(^3P)$ + $O(^3P)$ contributions arise from the following two features of the parallel distribution: there is no clear peak present and the maximum that is observed occurs at much lower distances. As a consequence, the observed shoulder at large particle separation and the structure observed for the remaining channels cannot be reproduced properly, in spite of the fact that the perpendicular distribution is more sharply peaked. The isotropic distributions give the best fit for all dissociation channels at all investigated collision energies between 0 and 300 meV. Additionally, the $O(^3P)$, $O(^1D)$, and $O(^1S)$ quantum yields as derived from the anisotropic fits at all energies are above 1.5, under 0.5, and 0, respectively. We can add two arguments against the use of these quantum yields apart from the experimental observation that the fits using isotropic distributions results in better fits. First, the $O(^1D)$ quantum yield has been determined to be closer to unity, which is in agreement with the present isotropic fit. Previous determinations include laboratory experiments other than storage-ring experiments [65, 78] and *in situ* [76, 77, 88, 89] measurements where values between roughly 0.8 and 1.5 are found at the altitude regions where the DR of ground state O_2^+ mainly determines the $O(^1D)$ production. Second, the experiment near 0 eV collision energy is expected to yield close to isotropic distributions. Using anisotropic distributions for higher collision energies causes drastic changes in the derived branching fractions and quantum yields that are not easily understood.

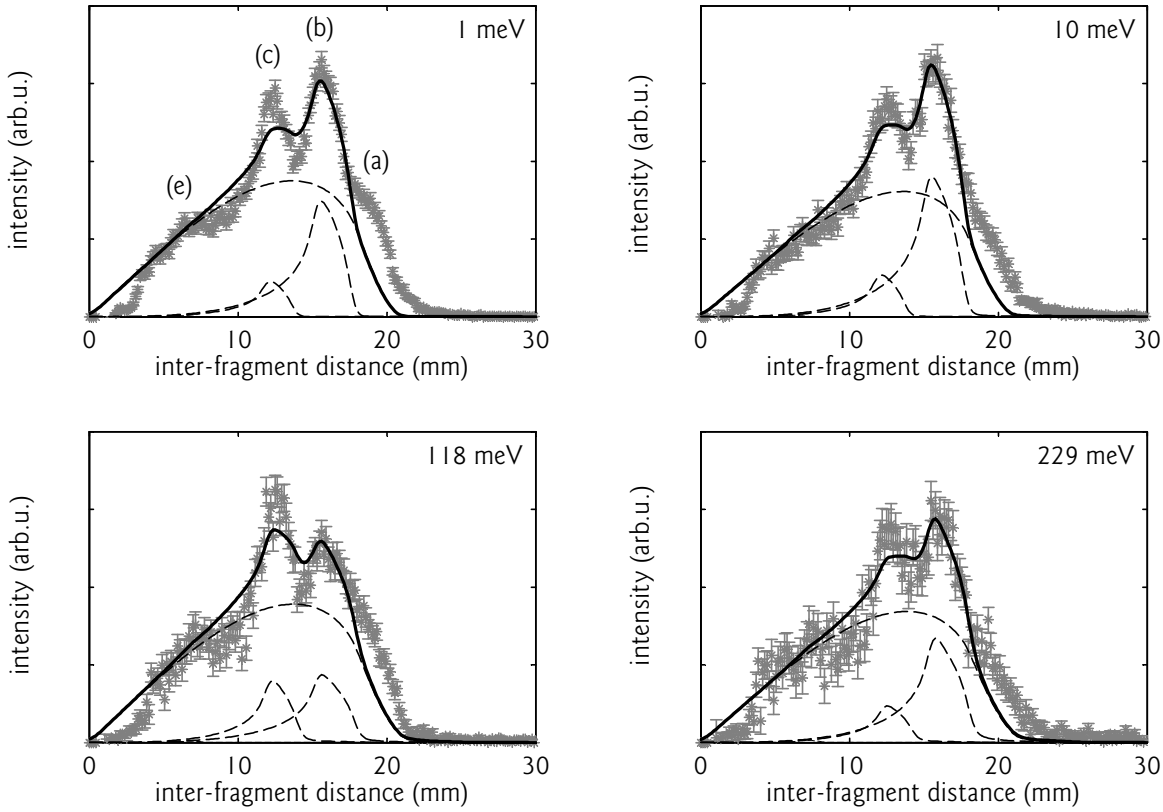

Figure 4.7: The distance distributions of the DR of O_2^+ at 1, 10, 118, and 229 meV (space-charge corrected energies). The stars are the experimental data and the solid curves are the fits based on the angular distributions predicted by Guberman. The peaks, (a)−(c), and (e), correspond to the dissociation limits given in Eqs. (4.1a)−(4.1c) and (4.1e), respectively. The dashed curves show the contributions of the individual dissociation limits as result from the fits, where the $O(^1S)$ contribution [peak (e)] is zero.

4.4 Discussion of the Electron-Energy Dependence

The branching behaviour in the DR of ground-state O_2^+ ions has been studied with a merged-beam technique at collision energies between 0 and 300 meV. The present experiment has covered the energy gap between the ground and first excited vibrational levels of O_2^+ (232 meV). Over this relatively small energy window the branching fractions depend strongly on the collision energy. The branching oscillates as a function of energy for the three dominant channels. The distance between the observed minima is about 150 meV, smaller than the vibrational spacing in the parent ion state (see Fig. 4.4). Dissociation towards the $O(^1D)$ + $O(^1S)$ limit behaves differently. The branching starts at a value of about 5% at 0 eV and then drops to 2% around 10 meV, which is consistent with the previous observation, where the $O(^1D)$ + $O(^1S)$ branching was found to disappear between 11 and 22 meV. Above 40 meV, the present branching remains between 4% and 6% with small, but significant variations. The $O(^1D)$ and $O(^3P)$ quantum yields have only a weak sensitivity to the collision energy and changes stay within 5%, quite similar to the small percentile changes (10%) in the results of Peverall *et al.* [46]. Average values of 0.99 ± 0.04 and 0.95 ± 0.04 for the $O(^3P)$ and $O(^1D)$ yields, respectively, may be used in practice. Interestingly, the quantum yields as predicted by a model involving only statistical branching arguments and spin-conservation rules are 1.06,

0.82, and 0.12 for $O(^3P)$, $O(^1D)$, and $O(^1S)$, respectively [25].

According to Guberman [86], six diabatic channels provide effective routes for the DR of the lower vibrational levels of O_2^+ (see Fig. 4.1): $^3\Pi_u$ ($^3P + ^3P$),$^1\Pi_u$ ($^3P + ^3P$), $A\,^3\Sigma_u^+$ ($^3P + ^3P$), $B\,^3\Sigma_u^-$ ($^1D + ^3P$), $f\,^1\Sigma_u^+$ ($^1S + ^1D$), and $^1\Delta_u$ ($^1D + ^1D$). The dissociation limit corresponding to each capture state is given between the parentheses, i.e., the limits that are linked to the capture states when the Rydberg-valence interactions do not affect the dissociation behaviour. Apart from the ground-state dissociation limit, the three excited limits are served by only one symmetry, allowing for the predictions on the expected anisotropy [86]. A number of other electronic states, such as the $O_2^*(^{1,3}\Pi_g)$, have favourable crossings but unfavourably small electron-capture matrix elements [81]. These states are regarded as irrelevant because of the small associated electron-capture widths. The reason for mentioning them here is the fact that, for example, the diabatic $O_2^*(^1\Pi_g)$ valence state has a crossing with an excited $O_2^*(^1\Pi_g)$ valence state resulting in a distribution of flux over the $O(^3P)$ + $O(^3P)$ and $O(^1D)$ + $O(^1D)$ dissociation limits, such as is seen in the present results. The dominance of the mixed $O(^3P)$ + $O(^1D)$ limit points to the importance of the $^3\Sigma_u^-$ state in the DR process, although this limit is also the dominant channel for the $O_2^*(^3\Pi_g)$ valence state. Another reason for mentioning states other than the six states nominally taken into account is the apparent contradiction between the predicted anisotropy of the fragments and the observed distance distributions. Although heavy-ion storage-ring *2D* experiments do not have sufficient resolving power for precise angular distributions, dissociations with the molecular axis parallel to the collision velocity will show up clearly as being anisotropic [87].

The lack of agreement between our observed isotropy and the predicted angular dependencies [86] deserves further attention. The theoretical predictions agree with the rules derived by Dunn [90] for electron-impact processes and with the predictions of O'Malley and Taylor [91] for dissociative attachment. Dissociative attachment has distinct similarities with DR, but it lacks the long-range Coulomb attraction between the electron and the target. Additionally, the predicted angular dependencies involve both a selection of the active valence states in the process, based on the magnitudes of the Franck-Condon overlap and electron-capture matrix element, as well as the identification of the active electron partial waves in the process at our low electron energies. The treatment of the anisotropy further assumes that the DR process is sudden on the time scale of molecular rotation. This aspect is generally assumed to be correct for DR, as the reaction competes with autoionisation, which is a very fast process (fs).

In an early paper by Guberman [68], a mechanism was proposed that explained the production of a quantum yield of $O(^1S)$ atoms of a few percent in the DR of O_2^+ at small energies. In this mechanism, spin-orbit coupling between Rydberg states of $^3\Sigma_u^-$ and $^1\Sigma_u^+$ characters results in a flux to the $O(^1D)$ + $O(^1S)$ limit. The initial electron capture takes place into the $^3\Sigma_u^-$ state while forming a Rydberg state of the same symmetry resonantly near zero energy. The vibrational excited character of this Rydberg state takes care of a sufficient elongation of the molecular bond such that the Franck-Condon overlap with the $f\,^1\Sigma_u^+$ allows dissociation towards an $O(^1S)$ atom. The rapid decrease in the $O(^1S)$ quantum yield observed below 20 meV collision energy provides strong support of this *resonant* mechanism [22]. The relevance of the small $O(^1D)$ + $O(^1S)$ channel should not be underestimated. Before invoking this spin-orbit mechanism, $O(^1S)$ quantum yields of much less than 0.01 were expected. If direct access of the repulsive $f\,^1\Sigma_u^+$ becomes possible, a strong increase in the branching fraction could be expected to result from the exponential increase in the

overlap between the vibrational wave functions in the initial and final electronic states. Indirect processes can also have significant influence on the final branching when varying the collision energy. The spin-orbit coupling and indirect processes have been included in Guberman's calculation of the $O(^1S)$ quantum yield and show many resonances with varying collision energies, especially above 100 meV (see Fig. 2 in Ref. [22]). The mechanism cannot explain the observed weakly oscillating branching above 40 meV. The present $O(^1S)$ quantum yields are much more constant, even after accounting for the decrease in resolution with increasing collision energy, which has a smoothing effect on the resonant structure of Guberman's prediction.

The results reported here agree with our previous results from measurements at 0 eV in a vibrationally hot ion beam [85]. The branching fractions and quantum yields do not entirely agree with earlier measurements from our group that were taken at energies between 0 and 40 meV in a cold ion beam [46] nor with the measurements performed at ASTRID by Kella *et al.* (at 0 eV) [67]. The latter experiment, however, involved the vibrationally excited mixed-isotope $^{16}O^{18}O^+$ and a single determination using vibrationally independent branching behaviour. Both vibrational-dependent branching and isotope effects may contribute [85, 92]. Our earlier experiment at 0–40 meV differs from the present setup as it involved a more complicated data acquisition method in order to record arrival-time differences of the product atoms. A multi-line photomultiplier was set to select two-particle events only, requiring accurate settings of all trigger levels. In all position-sensitive detection techniques, detector inhomogeneities may affect the results. Fortunately in storage-ring experiments, the fragment distances are not much larger than the distribution of centre-of-mass positions, which is a measure for the O_2^+ beam size at the position of the detector. The large beam size reduces the effects of detector inhomogeneities. On the other hand, a large beam size may have a discriminating effect on large KER events; the associated large fragment distances may more easily result in one of the fragments falling outside the detection area. For the DR of O_2^+ this would especially affect the $O(^3P) + O(^3P)$ channel [see Eq. (4.1a)], resulting in an underestimation of the $O(^3P)$ and subsequently in a too large $O(^1D)$ quantum yield. We investigated the beam size and found no indication of missing events. Additionally, we simulated a DR experiment at 0 eV using the present branching fractions and then assumed a too large beam size to investigate its effect. This simulation shows that our branching fractions in combination with a discriminating effect due to a large beam size can give rise to distance distributions as observed in Ref. [46]. It seems possible that discrimination of the large KER events contributed to the earlier measurements. There is no reason known to us to explain the reverse situation, i.e., where the $O(^3P) + O(^3P)$ branching fraction would be overestimated instead of underestimated. Although the current results have been reproduced in two independent experimental runs, the presence of an unidentified systematic effect cannot be ruled out. Since the variations in the collision energy are very small with respect to the KER values, each systematic effect will impact all the results in a similar way.

4.5 Conclusions on the Electron-Energy Dependence

The present measurements of O_2^+ DR products are made over a sufficiently wide range of electron collision energies to allow temperature-dependent quantum yields and branching

fractions to be defined at electron temperatures below 1000 K. We observe smooth and distinct oscillations in the branching fractions. Resonant behaviour does not seem to appear in the dissociative behaviour. The resulting quantum yields are largely independent of the collision energy. Moreover, we find that the distributions at all investigated energies can be described with isotropic distributions. In spite of the apparent simplicity of the DR reaction, it is clear that progress still has to be made in both experiment and theory before we arrive at a complete picture.

B. Vibrational-State Dependence

4.6 Experimental Details

The experimental work for the study of the vibrational-state dependence of the DR process was conducted both at SRI International (see §2.2) as well as at the heavy-ion storage ring, CRYRING. The ion source PHILIS (see §2.1.3) was specifically developed for the purpose of investigating the vibrational dependence in the DR of O_2^+. At SRI the vibrational populations produced by the ion source were studied using dissociative charge transfer (DCT) reactions between cesium and oxygen (see §4.7.1). The ion source was then integrated into the injection-line apparatus at CRYRING. A selection of five vibrational populations were reproduced using their corresponding ion-source settings. For each individual ion-beam population the total DR rate as function of collision energy and the product distributions at 0 eV collision energy were investigated. An uncertain factor in the measurements comes from SEC reactions, which may cool the vibrational degrees of freedom of the ions in the ring. These SECs give rise to a time varying vibrational population of the O_2^+ ions. We have assessed the importance of the SEC process by studying the DR dynamics at different storage times (see §4.8). A summary of the details on the experiments and data analysis is given in Appendix A.

Total Rate Coefficients

In the first part of the experiment on the vibrational-state dependence, the reaction rate for each of the selected vibrational populations was measured as function of collision energy up to 0.4 eV. The collision energy was varied between 2.25 and 1.5 s storage time. The count rate due to background reactions was measured for each population individually by turning the collision energy briefly up to 5 eV, where the DR cross section is negligible.

Partial Rate Coefficients and Branching Fractions

In the studies of the DR dynamics we restricted the collision energy to a nominal 0 eV. Only the position of the fragments were determined and not their difference in arrival time. The background contribution was measured for each vibrational population individually by turning the electrons off. Data from both the DR and the background reactions were collected during the full storage time. In addition, each event was labelled with a time stamp relative to the start of a measuring cycle in time increments of 50 ms.

In fitting the distance spectra, it has been assumed that the DR reaction is isotropic. Anisotropies have been observed in DR reactions, but these have only been seen at elevated collision energies and never at 0-eV collisions. The dissociation limit given in Eq. (4.1d) has not been included in the fits for the reasons mentioned earlier in §4.1.2. The fitting procedure generates a distance distribution for each individual $O_2^+(v)$ state dissociating into the four energetically possible dissociation limits, while taking into account a 300 K rotational distribution, the finite interaction length, and the projection of the total distance onto the *2D* detector. The free parameters in the fit are the relative partial cross section and branching fractions of each vibrational state. These parameters are assumed to be independent of the rotational state. Only vibrational levels up to $v = 5$ were taken into consideration since the higher vibrational levels were only very weakly populated and are assumed not to contribute significantly (see §4.7.2). The metastable $a\,^4\Pi_u$ state, when present, will decay and produce a time-varying effect on the vibrational population. Its radiative lifetime is short, most likely less than 100 ms [93–96]. This state has, however, not been included, since the decay of the metastable ions will produce an *a priori* unknown change in the vibrational distribution of the electronically ground state oxygen ions. Considering arguments based only on the Franck-Condon overlap factors it is not unlikely that these product states are very highly excited ions. An additional time-dependent behaviour was anticipated due to the possible presence of vibrational cooling related to the SEC processes. In order to investigate both of these time-dependent effects, complete analysis has been performed for data obtained during two storage-times, namely 2.5−4.0 s and 5.5−7.0 s. As is discussed later, there are indications that some changes occur in the first few seconds of the ring cycle, which may reduce the effect of the decaying metastable ion state after five seconds (see §4.9). Conversely, SECs may constantly reduce the vibrational excitation of the population with respect to the calibrated populations, which would favour the shortest possible storage time. By analysing both sets of data, these systematic uncertainties have been transformed into uncertainties in the vibrational dependent rates and branching behaviour.

4.7 Controlling and Characterising Vibrational Populations

4.7.1 Dissociative Charge Transfer between O_2^+ and Cs

In order to characterise the vibrational populations, we investigated the dissociative charge transfer (DCT) reaction between the oxygen ions and cesium [40, 42, 97, 98]. For each ion-source setting, the O_2^+ ions were extracted, magnetically mass selected and accelerated to 5 keV before entering a collision cell containing Cs vapour [see Fig. 2.8(a)]. The DCT reactions taking place in the collision cell are:

$$O_2^+(X\,^2\Pi_g, v) \xrightarrow{\text{Cs}} O_2^*(3s\sigma\,^{1,3}\Pi_g, v' = v)$$

$$\rightarrow \quad O(^3P) + O(^1D) + (\sim 1 + E_v)\ \text{eV} \quad (4.2a)$$

$$\rightarrow \quad O(^3P) + O(^1D) + (\sim 3 + E_v)\ \text{eV} \quad (4.2b)$$

$$\rightarrow \quad O(^1D) + O(^1D) + (\sim -1 + E_v)\ \text{eV} \quad (4.2c)$$

Of relevance to the present investigation is the conservation of the vibrational quantum number in going from the parent ion to the $3s$ Rydberg states. This conservation gives rise to

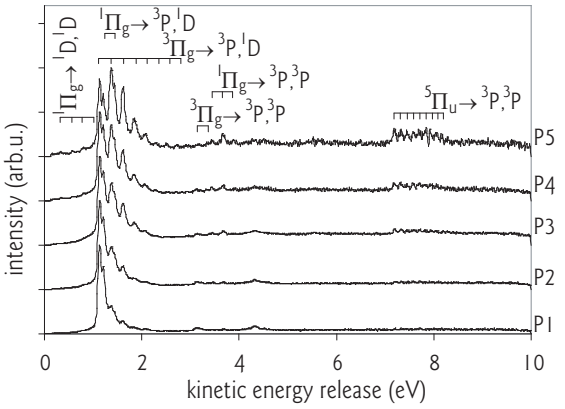

(a)

v	P1	P2	P3	P4	P5
1	15.6	21.5	26.3	29.2	30.3
2	6.5	9.2	14.0	15.5	21.6
3	3.7	5.2	7.8	8.7	10.4
4	2.1	2.6	3.7	3.5	4.7
5	1.1	1.3	1.5	1.3	4.2
a/X	0.013	0.053	0.105	0.136	0.294

(b)

Figure 4.8: (a) Measured spectra from the Cs$-O_2^+$ DCT reaction for the five different ion-source settings, i.e., five vibrational populations, P1$-$P5. (b) The populations (%) of the vibrational levels $O_2^+(X\,^2\Pi_g, v = 0-5)$ together with the ratio (a/X) of the metastable $O_2^+(a\,^4\Pi_u)$ state to the ground $O_2^+(X\,^2\Pi_g)$ state oxygen ions, for the vibrational populations, P1$-$P5.

spectra with KERs that mirror directly the vibrational structure of the O_2^+ parent ions. For $v = 0$ ions, the KER of Eqs. (4.2a) and (4.2b) is around 1 and 3 eV respectively. Equation (4.2c) is only energetically possible for $v > 3$. Whenever metastable $O_2^+(a\,^4\Pi_u)$ ions are produced, reactions with this state will also be observed, since there will be insufficient time for the metastable ion to decay before it reaches the collision cell. The KER then observed is around 7 eV and higher:

$$O_2^+(a\,^4\Pi_u, v) \xrightarrow{\text{Cs}} O_2^*(\text{Ryd}, v' = v) \rightarrow O(^3P) + O(^3P) + (\sim 7 + E_v)\ \text{eV} \qquad (4.3)$$

The resolution of the DCT experiment is more than sufficient to easily distinguish between the vibrational levels. By integration of the data in the DCT product-distribution spectra, the vibrational population of the O_2^+ ions created in the ion source can be determined directly. Explicit details on the DCT reaction between oxygen and cesium and the data analysis can be found elsewhere [98, 99]. The formation of the O_2^+ metastable state is an example in which the population determined using DCT does not describe the population as used during the DR experiment. Nearly all $O_2^+(a\,^4\Pi_u)$ molecular ions will have decayed via radiative decay to vibrational levels in the ionic ground state, modifying the vibrational population.

4.7.2 Selected Vibrational Populations

The DCT spectra corresponding to the five selected ion-source settings are shown in Fig. 4.8(a). DCT signals are observed with KERs ranging between 0 and 9 eV. The main contribution comes from dissociation events towards the $O(^3P) + O(^1D)$ channel [see Eq. (4.2a)] starting from the $^3\Pi_g$ state. The associated KERs start at about 1 eV for $O_2^+(X\,^2\Pi_g, v = 0)$ and increase with each vibrational level. Near 3 eV, events are observed corresponding to the dissociation towards the $O(^3P) + O(^3P)$ limit [see Eq. (4.2b)], and which show the same vibrational structure. The small signals below 1 eV are due to dissociation into $O(^1D) + O(^1D)$ [see Eq. (4.2c)] from $v' \geqslant 4$. For KERs of ~ 7 eV and higher, DCT signals arising

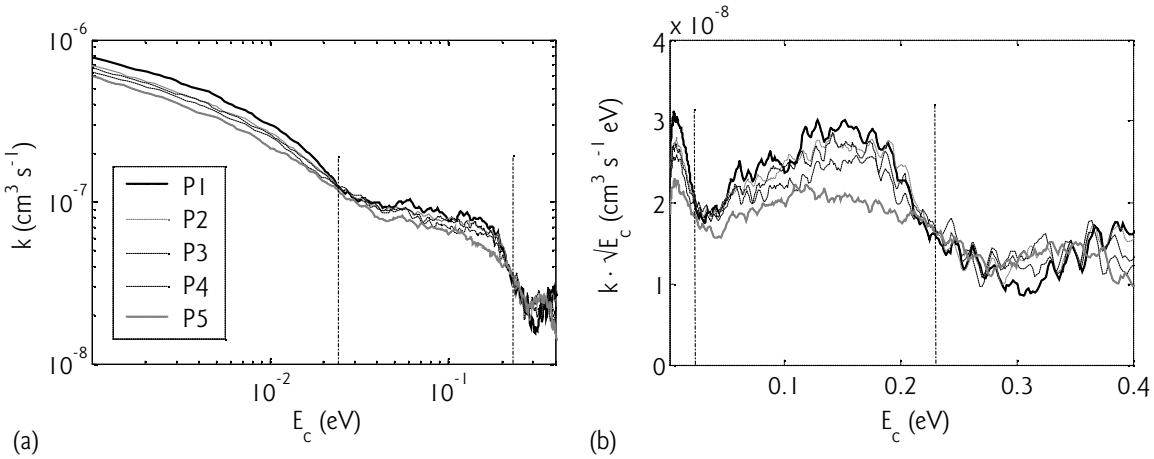

Figure 4.9: (a) The total rate coefficients, k_{Pi}, as function of collision energy, E_c, up to 0.4 eV where Pi = P1−P5. Note that both axes are on a logarithmic scale. (b) The total rate coefficients multiplied by the square root of the collision energy, revealing the resonances due to non-direct dissociation mechanisms. Note that the axes are both linear now. The dashed vertical lines at 24 and 232 meV indicate the energy of the spin-orbit splitting in the $X\,^2\Pi_g\,(\Omega = \frac{1}{2}, \frac{3}{2})$ states and the vibrational spacing, respectively. The observed small oscillation is related to the presence of a very small 50 Hz noise signal during data acquisition.

from the metastable $a\,^4\Pi_u$ state are also observed [see Eq. (4.3)]. Consideration of the complete spectrum unambiguously reveals the vibrational population of the ion beam. All five ion-source settings were chosen such that the vibrational excitation of the ions gradually increased. The label P5 refers to the most excited population. Here, the $v = 1$ population exceeds the $v = 0$ population and a significant fraction of metastable $a\,^4\Pi_u$ oxygen ions are observed. The DCT spectrum of P5 reveals the nascent population created by 100 eV electron-impact ionisation. It is noted that the coldest population, referred to as P1, does not contain $v = 0$ ions only. Table 4.8(b) lists the derived vibrational populations for the levels $v = 0 - 5$ together with the ratio between the ground and the metastable state. More details of the interpretation of the DCT dynamics can be found in literature [40].

4.8 The Rate Coefficients and Branching Fractions

4.8.1 Total Rate Coefficients

The measured total rate coefficients for the DR of O_2^+ in each of the five vibrational populations, P1−P5, have been obtained for electron energies up to 0.4 eV. The results are shown in Fig. 4.9(a). Though error bars are not shown, the main source of error in the relative data is statistical. Near 0 eV this error is smaller than the separation between the curves, while above 100 meV the statistical error starts to become significant. A systematic uncertainty in the absolute data arises from the measurement of the ion current, and is estimated [46] to be around 20%. We observe that the total rate coefficient decreases upon increasing vibrational excitation near 0 eV collision energy. This observation suggests that the partial cross section for $v = 0$ is higher than that for $v = 1$. The total rate coefficient of the hottest population, k_{P5}, is, in general, the slowest though for collision energies between 210 and 330 meV this rate is as fast as those of the less excited populations. The observed rates vary much less than

an order of magnitude. The corresponding thermal rate coefficients, $\alpha(O_2^+)$, can be derived from the total measured rates by determining the thermal average weighted by the thermal electron distribution. The thermal rate coefficients at 300 K are calculated to be (2.0, 1.9, 1.9, 1.8, and 1.5) $\cdot 10^{-7}$ cm^3 s^{-1} for P1 to P5, respectively. The small variation is consistent with the small range of thermal rates previously reported in literature (see §4.1).

The general behaviour of the rate coefficient due to the direct DR process is proportional to the inverse square root of the collision energy (see §4.1). Therefore, multiplying the rate by the square root of the collision energy will remove the $1/\sqrt{E_c}$ dependency and resonances in the DR process will appear as deviations around a collision-energy-independent level. These data can then be plotted on a linear scale [see Fig. 4.9(b)]. The total rate coefficient of the coolest population, k_{P1}, shows strong deviations from the purely $1/\sqrt{E_c}$ behaviour. Upon increasing excitation, the total rate coefficient becomes flatter and the variations are virtually absent for the hottest population P5. Clearly the different vibrational states have a qualitatively different behaviour. In the following section the total rate coefficients are used as a consistency check on the partial rate coefficients as derived from the imaging experiment.

4.8.2 Partial Rate Coefficients at 0 eV

Each of the five vibrational populations will produce a different distance distribution spectrum if the partial cross sections and branching fractions have a vibrational dependence. Figure 4.10 shows some of these measured distance distributions obtained for 0 eV collisions. The solid curves show the fits, which combine a series of known instrument parameters and, as free parameters, the relative partial cross section and branching fractions over the four dissociation limits for each vibrational level of the parent ion. As mentioned before, data have been obtained and analysed from two different storage times, 2.5−4.0 s and 5.5−7.0 s, respectively. The spectra for population P1 are shown in Figs. 4.10(a) and 4.10(b) and for population P5 in Figs. 4.10(c) and 4.10(d). The x-axes are the projected distances between the two O product atoms, which is roughly proportional to the square root of the KER [67]. The four dissociation limits can easily be distinguished (peaks a−c and e). The spectrum for P1 differs markedly from the spectrum for P5, indicating a vibrational dependence of the dissociation reaction. The width of the peaks is determined by the level of vibrational excitation present. Higher vibrational states give rise to higher KERs and thus broaden the electronic peaks to larger distances. The effect of vibrational excitation is most apparent in the O(^{1}S) dissociation (peak e), since there the vibrational energy spacing is on the order of the KER, 0.8 eV. Analysis of the peak-width shows that P1 is vibrationally more relaxed than P5. Due to the method of data acquisition, the absolute number of counts cannot be used to estimate the relative total rate coefficients for the different populations.

The spectra also differ in more subtle ways. The P5 distance distributions show a small tail at large distances, i.e., at higher KERs, which cannot be fitted when including only the first 6 vibrational levels. This tail is also observed in the distance distributions obtained from the populations P3 and P4 (not shown), but is not seen in the P1 and P2 distributions (P2 also not shown). This is consistent with the production of highly vibrationally excited O_2^+ ions resulting from the decay of the first electronically excited metastable $a\,^4\Pi_u$ state in P3−P5 (see Fig. 4.8(a)). Furthermore, signals are observed at very small KERs (distances below 6 mm) in the P5 spectra, which are not present in the P1 spectra. This may indicate the opening of the next highest dissociation channel, which can only occur for vibrational

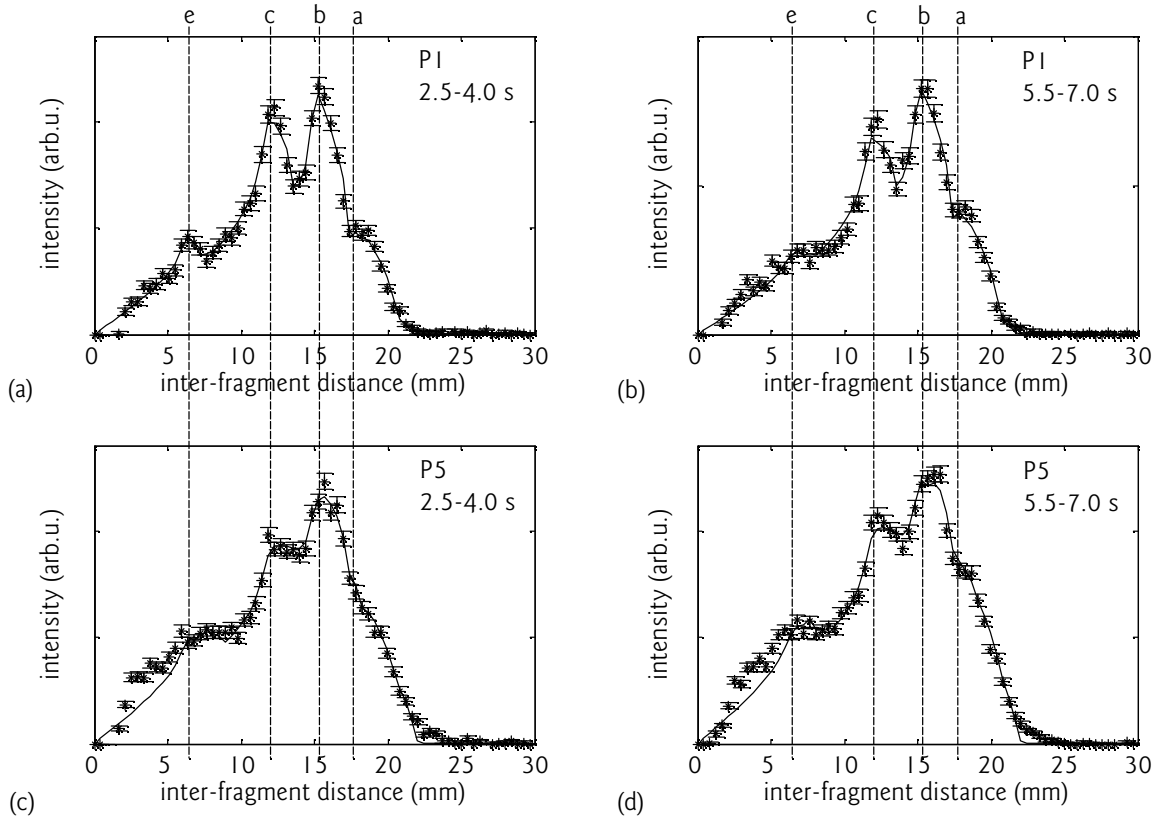

Figure 4.10: The distance distributions (stars) and their fits (black solid curves) normalised to unit area, of population P1, obtained during storage times (a) 2.5−4.0 s and (b) 5.5−7.0 s and of population P5, obtained during storage times (c) 2.5−4.0 s and (d) 5.5−7.0 s. The dashed lines labelled a−c and e indicate the four dissociation limits given in Eqs. (4.1a)−(4.1c) and (4.1e), respectively. The distance distributions are in fact the histograms of all the projected distances between the two O product atoms.

levels higher than $v = 7$ [see Eq. (4.1f)]. Finally, when comparing P1 to P5, it is noted that the dissociation peaks in the P5 spectra are not only broader, but have also moved slightly to larger distances, i.e., higher KER, reflecting the shift in vibrational population.

The distance distributions from P2−P5 were fitted with $v = 0 - 5$, while simultaneously optimising the partial cross section and branching fractions for each vibrational level. We have fitted the distance distributions from P1 separately, only considering the first four vibrational levels, $v = 0 - 3$. The latter fit serves as a consistency check for the simultaneous fitting of P2−P5. Since neither the product vibrational states created from the decaying metastable state nor the vibrational cooling effect of the SEC processes are quantitatively included in the fitting procedure, systematic errors are introduced, especially for the sparsely populated higher vibrational levels. We therefore present the vibrationally resolved results for the vibrational levels $v = 0$, 1 and 2 only.

The relative partial cross sections, σ_v, obtained for $v = 0 - 2$ during these two storage times are given in Fig. 4.11. The data are plotted relative to the cross section obtained for $v = 0$. It is observed that the cross section calculated for $v = 0$ is the highest. The cross sections obtained from the separate fit for P1 and the simultaneous fit for P2−P5 are consistent for the data taken during the storage time 2.5−4.0 s. The results obtained during the storage time 5.5−7.0 s are different, although not significantly. The cross section obtained for $v = 1$

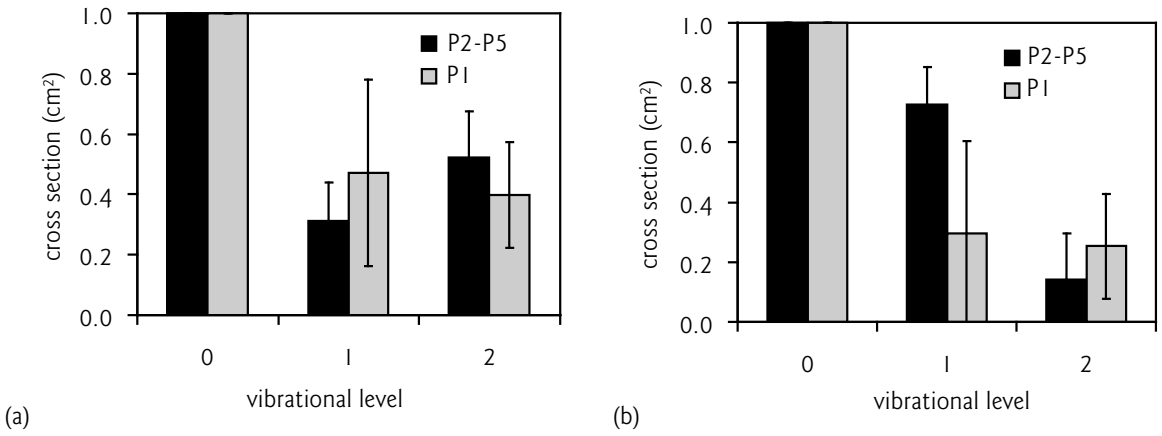

Figure 4.11: The partial cross sections, σ_v, for $v = 0 - 2$, relative to σ_0, at 0 eV collision energy resulting from the simultaneous fit of P2–P5 data (black) and the separate fit of P1 data (grey) obtained during storage times (a) 2.5–4.0 s and (b) 5.5–7.0 s.

from the fit to P1 data appears to be much lower. When comparing the data obtained during the two storage times to each other, the cross sections differ significantly. For the shorter storage time, the rate obtained for $v = 1$ is much lower than that calculated from the data obtained at longer storage time. The opposite is true for $v = 2$. The disagreement suggests that the vibrational population in the ion beam was different for the different storage times.

A second consistency test for the obtained results is the reconstruction of relative total cross sections, σ'_{Pi}, for Pi = P1 − P5 based on the partial cross sections, σ_v, and use these reconstructed total cross sections to compare with the relative total cross sections, σ_{Pi}, calculated from the five measured total rate coefficients, k_{Pi}, (see Fig. 4.9) near 0 eV collision energy:

$$\sigma'_{\mathrm{Pi}} = \sum_{v=0}^{2} \sigma_v \mathrm{Pi}(v) \quad \text{for i} = 1 \ldots 5 \tag{4.4}$$

The outcome of this test is given in Table 4.2. The reconstructed data is remarkably consistent with the measured total cross sections. The qualitative conclusion that the measured total rates can be understood by assuming a faster DR rate for $v = 0$ is corroborated quantitatively.

Table 4.2: The relative total cross sections σ_{Pi} deduced from the measured total rate coefficients together with the reconstructed relative total cross sections σ'_{Pi} using Eq. (4.4) with σ_v the partial cross sections from the simultaneous fit at 2.5–4.0 s and 5.5–7.0 s storage time, respectively.

		P1	P2	P3	P4	P5
σ_{Pi}		1.13	1.02	1.00	0.95	0.83
σ'_{Pi}	2.5 − 4.0 s	1.21	1.11	1.00	0.95	0.84
	5.5 − 7.0 s	1.19	1.11	1.00	0.96	0.83

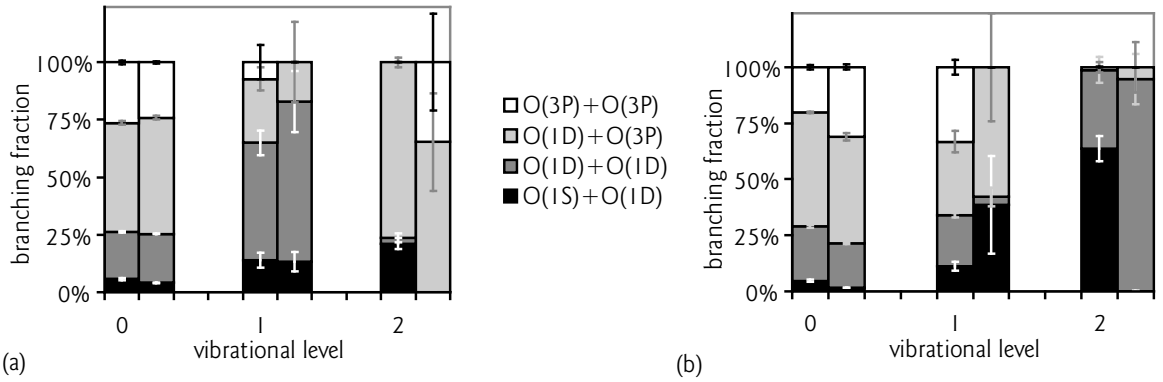

Figure 4.12: The partial branching fractions for $O_2^+(X\,^2\Pi_g, v = 0-2)$ towards the four dissociation limits given in Eqs. (4.1a)−(4.1c) and (4.1e) for the simultaneous fit of P2−P5 data (first column of each column pair) and the separate fit of P1 data (second column of each column pair) obtained during storage times (a) 2.5−4.0 s and (b) 5.5−7.0 s.

4.8.3 Partial Branching Fractions at 0 eV

Analysis of the vibrationally dependent partial rate coefficients also provides their branching behaviour. Figure 4.12 shows the partial branching fractions for the levels $v = 0-2$. Results are again presented based on the simultaneous fit of P2−P5 data and the separate fit of P1 data for the two investigated storage times, 2.5−4.0 s and 5.5−7.0 s, respectively. Table 4.3 lists the resulting partial branching fractions together with the partial cross sections as determined by the simultaneous fit at 2.5−4.0 s together with the vibrationally state dependent quantum yields for $O(^1S)$, $O(^1D)$ and $O(^3P)$. These quantum yields are easily derived from the partial branching fractions. The yields are the relevant observables for *in situ* atmospheric observations and also in afterglow or discharge type experiments. From both Fig. 4.12 and Table 4.3 it is concluded that the partial branching fractions are strongly dependent on the vibrational state. The $O(^1S)$ quantum yield increases upon vibrational excitation, and by more than a factor of three in going from $v = 0$ to $v = 2$. The $O(^1D)$ quantum yield is lowest at $v = 0$, whereas the $O(^3P)$ yield is highest at $v = 0$.

4.9 Temporal Behaviour

4.9.1 Vibrational Cooling

In an ion storage-ring experiment, the ion-beam population can change due to a one of several mechanisms. Ignoring DR for the moment, the main destruction of the ion beam arises from collisions with rest-gas molecules inside the ring. The efficiency of these collisions may be dependent on the vibrational state. However, we observe no changes in the ion-beam lifetime upon changing vibrational populations (electrons off). Although we have indications that the product distribution due to charge transfer induced dissociation depends on the vibrational state in the ion beam (see below), we have no information on the associated partial rates. Under very good vacuum conditions, which is the case in most heavy ion storage rings, the DR process in the electron cooler may be so efficient as to radically deplete certain states from the ion beam. This is observed [100] to be the case for the DR of H_2^+. In the current

Table 4.3: The partial cross sections, quantum yields and branching fractions for $O_2^+(X\,^2\Pi_g, v = 0-2)$ resulting from the simultaneous fit of the P2−P5 data obtained during storage time 2.5−4.0 s.

	branching fractions			
v	$O(^1D) + O(^1S)$	$O(^1D) + O(^1D)$	$O(^3P) + O(^1D)$	$O(^3P) + O(^3P)$
0	5.8 ± 0.5	20.4 ± 0.3	47.3 ± 0.8	26.5 ± 0.8
1	13.9 ± 3.1	51.0 ± 5.4	27.8 ± 5.1	7.3 ± 7.5
2	21.1 ± 2.5	2.5 ± 2.1	76.4 ± 2.2	0.02 ± 0.03
	cross sections	quantum yields		
v	σ_v	$O(^1S)$	$O(^1D)$	$O(^3P)$
0	1	0.06	0.94	1.00
1	0.31 ± 0.13	0.14	1.44	0.42
2	0.52 ± 0.16	0.21	1.02	0.76

experiment, the lifetime of the ion beam is not significantly affected when the electrons are turned on. Thus, the loss of ions due to the DR process is too small to compete with that due to collisions with rest gas. This leaves the SEC process as a possible mechanism to change the vibrational population of the ion-beam via a series of $\Delta v = -1$ transitions. This mechanism has been established in various experiments [101, 102] on H_2^+. In the current experiment, time dependent behaviour of the ion beam is observed indicating changes in the vibrational population. It is concluded that the SEC process is more efficient than the DR process in changing the vibrational population of the stored ion beam.

To investigate the efficiency of the SEC process in changing the characterised populations, imaging data were obtained during storage times up to 10 s. Fig. 4.10 already shows the distance distributions of both P1 and P5 obtained during the two storage times 2.5−4.0 s and 5.5−7.0 s (see §4.8.2). For the P5 data, neither the widths of the observed peaks narrow significantly nor do the highest KERs (at 23−25 mm) disappear. The only indication of a changing vibrational population is the change in the relative amplitudes of the peaks. Figure 4.13(a) plots the distance distribution from the P5 data obtained during 2.5−4.0 s together with the spectrum obtained during even longer storage time, 8.5−10.0 s. The $O(^1S)$ peak (at ca. 7 mm) has narrowed, indicating cooling has occurred. However, the high KER tail at 23−25 mm still shows no change. Figure 4.13(b) compares the data from P5 obtained at 8.5−10.0 s with that obtained from the somewhat less excited population P4 at 2.5−4.0 s. Analysis of these data suggests that it takes more than 8 s for the higher vibrationally excited population to cool down to the less excited population. The cooling mechanisms inside the ring seem to be less effective than those operating in the ion source.

4.9.2 State-Dependent Background Dynamics

Background imaging data taken for all populations P1−P5 give some evidence of vibrational dependence in the dynamics of the charge transfer process between the O_2^+ ions and the

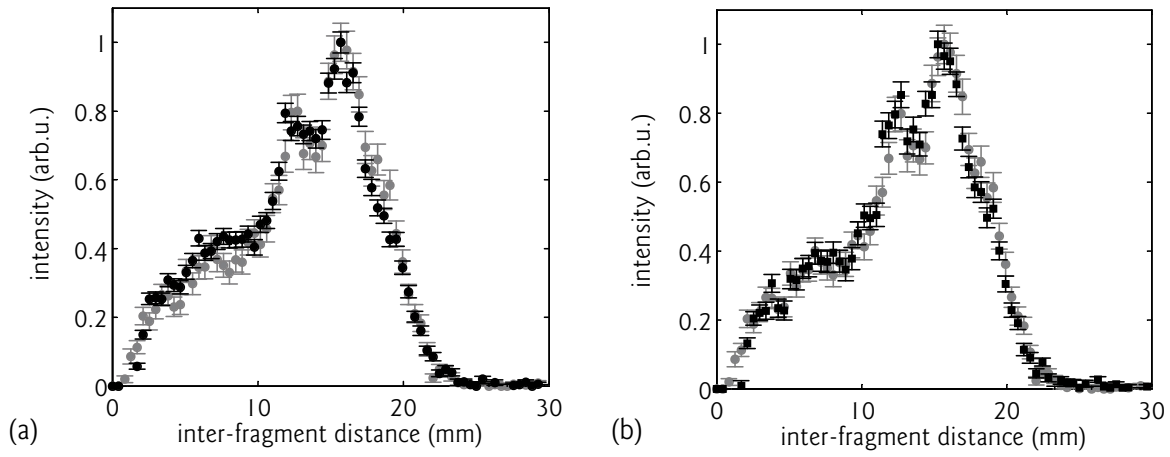

Figure 4.13: (a) The distance distributions of P5 obtained during 2.5—4.0 s (black circles) and 8.5—10.0 s (grey circles) storage time and (b) the distance distributions of P5 obtained during 8.5—10.0 s (grey circles) and of P4 obtained during 2.5—4.0 s (black squares) storage time. Note that all distributions are normalised to their own maximum.

residual gas molecules in the ring. The 2-particle events resulting from these reactions give rise to distance distributions that can be related to the ion-beam dynamics similar to the DR spectra. Here the interaction region is not determined by the length of the electron cooler but by the entire straight section. The associated distance distributions reveal different dissociation dynamics for the excited population P5 at 2.5—4.0 s storage time, compared to the other data. Such differences are no longer observed at 5.5—7.0 s storage time and, for all other populations, the charge transfer distance spectra were found to be almost identical. The main difference is observed at larger KERs. To investigate this, attempts were made to reduce the metastable fraction in the ion beam by decreasing the electron-impact energy in the ion source from 100 to 23 eV. At this energy the vibrational excitation of the ground state remains approximately the same. Although the data obtained under these conditions still showed differences at larger distances, their lower magnitude suggests that the product vibrational levels resulting from the decaying metastable state are at least partly responsible. The energy of these vibrational levels in the DR distance spectrum is unknown, though they must be different from those responsible for the signal seen at 23—25 mm (see Fig. 4.10) for the P3—P5 settings, since this tail did not disappear in the DR spectrum of P5 after 5.5 s of cooling.

4.10 Discussion of the Vibrational-State Dependence

In laboratory experiments the vibrational dependence of the DR reaction is difficult to study in a well-controlled way [61, 67, 78, 103]. In the research presented here we have managed to control and reproduce a number of significantly different vibrational populations. We were able to smoothly vary the ion population from vibrationally cool to vibrationally hot. This has allowed us to determine the vibrational dependence of the DR cross sections and branching fractions for the first few vibrational levels. The present experiment is limited by two factors. The first is the finite resolution of the imaging method, since the absence of vibrational resolution increases the uncertainty in the fitting procedure. A better spatial

resolution or maybe even arrival-time information of the product atoms will substantially improve the results. The second is related to time-dependent changes of the vibrational populations in the ion beam during its storage time. The lowest lying metastable $a\,^4\Pi_u$ state is formed efficiently in the source and decays down to the ground state with some unknown vibrational population. Furthermore, inelastic electron scattering, in SEC processes, also induce some changes in the vibrational population. Despite these effects, we believe that the estimates given here for the vibrationally dependent rates and branching behaviour are the most accurate laboratory estimates to date.

The observed total O_2^+ DR rate coefficient as function of collision energy and vibrational population were relatively straightforward to analyse and these data are the most reliable. The observations show that the total DR rate coefficient depends weakly on the vibrational population of the parent ion beam. For low collision energies the rate decreases with increasing vibrational excitation. This decrease is less than a factor of 2 and excludes vibrational specific rates that differ by an order of magnitude, as is found [104] for HD^+. The calculated thermal rate coefficient, $\alpha(O_2^+)$, at 300 K corresponding to the coolest population P1 is $2.0 \cdot 10^{-7}$cm^3 s^{-1} and decreases to $1.5 \cdot 10^{-7}$cm^3 s^{-1} for the hottest population P5. The small range is consistent with the small range of previously reported thermal rate coefficients (see §4.1). The total rate coefficient curves also show variations from the general behaviour $k(O_2^+) \sim E_c^{-0.5}$. These variations are due to resonances, which differ from the general behaviour arising from direct capture-dissociation mechanisms. The resonance structure decreases with increasing vibrational population, being most strong in the coolest population and almost nonexistent in the most excited population. Some characteristic energy signatures in the O_2^+ ion coincide with features in these observed resonances (See Fig. 4.9). The spin-orbit splitting in the $X\,^2\Pi_g$, ($\Omega = \frac{1}{2}, \frac{3}{2}$) states of 197 cm^{-1} ($\sim$24 meV) and the vibrational spacing of 0.23 eV both coincide with collision energies where the calculated total rate coefficients for the different vibrational populations are almost identical and which then all decrease towards a local minimum.

The interpretation of the imaging data at 0-eV collisions is less trivial, however, the effect of the SECs and the presence of the metastable state have been qualitatively studied by obtaining data at two different storage times. Additionally, the sensitivity of the fitting procedure has been investigated and based on this we have restricted our findings to the lowest three vibrational levels. We find that both the partial cross sections and branching fractions depend on the vibrational level. The partial rate coefficients are found to be consistent with the observed total rate coefficients at zero eV collision energy. The partial cross section is the fastest for $v = 0$ and decreases by a factor of more than 2 for $v = 1$ and 2. The O(^1D) quantum yield is lowest, and the O(^3P) yield highest, at $v = 0$. The O(^{1}S) quantum yield increases by more than a factor of 2 for $v = 1$ and 2. Our results display a very strong dependence on the vibrational level.

4.10.1 O_2^+ and Similar Systems

In the case of O_2^+ only a limited number of experiments exist that report any vibrational state-dependent behaviour, and these are mostly rate coefficient data. Kella *et al.* [67] measured the DR branching behaviour of an unknown vibrational population of the mixed isotopomer $^{16}O^{18}O^+$. In Kella *et al.*'s study, only the total quantum yields summed over all the vibrational levels are reported. The total O(^{1}S) yield for the vibrationally excited ions is

reported to be a factor of 2 larger than the $O(^1S)$ yield for ground state ions. The total $O(^1D)$ and $O(^3P)$ yields are reported to show no significant vibrational dependence. One further paper reports results on the branching behaviour of $O_2^+(X\,^2\Pi_g, v = 0)$ ions [46]. The results reported in this paper agree in the most part with those presented here. It is noted that their $O(^1D)$ quantum yield is higher than the $O(^3P)$ yield, whereas the reverse is true in our case. The reason for this discrepancy is not clear at present. The current results for the ground vibrational level of O_2^+ are consistent with data obtained from an independent experiment performed on the collision-energy dependence of the DR reaction [83].

It has been suggested that the DR process is very similar for small diatomic ions, i.e., predominantly direct dissociation, giving the equivalent order and temperature dependence of the thermal rate coefficient. In most of these systems we only have branching data for ground state ions, for examples NO^+ and CO^+. This may be because these ions easily relax radiatively to their ground state. Furthermore, little is known on the vibrational behaviour of their DR rate coefficients. However, a few measurements on the total rate coefficient of CO^+ show a higher rate for vibrational ground state ions [105, 106] than for vibrationally excited ions [107]. For NO^+, the measured thermal rate of vibrationally excited ions is also reported to be lower than that of vibrational ground state ions [108]. In the case of N_2^+ an experiment performed at CRYRING reported a weakly dependent total rate coefficient, where the rate of the vibrationally excited beam was again lower than that of the ground state [109]. In this paper there is also mention of the branching fractions of the $v = 1 - 3$ vibrational levels being roughly the same. Finally, a recently published review reports that the recombination rates measured for vibrationally excited N_2^+, O_2^+, and NO^+ are lower than their equivalent ground state ions [110]. Specifically, they report that the difference is about a factor of 2 in the case of O_2^+ over the temperature range 200 K to 4000 K.

4.10.2 Theory and Modelling

The issue of vibrationally dependent DR rates and branching fractions (and associated fragment quantum yields) has given rise to extensive and often inconclusive discussions in literature. Vibrationally dependent DR behaviour is often inferred from ionospheric observations [76, 77, 88, 89, 111], whereas studies of the production and quenching of $O_2^+(v)$ in the ionosphere often conclude the vibrational deactivation is fast [20, 23, 79]. Fox shows, however, that above 200 km the O_2^+ vibrational population can already be significant [112]. The present results, combined with Fox's populations, could already be used in modelling of the increasing green-line emission upon altitude. However, energetic information on the partial rates and yields is still needed for a precise comparison with atmospheric observation.

To the best of our knowledge no vibrational dependent branching has been predicted from purely *ab initio* calculations. The earlier work of Guberman identified a number of possible target states in the DR process though the complexity of molecular oxygen makes it difficult to draw general conclusions on the process [68]. As has been mentioned earlier, molecular oxygen is somewhat special due to the very large avoided crossings between the various repulsive molecular states and the lowest (n=3 and n=4) Rydberg states (see Fig. 4.2). As a consequence, there are potential barriers on the exit channels leading to the lower-lying dissociation limits. At most avoided crossings the dissociation flux tries to keep some Rydberg character. Furthermore, molecular oxygen is the first system in which a spin-orbit mechanism has been invoked to describe the production of $O(^1S)$ atoms near 0-eV collisions

for $v = 0$ ions. A resonance near 0 eV, which causes the colliding electron to be captured in a vibrationally excited Rydberg state, creates a sufficient time delay such that coupling of the $^3\Sigma_u^-$ and the $^1\Sigma_u^+$ becomes effective in redirecting flux over the repulsive $^1\Sigma_u^+$ valence state towards the $O(^1D)$ + $O(^1S)$ limit, explaining the experimentally observed finite quantum yield.

4.11 Conclusions on Vibrational-State Dependence

In summary, the present research details considerable progress in the control of vibrational populations and has provided more valuable insight into the vibrational dependence of the DR of O_2^+. Partial cross sections, branching fractions and quantum yields for $v = 0 - 2$ together with total rate coefficients for five different vibrational populations have been obtained and are reported here. The partial branching fractions and quantum yields together with the partial cross sections are strongly dependent on the vibrational level of the parent ion, with the yield of $O(^1S)$ increasing substantially upon increasing vibrational level. The partial cross sections agree with the measured total cross sections. The weak dependence of the total rate coefficients on the vibrational population is supported by the small range of thermal rates previously reported. Additionally, the decrease in total rate upon excitation seems to be in agreement with similar systems. The present results may be extended to higher vibrational levels once the difficulties in the experimental and analytical approaches have been overcome.

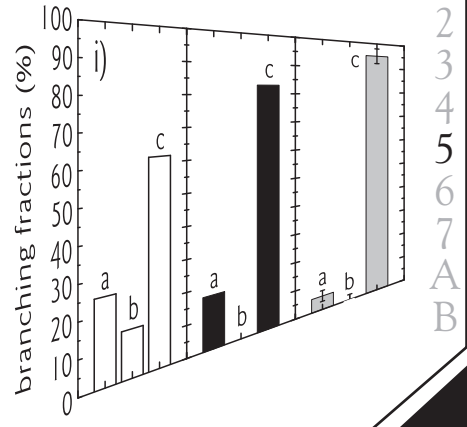

Physics is...

going places, meeting people...

so where are we going to celebrate our birthday this *year*

– twin-brother of – Annemieke

Chapter 5

Dissociative Recombination of Nitric-Oxide Ions

The dissociative recombination (DR) behaviour of the ground, $X\,^1\Sigma^+$, and first excited metastable, $a\,^3\Sigma^+$, states of NO^+ are reported along with the implementation of the DR reaction as direct probe for the lifetime of the metastable state. For ground-state ions, improved branching fractions at 0 eV as well as branching fractions at non-zero collision energies are reported along with anisotropic behaviour. For the metastable-state ions, the branching at 0 eV is qualitatively discussed. The lifetime of the $a\,^3\Sigma^+$ state is also given and discussed, using complementary ab initio calculations on the different radiative decay processes for both the $X\,^1\Sigma^+$ and $a\,^3\Sigma^+$ states. All branching behaviour is compared to a statistical branching model, which is based on the multiplicity of each dissociation limit in combination with spin conservation during the dissociation and the initial electron capture.

5.1 On the Dissociative Recombination of NO^+

One of the major constituent ions in the *D*, *E*, and *F* regions of the Earth's ionosphere is the nitric-oxide ion, NO^+. Both NO^+ and O_2^+ act as important sinks for low-energy thermal electrons in these regions via the DR reaction. For NO^+ this reaction has a number of product channels:

$$\begin{aligned}
NO^+(X\,^1\Sigma^+) + e^-(E_c = 0) &\rightarrow N(^4S) + O(^3P) + 2.77\text{ eV} && \text{(5.1a)}\\
&\rightarrow N(^4S) + O(^1D) + 0.80\text{ eV} && \text{(5.1b)}\\
&\rightarrow N(^2D) + O(^3P) + 0.38\text{ eV} && \text{(5.1c)}\\
&\rightarrow N(^2P) + O(^3P) - 0.81\text{ eV} && \text{(5.1d)}\\
&\rightarrow N(^4S) + O(^1S) - 1.42\text{ eV} && \text{(5.1e)}\\
&\rightarrow N(^2D) + O(^1D) - 1.59\text{ eV} && \text{(5.1f)}\\
&\rightarrow N(^2P) + O(^1D) - 2.78\text{ eV} && \text{(5.1g)}\\
&\rightarrow N(^2D) + O(^1S) - 3.81\text{ eV} && \text{(5.1h)}\\
&\rightarrow N(^2P) + O(^1S) - 5.00\text{ eV} && \text{(5.1i)}\\
&\rightarrow N(^4S) + O(^5S) - 6.38\text{ eV} && \text{(5.1j)}
\end{aligned}$$

The minus signs in Eqs. (5.1d)−(5.1j) indicate that these channels are energetically closed for electrons with energies less than 0.8 eV. The kinetic energies of the fragments grow with the electronic, vibrational, and rotational excitation energy of the parent ion. In the Earth's atmosphere, the following properties of the DR process are important. First, the total DR rate coefficient involving ground-state ($v = 0$) ions is of interest, as this determines the absolute importance of NO^+ as a sink for electrons. Second, the branching fractions deserve attention, as the product atoms are fast and reactive species. Also of great importance, for example, is that $O(^1D)$ is a source of the red airglow near 630 nm [46] and is relevant in reactive collisions forming the OH radical. $N(^2D)$ is the most reactive of the three lowest states of nitrogen [113]. For these reasons it is important to determine the branching fractions accurately. Furthermore, the $N(^2D) \rightarrow N(^4S)$ transition is responsible for airglow emission at 520 nm. Using satellite observations of neutral and ion concentrations, together with the local electron temperature and the 520-nm airglow emission profile in the ionosphere and

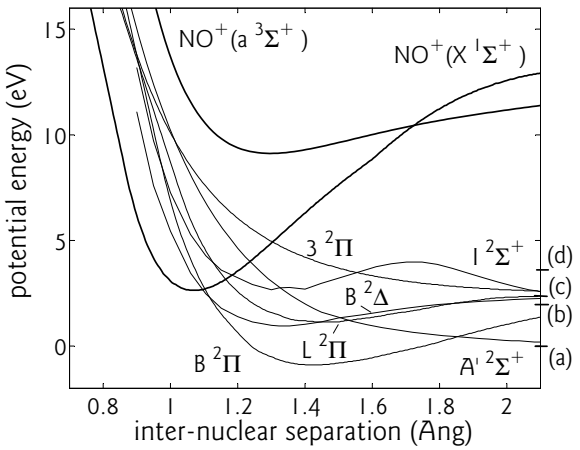

Figure 5.1: Potential curves relevant to the DR of NO^+ taken from Ref. [117]. The $a\,^3\Sigma^+$ potential curve has been calculated in the present work. The bold curves are the ionic potential curves. The four lowest dissociation limits are indicated on the right-hand side and labelled (a)–(d) in accordance with Eqs. (5.1a)–(5.1d).

ground-based measurements of the emission line, a quantum yield for $N(^2D)$ of 0.8–1.0 was inferred [114].

Both the DR thermal rate coefficients and branching fractions have been the subject of earlier research. Thermal rate coefficients of NO^+ have been determined using flowing afterglow measurements [108, 115]. For example, Dulaney, Biondi, and Johnsen [115] reported a value of $4.2 \cdot 10^{-7}\,(T/300)^{-0.75}\,cm^3\,s^{-1}$, with T being the electron temperature. The kinetic temperature of the ions in these experiments was 295 K. A similar thermal rate coefficient was deduced from a recent merged-beam experiment using the heavy-ion storage ring ASTRID by Vejby-Christensen *et al.* [51] (VC from here on). VC determined DR rates as a function of electron collision energy. In these measurements a broad local maximum was found around 5 eV. At a collision energy of 5 eV, it is possible for the electron to be captured by the positive ion into the repulsive $A'\,^2\Sigma^+$ state. This target state is connected with $N(^4S)$ + $O(^3P)$ ground-state fragments and may produce nitrogen and oxygen atoms with kinetic energies of 4.1 and 3.6 eV, respectively, sufficiently high to allow escape from planetary bodies such as Mars [2]. VC also determined branching fractions of the different energetically allowed channels for collision energies over the range 0–1.35 eV. In another experiment Kley, Lawrence, and Stone [116] used flash photolysis of NO to determine the yield of $N(^2D)$ atoms from the DR of NO^+, and they report a yield of 0.76(6).

Theoretical calculations have been performed by Schneider *et al.* [117] to try to explain the resonant feature in the cross section at 5 eV collision energy. Their calculations suggest that the branching fraction generating ground-state atoms may be as large as 30% at these energies. Figure 5.1 shows a potential-energy diagram of the ionic and some of the neutral states that play a role in the DR process involving the $X\,^1\Sigma^+$ and the first metastable $a\,^3\Sigma^+$ states of NO^+. The ionic ground-state curve was taken from Schneider *et al.* [117], which contains the neutral doubly excited curves shown in Fig. 5.1. All these doubly excited states have been invoked in the theoretical treatments of the DR of NO^+. The metastable potential-energy curve has been calculated as described in §5.3.2. The curves in Fig. 5.1 explain the choices made in the present experiment: (1) For the $X\,^1\Sigma^+$ state at 0 eV, three channels are available of which the $N(^4S)$ + $O(^1D)$ first excited channel is spin-forbidden. As this dissociation limit only correlates with quartet molecular states, a spin flip is required during the electron capture or the dissociation process. Nevertheless, VC observed this channel [51]. For the upper atmosphere, channels producing $O(^1D)$ atoms are very important, and therefore it is of interest to try to find details on this channel. (2) The overlap with the

$A'\,^2\Sigma^+$ state becomes significant at 5 eV electron energy. (3) The metastable state can decay to many different dissociation limits. Ground-state fragments would have kinetic energies of 4.9 eV for the nitrogen and 4.3 eV for the oxygen fragment. (4) The availability of a direct probe for the metastable state would provide a direct method to assess the lifetime of this state.

5.2 Experimental Details

The study of NO^+ was performed using the ion storage ring, CRYRING. MINIS was employed to create the NO^+ ion using NO gas using a mixture of NO and Ar for protection of the filament (see §2.1.3). The ions were accelerated to the maximum energy of 3.15 MeV and stored for roughly 8 s to allow the ions to radiatively relax to the lowest vibrational level. In this experiment, a high count rate was considered to be more important than arrival-time information, and so data sets of dissociation events without arrival-time information were recorded. In the analysis, the DR events were assumed to occur randomly throughout the electron cooler. The rotational temperature of the ions and the demagnification factor between the phosphor screen and the CCD camera were determined once for all simulations. The toroidal effect, although typically taken into account in DR rate measurements [118], is applied as a first to the imaging measurements. As much as possible, experimentally determined branching values were used for the branching at the toroidal collision energies. Equal branching between the open channels was assumed at elevated energies. Various branching ratios were used to check the sensitivity of that assumption. The DR signal generated in each segment of the toroidal parts of the electron cooler was weighed using the known DR cross section of NO^+ at that energy [51]. The estimated contribution of the toroidal part was subtracted from the signal before the distance distributions were fitted with analytical distributions, assuming mono-energetic electron collisions. A summary of the details on the experiment and data analysis can be found in Appendix A.

5.3 On the $a\,^3\Sigma^+$ Radiative Lifetime

5.3.1 The Current Status

The first electronically excited state in NO^+ is the $a\,^3\Sigma^+$ state, which is metastable by virtue of the spin-selection rule, $\Delta S = 0$, in radiative transitions. The different properties of the metastable NO^+ state have been subject to both experimental and theoretical research. The lifetime has been reported in the literature before and these data are listed in Tables 5.1 and 5.2. The first experimental results concerning the lifetime of the $a\,^3\Sigma^+$ electronic state used Fourier-transform ion cyclotron resonance (FT-ICR) spectrometer techniques [93, 95, 96, 121], in which the reaction rate of NO^+ ions with different monitor gases was studied as a function of storage time in single or triple ICR cells. The different techniques showed large differences in the determined lifetimes. Calamai and Yoshino [120] used a different technique to measure the radiative decay of the $a\,^3\Sigma^+$ state. They monitored uv-photons emitted in a radio-frequency ion trap, which was a direct measurement of the decay. Furthermore, they were able to distinguish between different vibrational levels. Wester *et al.* [119] used a different type of ion trap in which the ions were stored at energies of a few

Table 5.1: Experimental results of the radiative lifetime of the $a\,^3\Sigma^+$ state.

Lifetime (ms)	Level	Method	References
730 ± 50		Dissociative recombination	Present work
760 ± 30	$(v = 0)$	Collisional loss in an ion trap	Wester *et al.* [119]
720 ± 70	$(v = 0)$	Optical experiment	Calamai and Yoshino [120]
$465 \pm 69/90$	$(v = 1)$		
$330 \pm 30/60$	$(v = 2)$		
$680 \pm 91/87$	$(v \geq 0)$	FT-ICR [a]	Marx *et al.* [96]
100 ± 20	$(v \geq 1)$	FT-ICR	Marx *et al.* [121]
135 ± 25	$(v \geq 0)$		
$530 \pm 300/100$		FT-ICR	Kuo *et al.* [95]
$1450 \pm 1150/450$		FT-ICR, single-cell	O'Keefe and McDonald [93]

[a] improved measurement

keV. The time-dependent rate of the stored ions undergoing charge-exchange collisions with residual gas was monitored. The results of Wester *et al.* agree well with Calamai and Yoshino and the most recent FT-ICR measurements [96]. Calculation of the metastable-state lifetime has turned out to be difficult. For example, the calculations do not agree on which singlet excited state provides the necessary dipole moment for the metastable state to decay to the singlet electronic ground state [93, 95, 122–124]. It is of interest to note that in all these theoretical calculations, the vibrational radiative relaxation within the $a\,^3\Sigma^+$ state has not been discussed in connection to the lifetime of metastable vibrationally excited levels. The present chapter contains such calculations, indicating that the *intrastate* decay is significant. To the best of our knowledge the metastable state has never been an explicit subject of experimental DR studies.

5.3.2 Theoretical Considerations

Calculations were performed in order to estimate the rotational radiative lifetime of the lowest vibrational level ($v = 0$) of the $^1\Sigma^+$ ground electronic state and the vibrational radiative

Table 5.2: Theoretical results of the radiative lifetime of the $a\,^3\Sigma^+$ state.

Lifetime (ms)	Level	Perturber	References
$183 \rightarrow 190$	$(v = 0 \rightarrow 4)$	Predominantly $A\,^1\Pi$	Bearpark *et al.* [122]
$270 \rightarrow 250$	$(v = 0 \rightarrow 5)$	$B\,^1\Pi$ more than $A\,^1\Pi$	Palmieri *et al.* [123]
$455 \rightarrow 495$	$(v = 0 \rightarrow 4)$	$A\,^1\Pi$ dominates	Manaa and Yarkony [124]
758	$(v = 0)$	Rotationally averaged	
780		Extended calculation of Ref. [93]	Kuo *et al.* [95]
989		$A\,^1\Pi$	O'Keefe and McDonald [93]

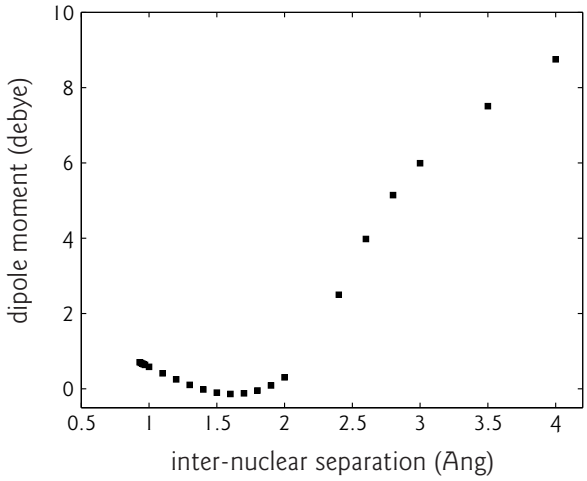

Figure 5.2: Dipole moment of the $a\,^3\Sigma^+$ state of NO^+ determined by *ab initio* calculations.

lifetime of the metastable $^3\Sigma^+$ state. The radiative lifetime τ of a rovibrational state with vibrational and rotational quantum number v' and J', respectively, can be expressed as

$$\tau_{v'J'} = \frac{1}{A_{v'J'}} \tag{5.2}$$

where $A_{v'J'}$ is the sum of all Einstein coefficients which correspond to all possible radiative transitions $v'J'$ to $v''J''$. The Einstein coefficient A (cm^{-1}) can be expressed as [125]

$$A = 3.136 \cdot 10^{-7}[S(J',J'')/(2J'+1)]\,\nu^3\,|\langle\psi_{v'J'}|M(R)|\psi_{v''J''}\rangle|^2 \tag{5.3}$$

where $M(R)$ is the dipole moment function (in debye), ν the emission energy (in cm^{-1}), $S(J',J'')$ the Hönl-London rotational intensity factor and $\psi_{v'J'}$ and $\psi_{v''J''}$ are the initial- and final-state wave functions. The FORTRAN program LEVEL 7.4 by Le Roy [125] was used to calculate the transition probabilities. LEVEL 7.4 solves the one-dimensional Schrödinger equation numerically and determines the initial- and final-state wave functions. The potential curve and dipole moment function of the $^1\Sigma^+$ ground state were taken from Fehér and Martin [126]. Not only rovibrational transitions but also pure rotational transitions have been calculated. *Ab initio* calculations were performed, using the GAUSSIAN 98 program [127], in order to calculate the potential curve and dipole moment function of the metastable $a\,^3\Sigma^+$ state. The calculations were performed at the complete active-space self-consistent field (CASSCF) level, including 8 electrons and 8 molecular orbitals as an active space. The basis set used was 6-311G*. The potential energy and the dipole moment were calculated for 21 internuclear distances in the interval 0.9–4.0 Å. The calculated potential curve is presented in Fig. 5.1 and the dipole moment in Fig. 5.2.

5.4 Branching Behaviour of the Ground $X\,^1\Sigma^+$ State

Figure 5.3(a) shows a particle distance spectrum taken at 0 eV collision energy. The ion beam was produced in the MINIS source. Data was collected after a storage time of NO^+ in the ring of 4 s. This storage time removes possible signal from ions in electronically or vibrationally excited states (the vibrational radiative lifetime of the $X\,^1\Sigma^+$ ground state is less than 100 ms [128]). Dissociation events with small particle distances are not detected

Table 5.3: Calculated rotational lifetime of $NO^+(X\,^1\Sigma^+)$ ions.

	$J=10$	$J=20$	$J=30$	$J=40$	$J=50$	$J=60$	$J=70$
τ (s)	1559	189	55	23	11	6	4

in our spot-finding routine, which explains the cutoff below 3 mm ($\sim$ 3 pixels). One peak dominates the spectrum and a much smaller peak is observed at larger particle separation. The dominant peak reflects dissociation to the $N(^2D)$ + $O(^3P)$ product pair. The small peak is due to $N(^4S)$ + $O(^3P)$ ground-state atoms. The position of the spin-forbidden $N(^4S)$ + $O(^1D)$ channel is very close to the dominant peak. In our analysis of the spectrum, we noticed two aspects. First, the peak shape was fitted with a rotational temperature of 1300 K (as done by VC), whereas the temperature of the MINIS ion source is estimated to be on the order of 900 K. The rotational state lifetimes are very long (see Table 5.3). For example, the $X\,^1\Sigma^+(v=0, J=40)$ level, which has an energy of about 0.4 eV, has a radiative decay time of 23 s. Hence, storage of the NO^+ ions does not change the population of these highly excited levels. Second, it was realised that the high-energy side of the dominant peak was affected by the toroidal effect. A corrected spectrum as well as the magnitude of the correction is shown in Fig. 5.3(a). The final branching was found to be 5(2)% : 0(2)% : 95(3)% over the first three allowed dissociation limits, i.e., [$N(^4S)$,$O(^3P)$] : [$N(^4S)$,$O(^1D)$] : [$N(^2D)$,$O(^3P)$]. Without including the toroidal correction, the spin-forbidden channel was found to be on the order of 1.5(2)%. The effect of the toroidal regions is complicated. The particle separation on the detector depends on the place of dissociation in the electron cooler. Being on either side of the parallel section, the toroidal sections give extra counts at small and at large particle separation. The enhanced collision energy due to the nonzero angle between the electron- and the ion-beam velocity vectors, means a shift to higher apparent kinetic energy release values and, hence, larger particle separations. VC reported a significantly higher contribution of the spin-forbidden channel. In their analysis also signal from a metastable state was inferred. The difference with our results is due to an ill-understood effect operating in ion sources, producing NO^+. In the MINIS ion source and in another ion source, a hollow cathode ion source, distance spectra were observed that depended on the ion-source conditions and that resembled strongly the structure reported in VC. Although the product mechanism is unknown, we conclude that a small fraction of the NO^+ ions is formed with large internal rotational energy. We stress that this is a problem probably intrinsic to NO and that this effect has not been observed in other diatomic species studied before at CRYRING. As this aspect does not affect the results presented in this chapter, this detail is left for future research.

At 1.25 eV collision energy, the $N(^2P)$ + $O(^3P)$ channel opens and is observed. A spectrum obtained from the data taken at this energy is shown in Fig. 5.3(b) together with a fit to the distance distribution. The dominant $N(^2D)$ + $O(^3P)$ channel was best fitted using an anisotropic $\sin^2\theta$ distribution [51], which suggests a preference for the ions to dissociate perpendicularly to the relative collision vector. This preference has implications for the possible symmetries of the target states, as has been described by Dunn [90] and also O'Malley and Taylor [91] (see later). The toroidal correction shows two peaks, associated

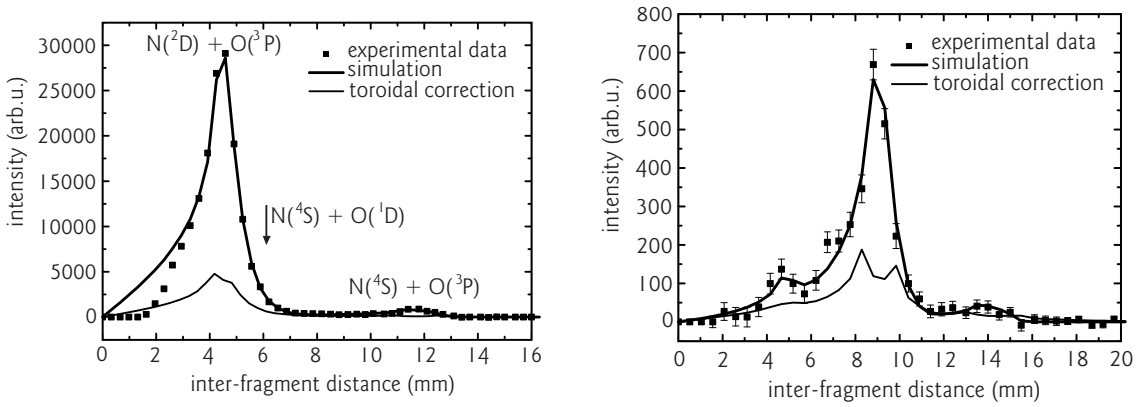

Figure 5.3: Histograms of inter-fragment distances due to the DR of NO^+ at (a) 0 eV and (b) 1.25 eV collision energy measured with the imaging detector. The squares are the experimental data points, and the bold curves are the least-squares optimised model spectra using the branching fractions as free parameters. The thinner curves are the magnitude and shape of the toroidal corrections (see text). The positions of the dissociation limits at 0 eV are indicated.

with dissociations in the region before the electron cooler (large separations) and after the cooler (smaller inter-fragment separations). Also in this case, the toroidal correction reduces the branching to the spin-forbidden $N(^4S) + O(^1D)$ channel and, after this correction, it decreases from 18(10)% to 10(10)%.

The cross section decreases steeply as function of electron energy and the experiments become more difficult to perform because the signal-to-background ratio decreases. As a consequence, the branching fractions are less accurate at elevated energies. All branching fractions are collected together and presented in Fig. 5.5.

At 5.6 eV collision energy, we hoped to observe a clear nonzero branching fraction to ground-state atoms. The presence of this channel was suggested by Schneider *et al.* [117]. Figure 5.4 shows the inter-fragment distance spectrum of this energy. The arrow indicates the maximum separation of the ground-state atoms. We conclude that either the $A'\,^2\Sigma^+$ state is not dominant as a capture state or the $A'\,^2\Sigma^+$ state does not correlate uniquely with ground-state atoms as was suggested by the potential curve given in Fig. 5.1. Nine different dissociation channels are open at 5 eV and the wide range of detected inter-fragment distances (see Fig. 5.4) indicates that several of these channels are populated. The distributions of the different channels are assumed to be isotropic except for the $N(^2P) + O(^1S)$, for which a $\cos^2\theta$ distribution was used to yield a more accurate fit to the experimental data points at low kinetic energy release. This $\cos^2\theta$ distribution indicates a larger probability for the ions to dissociate parallel to the relative velocity vector. A rotational temperature of 1300 K was used for all channels. A least-squares fit weighted to the statistical error bars of the experimental data points, though not including the spin-forbidden channels $N(^4S) + O(^1D)$ and $N(^4S) + O(^1S)$, gives rise to the branching fractions presented in Fig. 5.5. It is of interest to note that inclusion of the spin-forbidden channel $N(^4S) + O(^1S)$ reduces the quality of the fit and that the $N(^4S) + O(^1D)$ channel only contributes with a few percent if included. We varied a number of parameters (for example, rotational temperature and collision energy) within the accuracy to get a better estimate of the error. The anisotropy has been kept fixed

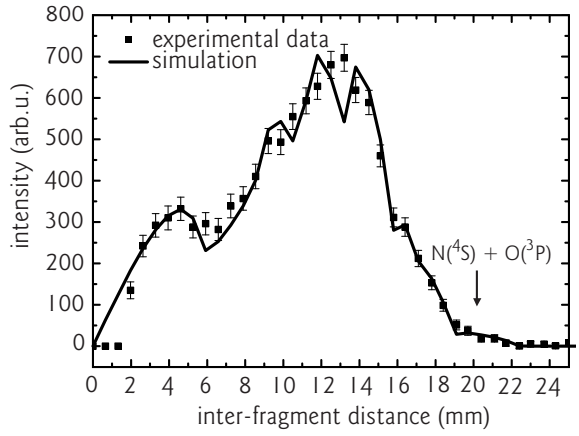

Figure 5.4: Histogram of DR fragments taken at 5.6 eV collision energy. The arrow indicates the maximum distance where ground-state fragments are to be detected. The squares are the experimental data points and the curve is the result of a least-squares optimisation including the model distributions for all but the spin-forbidden channels.

for all channels.

It has been noted earlier that the branching behaviour in DR compares favourably with the results of a statistical model, in which the number of molecular states connected to a certain dissociation limit determines the probability to reach this limit [25, 129]. For example, if the spin multiplicity and the orbital angular momentum degeneracy of both atoms are multiplied, $N(^4S) + O(^3P)$ yields a multiplicity of $(4 \cdot 1 \cdot 3 \cdot 3 =)$ 36, $N(^4S) + O(^1D)$ yields 20, and $N(^2D) + O(^3P)$ yields 90. If a $NO^+(X\,^1\Sigma^+)$ ion captures an electron, it forms a repulsive state with spin $S = \frac{1}{2}$, and so a multiplicity of 2. Hence, if only dissociation products of spin-allowed transitions are considered, the $N(^4S) + O(^1D)$ channel will not contribute at all and branching fractions of 17%, 0%, and 83% are obtained. These numbers compare well with the observations at 0 eV, 5(2)% : 0(2)% : 95(3)%. The results of the statistical behaviour for NO^+ at 0 eV collision energy has been reported before [25]. The expectations from the statistical model are presented in Fig. 5.5. In each of the panels (i)—(iii) in Fig. 5.5 the experimental results (III) are plotted together with the expectations from the spin unconstrained (I) and spin-constrained models (II). In all cases, the dominant dissociation limit is correctly predicted by the spin-constrained model.

5.5 Branching Behaviour and Lifetime of the $a\,^3\Sigma^+$ State

Figure 5.6 shows a series of spectra in which data have only been taken during different time windows after injection. The aim of this experiment was to observe DR products from metastable states in NO^+. The intensity in each spectrum was normalised using the intensity of the dominant $N(^2D) + O(^3P)$ peak formed from ground-state ions. From this analysis a time-dependant signal is observed at large particle separations, i.e., those for which the DR products have large kinetic energy release values. The arrow indicates the separation of ground-state fragments if starting from the $a\,^3\Sigma^+$ state. The associated kinetic energy in the spectrum is as high as 9 eV. As in nearly all molecular systems, this state can also dissociate to many different limits. Figure 5.7 shows the result of the least-squares fit together with the predicted distance distribution using the statistical model discussed earlier. As the collision energy is 0 eV, all channels are described using an isotropic distribution. The last panel (iv) in Fig. 5.5 shows the similarities between the parameter-free statistical model and the results from the least-squares fit. Since the energy difference between the $X\,^1\Sigma^+$ and the $a\,^3\Sigma^+$

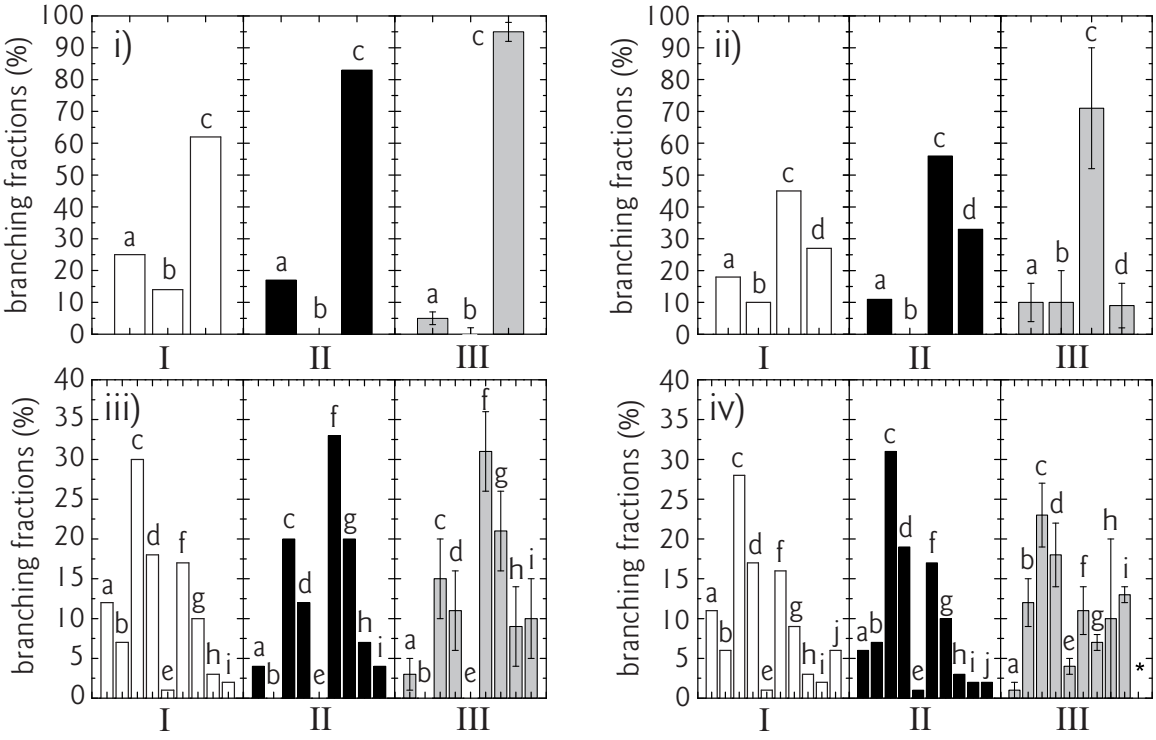

Figure 5.5: Experimental and model branching fractions for the ground $X\,^1\Sigma^+$ state at (i) 0 eV, (ii) 1.25 eV, (iii) 5.6 eV collision energies, and (iv) the metastable $a\,^3\Sigma^+$ state at 0 eV collision energy. In each case, three data sets are plotted: (I) is the branching ratio determined from the multiplicity of available states. (II) is (I) but also accounts for spin-selection rules. (III) is the experimental data. The histogram bars correspond to the branching fractions of (a) $N(^4S) + O(^3P)$, (b) $N(^4S) + O(^1D)$, (c) $N(^2D) + O(^3P)$, (d) $N(^2P) + O(^3P)$, (e) $N(^4S) + O(^1S)$, (f) $N(^2D) + O(^1D)$, (g) $N(^2P) + O(^1D)$, (h) $N(^2D) + O(^1S)$, (i) $N(^2P) + O(^1S)$, (j) $N(^4S) + O(^5S)$. The asterisk denotes that the $N(^4S) + O(^5S)$ channel could not be detected due to the small particle separation.

states is 6.3 eV, the statistical prediction using the spin unconstrained model (I) of the $a\,^3\Sigma^+$ state at 0 eV collision energy is similar to the prediction for 5.6 eV collision energy of the $X\,^1\Sigma^+$ ground state. The $a\,^3\Sigma^+$ state is a triplet and so can form doublet and quartet states when recombining with an electron. Therefore, none of the open channels are spin forbidden. Implementation of the spin-selection rules affects the predicted branching of ground-state ions and improves agreement with experiment considerably [see Figs. 5.5 (iii) and (iv)]. The highest excited channel $N(^4S) + O(^5S)$ has not been included in the simulation since it can not be detected due to the small particle separation. Discrepancies between the statistical model and the fit is larger for the two highest observed excited channels. The discrepancies could be related to the difficulties in obtaining reliable branching to these two channels due to the poor signal-to-noise ratio. It is noted that the statistical model predicts a small contribution from these two channels. Overall, the experimental branching ratios and the predictions from statistical arguments agree well.

Figure 5.6 shows the contribution from ground-state molecular ions and from the metastable $a\,^3\Sigma^+$ state. By normalising the metastable signal with respect to the ground-state

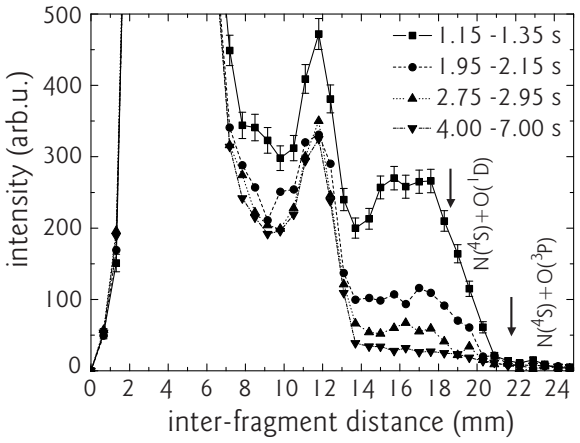

Figure 5.6: The distance spectra taken at different time intervals after ion injection into CRYRING in order to detect DR events from the metastable $a\,^3\Sigma^+$ state.

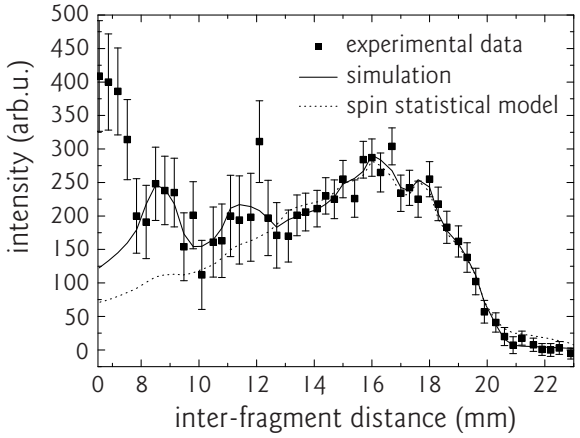

Figure 5.7: The distance distributions of DR events from the metastable $a\,^3\Sigma^+$ state, which are used to determine the branching fractions of the nine lowest open channels. The solid curve is the result of a least-squares optimisation with the branching fractions as free parameters. The dotted curve is the result of a simulation in which the branching fractions are predetermined using the spin-statistical model.

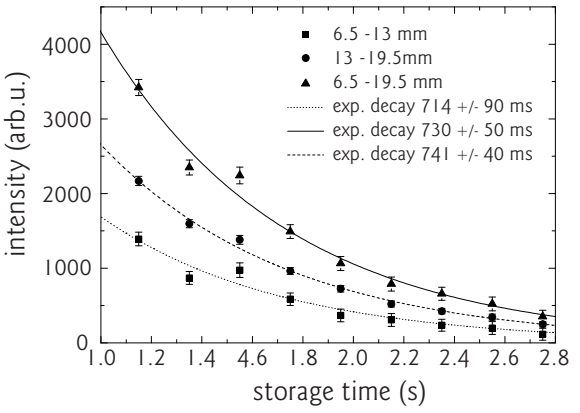

Figure 5.8: The number of DR events from the metastable $a\,^3\Sigma^+$ state as function of storage time. Each displayed data set corresponds to a different inter-fragment distance-interval of the spectra shown in Fig. 5.6.

Table 5.4: Calculated vibrational decay lifetimes, $\tau_{intra}(v)$, within the NO^+ $a\,^3\Sigma^+$ state and also estimated and reported lifetimes adding the *interstate* lifetime of 730 ms, $\tau_{inter}(v)$.

$a\,^3\Sigma^+(v)$	$\tau_{intra}(v)$ (ms)	$\tau_{eff}(v)$ (ms)	$\tau(v)$ (ms) [120]
1	522	304	465 $\pm$ 69/90
2	272	198	330 $\pm$ 30/60
3	190	151	

counts within each time window, it is possible to extract the lifetime of the metastable state. Figure 5.8 shows the relative number of counts from the total number of counts (at all observed distances) as well as for two selected distance regions (high and low distance values). The decay time is found to be 730(50) ms, independent of the selected part of the distance spectrum. In the ion source, vibrational excited levels will probably be populated in the metastable $a\,^3\Sigma^+$ state. The decay of the $a\,^3\Sigma^+$ state may be dependent on the vibrational level. From the absence of a dependence on inter-fragment separations, we could conclude that the branching over the possible dissociation limits does not strongly depend on the vibrational level. Alternatively, the vibrational excited levels may decay quickly to the vibrational ground state (*intrastate* decay), followed by a decay of the a state($v = 0$) level to the NO^+ ground state. In our experiment, it is clear that we have no vibrational resolution in the distance spectra. In order to estimate the *intrastate*-decay rate, associated radiative lifetimes have been calculated. These results (see Table 5.4) indicate that the *intrastate* decay will be faster than the spin-forbidden radiative decay to the electronic ground state. At present, a delay exists between the formation of the ions in the ion source and the data acquisition due to the acceleration time required, which is about 1.1 s. During this time, most of the vibrationally excited states have already decayed. The only experiment that has reported a vibrational state-dependent lifetime is the optical experiment by Calamai and Yoshino [120]. These authors reported a lifetime that strongly depended on the vibrational level, 720 ms for $v = 0$, 465 ms for $v = 1$, and 330 ms for $v = 2$. Table 5.4 shows the expected vibrational lifetimes combining the observed decay of the $v = 0$ state with the calculated *vibrational* decay using $\tau_{eff} = \tau_{intra} \cdot \tau_{inter}/(\tau_{intra} + \tau_{inter})$. The trend reported by of Calamai and Yoshino is reproduced in the calculations here.

5.6 Discussion

We have performed a series of experiments to determine the product formation in the DR of NO^+. The $N(^2D)$-containing channel has a branching fraction close to unity near 0 eV collision energy. In aeronomical applications quantum yields are usually used to express branching fractions, i.e., the number of atoms formed in a specific state per dissociating molecule. At small collision energies, the branching fraction of the $N(^2D)$ + $O(^3P)$ channel equals the $N(^2D)$ quantum yield. The spin-forbidden channel at 0 eV, $N(^4S)$ + $O(^1D)$, is virtually closed, and the present value differs significantly from earlier reported values [51, 116]. At elevated collision energies, new dissociation channels open up and the present experiments reveal that these limits are also populated. Within our experimental accuracy we

have no indication that spin-forbidden channels are populated. At 5.6 eV collision energy the production of ground-state fragments is only a few percent, and this is in contrast to recent predictions, in which Schneider *et al.* proposed that a significant fraction of 30% would populate the $^2\Sigma$ states [117]. It has been shown in numerous cases that the dissociation behaviour in the DR process is very complicated. Nearly all channels are populated, even in those cases for which only a limited number of capture states seems to be relevant.

The complexity of the dissociation behaviour seems to be described in an empirical way by the simple statistical model applied to the observed branching. Figure 5.5 shows the remarkable agreement with the branching obtained from fittings to experimental data and branching predicted empirically. At the moment, it is not clear why these predictions are accurate. The theoretical approach to the DR process requires accurate calculations of states that have to cross the vibrational wave function of the ionic state. Such a calculation excludes many neutral doubly excited states. To determine the capture efficiency demands a second independent calculation, which again selects specific states on the requirement of a sufficiently large capture matrix element [82]. The complexity of DR branching calculations is enormous. To date, no complete calculation exists for the branching behaviour for molecules heavier than H_2 and HeH [130–132].

In DR studies of molecular oxygen, spin-orbit coupling has been invoked to explain the product $O(^1S)$ atoms at near 0-eV collisions. The spin flip associated with this coupling was mediated by the formation of a triplet Rydberg state and increased the $O(^1S)$ yield from near 0% to 5% [46, 68]. So, although, spin changes and the involvement of spin-orbit coupling cannot be completely ruled out, the impact on product branching is expected to be small.

DR is not always an isotropic process and, at collision energies larger than 0 eV, a well-defined relative collision vector is established in the experiment. As a consequence, for example, capture processes that favour a molecular-axis orientation parallel to the relative velocity vector will dissociate by preference perpendicular to the detector and are described by a $\cos^2\theta$ distribution. Figure 5.4 shows such an example at small inter-fragment separations. Figure 5.3(b) shows an example of a $\sin^2\theta$ distribution. Dunn [90] and O'Malley and Taylor [91] have addressed this problem in electron-capture processes, using conservation of symmetry before and after the reaction. O'Malley and Taylor [see Eq. (14) in Ref. [91]] provide an attractive approximate prediction. The $\sin^2\theta$ distribution for the dominant $N(^2D) + O(^3P)$ channel at 1.25 eV collision energy is in agreement with the formation of a $^2\Pi$ state by a $p\pi$ partial electron wave. The $\cos^2\theta$ distribution found for the $N(^2P) + O(^1S)$ channel suggests a product state of $^2\Sigma^+$ symmetry in a collision reaction in which the $p\sigma$ partial wave has a larger cross section than the $s\sigma$ partial wave. If a large kinetic energy resolution could be achieved in combination with accurate anisotropy determination, much more insight could be gained on the dynamics of the DR process. At present, the length of the electron target (85 cm) is an important resolution-limiting factor.

DR from the metastable $a\,^3\Sigma^+$ state has been studied and the radiative lifetime of this state measured. It cannot be ruled out that the ion source will produce other electronically excited ions in several more states other than the $a\,^3\Sigma^+$ state. The two states that are closest in energy to the $a\,^3\Sigma^+$ state are the $b\,^3\Pi$ and the $w\,^3\Delta$ states [133]. However, results from experiments studying uv photon emission from electronically excited states of NO^+ indicate that the $b\,^3\Pi$ and $w\,^3\Delta$ states of NO^+ have much shorter lifetimes [120] and would not influence the population of the $a\,^3\Sigma^+$ state in our experiment.

Tables 5.1 and 5.2 summarise the experimental and theoretical results for several prop-

erties of the $a\,^3\Sigma^+$ state. The experimental [93, 95, 96, 119–121] as well as theoretical [93, 95, 122–124] work concentrated on the direct decay channels to the electronic ground state. It seems that the decay of vibrationally excited levels through infrared radiation within the metastable state has never been treated, in spite of the importance of this decay channel with respect to the lifetime on a vibrational-state-resolved level. Our calculations reveal that the *intrastate* decay of vibrationally excited levels is faster than the decay to the electronic ground state. Thus, the 1.1-s delay between ion generation and the start of our experiment is sufficient for an almost complete loss of vibrationally excited states. In the future, experimental improvements will allow for a reduction of this delay to 200 ms [134]. The data in Tables 5.1 and 5.2 also illustrate the variation in both the theoretical calculations and in experimental lifetime determinations. Recent experimental determinations [119, 120] agree on a $v = 0$ lifetime of about 730 ms. The most recent theoretical calculations predict lifetimes that are much shorter than the observed values. It is of interest to note that the different calculations do not agree on those states that cause the finite radiative decay on the triplet state.

The dissociation behaviour has been determined for the metastable state. For these data also the statistical model seems to describe the observed distance distribution well. Fragments are formed with energies up to 5 eV for nitrogen and 4.3 eV for oxygen and with a total kinetic energy release as high as 9.3 eV. This observation may make metastable NO^+ a source of hot atoms in the geocorona and in other relevant plasmas.

5.7 Conclusions

This chapter presents experimental and theoretical results on the behaviour of $NO^+(X\,^1\Sigma^+)$ ground-state ions and the $NO^+(a\,^3\Sigma^+)$ metastable-state ions in reactions with electrons at different collision energies. Our results provide an improved upper limit on the absence of the spin-forbidden dissociation channel in the dissociative recombination reaction involving ground-state NO^+ at 0 eV and 1.2 eV collision energies. The branching behaviour has also been studied at 5.6 eV for the $X\,^1\Sigma^+$ state and at 0 eV for the $a\,^3\Sigma^+$ state. Those results show a complex branching to a large number of open channels. In all cases the DR dissociation dynamics can be compared favourably with the results of a model that involves only statistical arguments and spin-conservation rules during the electron-capture and dissociation processes. The radiative lifetime has been determined for the $a\,^3\Sigma^+$ metastable state. These results together with *ab initio* calculations indicate that vibrational excited levels in the $a\,^3\Sigma^+$ metastable state first decays via *intrastate* radiative decay to $v = 0$, prior to radiative relaxation to the electronic ground state.

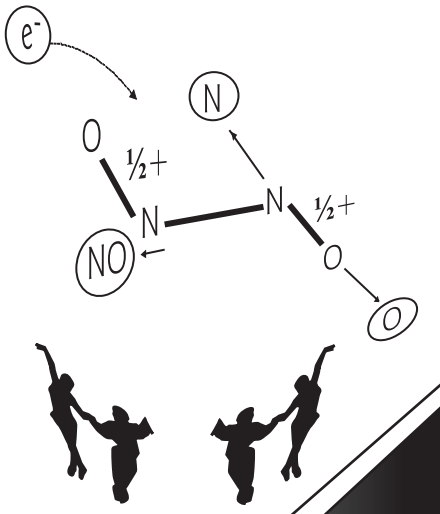

1
2
3
4
5
6
7
A
B

Physics is...

making small things great

– eldest brother of –

Annemieke

Chapter 6

Super Dissociative Recombination of Weakly-Bound Nitric-Oxide Dimer Ions

Dissociative recombination (DR) of the dimer ion $(NO)_2^+$ has been studied with the aim of investigating the underlying mechanisms responsible for the strongly enhanced thermal rate coefficient for the dimer, interpreting the dissociation dynamics of the dimer ion, and studying the degree of similarity between the DR of $(NO)_2^+$ and the DR of its monomer. In this chapter, data is presented on the energy-dependence in the efficiency of the DR process as well as new data on the chemical branching, identifying the product fragments, and on the physical branching, qualitatively identifying the internal state and kinetic energy distribution of the nascent products. In addition, the energy-dependent cross section of the dissociative excitation (DE) of $(NO)_2^+$ into $NO + NO^+$ is presented as well. The results from the DR study are compared with those found for other weakly- and strongly-bound dimer ions.

6.1 On the NO-Dimer Ion

Diatomic ions like O_2^+, NO^+, and N_2^+ are of major importance to the Earth's ionosphere and play an important role in the ionospheric chemistry and heating [7, 8]. Cluster ions are of importance in the lower part of the *D* region [2]. Below roughly 85 km, water-cluster ions dominate over O_2^+ and NO^+, and become more important as sinks for low-energy electrons and as source of reactive and kinetic species. Of special importance to the water-cluster ion formation is the production and loss of O_2^+ and NO^+ dimer ions, where NO^+ clusters with other neutrals rather than with its neutral counterpart due to low NO densities. The dimer ions are weakly bound and experiments suggest that their thermal DR rate coefficients are an order of magnitude faster than their monomer counterparts [135]. This large recombination rate is referred to as super-DR and is not restricted to weakly-bound dimer ions, but hold for strongly-bound (proton-bridged) and rare-gas dimer ions as well [136, 137]. As far as we know, neither branching nor collision-energy-dependent rate coefficients have been determined for weakly-bound dimer ions. Although the $(NO)_2^+$ has no direct importance to the Earth's atmosphere, its study can provide insight on the behaviour of the rate and on the influence of this bond-type on the DR reaction.

The NO-dimer cation has been characterised experimentally using various spectroscopic methods such as matrix spectroscopy [138, 139] and more recently using ZEKE (zero electron kinetic energy) spectroscopy [140]. This ion has posed theoreticians many problems both in explaining the spectroscopic results as well as in establishing the theoretical tools for predicting the correct binding properties [140–142]. The *trans* (ON-NO) configuration is the minimum energy configuration; the *cis* (ONNO) configuration is nearly iso-energetic. A *cyclic* (.ONON.) structure is positioned about 0.2 eV above the ground state [143]. This *cyclic* configuration is invoked in explaining some vibrational frequencies observed using matrix spectroscopy. The N-N bond strength that binds the NO moieties has been determined to be around 0.6 eV [144–146]. The vibrational frequency of the NO-moiety in the dimer ion is larger than that of NO and smaller than that of NO^+, indicating that in the dimer ion the effective charge is 0.5 on each NO-moiety [144]. The $N - N$ equilibrium distance in the dimer ions is calculated to be 2.22 Å (*cis*) and 2.24 Å (*trans*), illustrative of the relatively weak bond [141]. Although we do not have explicit information on the configurations from our ion source, we believe that the dimer ions are predominantly produced in the *cis* and

trans configurations.

At 0 eV collision energy, E_c, and for electronic and vibrational ground state ions, the DR of $(NO)_2^+$ may result in the following *chemical* fragmentation processes and corresponding kinetic energy releases (KERs),

$$(NO)_2^+ + e^-(E_c = 0) \rightarrow N_2 + O_2 + 10.54 \text{ eV} \quad (6.1a)$$
$$\rightarrow NO + NO + 8.66 \text{ eV} \quad (6.1b)$$
$$\rightarrow N_2O + O + 7.07 \text{ eV} \quad (6.1c)$$
$$\rightarrow N_2 + O + O + 5.43 \text{ eV} \quad (6.1d)$$
$$\rightarrow NO_2 + N + 5.25 \text{ eV} \quad (6.1e)$$
$$\rightarrow NO + O + N + 2.17 \text{ eV} \quad (6.1f)$$
$$\rightarrow O_2 + N + N + 0.78 \text{ eV} \quad (6.1g)$$

The KER values given in Eqs. (6.1a)–(6.1g) are valid when all product fragments are created in their electronic and vibrational ground state. Internal excitation of the fragments increases the number of dissociation pathways. Equation (6.1f) would for example split into the following *physical* branching channels,

$$(NO)_2^+ + e^-(E_c = 0) \rightarrow NO + O(^3P) + N(^4S) + 2.17 \text{ eV} \quad (6.2a)$$
$$\rightarrow NO + O^*(^1D) + N(^4S) + 0.21 \text{ eV} \quad (6.2b)$$
$$\rightarrow NO^*(v, J) + O(^3P) + N(^4S) + (2.17 - E_{v,J}) \text{ eV} \quad (6.2c)$$
$$\rightarrow NO + O(^3P) + N^*(^2D) - 0.21 \text{ eV} \quad (6.2d)$$

The stars indicate internal excitation of the specific fragment. The KER values given in Eqs. (6.2a), (6.2b), and (6.2d) are valid for 0-eV collisions and for the parent ion as well as the NO product fragment in their rovibrational ground state. Equation (6.2c) groups together a number of energetically possible channels, expressed as $NO^*(v, J)$, where $E_{v,J}$ is the excitation energy of the respective states with respect to the rovibronic ground state of NO. Equation (6.2d) is not energetically possible at 0-eV collisions unless aided by 0.21 eV of internal excitation in the $(NO)_2^+$-parent ion. We note that this energetically inaccessible dissociation towards $O(^3P) + N^*(^2D)$ is in fact the dominant dissociation pathway in the DR of the monomer NO^+. We also note that dissociation towards $O^*(^1D) + N(^4S)$, which is energetically and spin-allowed in the dimer ion, is not observed in the DR of the monomer ion in accord with conservation of electron spin during the DR reaction [87].

Figure 6.1(a) summarises the reactions (6.1a)–(6.1g). The three-body-reaction channels are given on the left-hand side. The two-body-reaction channels on the right-hand side. The binding energy of the neutral dimer (0.09 eV) is much smaller than that of the ionised dimer (0.6 eV). Figure 6.1(b) shows the geometry associated with the ground state *trans*-configuration of the NO-dimer ion. For illustration purposes, the outcome of a dissociation process involving recoil along one of the NO bonds is indicated; the result being energetic O and N fragments and a smaller kinetic energy of the NO product.

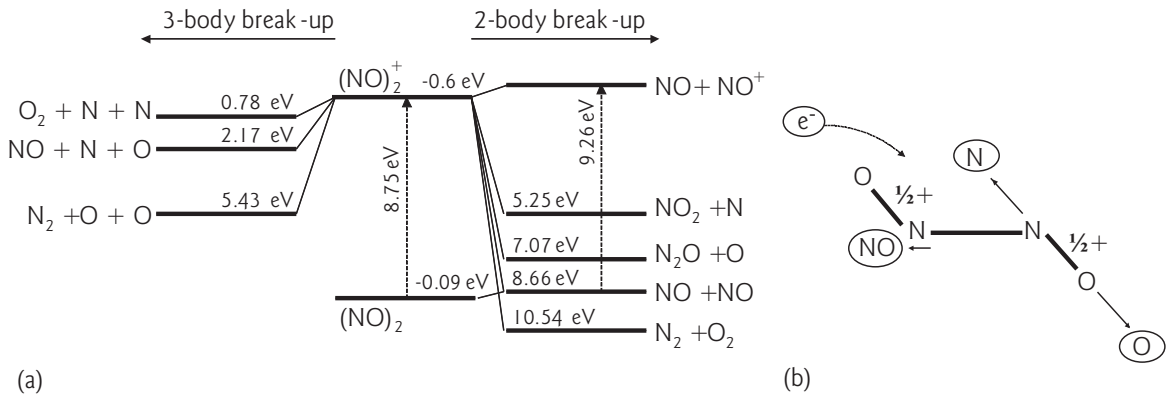

Figure 6.1: (a) Level diagram concerning the DR of the NO-dimer cation. The three-body break-up is displayed on the right and the two-body break-up on the left. The dashed vertical arrows denote the ionisation energy of the dimer and monomer molecule. The two negative values are the binding energies of the dimer neutral and ion. (b) Geometric structure of the *trans* isomer of $(NO)_2^+$. The circled labels are the particles involved in the DR reaction branching towards the NO + O + N channel. The positive charge in the parent ion is equally divided over the NO-moieties. The solid arrows illustrate the momentum vectors of the product fragments when no rearrangements occur upon dissociation into NO + O + N.

6.2 Experimental Details

The $(NO)_2^+$ measurements have been carried out at the heavy-ion storage ring, CRYRING. The experimental procedures for measuring cross sections, chemical fragmentation [45, 147], and physical fragmentation [87] have been presented in detail in literature and are also described in Chapters 2 and 3. A summary of the details on the experiment and the analysis can be found in Appendix A. The $(NO)_2^+$ ions were produced from pure NO vapour in a high-pressure hollow cathode ion source (JIMIS) [109]. The ion beam was accelerated to the maximum energy of 1.6 MeV and stored for 8 s. The cross-section measurements employed a SBD with an active area of 900 mm^2, mounted at a distance of ca. 4.3 m from the centre of the electron cooler (see §2.1.4). Events with the total neutral mass 60 (a.m.u.) were measured while ramping the collision energy between 0 and 1 eV in order to extract the energy-dependent DR rate. For the DE cross section towards NO + NO^+, events with a total neutral mass 30 (a.m.u.) were measured while ramping the collision energy between 0 and 4 eV. Both measurements used acceleration and deceleration of the electrons to ensure a collision energy of 0 eV is achieved. The grid and imaging technique were employed to determine the fragmentation and the dynamics of $(NO)_2^+$ at 0 eV collision energy, respectively (see Chapters 2 and 3). The imaging system was setup identical to the dynamics study in the DR of diatomic ions [87]. For each event, the positions of all hits on the detector were recorded irrespective of the amount of particles. The identities and the difference in time-of-arrival of the particles were not measured. Particle identification has been employed for measurements of the three-body break-up in polyatomic ions where two of the product fragments are considerably lighter than the heavier fragment [48]. In the data analysis of the DR dynamics, we focused on all recorded 3-particle events. The background contribution to this signal is estimated through the presence of apparent 4-particle events. As the latter are very unlikely, we assume that they relate to events in which a noise count is attributed to a fragment. Consequently we estimate that about 5% of all 3-particle events may be due to such a correlation. It is noted that we did not investigate the 2-particle events;

the unquantifiable contribution from 3-particle events, in which one fragment is missed, renders two-body channel analysis infeasible at present. From injection until the starts of the measurements the electrons were set to 0 eV collision energy to ensure cooling. As the electron gun cathode was around a mere 16 eV electron collision energy, Eq. (3.3) has been used to include the electron space-charge effect in the cross-section measurements. The toroidal correction has been included in the data analyses as well as in the simulation of the physical branching.

6.3 Absolute DR and DE Cross Sections

The DR cross section has been measured for collision energies up to 1.4 eV and is shown in Fig. 6.2(a) together with the DR cross section of the NO^+ monomer [51]. The absolute $(NO)_2^+$ cross section is almost 10^{-11} cm^2 near 1 meV, which is indeed large compared to the value for the monomer ion. However, the cross sections of the dimer and the monomer are comparable near 0.2 eV. Apparently the unusually large DR rate is limited to collision energies below 200 meV. The enhanced DR rate at very small energies suffices to arrive at a high thermal rate. Using the data in Fig. 6.2(a), we derive a thermal rate of $1.5 \cdot 10^{-6}$cm^3 s^{-1} at 300 K, which is indeed a factor of 4 higher than the thermal rate of the monomer. Since the threshold behaviour of DR predicts a cross section ($\langle \sigma v \rangle / v$, with $\langle\ \rangle$ the averaging over the relative velocity distribution) scaling as $1/E_c$ at low collision energies, we also present

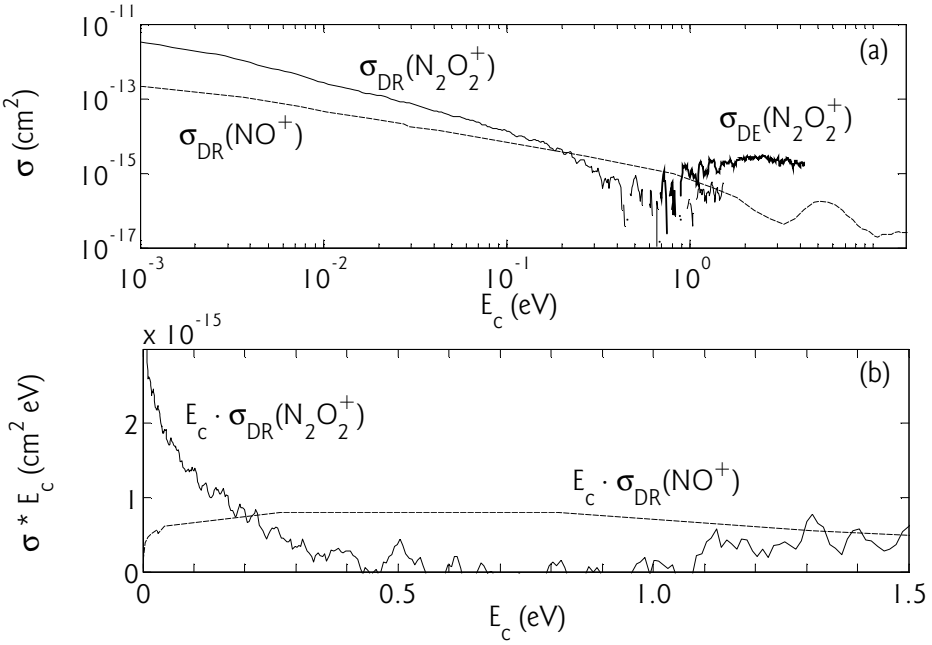

Figure 6.2: (a) The DR and DE cross sections of $(NO)_2^+$ together with the DR cross section of NO^+ measured by Vejby-Christensen *et al.* [51]. The DR cross section of the dimer shows a steeper decrease upon increasing collision energy than that of the monomer. This results in the DR cross section of the dimer becoming comparable to that of the monomer around 0.2 eV. The DE cross section of the dimer is observable as soon as the energy is high enough for the N-N bond to break. The DE rate is comparable to the DR rate at the same energies. (b) The reduced DR cross section, $E_c \cdot \sigma_{DR}$, of $(NO)_2^+$ and NO^+. Note that both axes are on a linear scale. The cross section of the monomer shows an energy dependence that is roughly $1/E_c$, whereas that of the dimer shows a much faster decrease upon increasing collision energy.

the data in the form of a reduced cross section, which is the energy-dependent cross section multiplied with the collision energy. Figure 6.2(b) shows this reduced DR cross section on a linear scale, both in energy and in reduced cross section. A constant value would imply a $1/E_c$ behaviour of the cross section. However, as can be observed, the energy dependence in the cross section of the dimer is much steeper than $1/E_c$. After accounting for the 2 meV collision-energy resolution in our experiment, the dependence is determined to be $\sigma_{DR} \sim E_c^{-1.4}$. In Fig. 6.2(b), the beginning of an increase around 1 eV can be observed, which may be related to a secondary maximum in the cross section. Figure 6.2(a) shows that at this maximum the cross section approaches values that are again consistent with the $\sigma \sim E_c^{-1.4}$ behaviour, whereas the intermediate values have a lower cross section. This behaviour is similar to that observed in the DR cross section of the NO-monomer [see Fig. 6.2(a)], where a secondary maximum is observed around 5 eV. Finally, Fig. 6.2(a) also shows the DE cross section of $ONNO^+ \rightarrow NO^+ + NO$. The DE signal is observed as soon as the collision energy is high enough to break the N-N bond (0.6 eV). The DE curve is consistent with the fact that the $(NO)_2^+$ is not hot or contains metastable isomers with small binding energies. The intensity and the trend of the DE cross section is comparable to that of the DR cross section at the same energies. In fact, the NO monomer and the NO dimer share a feature which may be coincidental. In the monomer, one finds an increase in the DR rate around 13 eV, where also the DE rate has its first onset (see Fig. 6 in Ref. [[51]]). The increase for the dimer ion below one eV also coincides with the onset of the DE signal, in accord with the idea that both DE and DR often proceed through the same capture states.

6.4 Chemical Branching Fractions at 0 eV

The measured fragment-energy spectrum of the DR signal at 0-eV collisions is shown in Fig. 6.3(a). The background contribution was measured with the electrons turned off =and subtracted from the total signal after normalisation. The DR spectrum shows four broad peaks containing DR events, of which 1, 2, 3 or 4 of the atoms passed through the grid. These broad peaks actually consist of more than one mass contribution. For example, the first peak corresponds to a combination of mass 14 (N) and 16 (O) respectively, while the second peak corresponds to some fragment combination of mass 28 (N_2 or N+N), 30 (NO or N+O), and 32 (O_2 or O+O). A separate experiment was carried out where NO^+ was stored in the ring at the same kinetic energy per a.m.u. as used in the $(NO)_2^+$ experiment. The purpose of this experiment was to determine the shape and width of the peak resulting from mass-30 fragments to determine its contribution in the $(NO)_2^+$ energy spectrum. The observed NO^+ energy distribution is shown in Fig. 6.3(b), where the second peak corresponds to mass 30 only. A detailed comparison between the spectra in Figs. 6.3(a) and (b) shows that the second peak in Fig. 6.3(a) can almost fully (to 95%) be explained by a combination of NO and O + N fragments. This indicates that the fragment contribution of mass 28 and 32 (N_2, N + N, O_2, and O + O) to the second peak is small, and the branching fractions for Eqs. (6.1a), (6.1d), and (6.1g) are low. The energy spectrum shown in Fig. 6.3(a) was fitted with a set of model distributions for the different masses. The model distributions for mass 28, 30, and 32 were assumed to all have the shape and width as observed for NO in Fig. 6.3(b). The contributions of the other masses were described by Gaussian distributions with the width treated as fitting parameter and the restriction that the overlapping Gaussians

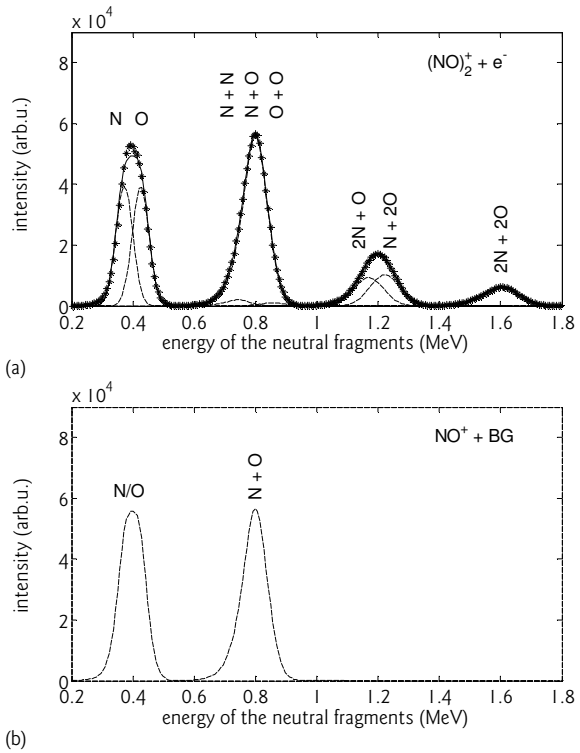

Figure 6.3: (a) The energy spectrum of neutral fragments formed in DR of $(NO)_2^+$ detected with a grid in front of the surface barrier detector. The experimental data (∗), the total fit to the experimental data (solid curve), and the transmitted fragment compositions resulting in the different peaks (dashed curves) are indicated. (b) The energy spectrum observed when NO^+ was stored in the ring at the same beam energy per atomic mass unit as used in the $(NO)_2^+$-cluster experiment.

have equal widths.

The number of counts in each mass contribution is used to determine the chemical branching fractions (see §6.2). The results obtained after solving the matrix equation and after normalisation are summarised in Table 6.1. The three-body break-up into NO + O + N dominates the chemical fragmentation with 69%. The two-body break-up into NO + NO is the second-largest fragmentation channel. The other fragmentation channels are small or not significantly present.

Table 6.1: The chemical branching fractions for the DR of $(NO)_2^+$ at a collision energy of 0 eV. The values are given with 95% confidence intervals.

channel	product fragments	chemical branching fraction
1a	$N_2 + O_2$	0.00 ± 0.04
1b	NO + NO	0.23 ± 0.02
1c	N_2O+ O	0.00 ± 0.04
1d	N_2 + O + O	0.02 ± 0.03
1e	NO_2 + N	0.03 ± 0.01
1f	NO + O + N	0.69 ± 0.01
1g	O_2 + N + N	0.03 ± 0.02

6.5 Physical Branching Behaviour at 0 eV

Using the fragment imaging system, we analysed only the 3-particle events, which are dominated by the NO + O + N channel, complemented with a small probability of N_2 + O + O, O_2 + N + N, and a small fraction of false events (see §6.2). All 3-particle events, after background subtraction from rest-gas collisions, were assumed to come from NO + O + N dissociations. For each event the fragment positions were recorded, which determine two of the three components of the fragment velocities originating from the kinetic energy released in the reaction. Each event on our detector provides the parameters shown in Fig. 6.4. The micro-channel plate detector cannot establish the fragment identities. The centre-of-mass (CM) is therefore undetermined and we use the centre-of-geometry (CG) instead. As we record projected values, we cannot deduce the physical branching for each event but have to draw conclusions based on observed distributions. For an unambiguous determination of the physical branching the KER associated to each event has to be known. To this end, the so-called total displacement (TD) is determined, which relates the observed positions and inter-fragment distances on the detector to the total 'projected' KER per event. TD distributions are used to extract the branching fractions. For the DR of $(NO)_2^+$ the TD is expressed as,

$$\mathrm{TD} = \sqrt{2 \cdot (d^2_{\mathrm{CG}-P_s} \cdot m_{NO}/m_{15} + d^2_{\mathrm{CG}-P_m} + d^2_{\mathrm{CG}-P_l})} \tag{6.3}$$

Here, m_{NO} and m_{15} stand for the mass of NO and O/N, respectively. The distances, $d_{\mathrm{CG}-P_s}$, $d_{\mathrm{CG}-P_m}$, and $d_{\mathrm{CG}-P_l}$ indicate the shortest, intermediate, and longest distance from the CG, respectively. The TD converges to an inter-fragment distance as in a diatomic dissociation when the particle P_s receives no kinetic energy [148]. As can be seen, the determination of the TD values does require an identification of the fragments. The TD is therefore based on the assumption that the NO fragment is closest to the CG, whereas the remaining fragments were assumed to be identical fragments of mass 15 instead of 16 (O) and 14 (N). We can check the consequence of incorrect identifications of fragments in the data analysis with the Monte-Carlo simulations.

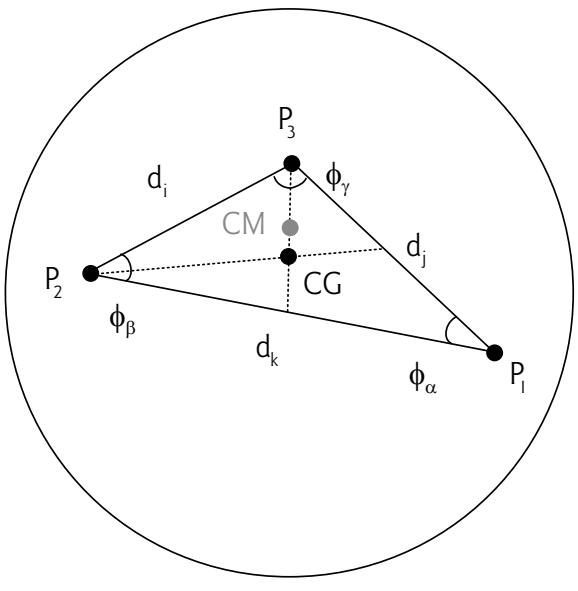

Figure 6.4: An example of the positions of the hits on the imaging detector in a 3-particle event is shown together with the imaginary triangle that can be drawn through these coordinates. The hits, labelled P_1, P_2, and P_3, do not identify the fragments. The centre-of-geometry (CG) is therefore calculated instead of the centre-of-mass (CM). The positions of the particles in the CG-frame relate to the kinetic-energy fraction of each fragment. In the analysis of all 3-particle events, the following parameters are calculated and investigated: the CG, the three projected inter-fragment distances (d_i, d_j, and d_k, and the three projected inter-fragment angles (ϕ_α, ϕ_β, and ϕ_γ). All parameters are sorted by size per event in order to investigate the parameters and their ratios on an event-by-event basis.

6.5.1 Analysis of the Dissociation Dynamics

In the following, we present our observations through the parameters illustrated in Fig. 6.4. In the next section, the observed spectra are recreated with a parameterisation of the dissociation process. Figures 6.5(a)−(d) show the parameter distributions using the measured events. Figure 6.5(a) shows the TD distribution as determined with Eq. (6.3). For reference purposes, an example distance distribution of a dissociating NO-monomer is included assuming similar storage-ring conditions (beam velocity, travel distance) and a KER value of 2.17 eV. If the NO fragment from the dimer ion would receive neither kinetic nor internal energy, the TD distribution of the NO + O + N limit would be exactly this distribution [see Eqs. (6.2a) and (6.3)]. Our TD distribution is clearly different with many more events at small TD values. However, the agreement of the position of the NO-monomer distribution with the shoulder of the TD distribution must be noted. Apparently, upon the DR of the dimer ion, the available energy is released by preference in kinetic energy. We will first deduce the shape of the TD distribution for a single KER-value and then we will reproduce the broad TD distribution using internal excitation of the NO fragment. Figure 6.5(b) shows all observed inter-fragment distance distributions derived from the 3-particle events (as shown in Fig. 6.4). The total distribution is shown together with the underlying distributions with the three distances sorted on length for each event. The long distance (d_l) distribution extends to large distances. The maxima in the short (d_s) and the intermediate (d_m) distance distributions are relatively close. Figure 6.5(c) shows the ratios between these inter-fragment distances determined on an event-by-event basis. Both the d_m/d_l and d_s/d_l distributions show a strong maximum at 0.5; the largest distance is often twice as large as the smaller ones. The above observations are consistent with NO receiving a small fraction of the KER while remaining in the middle. Fig. 6.5(c) shows a broad d_s/d_m distribution with a weak maximum around 0.87. The maximum agrees with a conservation of linear momentum between the oxygen and nitrogen atoms. The breadth of this distribution suggests that the dissociation mechanisms often result in a disproportionate kinetic energy distribution over the O and N atoms as a consequence of the presence of the NO fragment. Figure 6.5(d) shows the distributions over the observed inter-fragment angles in the detection plane (as shown in Fig. 6.4). Again, the angles are sorted by size for each event. The angular distributions show a preference for the large ϕ_l angles near 180 degrees and a preference for the intermediate ϕ_m and small ϕ_s angles near 0 degrees. Also this is consistent with a dissociation model in which one fragment, probably the NO fragment, is closest to the CG, receiving little kinetic energy in the dissociation process.

In Fig. 6.5 we discussed all events. We will now check the first impressions on the dissociation process derived from these data by selecting events with specific TD values. Events with TD values larger than 19 mm comprise events with large KER values that dissociate near-parallel to the detector plane. Selecting only these events produces the parameter distributions that are displayed as solid curves in Fig. 6.5. Note, that the d_l-distance distribution no longer has an overlap with the smaller distances, further supporting near-linear dissociation with the heavier NO in the middle. The angular distributions peak even more at very small or 180 degree inter-fragment angles. A next step was to divide the TD distribution in slices with different TD values to investigate the contribution of internally excited states. For each slice with smaller TD value, a contribution of events with smaller KER values is added. The TD division showed that upon decreasing TD, all d_s, d_m,

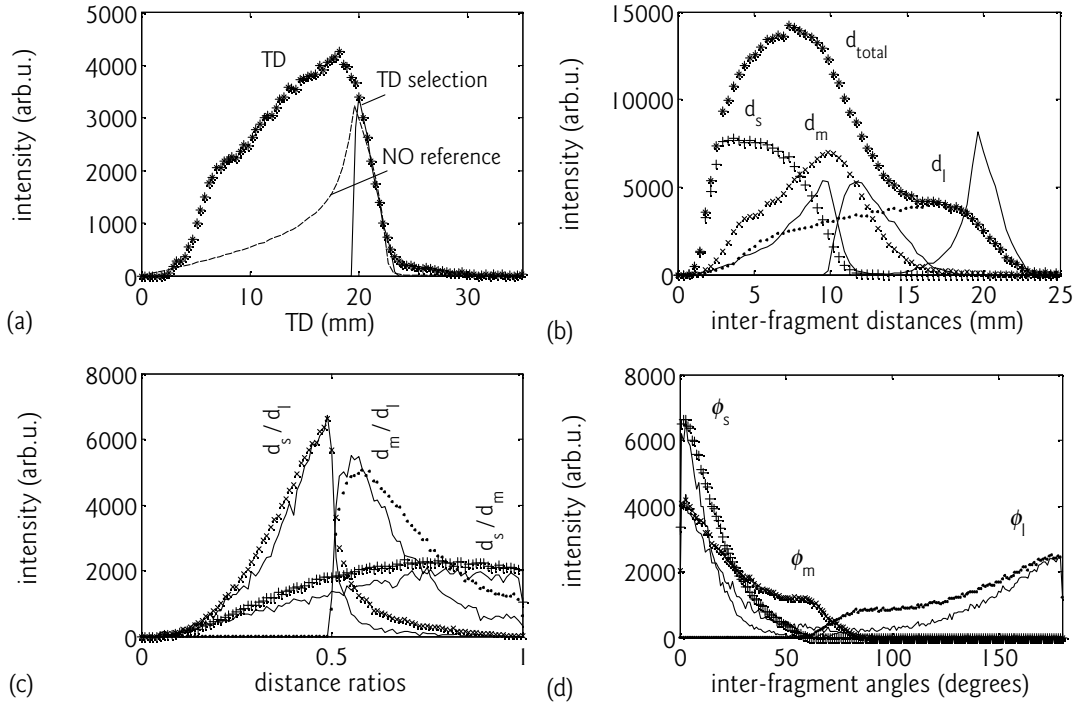

Figure 6.5: The parameter distributions as determined from the measured data. (a) The TD distribution (∗) together with a reference spectrum of NO^+-monomer ions dissociating with a KER of 2.17 eV (dashed curve) similar to the ground-state dissociation of the dimer ion [see Eq. (6.2a)]. The TD distribution is based on the assumption that the NO fragment is nearest to the CG. The TD selection (solid curve) corresponds to events of NO($v = 0$) dissociating near-parallel to the detector plane. (b) The total inter-fragment distance distribution (∗) and its underlying distributions, where for each event the distances, d_i with $i = s, m$, and l, are sorted on smallest (+), intermediate (×), and longest (·) distance, respectively. The solid curves are the sorted distance distributions associated with events from the TD selection and are scaled by a factor of 3. (c) The distributions of the ratios between the sorted distances, d_s/d_m (+), d_m/d_l (·), and d_s/d_l (×). The ratios are defined to range between 0 and 1. The solid curves are the sorted distance ratios associated with events from the TD selection and are scaled by a factor of 6. (d) The angular distributions sorted by size, ϕ_s (+), ϕ_m (×), and ϕ_l (·) for each event. The solid curves are the sorted angular distributions associated with events from the TD selection and are scaled by a factor of 5.

and d_l distances decrease approximately proportionally and the associated distance-ratio and angular distributions remained relatively the same. Apparently, the dissociation dynamics leading to vibrationally excited NO fragments are similar to the dynamics leading to the ground state.

6.5.2 Parameterisation of the Dissociation Dynamics

In the following we present the parameterisation of the dissociation dynamics using a Monte-Carlo simulation procedure. The aim was to minimise the differences between simulated and observed data with a minimum set of free parameters. This parameterisation is not a dissociation model in the sense that intramolecular properties of potential-energy surfaces of the dimer are invoked. The procedure is very similar to the one used for imaging studies of XH_2^+ ions in Stockholm [52, 53]. The simulation introduces the storage-ring experiment

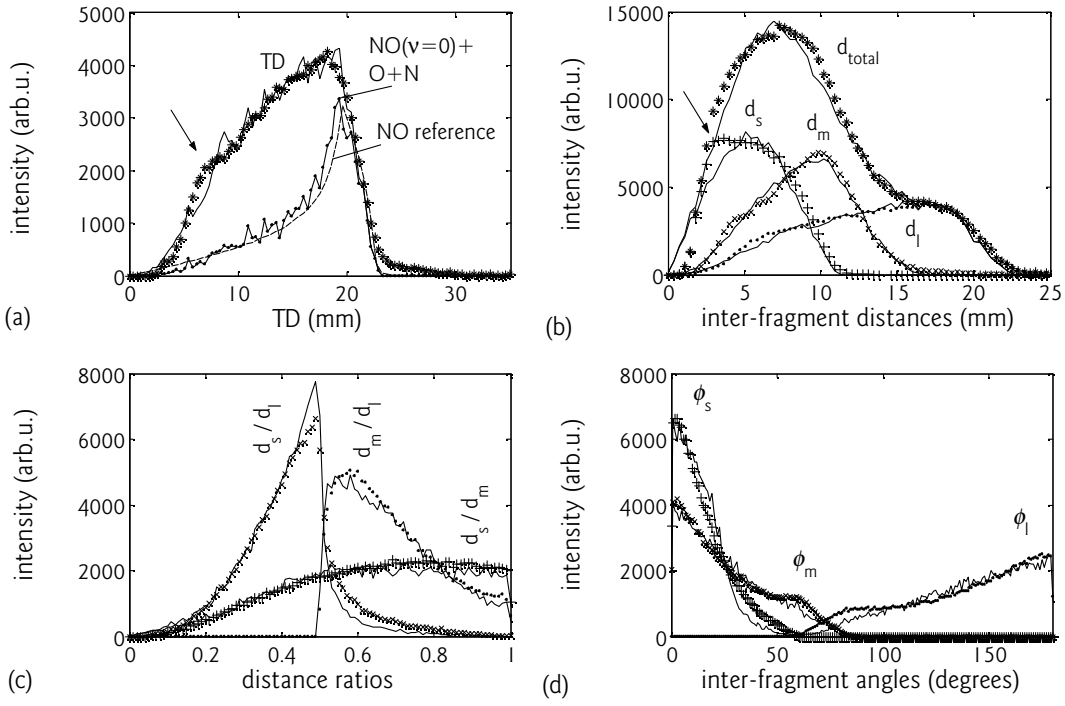

Figure 6.6: The simulation (solid curves) that best fit the measured data (stars). (a) The TD distributions together with the simulated contribution from the NO($v = 0$) + O + N fragmentation limit [see Eq. (6.2a)] and a reference spectrum of NO^+-monomer ions dissociating with 2.17 eV kinetic energy release. The arrow points at a possible indication of the opening of the NO($v = 0$) + O*(^1D) + N limit [see Eq. (6.2b)]. (b) The total distance and underlying d_s-, d_m-, and d_l-distance distributions. The arrow points at the d_s signal associated to the bump observed in the measured TD distribution. (c) The sorted distance ratios d_s/d_m, d_m/d_l, and d_s/d_l distributions. (d) The sorted ϕ_s, ϕ_m, and ϕ_l angular distributions.

taking the length of the interaction region, travel distance, beam velocity, and the toroidal effect into account. In a Monte-Carlo procedure dissociations are generated and distributed randomly over the interaction region with random orientations with respect to the beam axis. For each realisation, the total kinetic energy available, ε, is an input. The first free parameter is the angle, χ, formed by the asymptotic momenta of the O and N fragments with respect to the CM. The smaller this angle, the larger the recoil of the heavy NO fragment. The second parameter divides the remaining kinetic energy over the two light fragments and is specified by the parameter ρ, which is defined as $\rho = v_2^2/v_1^2$ such that $0 \leq \rho \leq 1$ with v_1 and v_2 the velocity vectors of the two light O and N atoms. These atoms were treated as identical particles of mass 15. Using distributions over the two free parameters, χ and ρ, the positions of the fragments on the detector were calculated for each event (see Fig. 6.4). The simulation procedure allows a direct comparison with the observed spectra as the Monte-Carlo procedure does take into account the misidentification of fragments. For example, the simulated TD distribution was determined based on the assumption that the NO fragment is the one closest to the CG. This proved to be the case in 80-95% of all events in our dissociation parameterisation.

The selection comprising of events with the largest TD values (> 19 mm) as shown in Fig. 6.5 (solid curves) was parameterised first. Subsequently, dissociation events giving

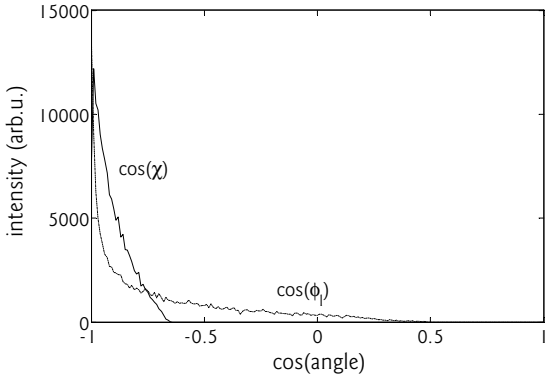

Figure 6.7: The total $\cos(\chi)$ (solid curve) and associated $\cos(\phi_l)$ (dashed curve) distributions as used in the simulation shown in Fig. 6.6. The ϕ_l angles are the $\angle$(O–NO–N) angles as would be measured on the detector, assuming NO is closest to the CG. The χ angles are in the range of $130-180°$ and the ϕ_l angles are in the range of $60-180°$.

internally excited NO product states were included, taking the observation into account that the dissociation dynamics leading to excited NO fragments are very similar to that leading to the ground state. The total kinetic energy in the simulation was decreased in steps of 250 meV, which is approximately the vibrational spacing in the NO-moiety. This simulated the production of NO fragments with internal energy. Figure 6.6 shows how in our best simulation all experimental data are reproduced. The presented simulation includes events ranging from maximum kinetic energy and no internal energy to no kinetic energy and maximum internal energy. For illustration, we show the contribution of NO($v = 0$) + O + N. Note that the distribution is strikingly identical to the reference NO-monomer distribution, which stands for two-particle dissociation dynamics.

The simulation reproducing optimally all observations resulted in the following conclusions. The dissociation dynamics does not depend on the NO internal energy. Furthermore, the angle, χ, peaks near 180 degrees. To get a feeling for the convoluting effect of our detector, Fig. 6.7 shows the cosine-distribution of χ together with that of the associated largest inter-fragment angles on the detector, ϕ_l. Additionally, we found it necessary to correlate the distribution of $\cos(\chi)$ with that of ρ. When χ is close to 180 degrees, $\rho = 1$. At smaller values of ρ, we allow for a broader range in values of $\cos(\chi)$. For example, a flat distribution in $\cos(\chi)$ for $\chi = 130-180°$ seems best in the case of $\rho = 0.3$. To summarise, we conclude that our data set is well described with dissociation events with the following properties. In linear dissociation events, conservation of linear momentum between O and N is observed, as if the NO is a spectator. With increasing kinetic energy of the NO fragments (smaller values of χ), the momenta of the O and N fragments are no longer correlated. It is tempting to conclude that the enhanced kinetic energy of the NO fragments is partially due to intramolecular elastic scattering process of one of the O/N fragments leaving initially with rather high recoil. Our findings agree with a picture in which the dissociation dynamics starts within one of the NO monomers.

Two questions are of interest at this point. First, do the derived dissociation dynamics imply large or small momentum correlations between the fragments? To answer this, we plot the parameterised dissociation behaviour in a so-called Dalitz plot [149], which has been used in various DR dissociation studies lately [150, 151]. This plot makes optimal use of the consequences of the momentum and energy conservation laws in the case of three-particle fragmentation. For a fixed KER, the dissociating systems can be described using only two coordinates, which are linear combinations of the energies of the fragments. These Dalitz coordinates are as follows,

$$Q_1 = \frac{\sqrt{M/m_{NO}}(E_2 - E_1)}{3\,\mathrm{KER}} \tag{6.4a}$$

$$Q_2 = \frac{(1 + m_{NO}/m_{15}) \cdot E_{NO} - E_2 - E_1}{3\,\mathrm{KER}} \tag{6.4b}$$

where m_{NO} and m_{15} are the masses of NO and the assumed identical O and N fragments, respectively, M is the total mass, and E_{NO}, E_2, and E_1 are the kinetic energies of the NO and the identical O and N particles of mass 15, respectively. The strengths of the Dalitz plot are the following. The plot is uniform when the momenta of the particles are fully uncorrelated only obeying momentum conservation. Further, each position in the plot reflects a specific asymptotic dissociation geometry (see Fig. 2 in Ref. [150]). Figure 6.8 presents two Dalitz plots. Figure 6.8(a) reflects the parameterised dissociation events. Clearly, a very small part of the allowed area is occupied pointing at highly correlated dissociation dynamics with an enhanced probability of linear dissociation leaving the NO fragments little kinetic energy. It is of interest to note that the parameters chosen to parameterise the dissociation dynamics, χ and ρ, do not generate a flat Dalitz plot, even if chosen randomly and uncorrelated. Figure 6.8(b) contains parameter plots in the case of random numbers for the two parameters. Although much more flat than found in our experiment, the resulting plot still reveals a non-flat phase space. The enhancement of probability at near-zero dissociation angles is a consequence of our choice to parameterise the angle of the light fragments with respect to the CM. The second question is whether the measured data set excludes other parameterisations of the dissociation dynamics? Although a quantitative answer to this question is difficult, already removing the correlation between the parameters in a simulation

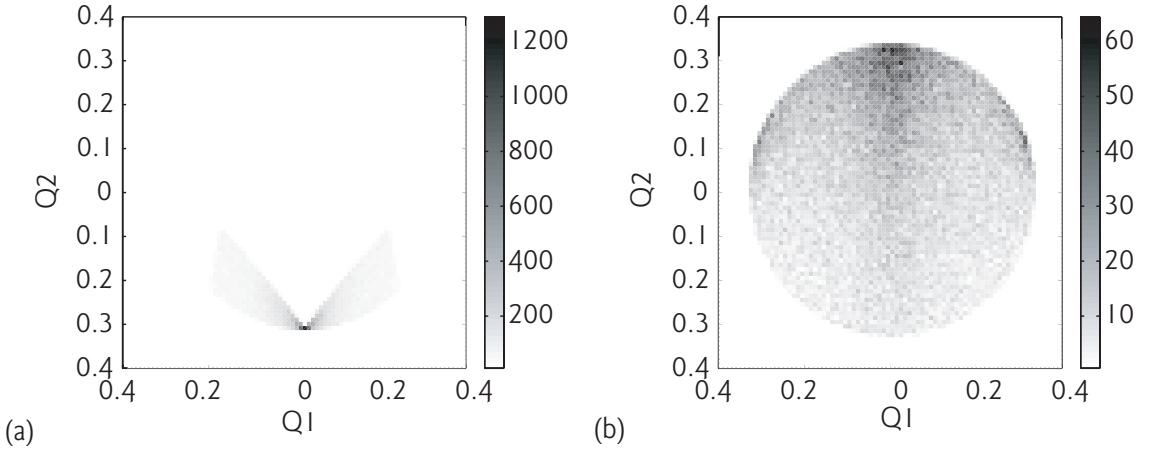

Figure 6.8: Dalitz plots for a fixed total energy, E, in the DR of $(NO)_2^+$. For all events, Q_1 and Q_2 as shown in Eqs. (6.4a) and (6.4b) are calculated. Conservation of momentum restricts all events to a circle. For $Q_1 = 0$ and $Q_2 = -0.4$ the events describe linear dissociation, O–NO–N. For $Q_1 = 0$ and $Q_2 = +0.4$ the events describe dissociation in which the O and N fragments recoil in the same direction. In case of uncorrelated dynamics or flat phase space, the resulting plot is flat, whereas correlation results in structure in the plot. (a) The Dalitz plot associated to the simulation shown in Fig. 6.6. An fixed KER value was chosen, since the dissociation dynamics for all internal energies of the NO fragment proved to be similar. The plot reveals significant correlation. (b) The Dalitz plot associated with the parameterisation in which the χ and ρ distributions are random and uncorrelated. This is close, but not equal, to completely uncorrelated dynamics.

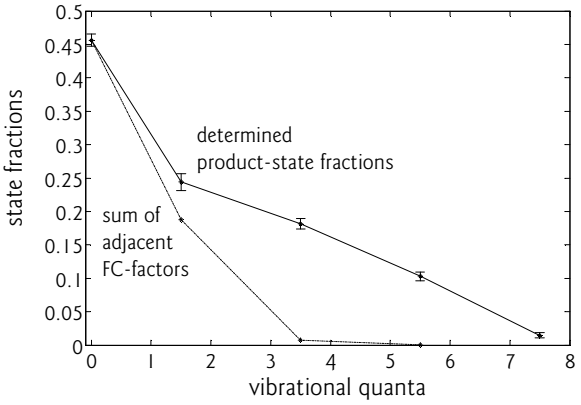

Figure 6.9: The internal-energy distribution as follows from simulations with slightly differing parameter sets of χ and ρ and with internal-energy increments of 500 meV, equivalent to two vibrational quanta (solid curve). The production of $v = 0$ and $v = 1 + 2$ shows resemblance with the Franck-Condon overlap between the NO-moiety in a $(NO)_2^+$ ion and a free NO, which accounts for the addition of two adjacent vibrational levels (dashed curve). The values used were $\omega_e(NO) = 1904\ cm^{-1}$, $r_e(NO) = 1.15$ Å for the free NO [152] and $\omega_e(NO^{1/2+}) = 2110\ cm^{-1}$, $r_e(NO^{1/2+}) = 1.11$ Å for the NO-moiety of the NOdimer ion [141].

reduces the agreement with the different parameter plots as in Figs. 6.5 and 6.6. Nature is benignant in this case as the high degree of correlation with in general a small fraction of the energy going to the NO fragment facilitates the correct interpretation of the observed events.

The simulations provide the product-state distribution of NO(v), since the energies needed to excite the light fragments, O and N, are much larger. We have estimated the error in the branching fractions from simulations with varying distributions of χ and ρ that still describe the measured data reasonably well. The obtained product-state distribution shown in Fig. 6.9 is the mean internal-state density determined from each fit to the TD distribution with the error being the standard deviation. Contrary to the above analysis, the total kinetic energy in these simulations was set to decrease in steps of roughly two vibrational quanta (500 meV). The smaller ($\Delta v = 1$)-step gave rise to some erratic changes in neighbouring state contributions, while the larger bin turned out to be quite stable. Figure 6.9 shows that the NO($v = 0$) limit is dominant. Additionally shown is the Franck-Condon overlap that we determined between the NO-moiety of a NO dimer ion and a free NO. These Franck-Condon factors are scaled to the simulated NO($v = 0$) product-state fraction and take the summation over adjacent vibrational levels into account. The Franck-Condon overlap predicts the minimum changes that are expected when a passive NO fragment goes from a bound NO-moiety to a free NO in a sudden process. Although this figure shows discrepancies, the model may be correct still. We note that the total fragment internal energy, vibration plus rotation in the simulation, is compared to the vibrational energy spacing via the Franck-Condon factors. If a fraction of the excess energy ends up in rotational energy, the product vibrational distribution would agree more with the Franck-Condon factor prediction.

Finally, we want to point out a few minor points. In Fig. 6.6(a), there is a small signal at TD values above 22 mm, which is too high to be accounted for by a KER of 2.17 eV. The analysis of these events yield random dissociation dynamics without much correlation. This signal might be due to the small contribution of $N_2 + O + O$ fragmentation, which can have a much higher KER, or to false three-body events. The $O_2 + N + N$ fragmentation channel can only contribute to TD values of around 13 mm or lower. Furthermore, a small bump near TD values of 4−5 mm (arrow) is located around the position where the physical branching channel, $NO + O^*(^1D) + N$, is to be expected if present. The same events give the extra signal in the measured d_s-distances indicated with an arrow [see Fig. 6.6(b)] that cannot be accounted for by the simulation when assuming similar dynamics as for the other branching channels.

6.6 Discussion

We have studied the energy-dependent cross section, the chemical fragmentation pathways, and the fragmentation dynamics of the NO-dimer cation. Two scientific questions interested us prior to the experiment. The first interest was to look into the surprisingly large thermal rates observed in weakly-bound dimer ions [135, 137]. The second interest was to find out whether the dissociation of the dimer ion could be approximated as the DR of $NO.NO^+$, where the NO^+ would dissociate and the NO moiety would act as a spectator.

The thermal rate coefficients of dimer ions are surprisingly high. The $(NO)_2^+$ thermal rate coefficient determined from our data is around $1.5 \cdot 10^{-6}$ cm^{-3}, in agreement with the thermal rate of $1.7 \cdot 10^{-6}$ cm^{-3} determined by Weller and Biondi [153]. This rate is roughly a factor of 4 higher than that of the monomer, which is about $4 \cdot 10^{-7}$ cm^{-3}at 300 K [51]. The thermal rates of O_2^+ and $O_2.O_2^+$ even differ with a factor of 20 [135]. The high efficiency of the DR reaction in dimer ions is referred to as super-DR. A mechanism for this super-DR proposed by Bates [136, 137] points at the consequence of potential-energy curves that cross with relatively small slopes. This increases the Franck-Condon overlap locally but not necessarily at low collision energy only. Our measurement gives a cross-section dependence of $\sigma_{DR} \sim E_c^{-1.4}$, which is steeper than for the monomer ion. As a consequence, the cross section of the dimer becomes comparable to that of the monomer already at 0.2 eV. A strong energy dependence is also observed in the DR of the proton-bridged $D_5O_2^+$ cluster ion [154]. Comparing the latter cross section to that of the DR of H_2O^+ reported by Jensen *et al.* [155] reveals a similar behaviour; the cross sections are similar at 0.2 eV, while near 0 eV they differ a factor of 10. As far as we know, no cross sections of other weakly-bound dimer ions have been measured as function of collision energy. The present observations may point at the importance of a high density of low-energy rovibrational states in the recombining system, promoting the capture efficiency or slowing the autoionisation of the intermediate excited $(NO)_2^*$. Also, as Bates remarked, the DR of weakly-bound dimer ions allows formation of Rydberg state fragments at low-energy electron collisions [136]. If this mechanism would be responsible for the high DR rates, than the dimer bond has to be very important in the DR reaction. Also in this case it is not clear why the high DR rate is restricted to the first 200 meV.

The chemical fragmentation study gave the interesting result that only two channels were represented (apart from a very small contribution of a third channel), while there are in total 7 fragmentation channels energetically possible. The three-body channel NO + O + N is dominant with a branching fraction of 69%. The next dominant channel is the two-body channel NO + NO with a branching fraction of 23%. The dominance of the three-body channel is consistent with studies of the DR of other polyatomic ions, in which the dominant fragmentation often is the three-body break-up. However, there is an important difference. In systems with equivalent covalent bonds and lighter atoms as in XH_2, the DR process seems to be nearly a statistical process. Indications for this exist both in the chemical fragmentation in the ratios, X + H_2 versus XH + H, and in the three-body dissociation dynamics. It was concluded that the DR generates doubly excited states that are repulsive in more than one coordinate [52, 53]. In these systems, it has been shown that strong repulsive forces are accompanied by large torques that allow for considerable rearrangements. In the present system, the three-body dissociations may well be a consequence of repulsion in one coordinate (N...O) with the weak dimer bond unable to bind both atomic fragments. In

this system, the special situation exists that the dominant channel for the monomer forming $O(^3P) + N^*(^2D)$ is energetically closed for the dimer ion. If the system depends on a repulsive curve leading to this channel, it finds itself a bound system, which will undoubtedly affect the final outcome. Due to the low signal-to-noise ratio, we have not been able to study the chemical branching nor the dissociation dynamics of $(NO)_2^+$ near 0.21 eV, which is the energy required to dissociate towards $O(^3P) + N^*(^2D)$. If this channel would also be dominant, the three-body branching may even further increase at this energy.

The dynamics of the three-body break-up into NO + O + N reveals that the NO fragment can largely be considered as a passive spectator in the DR process. The vibrational ground state of the NO fragment is dominant and accounts for at least 45% of the dissociations, depending on the fraction of rotational energy imparted in the NO. Channels leading to internal excitation of the NO up to two vibrational quanta account for 69%. We find that the internal energy of the NO has little influence on the dissociation dynamics. However, the NO fragment is not fully passive as the energy partitioning over the O and N product atoms is correlated to the fragment dissociation angle. As the NO fragment receives less kinetic energy, the linear momentum between the O and N atoms is increasingly obeyed and the $(NO)_2^+$ dissociates increasingly as a linear system with angles close to 180°. In view of the present research on $(NO)_2^+$, it would be of interest to study the DR of O_4^+ for several reasons; it is a weakly-bound system directly comparable to $(NO)_2^+$, the analysis and identification is simplified due to equal fragments and masses in the fragmentation and the possible three-body dissociations, the dynamics of the monomer have been intensely investigated, the dominant physical branching channels of the monomer are also allowed for the dimer ion, and it has direct atmospheric relevance. A previous storage-ring experiment on O_4^+ failed due to insufficient current production.

6.7 Conclusions

The DR cross section of the $(NO)_2^+$ is an order of magnitude higher than its monomer counterpart at low energies. Nonetheless this cross section drops more steeply upon increasing collision energy than that of the monomer, resulting in comparable rates above 0.2 eV. This has large implications on the validity of the super-DR theorem suggested by Bates for dimer ions [136, 137]. The $(NO)_2^+$ breaks up into mainly two channels, the NO + O + N (69%) and the NO + NO (23%) channel. The three-body break-up is dominant as is seen in the DR of many polyatomic ions. The DR of $(NO)_2^+$ into NO + O + N certainly has characteristics of a mechanism in which the recoil in the DR process is along one of the NO-bonds. This forms the first detailed study into the DR mechanisms operating in weakly-bound clusters. It is important to gather data on other systems in order to distinguish trends. Experimentally, we approach the limit of what is possible with the presently used imaging technology. Further detector development that combine high detection efficiency with fragment identification would give real progress.

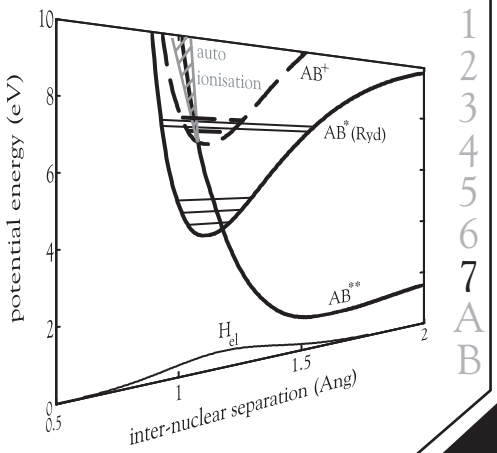

Physics is...

all about perspective

Annemieke

Chapter 7

Computational Study of Dissociative Recombination

This chapter presents model calculations performed on the dissociative recombination reaction of O_2^+. These calculations are concentrated on the effects of couplings between the doubly excited capture states on one hand and the n=3 to n=8 Rydberg states on the other hand; the Rydberg-valence couplings. Our model combines electron capture, autoionisation, and dissociation, the rates of which all depend on a single parameter. The electron capture is taken from literature, the autoionisation involving the doubly excited capture state is introduced through a local complex potential, and the dissociation and mixing between valence and Rydberg states is treated exactly by solving the coupled equations for the nuclear motion in a diabatic basis. We find that large Rydberg-valence couplings significantly reduce the dissociative recombination reaction. Comparison with experiment is only qualitatively possible.

7.1 Dissociative Recombination Mechanisms

Dissociative recombination (DR) has been described in this thesis predominantly from an experimental perspective. In this chapter, we introduce a model that should clarify consequences of mechanisms that are invoked by theoreticians to describe DR. Our model does not provide a full solution of the Schrödinger equation for this problem, but contains certainly relevant aspects of the process. We borrow heavily from the results of more complete calculations that provide potential-energy curves, electron-capture widths, and coupling strengths necessary in the dynamics calculations presented here.

DR is an important process in those situations, in which both low-energy electrons and positively charged molecular ions are present, such as in planetary atmospheres and plasmas. The very high recombination rate between low-energy electrons and molecular ions is the reason that DR is such an important reaction. Electron recombination with atomic ions is slower by a few orders of magnitude; atoms cannot dissociate and electron capture is nearly always followed by autoionisation. In other words, the presence of a dissociation continuum in molecular ions is very relevant for the success of DR. This dissociation continuum allows the systems to remain neutral, since it provides a pathway for the doubly excited neutral molecule to escape the region of small inter-nuclear separations, where autoionisation would occur.

One often distinguishes three mechanisms in the DR process: the direct (1), indirect (2), and non-crossing (3) mechanisms. Figure 7.1 provides an illustration of these mechanisms for a diatomic ion and Eq. (7.1) summarises the different pathways towards dissociation for a molecular ion in general,

$$\mathrm{M}^+(\mathrm{n},v,J)+e^-(E_c)\rightarrow\left\{\begin{array}{l}(1)\ \mathrm{M}^{**}\\(2)\ \mathrm{M}^{*}(\mathrm{Ryd})\rightarrow\mathrm{M}^{**}\\(3)\ \mathrm{M}^{*}(\mathrm{Ryd\ continuum})\end{array}\right\}\rightarrow \mathrm{A}^{(*)}+B^{(*)}(+\mathrm{C}^{(*)})+\mathrm{KER}\quad(7.1)$$

where the parent molecular ion, M^+, can be in any rovibronic initial state, indicated by n, v, and J, any amount of collision energy, E_c, can be added to the reaction through the electron energy, a star stands for a single electronic excitation, and the parentheses around the stars that are shown on the product side indicate the possibility of internal excitation. A description of the three mechanisms follows here.

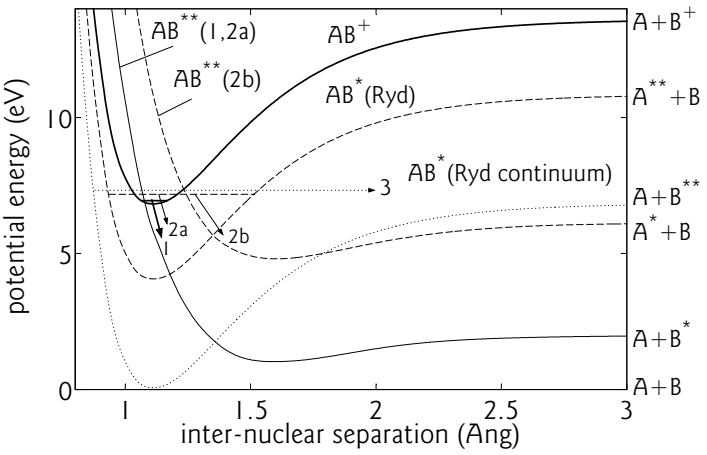

Figure 7.1: The three main DR mechanisms that are distinguished while treating the dissociative recombination reaction: the direct (1) and indirect (2) dissociations in the case of a favourable curve crossing and the non-crossing mechanism (3) when a curve crossing between a capture state and the ionic curve is absent. The labels are the same as used in Eq. (7.1). The description of the different pathways is explained in the text.

In the first and main mechanism (1), called *direct dissociation*, the incoming electron excites one of the electrons in the ion and a doubly excited valence-type state (M^{**}/AB^{**}) is formed. This state is nearly always strongly repulsive. The generation of the doubly excited state is a resonance phenomenon from the perspective of the incoming electron. The repulsive nature of the doubly excited product state ensures a rapid dissociation to neutral product atoms or product molecules. The nature of the products depends on the composition of the initial molecular ion. In the case of molecular oxygen, always two O atoms are formed in various excited states.

In the second mechanism (2), called *indirect dissociation*, a repulsive valence state is coupled to one of many Rydberg states of the same (or similar provided a coupling mechanism is present) symmetry, $M^*(\text{Ryd})/AB^*(\text{Ryd})$ (dashed curve). The coupling allows an intermediate Rydberg state to be formed in which only one electron is excited. The energy of the captured electron is partially converted into vibrational excitation. The formation of vibrationally excited resonances of the Rydberg state (represented by the dashed horizontal line) delays the dissociation and affects the DR cross section. As the whole system is still at an energy allowing for autoionisation, Rydberg resonances often cause local dips in the cross section. The dissociation process that necessarily has to take place involves re-coupling to the doubly excited valence state. In other words, doubly excited states are the doorway into producing the Rydberg resonances as well as the cause of predissociation of these resonances (2a). The indirect mechanism may also involve a direct formation process of a Rydberg resonance. The capture into a Rydberg state involves a coupling mechanism driven by the kinetic operator of the nuclei, an explicit example of the breakdown of the Born-Oppenheimer approximation. In many treatments of the dissociative recombination process, this channel is neglected as the kinetic operator is assumed to be rather ineffective. In the absence of an accessible doubly excited state, direct Rydberg-state formation may become important as it can open up dissociation channels that are otherwise inaccessible. For example in Figure 7.1 the pathway labelled AB^{**}(2b) can only be reached because of intermediate capture in the Rydberg state, which lengthens the inter-nuclear bond.

A third mechanism (3) involves a direct capture in the dissociation continuum of a neutral singly excited Rydberg state (dotted curve). This mechanism also involves the kinetic energy operator, in contrast to the two mechanisms mentioned above in which an electronic coupling mechanism mixes the electron continuum with bound character. The third mechanism is related to the *tunnelling mechanism* introduced by Bates [156], but is known as DR without a

curve crossing. This mechanism is often less efficient and is accompanied with smaller cross sections. Nevertheless, it is very relevant in systems that possess no doubly excited valence states that cross near the initial ionic state, such as HeH^+ and He_2^+ [131, 157].

Theories have become much more refined over the last decades, often in response to experimental observations. The finite DR rate of HeH^+ resulted in the DR mechanism without a curve crossing [131, 157]. The DR rate of H_3^+ has attracted enormous theoretical attention because of the astrophysical importance of H_3^+ and because the fact that merged beam and some flowing afterglow experiments produced DR rates that differed considerably for ill-understood reasons. The observation of the green airglow, ascribed to $O(^1S)$ atoms from the DR process, led Guberman into exploring spin-orbit coupling as a means to switch between one valence state to another valence state mediated by a Rydberg-state resonance [68]. Calculations of DR involve the identification of doubly excited states that share the following two characteristics. The initial ionic state and the neutral doubly excited state must have a sufficiently large overlap and the electronic character of the doubly excited neutral state has to be such that the electron-capture efficiency is sufficiently large.

Although theory has made impressive progress, surprises remain. The observed DR rates and hence also the cross sections are remarkable insensitive to molecular detail, in apparent contrast to the enormous variation in wave-function overlap upon small shifts of the potential curves involved and to the large range in capture efficiencies being calculated. Additionally and not unimportantly, the experiment presented in Chapter 4 reveals contradictions between the observed and calculated anisotropy of the DR fragments, whereas the arguments regarding the anisotropy are based on symmetry principles. Finally, observations reveal that, in many cases, all possible combinations of internally excited atomic fragments are in fact observed, provided that they are energetically possible and allowed according to spin-conservation rules. These observations suggest that DR has contributions from many capture states and that the efficiencies of various states are comparable. Again, this is in surprising contrast to the assumed sensitivity of the capture efficiency to the molecular details. Unfortunately, very few complete calculations exist to date that predict the full branching behaviour over all allowed dissociation channels from first principles. Although not impossible, full *ab initio* calculations on this process are just computationally very costly.

In the following, we will sketch a number of theoretical methods that have been developed over the last decades to treat the DR process. Thereafter, we present our computational model. Our results describe different aspects of the DR process, where we use as many known parameters of the molecular oxygen reaction as possible.

7.2 Theoretical Background

Historically, Bates was the first to suggest that molecular ions may be efficient in removing thermal electrons in dissociative collisions [17]. Prior to this date, this process was considered impossible because of concepts related to the Born-Oppenheimer approximation, which turned out to be incorrect. In this first short paper, the direct process was introduced. Bardsley introduced the indirect process in 1968 [158]. In the early eighties, a whole new series of papers appeared on these processes by theoreticians. An early paper by Giusti introduced the multichannel quantum defect (MQDT) theory in the description of the DR process [159] and O'Malley considered the role of Rydberg states [160]. The method of

quantum defect and MQDT was developed by Seaton and coworkers [161–163] and Fano and coworkers [164–167] in the sixties to the eighties. MQDT makes use of an important insight in the wave functions of colliding electrons. In simple terms, collisions between a free positive-energy electron and a molecular ion are similar in nature to the repetitive collision of a Rydberg electron (with a small binding energy and a large size classical orbit) with its molecular ion core. Thus, a stationary wave function can be divided in an outer region, where it experiences only the effective charge of the ion core, and an inner region where it samples the molecular structure. This scattering process with the core results in phase shifts that contain all the information needed to assess the dynamics for the complete Rydberg series and the collision of low-energy electrons. These phase shifts are expressed in the form of quantum defects, which describe level shifts. Jungen and coworkers have introduced this method in molecular photo-physics with large success [168–170]. The multichannel aspect of the theory stresses the fact that the quantum-defect principle allows one to combine processes as different as predissociation and autoionisation in one calculation.

In accord with the ideas of MQDT, the matrix elements involved in the capture of a free electron into a doubly excited valence state are intimately related with the interaction strength between this same valence state and the different molecular Rydberg states. Guberman explained this very clearly when deriving the capture width from the coupling strengths between the $^3\Pi_g$ valence and Rydberg states in molecular oxygen [80]. Nevertheless, even in the various MQDT treatments approximations are common, as a fully converged solution of the Schrödinger equation remains elusive. Often, the physics of the capture process and the physics of the dissociation process are implicitly performed in a perturbative manner. Giusti-Suzor, Bardsley and Derkits introduced the possibility to treat the dissociation dynamics more exact using configuration interaction [171]. In other treatments, it is not always clear to what extent the different aspects have been taken into account exactly or perturbatively. Only in the work of Takagi on molecular hydrogen, the impression is that the results converge to reality, reproducing the experimental situation [172]. What has been explained, sofar, pertains to the dynamic part of the calculations on DR. The input parameters that are essential for these calculations are the potential-energy curves or, in terms of MQDT, the quantum-defect curves as function of inter-nuclear separation. Potential curves are needed for many molecular symmetries and multiplicities, formally even 82 in the case of molecular oxygen. Also, many matrix elements are required that couple the electron continuum, the dissociation continuum, and the many quasi-bound states or closed channels in MQDT. These numbers are derived with computationally intensive quantum-chemical methods from which we make thankfully use in the present calculations. Our calculations would not have been possible without the insights gained from extensive calculations by Guberman on molecular oxygen and nitrogen using MQDT methods [82, 173, 174].

The perceived conflict between experimental observations on the DR process and consequences of the theoretical models formed the inspiration for the present computational approach. This work is not a complete treatment and, as mentioned, relies heavily on input from quantum-chemical calculations. In the present research, we concentrate on the effect of the Rydberg-valence (RV) couplings, not only on the dissociation process but indirectly on the capture process itself. As a large capture efficiency scales with a large RV coupling, a strong effect is expected on the dissociation dynamics and level structure in the dissociation continuum. Figure 7.2 shows this schematically. A strong RV coupling may change the nature of the products and may delay dissociation through the generation of quasi-bound res-

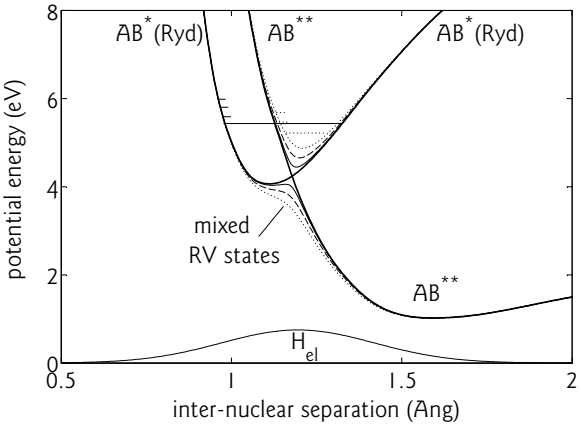

Figure 7.2: The effect of Rydberg-valence couplings on the the potential-energy curves. The thick curves are the diabatic representations of the Rydberg [AB^*(Ryd)] and the valence (AB^{**}) states. The thinner solid, dashed, and dotted curves are the adiabatic representations of the mixed Rydberg-valence states at coupling strengths, H_{el}, of 0.25, 0.5, and 0.75 eV, respectively. The upper mixed Rydberg-valence states give rise to quasi-bound vibrational levels at energy positions another than those of the unperturbed Rydberg state. H_{el} is represented by the thin solid line on the bottom, which has an intensity that varies according to the coupling strength.

onances in the dissociation continuum. A time-delay in dissociation increases autoionisation and hence changes the outcome of the DR process.

7.3 The Coupled-Channel Method

As explained in the previous section, we are interested in the consequence of the RV couplings on the outcome of the DR process in the case of molecular oxygen. For this reason, we have chosen a method that treats the dissociation dynamics exactly, i.e., in so far the states and couplings that we introduce in our calculation cover all relevant states. An exact solution of the dissociation process is offered by solving the Schrödinger equation using a coupled-channel approach. Lewis and coworkers have applied this method to understand the electron-scattering and photodissociation processes in molecular oxygen [175, 176]. These authors derived in their work highly accurate couplings between Rydberg and valence states by minimising the differences between observations and the outcome of their coupled-channel program. In the present calculations, we make use of these numbers. We have adapted the coupled-channel code using a discrete variable representation developed at the Radboud University in Nijmegen by Groenenboom for quantum scattering purposes [177]. This program solves the time-independent Schrödinger equation,

$$\mathbf{H}\,\mathbf{\Psi}(\mathrm{R},\mathbf{r}) = \mathrm{E}\,\mathbf{\Psi}(\mathrm{R},\mathbf{r}) \tag{7.2}$$

where $\mathbf{H}$ is the total Hamiltonian, $\mathbf{\Psi}$ is the total wave function, E is the total energy, R is the inter-nuclear separation, and $\mathbf{r}$ represents all electrons. The total wave function is written as the sum of products of the R-dependent coefficients, $\mathbf{u}_i(\mathrm{R})$, and the electronic wave functions, $\psi_i(\mathrm{r_i},\mathrm{R})$,

$$\mathbf{\Psi}(\mathrm{R},\mathbf{r}) = \sum_i \mathbf{u}_i(\mathrm{R})\psi_i(\mathrm{R},\mathrm{r_i}) \tag{7.3}$$

Equation (7.2) may be rewritten, after some manipulation and integration over the electronic degrees of freedom, into a set of coupled equations as function of the inter-nuclear separation. In matrix form, the equation reads,

$$\mathbf{U}''(\mathrm{R}) + \frac{2\mu}{\hbar^2}\left[\mathrm{E}\mathbf{I} - \mathbf{W}(\mathrm{R})\right]\mathbf{U} = 0 \tag{7.4}$$

where μ is the reduced mass of the system, **U** is the vector containing the radial wave functions, **U**$''$ is the vector containing all the second derivatives, **I** is the unity matrix, and **W** is the interaction matrix, for which the diagonal elements are the diabatic potential-energy curves and the off-diagonal elements are the various R-dependent electronic (or spin-orbit) couplings, H_{ij},

$$\mathbf{W} = \begin{pmatrix} V_{11} - i\,\Gamma_{11}/2 & H_{12} & H_{13} & \dots \\ H_{21} & V_{22} - i\,\Gamma_{22}/2 & H_{23} & \dots \\ H_{31} & H_{32} & V_{33} - i\,\Gamma_{33}/2 & \dots \\ \dots & \dots & \dots & \dots \end{pmatrix} \tag{7.5}$$

A complex potential is added to the diagonal, which ensures the possibility of loss of dissociation flux through the presence of autoionisation as competitive channel. The Γ's are the R-dependent autoionisation widths. The imaginary potential is only non-zero at inter-nuclear separations where the potential curve of the capture state is embedded in the ionisation continuum. In applying the complex potential we use the so-called local approximation: the rovibrational quantisation of the ion after the autoionisation process is ignored. In order to avoid first derivatives in the coupled equations, all potential curves are used in a diabatic representation. This implies that in a potential-energy diagram, curves of the same symmetry cross. At the crossing point, the states are no longer Eigenstates of the electronic Hamiltonian, giving rise to the off-diagonal electronic coupling matrix-elements. Figures 7.3(a) and 7.3(b) show how reality can be represented by two different potential-energy diagrams, using diabatic and adiabatic curves, respectively. Fig. 7.3(a) gives the 'natural' situation for very small RV coupling; a nearly unperturbed Rydberg state crosses the doubly excited valence state. In Fig. 7.3(b), the RV coupling is sufficiently strong that the 'adiabatic representation' is more natural, illustrating that the doubly excited character mixes with Rydberg character in forming a quasi-bound state that may only be slowly predissociated by the lower lying mixed RV state. We note that the situation in Fig. 7.3(b) is close to the situation in the case of the Schumann-Runge (SR) states of molecular oxygen. From photoabsorption experiments, it follows that the SR system consists of a strongly coupled pair of an n=3 Rydberg state and a valence state. In spectroscopy experiments, no Rydberg vibrational structure in this n=3 Rydberg state can be observed. In general, in a single state approximation, adiabatic and diabatic potential representations give different predictions. In a fully coupled-channel calculation, the final observables are independent of the chosen representation.

The coupled-channel equations are solved for a fixed total energy, which is the sum of the initial-state energy and the electron collision energy. The direct output is a matrix with linearly independent solutions, involving outgoing flux to the different coupled channels. The electron energy is varied by changing the total energy and repeating the calculation. The DR efficiency and branching behaviour are evaluated by calculating the overlap between the initial ionic state, which is determined in an independent calculation, and the relevant continuum states. In our case, we assume electron capture to take place only in one repulsive valence state. As will be seen below, we find that the DR efficiency decreases with increasing strength of the autoionisation. The efficiency, ϵ, is defined as the relative dissociation flux that is found in the calculation; the values are not normalised. The autoionisation process is connected to the electron-capture efficiency as the capture and autoionisation widths are one and the same number; in general physics terms, when the door is open for the electron

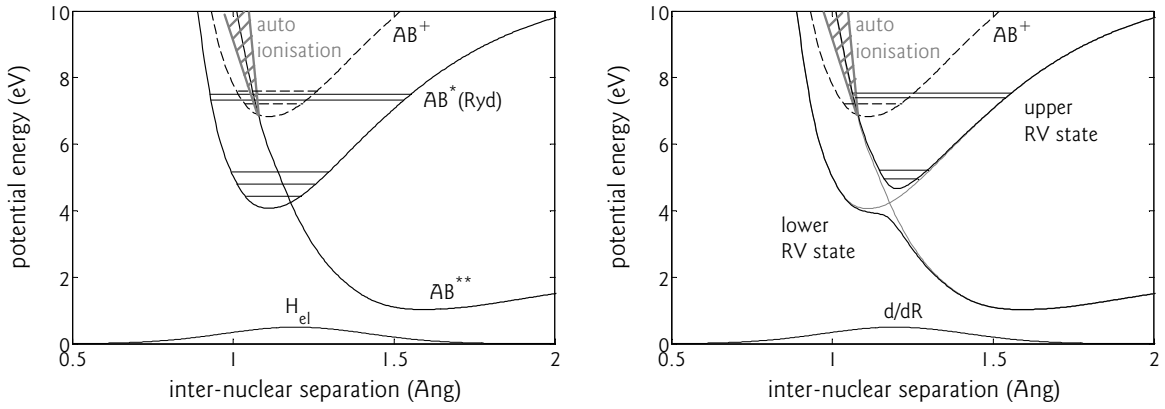

Figure 7.3: (a) The diabatic representation of a valence and a Rydberg state of the same symmetry (solid curves) together with the ionic state (dashed curve). A possible electronic coupling is represented by the thin solid line on the bottom, its value peaks at the crossing. In our calculations, the autoionisation is attached to the valence state as a complex potential, which is represented by the grey area. Additionally shown are a few vibrational levels of the ionic (dashed lines) and Rydberg (solid lines) states. (b) The adiabatic representation of the same potential curves at a RV coupling of 0.5 eV. Two mixed Rydberg-valence states (solid curves) result. The upper mixed state has a quasi-bound character, which introduces its own vibrational levels (solid lines) at other energy positions than the original Rydberg state. The thin solid line at the bottom now represent the d/dR derivative coupling as derived from the nuclear kinetic operator.

to leave, the same door ensures effective entrance. Hence, we estimate the relative DR cross sections by multiplying the DR efficiency with the autoionisation width in eV, $\sigma = \epsilon \cdot \Gamma$. In our calculations as function of electron collision energy, we do not introduce a factor to account for the $1/E_c$ threshold law related to the Coulomb interaction between ion and electron. We introduce three highly correlated quantities; the RV coupling for Rydberg state n, $H_{el}(n)$, the autoionisation width, Γ, and the electron-capture efficiency, also given by Γ. The relation between H_{el} and the capture width is taken from Guberman [80],

$$\Gamma = 2\pi(n^*)^3 H_{el}^2 \tag{7.6}$$

where n^* is the effective principal quantum number, $n^* = n - \delta$, with δ the quantum defect. In this equation, Γ scales with the electronic coupling squared. The estimate of the capture and autoionisation widths becomes more accurate when using the predissociation behaviour of higher-lying Rydberg states. Unfortunately, only values are known for H_{el} for n=3 and sometimes for n=4 Rydberg states. We derive best estimates for Γ from the n=3 values. Apart from test calculations, the above implies that the calculations are performed without any adaptable parameters.

7.4 Model Calculations on O_2^+

Our treatment is exact in the dissociation dynamics, but is approximate in the electron scattering process in the sense that we ignore the molecular structure of the ion after the autoionisation. As mentioned the autoionisation process is introduced through a complex potential added to the doubly excited state for those inter-nuclear distances where classically

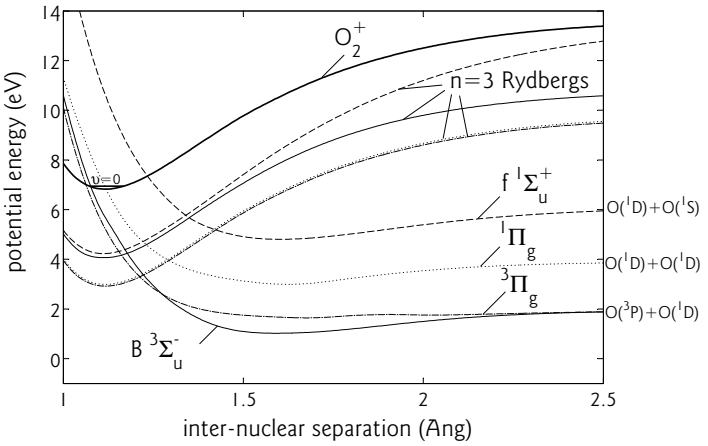

Figure 7.4: The potential-energy curves that are used in our coupled-channel calculations. Except for the f state (dashed), all valence curves cross near the ionic ground state. The $^{1,3}\Pi_g$ states (dash-dotted, dotted), however, are known to have small electron-capture widths. The RV coupling of the B state (solid) is particularly large, leaking dissociation flux via SO coupling between the respective Rydberg states to the f state.

autoionisation is possible. If the molecular system during the dissociation process enters the region where classically autoionisation is no longer possible, a DR event is a fact. The time between capture and reaching this point is the stabilisation time, τ_s, as introduced by Bates [17] (see also Giusti, 1980 [159]). The ratio of this stabilisation time and the autoionisation time, τ_a, determines the so-called survival factor. We will sometimes refer to these qualitative terms.

Calculations are performed on the following symmetries. The $B\,^3\Sigma_u^-$: the potential curves for the $B\,^3\Sigma_u^-$ symmetry, known as the upper state of the SR system, along with the couplings strengths (H_{el} = 0.5eV for n=3) and the quantum defect are taken from Lewis and coworkers [175, 178]. The $f\,^1\Sigma_u^+$: the potential curves, the quantum defect and the electronic, H_{el} = 0.19eV, as well as the spin-orbit $H_{so} = 92\text{cm}^{-1}$, couplings are again from Lewis and coworkers [175, 178]. The $^{1,3}\Pi_g$: the potential curves for these symmetries are adapted from Ref. [179] and the couplings, H_{el} = 55 meV for the $^1\Pi_g$ state and 79 meV for the $^3\Pi_g$ state, and the respective quantum defects are taken from Refs. [99, 180]. The electronic coupling is represented as a Gaussian function around the crossing points in order to avoid long range couplings. Γ(R) is constant at small inter-nuclear separation and goes to zero smoothly around the crossing of the valence state with the ionic curve to avoid spurious effects due to discontinuities in the differential equations. The diabatic potential curves and the associated dissociation limits are shown in Fig. 7.4.

In the following, we present a series of calculations in which the initial state is fixed at $O_2^+(v = 0)$. In the first series of calculations, we use a model system of one doubly excited state and one (n=3) Rydberg state. The relationship between the RV couplings and the electron-capture matrix-elements are ignored in order to look for the individual effects of these two quantities on the DR dynamics. We selected the molecular oxygen SR system for the reason that the couplings are well known and the state is considered to be one of the most important states in the DR process and responsible for the dominant $O(^3P)$ + $O(^1D)$ branching channel [80, 175, 176]. In the second series of calculations, the n=4 to n=8 Rydberg states are added to this model system and their influence on the effective DR cross section is determined for the true electronic-coupling and autoionisation strengths. The third series of calculations introduces the spin-orbit coupling between the SR and the $f\,^1\Sigma_u^+$ state as suggested by Guberman leading to the production of $O(^1S)$ atoms [68]. Here, the known coupling strengths are again used. Finally, the fourth series compares the cross sections of capture in different valence states, giving a first insight in branching behaviour. Here, we

added, for demonstration purposes, the states with $^{1,3}\Pi_g$ symmetry in our calculations, which also cross the ionic state near $v = 0$, but are generally believed not to contribute to the DR reaction due to the small electron-capture widths [174].

7.4.1 A Model involving One Valence and One Rydberg State

The following calculations have been performed by varying the electron collision energies between 0 and 500 meV, covering a few resonances. The capture takes place into the $B\,^3\Sigma_u^-$ valence state and the initial wave function is that of the O_2^+ vibrational ground state. We investigated the electron-energy-dependent efficiency, ϵ, and cross section, $\sigma = \epsilon \cdot \Gamma$, and the shape of their resonances in the following three situations. First, the RV coupling was varied between 0 and 1 eV with $\Gamma = 0$. Second, the autoionisation width was fixed at an intermediate value of $\Gamma = 200$ meV and again the effect of the RV coupling on the cross section and its resonances was investigated. Third, Γ was related to H_{el} using Eq. (7.6), while varying both quantities simultaneously, and fourth, for reference purposes, the latter calculation was repeated taking only the valence state, while varying Γ.

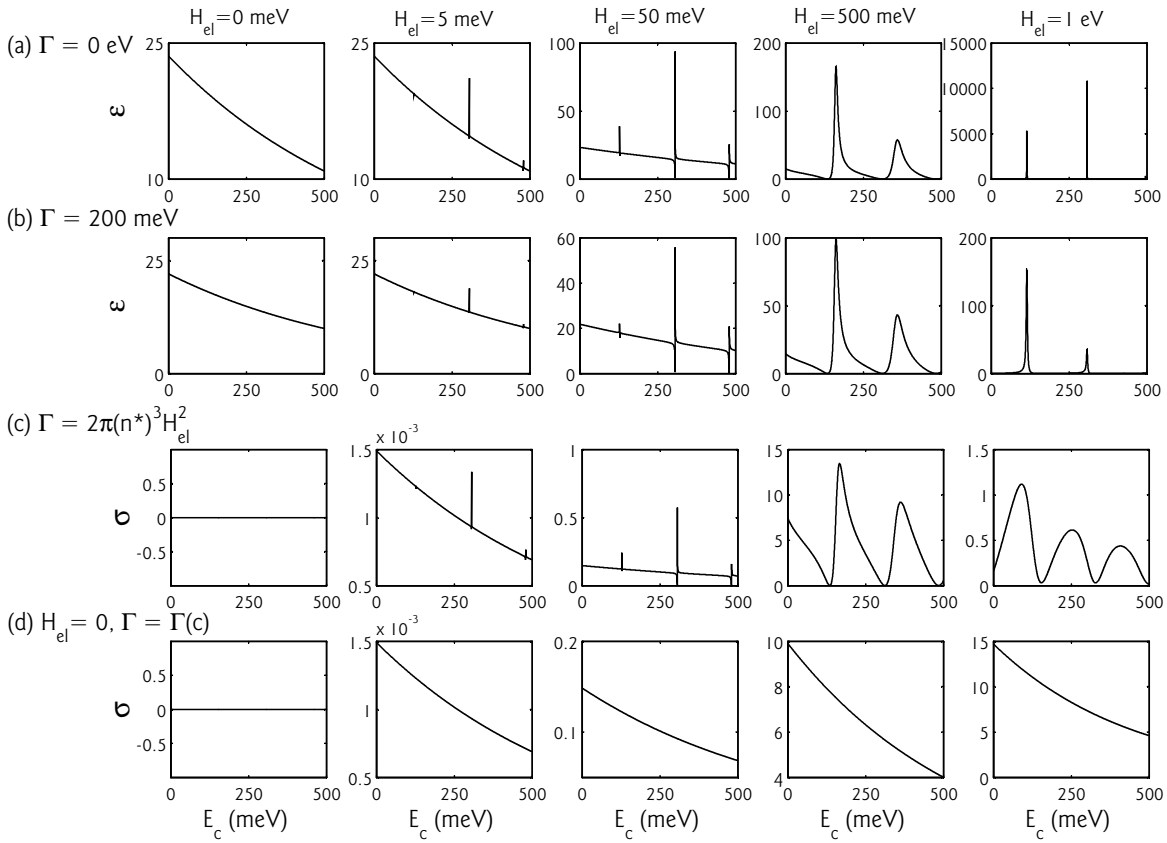

Figure 7.5: The calculated DR efficiency, ϵ, as function of collision energy for RV couplings of 0, 5, 50, 500, and 1000 meV, where Γ is set to (a) zero and (b) 200 meV. (c) The cross section, $\sigma = \epsilon \cdot \Gamma$, at the same RV-coupling strengths as before and with Γ according to Eq. (7.6). (d) The cross section, σ, at the same autoionisation values as (c), now excluding the RV coupling.

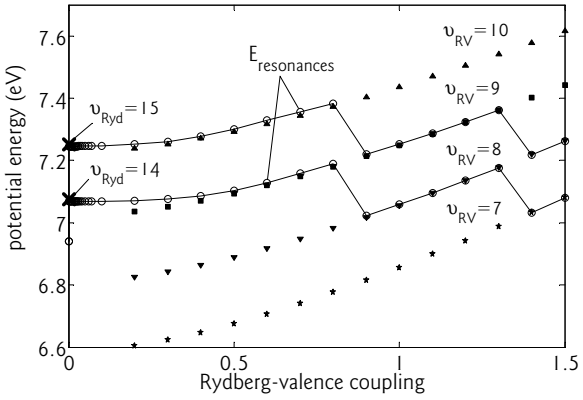

Figure 7.6: Comparison between the position of the resonances calculated at $\Gamma = 0$ eV and the vibrational levels of the quasi-bound mixed RV states on an absolute energy scale. The solid curves with the circles are the energy-positions of the cross-section resonances (see Fig. 7.5) for RV coupling strengths between 0 and 1.5 eV. For each coupling strength, the quasi-bound-RV vibrational levels that are found at comparable potential energies (see Fig. 7.3(b)) are shown: $v = 7(\bigstar), v = 8(\blacktriangledown), v = 9(\blacksquare), v = 10(\blacktriangle)$. At 0 eV coupling strength, the relevant vibrational levels of the pure Rydberg state are shown.

The Effect of Electronic Coupling at zero Autoionisation

Figure 7.5 shows the results for the $^3\Sigma_u^-$ states in which the DR efficiency is plotted against the electron collision energy. Figure 7.5(a) shows the results for zero autoionisation rate, $\Gamma = 0$ eV, while varying the RV coupling strengths, H_{el}. At $H_{el} = 0$ eV, the calculated electron collision-energy-dependent efficiencies, ϵ, decrease monotonically, revealing the change in overlap between the initial $O_2^+(v = 0)$ vibrational state and the dissociation continuum and illustrating the near optimal overlap in case of the SR state and the ionic ground state. Resonances appear upon an increase of the RV coupling. These resonances have a Fano-like profile. It has been noted before by Giusti-Suzor *et al.* that Fano-shape parameters are not easily interpreted in the case of DR [171]. The occurrence of Fano profiles are not a surprise in a process in which the continuum interferes with quasi-bound Rydberg resonances. Figure 7.5(a) also reveals changes for larger values of the RV coupling. A continuous DR efficiency spectrum with resonances changes in an energy-dependent cross section that is everywhere nearly zero apart from a few strong resonances also having Fano profiles. Further insight can be obtained by looking at (I) the positions of the resonances in comparison with bound states calculated in the Rydberg state or in the mixed adiabatic upper RV states [see Figs. 7.3(a) and 7.3(b)], (II) the width of these resonances, and (III) the mean efficiency or cross section over the collision-energy range to judge the effect on the total efficiency.

Here, we present our observations concerning the three features mentioned above. (I) The positions of the cross-section resonances are shown on an absolute energy-scale as function of RV coupling in Figure 7.6. The energy positions at small RV coupling agree with the $v = 14$ and $v = 15$ levels of the n=3 Rydberg state. The spacing between the resonances increases initially, as the long-lived resonances move over to the mixed-RV well. At even higher values of the RV coupling, the mixed state deforms and the spacing becomes smaller again. The saw-tooth behaviour of the absolute positions is due to our fixed and limited collision-energy range. The symbols show the positions of Eigenstates in the mixed RV states, identifying the resonances that are found in the coupled-channel calculations. (II) The width of the resonances also has a characteristic behaviour [see Fig. 7.5(a)]; it is initially very narrow, then widens in the region of intermediate mixing, and ends in narrow resonances again in the mixed RV state. (III) The mean efficiency over the electron-energy range is largely independent of the strength of the RV coupling, indicating that at a fixed and very small autoionisation widths, the total efficiency simply redistributes itself over the range of collision energies.

The Effect of Electronic Coupling at finite Autoionisation

Figure 7.5(b) is similar to Fig. 7.5(a), with the difference that the value for Γ has been increased to 200 meV, which according to Eq. (7.6) is associated with $H_{el} = 90$ meV for the n=3 ($n^* = 2.2$) RV coupling. The autoionisation decreases the efficiency, as expected. The decrease in ϵ is small at low RV-coupling strengths and becomes larger at the high values. This decrease at small H_{el} can be understood from the associated dissociation and autoionisation times. Regarding the position and width of the resonances and the mean efficiency, the following observations are noted. (I) Very unexpectedly, the energy spacing between the resonances remains constant for the first values of H_{el}. The energy positions agree with the positions of the $v = 14$ and $v = 15$ levels in the unperturbed n=3 Rydberg state. In general, we find that the higher the autoionisation rate, the more the positions of the resonances remain at the unperturbed vibrational Rydberg-state levels. Apparently, autoionisation from the inner limb of the mixed RV state reduces the manifestation of the vibrational levels of the quasi-bound RV states. (II) The introduction of autoionisation also increases the width of the resonances, especially at larger values of H_{el}, where autoionisation is important for the decay. The latter observation is not a surprise as only the repulsive valence state may autoionise in our calculation and the mixed RV resonances will have significant valence state character. (III) For this small constant value of Γ, the total efficiency still is nearly constant.

Electronic Coupling and Autoionisation Related

Figure 7.5(c) displays the electron-energy-dependent cross section from calculations in which the RV coupling and the autoionisation width are correlated as given in Eq. (7.6), using $n^* = 2.2$, which is determined with the n=3 Rydberg state. As can be observed, the shape of the cross section changes when Γ becomes larger than 200 meV ($H_{el} = 0.5$ eV). At these high coupling strengths, H_{el}, the cross section decreases steeply. Figure 7.5(d)shows the results of the calculation varying the value of Γ under the exclusion of the RV coupling. Here the DR cross section are much larger at larger values of H_{el}.

Figure 7.7 shows the mean electron-energy-dependent cross section, σ_m, for these two calculations. The initial increase of the total cross section reflects the increase in capture efficiency, as the autoionisation width is too small to compete effectively with the molecular dissociation process. At larger values, the RV couplings become effective and a significant effect is seen when ignoring the Rydberg state. The resonances and the autoionisation effects

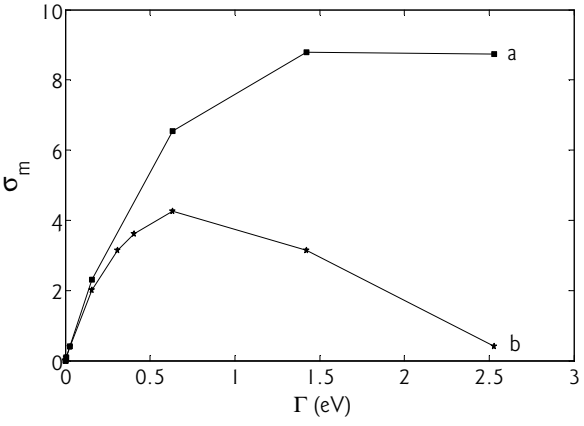

Figure 7.7: The mean cross section, σ_m, as a function of capture width, where Γ varies according to Eq. (7.6). This cross section is the mean value over the collision-energy range of 0–500 meV at the different Γ values. Curve (a) presents the mean cross section for the valence state only, and curve (b) shows the situation in which the valence state interacts with the n=3 Rydberg state, revealing a maximum around $\Gamma = 0.6$ eV.

conspire to reduce the total cross section. Thus, the enhanced autoionisation reduces the survival fraction, while, the enhanced RV coupling causes resonance structure with longer delay times (increasing τ_s). The peak in the mean DR cross section is found at values of the capture width around that of the $B\,^3\Sigma_u^-$ state. Hence, in the present model calculations, the properties of this state is such that the $B\,^3\Sigma_u^-$ still forms an effective DR channel.

We believe that insights are to be gained from the results presented above. The fact that RV interactions are connected to the electron capture and autoionisation process affects the efficiency of the DR process through the creation of a quasi-bound vibrational structure in the capture continuum. In the following we study whether these effects on the total cross section will remain when the number of Rydberg states is increased until no further changes are observed in the cross section.

7.4.2 Adding More Rydberg States

Figure 7.8 shows in different panels the electron-energy-dependent cross sections for n=3 up to n=3−8 Rydberg states, each time adding one more Rydberg state. The diabatic $^3\Sigma_u^-$ potential curves are chosen as input in the calculations. The n=3 and n=4 Rydberg states are from Lewis [178]. The higher-lying Rydberg states are shifted versions of the n=4 Rydberg state, making use of the quantum defect. The coupling strength associated to the Nth

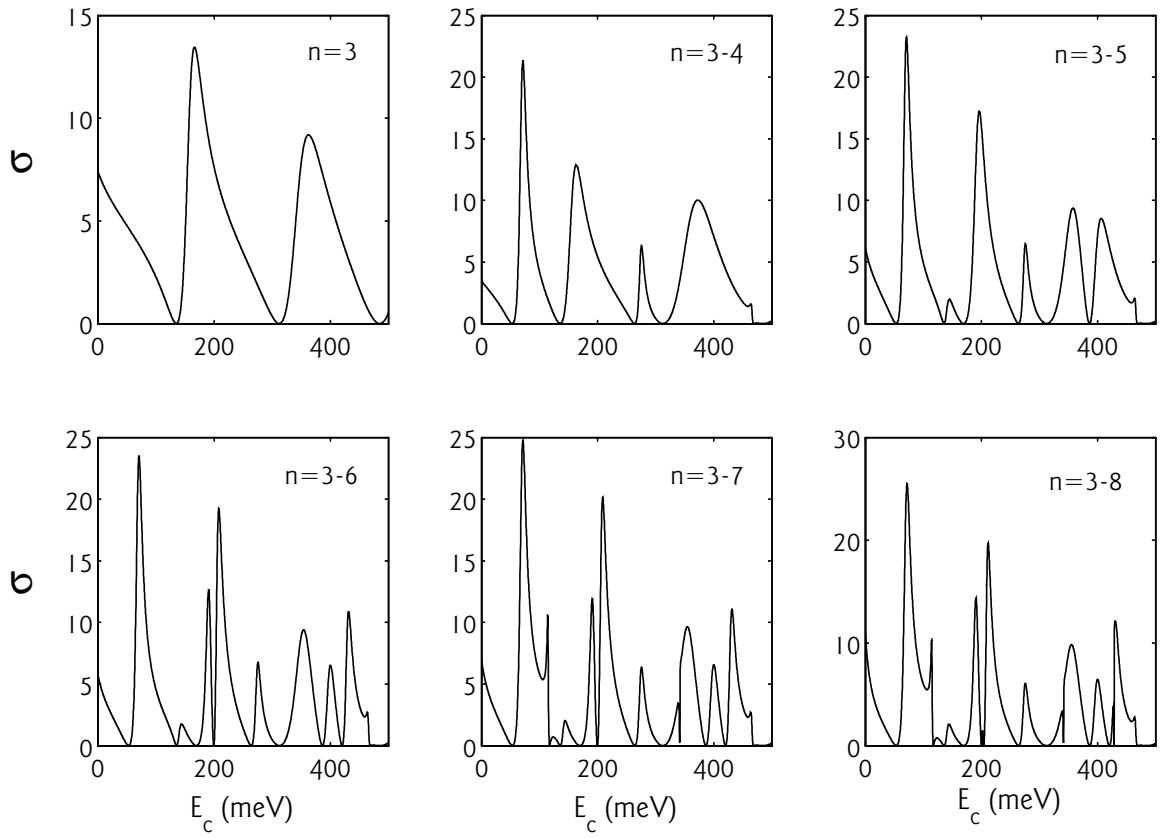

Figure 7.8: The effect of adding Rydberg states with higher principal quantum numbers to the electron-energy-dependent cross section concerning the $^3\Sigma_u^-$ states of O_2^+. The RV coupling for n=3 is 0.5 eV, corresponding to a capture width of 0.63 eV.

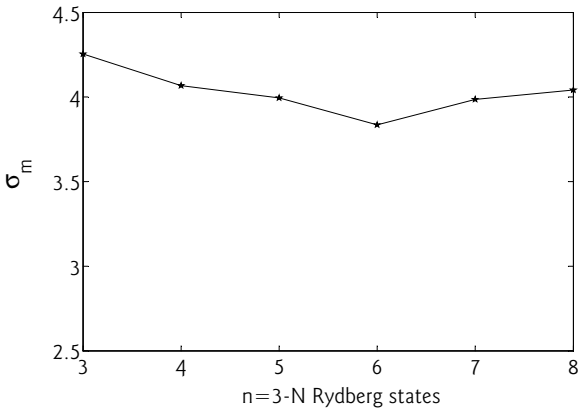

Figure 7.9: The effect of adding Rydberg states with higher principal quantum numbers on the mean cross section, σ_m, concerning the $^3\Sigma_u^-$ states of O_2^+. The RV coupling for n=3 is 0.5 eV, corresponding to a capture width of 0.63 eV. σ_m is averaged over the electron-energy range of 0 to 500 meV.

Rydberg state is determined via the relation $(n^*_N/n^*_{N+1})^3 = (H_{N+1}/H_N)^2$. The autoionisation only pertains to the valence capture state. As can be observed, each additional Rydberg state introduces extra resonances. As the RV coupling decreases upon increasing principal quantum number, the resonances narrow. This effect is most clearly observed in the addition of the n=4 to the n=3 Rydberg state. Above n=7, the effect of additional Rydberg states becomes negligible as the coupling strengths are too low to be of any influence. The mean cross section, σ_m, is shown in Fig. 7.9. The additional Rydberg states have little effect on the total cross section.

7.4.3 Introducing Spin-Orbit Coupling

Besides the high RV couplings, the DR of O_2^+ possesses another aspect that is thought to be of great importance to the production of $O(^1S)$ atoms. In order to arrive at a finite $O(^1S)$ production, Guberman included the spin-orbit (SO) coupling between the Rydberg states of $^3\Sigma_u^-$ and $^1\Sigma_u^+$ symmetry into his calculations [68]. Figure 7.10(a) shows the situation in which the $^1\Sigma_u^+$ state is added to the $B\,^3\Sigma_u^-$ state in order to find out whether our model provides similar results in the $O(^1S)$ branching as found in Ref. [82] and as found in our experiments (see Chapter 4). Electron capture occurs in the $B\,^3\Sigma_u^-$ valence state, while the n=3 Rydberg states of the respective symmetries couple with each other with a SO-coupling strength of 92 cm^{-1} [178]. Autoionisation is now possible via the $B\,^3\Sigma_u^-$ and the $f\,^1\Sigma_u^+$ valence states. Figure 7.10(a) shows for the first time branching behaviour in the present calculations. As function of collision energy, we see that the SO coupling gives a $O(^1D)$ + $O(^1S)$ production of about 0% near zero eV up to roughly 10% at the resonances in the cross section of the f state.

Figure 7.10(b) shows the effect of adding higher-lying Rydberg states to both the B and f states. The f Rydberg states are treated in the same way as those of the B state. For n > 4, the potentials and associated coupling strengths are determined based on the respective quantum defects and on the n=4 RV coupling, respectively. For all principal quantum numbers, the SO coupling between the B and f states is fixed at 92 cm^{-1} [178]. Figure 7.10(b) reveals that the branching towards $O(^1D)$ + $O(^1S)$ is around 3% of the B state dissociation flux. Supposing that $B\,^3\Sigma_u^-$ is the dominant channel towards $O(^3P)$ + $O(^1D)$ in the DR of O_2^+, the value of 3% is not much different from the 6–8% branching ratio, $O(^1D)+O(^1S) : O(^3P)+O(^1D)$, found experimentally.

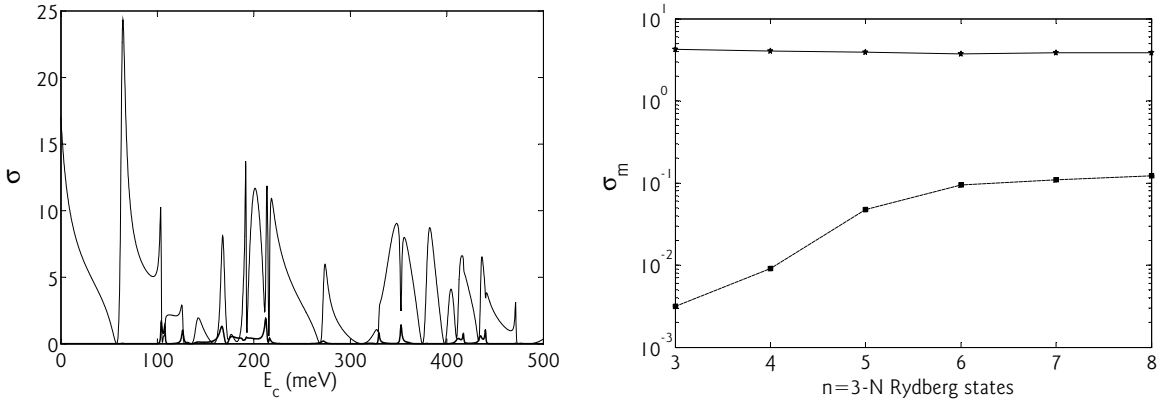

(a) (b)

Figure 7.10: (a) The effect of the spin-orbit coupling on the electron-energy-dependent cross section of the diabatic $O(^3P)$ + $O(^1D)$ limit of the $B\,^3\Sigma_u^-$ state (thin curve) and the diabatic $O(^1D)$ + $O(^1S)$ limit of the $f\,^1\Sigma_u^+$ state (thick curve), including the respective n=3−8 Rydberg states. (b) The mean cross section, σ_m, towards the $O(^3P)$ + $O(^1D)$ limit, the limit of the $B\,^3\Sigma_u^-$ state, and the $O(^1D)$ + $O(^1S)$ limit, the limit of the $f\,^1\Sigma_u^+$ state, as function of the number of Rydberg states. All Rydberg states have RV-coupling strengths that decrease with increasing quantum number and an SO-coupling strength fixed at 92 cm^{-1}. The autoionisation for both valence states is determined with Eq. (7.6). Electron capture is restricted to the B state. The cross sections are averaged over the collision-energy range of 0−500 meV.

7.4.4 Capture into the $^{1,3}\Pi_g$ Valence States

Although the optimum in the total cross section is observed at values of Γ near 0.6 eV and, from Fig. 7.7 and the value of H_{el}, a small contribution of the $^{1,3}\Pi_g$ states is expected, in the following we assess their possible contribution. As mentioned in the introduction, the almost statistical behaviour of the branching frequently observed in diatomic systems suggests that many more states play a role than the few states with large capture widths that are typically selected; about six states in the case of O_2^+. The $^{1,3}\Pi_g$ states of oxygen are worth mentioning as our experiments on the electron-energy and vibrational dependence of O_2^+ indicate several discrepancies between theoretical predictions and observation (see Chapter 4). In our discussion on the electron-energy dependence, we mention the crossing of the $^{1,3}\Pi_g$ states near the vibrational ground state of the ion for two reasons [83]. First, the branching fractions that oscillate with increasing collision energy may be a result of competing pathways and different $^1\Pi_g$ and $^3\Pi_g$ valence states are known to cross and to couple to the different dissociation limits, albeit that the interaction between the valence states in general favour one of the channels. Second, Guberman's prediction on the angular dependence for the DR of O_2^+ is not observed [86]. Other or additional molecular states playing a role in the dissociation could explain this disagreement. For the above mentioned reasons, we chose to perform the calculations on the $^{1,3}\Pi_g$ states as well. Figs. 7.11, 7.12, and 7.13 show the cross sections determined for the $^1\Pi_g$ state, leading to $O(^1D)$ + $O(^1D)$ atoms, and the $^3\Pi_g$ state, leading to $O(^3P)$ + $O(^1D)$ atoms, together with the cross section of the $B\,^3\Sigma_u^-$ and the $f\,^1\Sigma_u^+$ states in the case of no RV coupling, coupling to the n=3 Rydberg states, and coupling to the n=3−8 Rydberg states. Note that here, the DR cross section of direct capture into the $f\,^1\Sigma_u^+$ state is calculated.

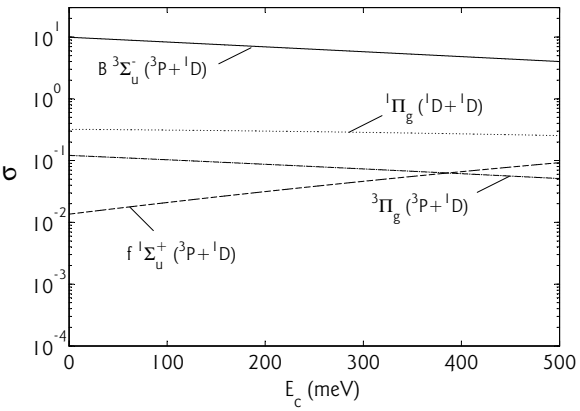

Figure 7.11: The calculated electron energy-dependent cross sections concerning capture into one doubly excited state for the $B\,^3\Sigma_u^-$, $f\,^1\Sigma_u^+$, $^1\Pi_g$, and $^3\Pi_g$ valence states ignoring the Rydberg states and with a capture width width as determined with Eq. (7.6), where $H_{el}(B) = 0.5$ eV, $H_{el}(f) = 0.1955$ eV, $H_{el}(^1\Pi_g) = 55$ meV, and $H_{el}(^3\Pi_g) = 79$ meV [99, 175, 180].

The last three figures of this thesis contain directly branching and cross-section behaviour. The information is not complete as only a limited number of states have been taken into account because of the lack of relevant information for many other states. Figure 7.11 shows that in the absence of RV couplings, the B state dominates the DR cross section. Direct capture into the f state is very ineffective, even less effective than the mechanism involving SO coupling. Her, our calculations agree with the conclusions from Guberman and Giusti-Suzor [68, 82]. The $^{1,3}\Pi_g$ states contribute only for a small fraction. In Fig. 7.12, the effect of the RV couplings and only one n=3 Rydberg state is given for the same four states. The B state reduces significantly in efficiency, but remains the dominating channel. The observed dips are rather wide (tens of meV). These results would agree with the fast

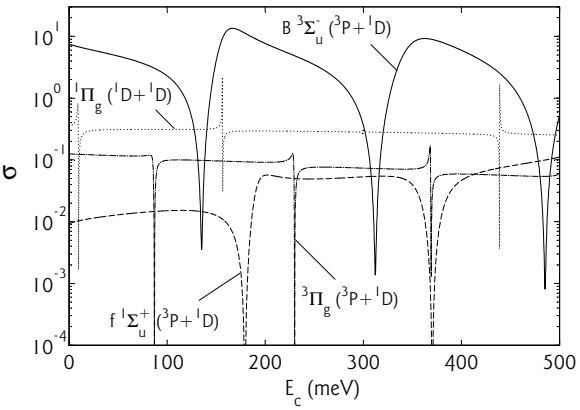

Figure 7.12: The calculated electron energy-dependent cross sections concerning capture into one doubly excited state for the $B\,^3\Sigma_u^-$, $f\,^1\Sigma_u^+$, $^1\Pi_g$, and $^3\Pi_g$ valence states with electronic coupling to the respective n=3 Rydberg states, where $H_{el}(B) = 0.5$ eV, $H_{el}(f) = 0.1955$ eV, $H_{el}(^1\Pi_g) = 55$ meV, and $H_{el}(^3\Pi_g) = 79$ meV [99, 175, 180] and with an autoionisation width as determined with Eq. (7.6).

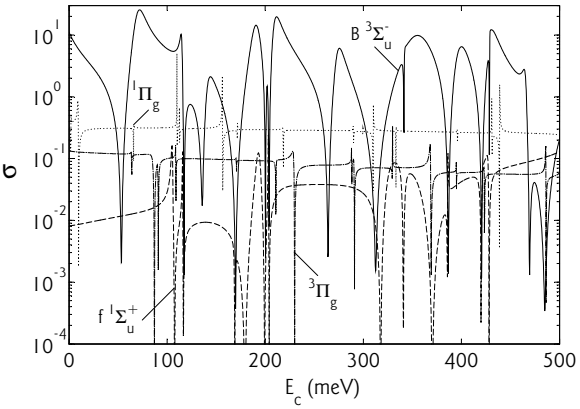

Figure 7.13: The calculated electron energy-dependent cross sections concerning capture into one doubly excited state for the $B\,^3\Sigma_u^-$, $f\,^1\Sigma_u^+$, $^1\Pi_g$, and $^3\Pi_g$ valence states with electronic coupling to the respective n=3–8 Rydberg states, where $H_{el}(B) = 0.5$ eV, $H_{el}(f) = 0.1955$ eV, $H_{el}(^1\Pi_g) = 55$ meV, and $H_{el}(^3\Pi_g) = 79$ meV [99, 175, 180] and with an autoionisation width as determined with Eq. (7.6).

oscillations in branching behaviour as function of collision energy. The other three channels show resonances, but their behaviour is not much affected by the RV interactions. Figure 7.13 shows the complex-looking spectra when the n=3−8 Rydberg states are incorporated in the calculations. The branching behaviour is qualitatively equal to the results in Fig. 7.12. Finally, all figures display cross sections that do not contain the $1/E_c$behaviour associated with the long-range Coulomb interaction between the electron and the ion. For the assessment of thermal rates, the cross section at very small collision energies is very important due to this $1/E_c$factor. The presence of a dip, as observed in the B state, in the cross section near 0 eV collision energy would have an enormous effect on the thermal DR rate coefficient.

7.5 Discussion and Conclusion

The aim of this work was to determine the consequences of the correlation between the three physical properties, RV coupling, autoionisation width and capture width, on the total efficiency of DR. In the situation with only a repulsive valence state, the DR cross section scales with the amount of overlap between the initial vibrational state and the vibrational continuum, and with the capture width. The DR cross section decreases with the autoionisation width as it reduces the so-called survival. In early treatments of the DR of O_2^+, it was found that survival does not dominate the DR cross section, even at an autoionisation-width value of the $B\,^3\Sigma_u^-$ state. Hence, states such as the $^{1,3}\Pi_g$ states with capture width that are smaller by almost two orders of magnitude were not taken into account [80, 174]. In fact, arguments of a reasonable Franck-Condon overlap and a significant capture width reduced DR calculations to six electronic states for only four dissociation limits [86, 174]. In the present computational study, we have quantified the coupling strengths where the effect of the associated large RV coupling on the structure of Rydberg and valence states affects the electron-capture process. Our results indicate that the largest DR cross section is found at a value of the capture width of 0.6 eV for the B-state potentials. The maximum value depends also on the magnitude of the Franck-Condon overlap. Our findings agree in general with the choices made by Guberman in selecting potential capture states. In that sense, the present results do not form a solution for the discrepancies found between theory and experiment. It is still unclear why, in experiments, we observe such similar dissociation flux to all dissociation limits, why we do not observe the anisotropy belonging to the $B\,^3\Sigma_u^-$ capture state, and why the cross section of all diatomic ions are so similar.

Important findings regarding the physics of strongly coupled states in the presence of significant autoionisation are the disappearance of mixed Rydberg-valence energy levels and the reappearance of resonances at unperturbed Rydberg-level positions, in spite of the very large H_{el} values. The resonances start to appear as very wide dips in the cross section, witnesses of the enhanced lifetime of the resonances and increased efficiency of autoionisation to occur. The present study lacks detail in order to look for quantitative agreement with various observations. It will be of interest to check whether the present conclusions on the optimum magnitude of Γ is also the outcome of the MQDT approaches that are generally used in studies of DR.

1
2
3
4
5
6
7
A
B

Science is...

to know that searching for things forgotten

is like fathering new memories

– brother of – Annemieke

Appendix A

Overview of the CRYRING Studies

The four experimental studies that are presented in this thesis consisted out of a single or multiple measurements (see Chapters 4–6). Table A.1 lists the details of these measurements. The ions are given along with our knowledge concerning their internal states. For $(NO)_2^+$, the terms *cis* and *trans* indicate the expected configurations of the ions. Quantities of physical interest are given next along with the collision energies at which they have been measured. The reaction rates are measured while ramping the electron-beam energy, which gives rise to a continuous variation of the collision energy. The dynamics are measured while fixing the collision energy. In the $O_2^+(E_c)$ measurement a number of collision energies have been selected between 0 and 0.3 eV. For the $(NO)_2^+$ fragmentation, only qualitative results have been determined. The rest of the table lists specifications that are relevant to the data analysis. The reader is referred to Appendix B for explanations of the abbreviations and symbols used.

Table A.1: Overview of the measurements performed in the four laboratory studies described in this thesis along with experimental and analytical specifications. A glossary and a list of abbreviations and symbols are given in Appendix B.

Study	$O_2^+(E_c)$	$O_2^+(v)$		NO^+			$(NO)_2^+$			
Chapter	4A	4B		5			6			
Internal state	$X\,^2\Pi_g$ $v=0$	$X\,^2\Pi_g$ Pn(v)		$X\,^1\Sigma^+$ $v=0$	$a\,^3\Sigma^+$ v		*cis, trans* $v\approx 0$			
Physical interest	$B_\beta(E_c)$	$k_{Pn}(E_c)$	$k_v, B_{\beta,v}$	$B_\beta(E_c)$	B_β	$\tau(a\,^3\Sigma^+)$	$k_{DR}(E_c)$	$k_{DE}(E_c)$	F_f	B_β
E_c (eV)	$\in\langle 0, 0.3\rangle$	0-0.4	0	0, 1, 5	0	0	0-1	0-4	0	0
Experiment										
Measured quantity	positions	rate	positions	positions	positions	positions	rate	rate	fragmentation	positions
Ion source	JIMIS	PHILIS	PHILIS	MINIS	MINIS	MINIS	JIMIS	JIMIS	JIMIS	JIMIS
Detection system	Imaging	SBD	Imaging	Imaging	Imaging	Imaging	SBD	SBD	SBD+grid	Imaging
Main issues	S/N	S/N, SEC	Δx, SEC	S/N	S/N	Δx, S/N	S/N	S/N	ΔE	identification
E_{ion} (MeV)	2.9	3.05	3.05	3.15	3.15	3.15	1.6	1.6	1.6	1.6
U_{cath}^{cool}	56	54	54	62	62	62	16	16	16	16
U_{cath}^{ramp}	-	26-92	-	-	-	-	9-25	9-36	-	-
Measuring gate (s)	7-9	2-4	2.5-10	5-7.5	1.2-1.4	1.2-7	5-6.5	5-6.5	5-8	4-6
Time stamp (50 ms)	-	-	yes	-	-	yes	-	-	-	-
BG gate separate (s)	7-9	2-4	2.5-10	5-7.5	5-7.5	5-7.5	5-6.5	2-5	5-8	4-6
BG gate in ramp (s)	-	0.2	-	-	-	-	0.1	-	-	-
E_c^{BG} (eV)	-	5	-	-	-	-	1	< 0.6	-	-
Cooling on	yes	no	-	yes	-	-	yes	yes	yes	yes
Analysis										
Measured spectrum	DD	MCS	DD	DD	DD	DD	MCS	MCS	MCA	DD
Analytical tool	*2D* model	-	*2D* model	*2D* model	*2D* model statistical model	-	-	-	-	parameterisation
Descriptive parameters										
Included channels (ß)	(4.1a)-(4.1e)	-	(4.1a)-(4.1c),(4.1e)	(5.1a)-(5.1i)	(5.1a)-(5.1j)	(5.1a)-(5.1j)	-	-	Eqs. (6.1a)-(6.1g)	Eqs. (6.2a)-(6.2c)
M (mm/pixel)	0.36	-	0.53	0.45	0.45	0.45	-	-	-	0.45
T_{rot} (K)	300	-	300	1300	1300	1300	-	-	-	no J
Free parameters	$B(\beta)$	-	$B(v,\beta), \sigma(v)$	$B(\beta)$	$B(\beta)$	-	-	-	-	TD(β)
model shape	(an)isotropic	-	isotropic	(an)isotropic	isotropic	isotropic	-	-	-	-
parameterisation	-	-	-	-	-	-	-	-	-	χ, β, ε

$$U''(R) + \frac{2\mu}{h^2}[EI - W(R)]U = 0$$

1
2
3
4
5
6
7
A
B

Physics is...

Annemieke wrecking my brains for the correct grammatical usage for some impossible scientific term

– sister-in-law of – *Annemieke*

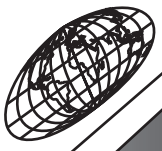

Appendix B

Glossary, Abbreviations, and Symbols

Glossary

BG gate The storage times during a cycle at which background data is acquired

Born-Oppenheimer approximation An approximation of the time-independent Scrödinger equation in which the electronic and nuclear motion are treated separately

CO_2 cooling The decrease in atmospheric temperatures due to the radiative infrared emission of CO_2

Franck-Condon factor The value of the overlap integral between two nuclear wave functions, related to the efficiency of the transition between the two states

Lyman α The emission arising from the $H(^2P) \rightarrow H(^2S)$ transition

Martian From the planet Mars

Schumann-Runge system The $B - X$ transition of O_2

Venusian From the planet Venus

ab initio From first principles

adiabatic electronic state Solution of the electronic Hamiltonian following the Born-Oppenheimer separation

airglow Radiative decay in the upper atmosphere driven by solar and galactic radiation

aurora Radiative decay in the atmosphere, often near the poles, driven by solar particles

auroral green-line The emission line arising from the decay of atomic $O(^1S)$ to $O(^1D)$

autoionisation time The time between electron capture en re-ionisation

branching fraction The percentage of the total branching into a specific dissociation channel

chemical branching The branching into the different combinations of product fragments

collision energy The electron energy in the molecular frame of the ion

collision time The average time between collisions

cooling energy The electron-beam energy in a storage ring at which the collision energy is zero

cross section The effective collisional area

cycle The full storage time of an ion beam from injection to dumping

diabatic electronic state Solution of an, often non-existing, Hamiltonian in which the internuclear-separation dependence of the states is minimised

direct dissociation Direct electron capture into a repulsive state leading to dissociation

dissociative recombination The recombination of a molecular ion and an electron, followed by dissociation of the formed molecule

electronic coupling Interaction between molecular diabatic states where the diabatic electronic states are not Eigensolutions of the electronic Hamiltonian

experiment In this thesis, a laboratory investigation involving one or more measurements

first IR atmospheric band The emission of the decay of $O_2(a)$ to $O_2(X)$

fragmentation The break-up possibilities of a polyatomic molecule into various fragment combinations

indirect dissociation Dissociation after an electron-capture process modified by a metastable intermediate Rydberg state

in situ Conducted at the actual site of the phenomenon under investigation

interstate Between vibrational levels of different electronic states

intrastate Between vibrational levels of the same electronic state

kinetic energy release The kinetic energy that is released in an exothermic reaction

mean free path Average travel distance between collisions

measurement In this thesis, acquisition of a specific data set integrated over many beam cycles

measuring gate The storage times within a cycle at which data is acquired

partial rate coefficient The rate coefficient of an individual vibrational level of the parent ion

phase space cooling Cooling of the momentum degrees of freedom

physical branching The branching into the different combinations of physical product states

predissociation The dissociation as intrinsic property of the Eigenstate, i.e., not driven by external perturbations

quantum defect The correction to the principal quantum number, n, due to the scattering of the Rydberg electron on the multi-electron ionic core

quantum yield The number of atoms produced in a specific state in an average dissociative recombination event

quenching Internal relaxation through collisions

ramp The storage times within a cycle at which the collision energy is varied

rate coefficient A measure of the possibility of a reaction to occur

red-doublet emission The two emission lines arising from the decay of atomic $O(^1D)$ to $O(^3P)$

rovibrational Combination of rotational and vibrational states

rovibronic Combination of rotational, vibrational, and electronic states

spin-orbit coupling Interaction between molecular states of different spin due to the the magnetic fields associated with the electron orbital motion and spin

survival factor The fraction of survival towards dissociation after recombination

survival time The time between capture and reaching the point where autoionisation is no longer possible and dissociation is a fact

total displacement A measure for the partitioning of the kinetic energy release over the product fragments in the dissociative recombination of a polyatomic ion

total rate coefficient The rate coefficient of the total vibrational population of the parent ions

vibronic Combination of vibrational and electronic states

Abbreviations

AMOLF Atoom en MOLekuul Fysica (Atomic and Molecular Physics)
BG Background
CASSCF Complete Active-Space Self-Consistent Field
CCD Charged-Coupled Device
CFD Constant Fraction Discriminator
CG Centre-of-Geometry
CID Collision-Induced Dissociation
CM Centre-of-Mass
CRYRING CRYsis-synchrotron-RING
CRYSIS CRYogenic Stockholm Ion Source
CT Charge Transfer
DCT Dissociative Charge Transfer
DD Distances Distribution as measured by the imaging technique
DE Dissociative Excitation
DI Dissociative Ionisation
DLD Delay-Line Detector
DR Dissociative Recombination
FOM Fundamenteel Onderzoek der Materie (Fundamental Research of Matter)
FT-ICR Fourier Transform Ion Cyclotron Resonance
II Image Intensifier
IR Infrared
JIMIS Jim Ion Source (named after Jim Peterson for his role in its development)
KER Kinetic Energy Release
MCA Multi-Channel Analyser
MCP Micro-Channel Plate
MCS Multi-Channel Scaler
MINIS Mini INjection Ion Source
MQDT Multichannel Quantum Defect
MSL Manne Siegbahn Laboratory
PHILIS Phil Ion Source (named after Philip Cosby for his role in its development)
PMT Photo-Multiplier Tube
RFQ Radio Frequency Quadrupole
RIP Resonance Ion-Pair
RV Rydberg-Valence
Ryd Rydberg state
SBD Surface Barrier Detector
SEC Super Elastic Collision

S/N Signal-to-Noise ratio
SO Spin-Orbit
SR Schumann-Runge
TD Total Displacement

Symbols

Δx the spatial resolution of the imaging technique
Δx_T the step size through the toroidal sections of the electron cooler
Γ the electron-capture width and a measure for the autoionisation strength
Ψ the total wave function

$\alpha()$ the thermal rate coefficient
α_0 the thermal rate coefficient at 300 K
γ the fit parameter for expressing the thermal rate in terms of α_0
δ the quantum defect
ϵ the relative dissociation flux that is found in the coupled-channel calculation
ε the kinetic energy release for a three-particle dissociation event
θ the angle between the molecular axis and the electron-velocity vector
μ the reduced mass of the molecular system
μ_{21} the reduced mass of the two lighter fragments in a three-body break-up
$\xi(E_e)$ the electron-energy dependent positive-ion-trapping function
ρ the momentum ratio between the two light fragments in a three-body break-up
σ the 'true' cross section derived from experiments
σ the cross section derived from the coupled-channel calculations
σ_v the partial cross section of vibrational level v of the parent ion
σ_{DR} the dissociative-recombination cross section
σ_{H_2} the ionisation cross section of H_2
σ_m the mean cross section averaged over the collision-energy range of 0—500 meV
σ_{meas} the measured cross section
σ_{tc} the toroidal-corrected cross section
τ the internal-state lifetime
τ_a the autoionisation time
τ_{eff} the effective decay time of an internal state decaying to any lower-lying state
τ_{inter} the decay time between electronic states
τ_{intra} the decay time between vibrational states of the same electronic state
τ_s the stabilisation time between recombination and irreversible dissociation
v the vibrational level
ϕ the inter-fragment angle $\angle(P_i - P_k - P_j)$ as measured on the detector in a three-particle event
$\phi_{l,m,s}$ the largest, intermediate, and smallest inter-fragment angles as measured on the detector in a three-particle event
χ the intra-fragment angle $\angle(P_i - \mathrm{CM} - P_j)$ in the molecular frame
ψ_i the electronic wave function
ω_e the vibrational frequency

$\boldsymbol{A}$ the Einstein coefficient for spontaneous emission

$\mathbf{A}$ the normalisation factor for positive-ion trapping related to H_2^+

$\mathbf{A'}$ the empirical factor for the average positive-ion trapping

$\mathbf{B}_r$ the rotational constant of a molecule

$\boldsymbol{B(v,\beta)}$ the *physical* branching fraction dissociating towards channel β that is associated with vibrational level v of the parent ion

$\boldsymbol{D}$ the model of the total *2D* distance distribution for the dissociative recombination of a diatomic ion in a storage ring

$\boldsymbol{D_\beta}$ the model of the *2D* distance distribution for a single physical branching channel β

$\mathbf{E}$ the total initial energy of the system under consideration

$\boldsymbol{E_{1,2}}$ the kinetic energy released to the O/N fragments in the dissociative recombination of $(NO)_2^+$

$\boldsymbol{E_v}$ the vibrational energy of the parent ion with respect to its rovibronic ground state

$\boldsymbol{E_{v,J}}$ the vibrational and rotational energy of the NO fragment produced in the dissociative recombination of $(NO)_2^+$ with respect to the rovibronic NO ground state

$\boldsymbol{E_{NO}}$ the kinetic energy released to the NO fragment in the dissociative recombination of $(NO)_2^+$

$\boldsymbol{E_c}$ the collision energy, being the electron energy in the molecular frame

$\boldsymbol{E_c^{BG}}$ the collision energy used to determine the background signal, where dissociative excitation or recombination are negligible

$\boldsymbol{E_{c,cath}}$ the collision energy based on the cathode voltage

$\boldsymbol{E_{c,sp}}$ the space-charge corrected collision energy

$\boldsymbol{E_{cath}}$ the cathode energy in the lab frame

$\boldsymbol{E_{cool}}$ the electron energy in the lab frame at cooling ($v_e = v_i$)

$\boldsymbol{E_e}$ the electron energy in the lab frame

$\boldsymbol{E_{ion}}$ the ion-beam energy in the lab frame

$\boldsymbol{E_{sp}}$ the electron space-charge energy in the lab frame

$\boldsymbol{E_t}$ the threshold energy required for dissociative excitation

$\boldsymbol{F_f}$ the *chemical* branching fraction of fragmentation channel *f*

$\mathbf{H}$ the Hamiltonian; the operator for the total energy of a system

$\mathbf{H_N}$ the electronic coupling between a valence and a n=N Rydberg state of the same symmetry

$\mathbf{H_{el}}$ the electronic coupling between molecular states of the same symmetry, often between a Rydberg and a valence state

$\mathbf{H_{ij}}$ the various couplings between diabatic electronic states

$\mathbf{H_{so}}$ the spin-orbit coupling between molecular states of differing symmetry

$\boldsymbol{I(\theta)}$ the angular distance distribution arising from anisotropic dissociative-recombination processes

$\mathbf{I}$ the unity matrix

$\boldsymbol{I_e}$ the electron current

$\boldsymbol{I_{ion}}$ the ion current

J the rotational quantum number

L the distance from the dissociation event to the imaging detector

L_0 the distance from the centre of the electron cooler to the imaging detector

L_1 the distance from the far-end of the electron cooler to the imaging detector

L_2 the distance from the near-end of the electron cooler to the imaging detector

M the dipole moment function

$\mathbf{M}(m)$ the number of counts in the energy-contribution peak of mass m as measured with the grid technique

$\mathbf{N}_{(f)}$ the number of counts to the fragmentation channel, f

Pn the vibrational population labelled n

$Q_{1,2}$ the Dalitz coordinates, describing linear combinations of the energies of the reaction products at a constant total energy

R the inter-nuclear separation

R_{meas} the reaction rate as extracted from an MCS spectrum

S the spin quantum number

T the transmission factor of the grid used to determine the chemical fragmentation

T the temperature

$\mathbf{T}_e$ the electron temperature

$\mathbf{T}_{e_{\parallel}}$ the longitudinal electron temperature

$\mathbf{T}_{e_{\perp}}$ the transversal electron temperature

$\mathbf{T}_{rot}$ the Boltzmann rotational temperature

$\mathbf{T}_{surface}$ the surface temperature of a planet

$\mathbf{T}_{upper}$ the upper-atmospheric temperature of a planet

U the vector containing the radial wave functions

U_{cath} the cathode potential of the electron gun in the electron cooler

U_{cath}^{cool} the cathode potential at cooling

U_{cath}^{ramp} the cathode potential during the ramp

$\mathbf{V}_i$ the diabatic electronic state labelled i

W the interaction matrix containing the diabatic molecular states on its diagonal and the various couplings on the off-diagonal elements

a the diameter of the vacuum tube at CRYRING

b the diameter of the electron beam at CRYRING

β the *physical* branching channel

c the speed of light

$d_{1,2,3}$ the distances on the detector from the centre-of-mass to the lightest two and the heavy fragments, respectively

$d_{CG\text{-}P_{l,m,s}}$ the distances on the detector from the centre-of-geometry to the farthest, intermediate, and closest fragments, $P_{l,m,s}$, respectively

d_{det} the inter-fragment distance as measured on the detector in a two-particle event

$d_{i,j,k}$ the inter-fragment distances as measured on the detector in a three-particle event
d_{lab} the inter-fragment distance for a two-particle event in the lab frame
$d_{l,m,s}$ the longest, intermediate, and shortest inter-fragment distances on the detector in a single three-particle event
f the *chemical* fragmentation channel
j the rotational level
$\mathbf{k}$ the Boltzmann constant
k the energy-dependent rate coefficient
$k(v)$ the partial rate coefficient of vibrational level v of the parent ion
k_{Pi} the total rate coefficient of the vibrational population Pi
k_{meas} the measured rate coefficient
l_c the length of the centre section of the electron cooler
m the particle mass
m_e the electron mass
m_i the ion mass
$\mathbf{n}$ the principal quantum number
$\mathbf{n}^*$ the effective principal quantum number
n_e the electron density
$\mathbf{n}[\ ]$ the density
$p(v)$ the population of vibrational level v of the parent ion
q_e the electron charge
$\mathbf{r}$ representation for all electrons in the molecular system
r_c the classical radius of the electron
$\mathbf{r}_e$ the equilibrium inter-nuclear separation of a system
$\mathbf{r}_i$ representation for one electron in the molecular system
$\mathbf{t}$ the storage time of the ions in the storage ring
$\mathbf{u}$ the momentum of the product fragment after dissociation
$\mathbf{u}_{i,j}$ the momenta of the two lightest product fragments in a three-body breakup
$\mathbf{u}_i$ the inter-nuclear-dependent coefficient
$\mathbf{v}_{1,2}$ the velocities of the two lightest product fragments in a three-body breakup
$\mathbf{v}_{cool}$ the electron velocity at cooling ($\mathrm{v}_e = \mathrm{v}_i$)
$\mathbf{v}_{det}$ the detuning velocity
$\mathbf{v}_e$ the electron-beam velocity in the lab frame
$\overline{\mathbf{v}}_{e_\parallel}$ the mean longitudinal velocity of the electron beam
$\mathbf{v}_{e_\parallel}$ the longitudinal electron-beam velocity
$\mathbf{v}_{e_\perp}$ the transversal electron-beam velocity
$\mathbf{v}_i$ the ion-beam velocity in the lab frame
x_{T} the position on the beam axis in the toroidal segments
$x_{\max}$ the end position of the toroidal segment relative to the start

Bibliography

2005
SEPTEMBER

Sun		4	sUK	18	25
Mon		5	sNL	19	26
Tue		6	sFR	20	27
Wed		7	Ack	21	28
Thu	1	A	CV	22	29
Fri	2	B	16	23	30
Sat	3	**Ref**	17	24	

[1] F. J. Garcia, M. J. Taylor, and M. C. Kelley. Two-dimensional spectral analysis of mesospheric airglow image data. *Appl. Opt.*, 36(29):7374–7385, October 1997.

[2] R. P. Wayne. *Chemistry of Atmospheres*. Oxford University Press, Oxford, third edition, 2000.

[3] J. W. Chamberlain. *Physics of the Aurora and Airglow*. American Geophysical Union, Washington, second edition, 1994.

[4] R. W. Schunk and A. F. Nagy. *Ionospheres: Physics, Plasma Physics, and Chemistry*. Cambridge University Press, Cambridge, first edition, 2000.

[5] S. Akasofu. Auroral spectra as a tool for detecting extraterrestrial life. *EOS*, 80:397, 1999.

[6] T. G. Slanger, P. C. Cosby, D. L. Huestis, and T. A. Bida. Discovery of the atomic oxygen green line in the Venus night airglow. *Science*, 291:463–465, January 2001.

[7] J. L. Fox. Spectrum of hot O at the exobases of the terrestrial planets. *J. Geophys. Res.*, 102(A11):24005–24011, November 1997.

[8] R. Richard Hodges, Jr. Distributions of hot oxygen for Venus and Mars. *J. Geophys. Res.*, 105(E3):6971–6981, March 2000.

[9] D. F. Martyn and O. O. Pulley. The temperatures and constituents of the upper atmosphere. *Proc. Roy. Soc. A*, 154(882):455–468, April 1936.

[10] D. R. Bates and H. S. W. Massey. The basic reactions in the upper atmosphere II; The theory of recombinationin the ionized layers. *Proc. R. Soc. London*, 192:1–16, December 1947.

[11] D. R. Bates. Electron recombination in helium. *Phys. Rev.*, 77(5):718–719, March 1950.

[12] M. A. Biondi and T. Holstein. Concerning the mechanism of electron-ion recombination. *Phys. Rev.*, 82(6):962–963, June 1951.

[13] M. A. Biondi. Concerning the mechanism of electron-ion recombination II. *Phys. Rev.*, 83(5):1078–1080, September 1951.

[14] D. R. Bates and M. R. C. McDowell. Recombination in the ionosphere during an eclipse. *J. Atmos. Terr. Phys.*, 10:96–102, 1957.

[15] W. H. Kasner, W. A. Rogers, and M. A. Biondi. Electron-ion recombination coefficients in nitrogen and in oxygen. *Phys. Rev. Lett.*, 7(8):321–323, October 1961.

[16] M. A. Biondi. Electron-ion and ion-ion recombination. *Ann. Geophys.*, 20:34–46, 1964.

[17] D. R. Bates. Dissociative recombination. *Phys. Rev.*, 78(4):492–493, May 1950.

[18] M. Nicolet. Origin of the emission of the oxygen green line in the airglow. *Phys. Rev.*, 93(3):633–633, February 1954.

[19] C. S. Warke. Nonradiative dissociative electron capture by molecular ions. *Phys. Rev.*, 144(1):120–126, April 1966.

[20] D. R. Bates and E. C. Zipf. The $O(^1S)$ quantum yield from O_2^+ dissociative recombination. *Planet. Space Sci.*, 28:1081–1086, 1980.

[21] D. R. Bates. Emission of forbidden red and green lines of atomic oxygen from nocturnal *F* region. *Planet. Space Sci.*, 40(7):893–899, 1992.

[22] R. Peverall et al. The ionospheric oxygen green airglow: Electron temperature dependence and aeronomical implications. *Geophys. Res. Lett.*, 27(4):481–484, February 2000.

[23] E. C. Zipf. A laboratory study on the dissociative recombination of vibrationally excited O_2^+ ions. *J. Geophys. Res.*, 85(A8):4232–4236, August 1980.

[24] M. R. Torr and D. G. Torr. The role of metastable species in the thermosphere. *Rev. Geophys. Space Phys.*, 20(1):91–144, February 1982.

[25] W. J. van der Zande. Dissociative recombination of diatomics: do we understand product state branching? In M. Larsson, J. B. A. Mitchell, and I. F. Schneider, editors, *Dissociative Recombination: Theory, Experiment and Applications IV*, pages 251–260, Singapore, 2000. World Scientific.

[26] C. J. Herrlander et al. CRYRING - a small storage and acceleration ring for heavy ions. *IEEE Transitions on Nuclear Science*, NS-32(5):2718–2720, October 1985.

[27] K. Abrahamsson et al. The first year with electron cooling at CRYRING. *IEEE Transitions on Nuclear Science*, 3:1735–1737, 1993.

[28] M. Larsson et al. Direct high-energy neutral-channel dissociative recombination of cold H_3^+ in an ion storage ring. *Phys. Rev. Lett.*, 70(4):430–433, January 1993.

[29] S. Datz and M. Larsson. Radiative lifetimes for all vibrational levels in the $X\ ^1\Sigma^+$ state of HeH^+ and its relevance to dissociative recombination experiments in ion storage rings. *Physica Scripta*, 46:343–347, 1992.

[30] E. Westlin and M. Engström. Control system for CRYRING. In *Proceedings of ICALEPCS 1999*, pages 550–551, 2000.

[31] H. Danared, A. Källberg, L. Liljeby, and K. G. Rensfelt. The CRYRING superconducting electron cooler. In S. Myers, L. Liljeby, Ch. Petit-Jean-Genaz, J. Poole, and K. G. Rensfelt, editors, *Proceedings of the 6th European Particle Accelerator Conference*, pages 1031–1033, London, 1998. Institute of Physics Publishing.

[32] G. Andler et al. Progress report for the CRYRING facility. In S. Myers, L. Liljeby, Ch. Petit-Jean-Genaz, J. Poole, and K. G. Rensfelt, editors, *Proceedings of the 6th European Particle Accelerator Conference*, pages 526–528, London, 1998. Institute of Physics Publishing.

[33] S. Rosén. *Imaging technique development for dissociative recombination studies at the CRYRING ion storage ring*. PhD thesis, Department of Physics, Stockholm University, 2001.

[34] G. Andler et al. Extending the use of the CRYRING storage ring. In J. L. Laclere, W. Mitaroff, Ch. Petit-Jean-Genaz, J. Poole, and M. Resler, editors, *Proceedings of the 7th European Particle Accelerator Conference*, pages 545–547, Vienna, 2000. Austrian Academy of Sciences.

[35] G. Andler et al. Development at the CRYRING facility. In T. Garvey, J. Le Duff, P. Le Roux, Ch. Petit-Jean-Genaz, J. Poole, and L. Rivkin, editors, *Proceedings of the 8th European Particle Accelerator Conference*, pages 587–589. European Physical Society Interdivisional Group on Accelerators and CERN, 2002.

[36] H. Danared et al. Electron cooling with an ultracold electron beam. *Phys. Rev. Lett.*, 72(24):3775–3778, June 1994.

[37] M. Larsson. Dissociative recombination with ion storage rings. *Annu. Rev. Phys. Chem.*, 48:151–179, October 1997.

[38] S. G. Lias. "Ion Energetics Data" in NIST Chemistry WebBook, NIST Standard Reference Database Number 69, Eds. P. J. Linstrom and W. G. Mallard, March 2003, National Institute of Standards and Technology, Gaithersburg MD, 20899 (http://webbook.nist.gov).

[39] A. Källberg et al. CRYRING progress: weak beams, rare ions and ordering. In J. Chew, P. Lucas, and S. Webber, editors, *Proceedings of the 2003 Particle Accelerator Conference*, pages 1590–1592, Piscataway, 2003. Institute of Electrical and Electronics Engineers.

[40] C. W. Walter, P. C. Cosby, and J. R. Peterson. Rovibrational product distributions of O_2^+ from the reaction of $O^+(^4S)$ with CO_2. *J. Chem. Phys.*, 98(4):2860–2871, February 1993.

[41] A. Barbara van der Kamp, Jaap H. M. Beijersbergen, P. C. Cosby, and Wim J. van der Zande. $N_2^+(A\,^2\Pi_u \leftarrow X\,^2\Sigma_g^+)$ excitation in the charge-exchange collision with ceasium: two-electron effects at keV energies. *J. Phys. B*, 27:5037–5053, 1994.

[42] H. Helm, I. Havell, C. W. Walter, and P. C. Cosby. On the branching in dissociative recombination of O_2^+. In D. Zajfman, J. B. A. Mitchell, D. Schwalm, and B. R. Rowe,

editors, *Dissociative Recombination: Theory, Experiment and Applications III*, pages 139–150, Singapore, 1996. World Scientific.

[43] A. Kerek, W. Klamra, L. O. Norlin, D. Novák, and S. Westman. A detection system for highly charged ions which have undergone charge exchange in the CRYRING electron cooler. In S. Myers, L. Liljeby, Ch. Petit-Jean-Genaz, J. Poole, and K. G. Rensfelt, editors, *Proceedings of the 6th European Particle Accelerator Conference*, pages 1638–1640, London, 1998. Institute of Physics Publishing.

[44] A. Al-Khalili et al. Absolute high-resolution rate coefficients for dissociative recombination of electrons with HD^+: Comparison of results from three heavy-ion storage rings. *Phys. Rev. A*, 68(4):042702, October 2003.

[45] A. Neau et al. Dissociative recombination of D_3O^+ and H_3O^+: Absolute cross sections and branching ratios. *J. Chem. Phys.*, 113(5):1762–1770, August 2000.

[46] R. Peverall et al. Dissociative recombination and excitation of O_2^+: Cross sections, product yields and implications for studies of ionospheric airglows. *J. Chem. Phys.*, 114 (15):6679–6689, April 2001.

[47] Z. Amitay and D. Zajfman. A new type of multi-particle three-dimensional imaging detector with subnanosecond time resolution. *Rev. Sci. Instrum.*, 68:1387–1392, 1997.

[48] S. Datz, R. D. Thomas, M. Larsson, A. M. Derkatch, F. Hellberg, and W. J. van der Zande. Dynamics of three-body breakup in dissociative recombination: H_2O^+. *Phys. Rev. Lett.*, 85(26):5555–5558, December 2000.

[49] F. Österdahl, S. Rosén, V. Bednarska, A. Petrignani, M. Larsson, and W. J. van der Zande. Position- and time-sensitive coincident detection of fragments from the dissociative recombination of O_2^+ using a single hexanode delay-line detector. In A. Wolf, L. Lammich, and P. Schmelcher, editors, *Dissociative Recombination: Theory, Experiment and Applications VI*, pages 286–289, London, 2005. Institute of Physics and IOP Publishing.

[50] J. N. Bardsley. The theory of dissociative recombination. *J. Phys. B*, 1(3):365–380, May 1968.

[51] L. Vejby-Christensen, D. Kella, H. D. Pedersen, and L. H. Andersen. Dissociative recombination of NO^+. *Phys. Rev. A*, 57(5):3627–3634, May 1998.

[52] R. Thomas et al. Investigating the three-body fragmentation dynamics of water via dissociative recombination and theoretical modeling calculations. *Phys. Rev. A*, 66: 032715, 2002.

[53] R. D. Thomas et al. Three-body fragmentation dynamics of amidogen and methylene radicals via dissociative recombination. *Phys. Rev. A*, 71:032711, March 2005.

[54] M. A. Biondi and S. C. Brown. The basic reactions in the upper atmosphere II; The theory of recombinationin the ionized layers. *Phys. Rev.*, 76(11):1697–1700, December 1949.

[55] W. H. Kasner and M. A. Biondi. Temperature dependence of the electron–O_2^+-ion recombination coefficient. *Phys. Rev.*, 174(1):139–144, October 1968.

[56] F. J. Mehr and M. A. Biondi. Electron temperature dependence of recombination of O_2^+ and N_2^+ ions with electrons. *Phys. Rev.*, 181(1):264–271, May 1969.

[57] D. Smith, C. V. Goodall, N. G. Adams, and A. G. Dean. Ion- and electron-density decay rates in afterglow plasmas of argon and argon-oxygen mixtures. *J. Phys. B*, 3(1): 34–44, January 1970.

[58] A. J. Cunningham and R. M. Hobson. Dissociative recombination at elevated temperatures III; O_2^+ dominated afterglows. *J. Phys. B*, 5:2320–2327, December 1972.

[59] E. Alge, N. G. Adams, and D. Smith. Measurements of the dissociative recombination coefficients of O_2^+, NO^+ and NH_4^+ in the temperature range 200–600 K. *J. Phys. B*, 16:1433–1444, April 1983.

[60] P. Španěl, L. Dittrichová, and D. Smith. FALP studies of the dissociative recombination coefficients for O_2^+ and NO^+ within the electron temperature range 300–2000 K. *Int. J. Mass Spec. Ion Proc.*, 129:183–191, November 1993.

[61] T. Gougousi, M. F. Golde, and R. Johnsen. Electron–ion recombination rate coefficient measurements in a flowing afterglow plasma. *Chem. Phys. Lett.*, 265:399–403, February 1997.

[62] F. L. Walls and G. H. Dunn. Measurement of total cross sections for electron recombination with NO^+ and O_2^+ using ion storage techniques. *J. Geophys. Res.*, 79(13): 1911–1915, May 1974.

[63] J. Wm. McGowan, P. M. Mul, V. S. D'Angelo, J. B. A. Mitchell, P. Defrance, and H. R. Froelich. Energy dependence of dissociative recombination below 0.08 eV measured with (electron-ion) merged-beam technique. *Phys. Rev. Lett.*, 42(6):373–375, February 1979.

[64] P. M. Mul and J. Wm. McGowan. Merged electron-ion beam experiments III; Temperature dependence of dissociative recombination for atmospheric ions NO^+, O_2^+ and N_2^+. *J. Phys. B*, 12(9):1591–1601, 1979.

[65] E. C. Zipf. The dissociative recombination of O_2^+ ions into specifically identified final atomic states. *Bull. Am. Phys. Soc.*, 15:418, 1970.

[66] E. C. Zipf. The OI(^1S) state: Its quenching by O_2 and formation by the dissociative recombination of vibrationally excited O_2^+ ions. *Geophys. Res. Lett.*, 6(10):881–884, October 1979.

[67] D. Kella, L. Vejby-Christensen, P. J. Johnson, H. B. Pedersen, and L. H. Andersen. The source of green light emission determined from a heavy-ion storage ring experiment. *Science*, 276:1530–1533, June 1997. Erratum in Science 277, 167 (1997).

[68] S. L. Guberman. Mechanisms for the green glow of the upper ionosphere. *Science*, 278:1276–1278, November 1997.

[69] S. L. Guberman. Potential curves for dissociative recombination of O_2^+. *Int. J. Quantum Chem.*, S13:531–540, 1979.

[70] G. Hernandez. The signature profiles of $O(^1S)$ in the airglow. *Planet. Space Sci.*, 19: 467–476, 1971.

[71] P. B. Hays and W. E. Sharp. Twilight airglow, 1, photoelectrons and OI(5577 Å) radiation. *J. Geophys. Res.*, 78:1153, 1973.

[72] J. E. Frederick, G. A. Victor, W. E. Sharp, D. G. Torr, P. B. Hays, and H. C. Brinton. The OI(5577 Å) airglow: Observations and excitation mechanisms. *J. Geophys. Res.*, 81:3923, 1976.

[73] J. P. Kopp, J. E. Frederick, D. W. Rusch, and G. A. Victor. Morning and evening behavior of the F region green line emission – evidence concerning the sources of $O(^1S)$. *J. Geophys. Res.*, 82:4715–4719, October 1977.

[74] W. E. Sharp and D. G. Torr. Determination of the auroral $O(^1S)$ production sources from coordinated rocket and satellite measurements. *J. Geophys. Res.*, 84:5345–5348, September 1979.

[75] R. R. O'Neil, E. T. P. Lee, and E. R. Huppi. Auroral $O(^1S)$ production and loss processes – ground-based measurements of the artificial auroral experiment Precede. *J. Geophys. Res.*, 84:823–833, March 1979.

[76] V. J. Abreu, S. C. Solomon, W. E. Sharp, and P. B. Hays. The dissociative recombination of O_2^+: The quantum yield of $O(^1S)$ and $O(^1D)$. *J. Geophys. Res.*, 88(A5):4140–4144, May 1983.

[77] J. H. A. Sobral, H. Takahashi, M. A. Abdu, P. Muralikrishna, Y. Sahai, and C. J. Zamlutti. $O(^1S)$ and $O(^1D)$ quantum yields from rocket measurements of electron densities and 557.7 and 630.0 nm emissions in the nocturnal F-region. *Planet. Space Sci.*, 40(5):607–619, 1992.

[78] J. L. Queffelec, B. R. Rowe, F. Vallée, J. C. Gomet, and M. Morlais. The yield of metastable atoms through dissociative recombination of O_2^+ ions with electrons. *J. Chem. Phys.*, 91(9):5335–5342, November 1989.

[79] H. Böhringer, M. Durup-Ferguson, E. E. Ferguson, and D. W. Fahey. Collisional vibrational quenching of $O_2^+(v)$ and other molecular ions in planetary atmospheres. *Planet. Space Sci.*, 31(4):483–487, 1983.

[80] S. L. Guberman. Ab initio studies of dissociative recombination. In J. B. A. Mitchell and S. L. Guberman, editors, *Dissociative Recombination: Theory, Experiment and Applications I*, pages 45–60, Singapore, 1989. World Scientific.

[81] S. L. Guberman. Potential curves for dissociative recombination. In F. Brouillard and J. W. McGowan, editors, *Physics of Ion-Ion and Electron-Ion Collisions*, pages 167–200, New York, 1983. Plenum.

[82] S. L. Guberman and A. Giusti-Suzor. The generation of $O(^1S)$ form the dissociative recombination of O_2^+. *J. Chem. Phys.*, 95(4):2602–2613, August 1991.

[83] A. Petrignani, P. C. Cosby, F. Hellberg, R. D. Thomas, M. Larsson, and W. J. van der Zande. Electron energy dependence of the branching in dissociative recombination of O_2^+. *J. Chem. Phys.*, 122(23):234311, June 2005.

[84] S. L. Guberman. Accurate *ab initio* potential curve for the ground state of O_2. *J. Chem. Phys.*, 67(3):1125–1135, August 1977.

[85] A. Petrignani, P. C. Cosby, F. Hellberg, R. D. Thomas, M. Larsson, and W. J. van der Zande. Vibrationally resolved rate coefficients and branching fractions in the dissociative recombination of O_2^+. *J. Chem. Phys.*, 122(1):014302, January 2005.

[86] S. L. Guberman. Product angular distributions in dissociative recombination. *J. Chem. Phys.*, 120(20):9509–9513, May 2004.

[87] F. Hellberg, A. Petrignani, W. J. van der Zande, S. Rosén, R. D. Thomas, A. Neau, and M. Larsson. Dissociative recombination of NO^+: Dynamics of the $X\,^1\Sigma^+$ and $a\,^3\Sigma^+$ electronic states. *J. Chem. Phys.*, 118(14):6250–6259, April 2003.

[88] J. Semeter, M. Mendillo, J. Baumgardner, J. Holt, D. E. Hunton, and V. Eccles. A study of oxygen 6300 Å airglow production through chemical modification of the nighttime ionosphere. *J. Geophys. Res.*, 101(A9):19683–19699, September 1996.

[89] H. Takahashi, B. R. Clemesha, P. P. Batista, Y. Sahai, M. A. Abdu, and P. Muralikrishna. Equatorial F-region OI 6300 Å and OI 5577 Å emission profiles observed by rocket-borne airglow photometers. *Planet. Space Sci.*, 38(4):547–554, 1990.

[90] G. H. Dunn. Anisotropies in angular distributions of molecular dissociation products. *Phys. Rev. Lett.*, 8(2):62–64, January 1962.

[91] Thomas F. O'Malley and Howard S. Taylor. Angular dependence of scattering products in electron-molecule resonant excitation and in dissociative attachment. *Phys. Rev.*, 176(1):207–221, December 1968.

[92] S. L. Guberman. Isotope effects in dissociative recombination. In M. Larsson, J. B. A. Mitchell, and I. F. Schneider, editors, *Dissociative Recombination: Theory, Experiment and Applications IV*, pages 111–120, Singapore, 2000. World Scientific.

[93] Anthony O'Keefe and J. R. McDonald. Radiative lifetimes and kinetic studies of metastable $NO^+(a\,^3\Sigma^+)$ and $O_2^+(a\,^4\Pi_u)$. *Chem. Phys.*, 103:425–436, 1986.

[94] S. W. Bustamente, M. Okumura, D. Gerlich, H. S. Kwok, L. R. Carlson, and Y. T. Yee. Spin-forbidden radiative decay of the $a\,^4\Pi_u$ state of O_2^+. *J. Chem. Phys.*, 86(2): 508–515, January 1987.

[95] Chau-Hong Kuo, Thomas Wyttenbach, Cindy G. Beggs, Paul R. Kemper, and M. T. Bowers. Radiative lifetimes of metastable $O_2^+(a\,^4\Pi_u)$ and $NO^+(a\,^3\Sigma^+)$. *J. Chem. Phys.*, 92(8):4849–4855, April 1990.

[96] R. Marx, S. Fenistein, G. Mauclaire, J. Lemaire, and M. Heninger. The radiative lifetimes of $O_2^+(a\,^4\Pi_u, v)$ and $NO^+(a\,^3\Sigma^+, v)$ revisited. *Int. J. Mass Spec. Ion Proc.*, 132:143–148, 1994.

[97] J. R. Peterson and Y. K. Bae. Product states of H_3^+, H_2^+, and O_2^+ electron capture in Cs. *Phys. Rev. A*, 30(5):2807–2810, November 1984.

[98] W. J. van der Zande, W. Koot, J. R. Peterson, and J. Los. Charge exchange of O_2^+ with Cs: spectroscopy and predissociation pathways for the Π_g Rydberg states of O_2. *Chem. Phys. Lett.*, 140(2):175–180, September 1987.

[99] W. J. van der Zande, W. Koot, J. R. Peterson, and J. Los. O_2^+, $a\,^4\Pi_u$ collisions with Cs and Mg: formation of $(3s\sigma)\,^{3,5}\Pi_u$ Rydberg and repulsive states of O_2. *Chem. Phys.*, 126:169, 1988.

[100] W. J. van der Zande, J. Semaniak, V. Zengin, G. Sundström, S. Rosén, C. Strömholm, S. Datz, H. Danared, and M. Larsson. Dissociative recombination of H_2^+: Product state information and very large cross sections of vibrationally excited H_2^+. *Phys. Rev. A*, 54(6):5010–5018, December 1996.

[101] S. Krohn, Z. Amitay, A. Baer, D. Zajfman, M. Lange, L. Knoll, J. Levin, D. Schwalm, R. Wester, and A. Wolf. Electron-induced vibrational deexcitation of H_2^+. *Phys. Rev. A*, 62(3):032713, September 2000.

[102] D. Zajfman, S. Krohn, M. Lange, H. Kreckel, L. Lammich, D. Strasser, D. Schwalm, X. Urbain, and A. Wolf. Physics with molecular ions in storage rings. *Nucl. Instrum. Methods B*, 205:360–366, May 2003.

[103] E. C. Zipf. The excitation of the $O(^1S)$ state by the dissociative recombination of O_2^+ ions: electron temperature dependence. *Planet. Space Sci.*, 36(6):621–628, 1988.

[104] Z. Amitay et al. Dissociative recombination of vibrationally excited HD^+: State-selective experimental investigation. *Phys. Rev. A*, 60(5):3769–3785, November 1999.

[105] M. Geoghegan, N. G. Adams, and D. Smith. Determination of the electron-ion dissociative recombination coefficiens for several molecular-ions at 300 K. *J. Phys. B*, 24(10):2589–2599, May 1991.

[106] S. Laubé, L. Lehfaoui, B. R. Rowe, and J. B. A. Mitchell. The dissociative recombination of CO^+. *J. Phys. B*, 31:4181–4189, 1998.

[107] J. B. A. Mitchell and H. Hus. The dissociative recombination and excitation of CO^+. *J. Phys. B*, 18(3):547–555, February 1985.

[108] T. Mostefaoui, S. Laubé, G. Gautier, C. Rebrion-Rowe, B. R. Rowe, and J. B. A. Mitchell. The dissociative recombination of NO^+: the influence of the vibrational excitation state. *J. Phys. B*, 32:5247–5256, 1999.

[109] J. R. Peterson et al. Dissociative recombination and excitation of N_2^+: Cross-sections and product branching ratios. *J. Chem. Phys.*, 108(5):1978–1988, February 1998.

[110] C. H. Sheehan and J. P. St. Maurice. Dissociative recombination of N_2^+, O_2^+, and NO^+: Rate coefficients for ground state and vibrationally excited ions. *J. Geophys. Res.*, 109(A03302):A03302, 2004.

[111] M. R. Torr and D. G. Torr. The dissociative recombination of O_2^+ in the ionosphere. *Planet. Space Sci.*, 29(9):999–1010, 1981.

[112] J. L. Fox. The vibrational distribution of O_2^+ in the dayside ionosphere. *Planet. Space Sci.*, 34(12):1241–1252, 1986.

[113] M. Alagia, N. Balucani, L. Cartechini, P. Casavecchia, and G. G. Volpi. Dynamics of chemical reactions of astrophysical interest. In E. F. van Dishoeck, editor, *Molecules in Astrophysics: Probes and Processes*, pages 271–280, Amsterdam, 1997. Kluwer.

[114] M. R. Torr, R. G. Burnside, P. B. Hays, A. I. Stewart, D. G. Torr, and J. C. G. Walker. Metastable ^2D atomic nitrogen in the mid-latitude nocturnal ionosphere. *J. Geophys. Res.*, 81:531, 1976.

[115] J. L. Dulaney, M. A. Biondi, and R. Johnson. Electron temperature dependence of the recombination of electrons with NO^+ ions. *Phys. Rev. A*, 36(3):1342–1350, August 1987.

[116] D. Kley, G. M. Lawrence, and E. J. Stone. The yield of $N(^2D)$ atoms in the dissociative recombination of NO^+. *J. Chem. Phys.*, 66(9):4157–4165, May 1977.

[117] I. F. Schneider, I. Rabadan, L. Carata, L. H. Andersen, A. Suzor-Weiner, and J. Tennyson. Dissociative recombination of NO^+: calculations and comparison with experiment. *J. Phys. B*, 33:4849–4861, 2000.

[118] Z. Amitay and D. Zajfman. Dissociative recombination of CH^+: Cross section and final states. *Phys. Rev. A*, 54(5):4032–4050, November 1996.

[119] R. Wester, K. G. Bhushan, N. Altstein, D. Zajfman, O. Heber, and M. L. Rappaport. Radiative lifetime measurement of the $a\,^3\Sigma^+$ metastable state of NO^+ using a new type of electrostatic ion trap. *J. Chem. Phys.*, 110(24):11830–11834, June 1999.

[120] A. G. Calamai and K. Yoshino. Radiative lifetimes of the $a\,^3\Sigma^+$ metastable state of NO^+. *J. Chem. Phys.*, 101(11):9480–9486, December 1994.

[121] R. Marx, Y. M. Yang, G. Mauclaire, M. Heninger, and S. Fenistein. Radiative lifetimes and reactivity of metastable $NO^+(a\,^3\Sigma^+, v)$ and $O_2^+(a\,^4\Pi_u, v)$. *J. Chem. Phys.*, 95(4): 2259–2264, August 1991.

[122] M. J. Bearpark, N. C. Handy, P. Palmieri, and R. Tarroni. Spin-orbit interactions from self consistent field wavefunctions. *Mol. Phys.*, 80(3):479–502, October 1993.

[123] P. Palmieri, R. Tarroni, G. Chambaud, and P. Rosmus. On the radiative lifetimes of the $a\,^3\Sigma^+$ state of NO^+. *J. Chem. Phys.*, 99(1):456–465, July 1993.

[124] M. R. Manaa and D. R. Yarkony. A theoretical treatment of the $a\,^3\Sigma_1^+ \rightarrow X\,^1\Sigma_{0^+}^+$ spin-forbidden dipole-allowed radiative transition in NO^+. *J. Chem. Phys.*, 95(9): 6562–6566, November 1991.

[125] R. J. LeRoy. Chemical Physics Research Report. University of Waterloo, 2001. No. CP-642 R3.

[126] M. Fehér and P. A. Martin. *Ab initio* calculations of the properties of NO^+ in its ground electronic state $X\,^1\Sigma^+$. *Chem. Phys. Lett.*, 215(6):565–570, December 1993.

[127] M. J. Frisch, G. W. Trucks, H. B. Schlegel, et al., 1998. *GAUSSIAN 98*, Revision A.3, Gaussian, Inc., Pittsburgh, PA.

[128] H. Partridge, S. R. Langhoff, and C. W. Bauschlicher, Jr. Radiative lifetimes for the $X\,^1\Sigma^+$ state of NO^+. *Chem. Phys. Lett.*, 170(1):13–16, June 1990.

[129] W. J. van der Zande. (private communication) Note that there is a printing error in Fig. 2, Ref. 28.

[130] Å. Larson and A. E. Orel. Ion-pair formation and product branching ratios in dissociative recombination of HD^+. *Phys. Rev. A*, 64(6):062701, December 2001.

[131] S. L. Guberman. Dissociative recombination without a curve crossing. *Phys. Rev. A*, 49(6):R4277–R4280, June 1994.

[132] Å. Larson and A. E. Orel. Dissociative recombination of HeH^+: Product distributions and ion-pair formation. *Phys. Rev. A*, 59(5):3601–3608, May 1999.

[133] D. L. Albritton and A. L. Schmeltekopf. Potential energy curves for NO^+. *J. Chem. Phys.*, 71(8):3271–3279, October 1979.

[134] CRYRING staff. (private communication).

[135] J. B. A. Mitchell and C. Rebrion-Rowe. The recombination of electrons with complex molecular ions. *Int. Rev. Phys. Chem.*, 16(2):201–213, 1997.

[136] D. R. Bates. Single-electron transitions and cluster ion super-dissociative recombination. *J. Phys. B*, 25:3067–3073, 1992.

[137] D. R. Bates. Super dissociative recombination. *J. Phys. B*, 24:703–709, 1991.

[138] L. Andrews and M. Zhou. Infrared spectra of $(NO)_2^-$ and $(NO)_2^+$ isomers trapped in solid neon. *J. Chem. Phys.*, 111(13):6036–6041, October 1999.

[139] C. L. Lugez, W. E. Thompson, M. E. Jacox, A. S. Snis, and I. Panas. Infrared spectra of $(NO)_2^+$, $(NO)_2^-$, and $(NO)_3^-$ trapped in solid neon. *J. Chem. Phys.*, 110(21):10345–10358, June 1999.

[140] B. Urban, A. Strobel, and V. E. Bondybey. The $(NO)_2$ dimer and its ions: Is the solution near? *J. Chem. Phys.*, 111(19):8939–8949, November 1999.

[141] Y. Xie and H. F. Schaeffer, III. The puzzling infrared spectra of the nitric oxide dimer radical cation: A systematic application of Breuckner methods. *Mol. Phys.*, 98(14): 955–959, 2000.

[142] Y. Xie, H. F. Schaeffer, III, X.-Y. Fu, and R.-Z. Liu. The infrared spectrum of the nitric oxide dimer cation: Problems for density functional theory and a muddled relationship to experiment. *J. Chem. Phys.*, 111(6):2532–2541, August 1999.

[143] Y. Xie, W. Wang, K. Fan, and H. F. Schaeffer, III. Ring structure of the NO dimer radical cation: A possible new assignment of the mysterious IR absorption at 1424 cm^{-1}. *J. Chem. Phys.*, 117(21):9727–9732, December 2002.

[144] I. Fischer, A. Strobel, J. Staecker, and G. Niedner-Schatteburg. High resolution photoelectron spectra of the NO dimer. *J. Chem. Phys.*, 96(9):7171–7174, May 1992.

[145] S. H. Linn, Y. Ono, and C. Y. Ng. Molecular beam photoionization study of CO, N_2, and NO dimers and clusters. *J. Chem. Phys.*, 74(6):3342–3347, March 1981.

[146] C. Y. Ng, P. W. Tiedemans, B. H. Mahan, and Y. T. Lee. The binding energy between NO and NO^+. *J. Chem. Phys.*, 66(9):3985–3987, May 1977.

[147] L. Vikor et al. Branching fractions in the dissociative recombination of NH_4^+ and NH_2^+ molecular ions. *Astron. Astrophys.*, 344:1027–1033, 1999.

[148] It is noted that other papers do not always include the $\sqrt{2}$-factor in the expression of the total displacement.

[149] R. H. Dalitz. On the analysis of τ-meson data and the nature of the τ-meson. *Phil. Mag.*, 44:1068–1080, 1953.

[150] D. Strasser, L. Lammich, H. Kreckel, M. Lange, S. Krohn, D. Schwalm, A. Wolf, and D. Zajfman. Breakup dynamics and isotope effects in D_2H^+ and H_2D^+ dissociative recombination. *Phys. Rev. A*, 69:064702, 2004.

[151] L. Lammich, H. Kreckel, S. Krohn, M. Lange, D. Schwalm, D. Strasser, A. Wolf, and D. Zajfman. Breakup dynamics in the dissociative recombination of H_3^+ and its isotopomers. *Rad. Phys. Chem.*, 68:175, 2003.

[152] S. G. Lias,"Constants of Diatomic Molecules" in NIST Chemistry WebBook, by K. P. Huber and G. Herzberg (data prepared by J. W. Gallagher and R. D. Johnson, III), NIST Standard Reference Database Number 69, March 2003, National Institute of Standards and Technology, Gaithersburg MD, 20899 (http://webbook.nist.gov).

[153] C. S. Weller and M. A. Biondi. Recombination, attachment, and ambipolar diffusion of electrons in photo-ionized NO afterglows. *Phys. Rev.*, 172(1):198–206, August 1968.

[154] M. B. Någård et al. Dissociative recombination of $D^+(D_2O)_2$ water cluster ions with free electrons. *J. Chem. Phys.*, 117(11):5264–5270, September 2002.

[155] M. J. Jensen et al. Dissociative recombination and excitation of H_2O^+ and HDO^+. *Phys. Rev. A*, 60(4):2970–2976, October 1999.

[156] D. R. Bates. Dissociative recombination: Crossing and tunneling modes. *At. Mol. Opt. Phys.*, 34:427–486, 1994.

[157] B. K. Sarpal, J. Tennyson, and L. A. Morgan. Dissociative recombination without curve crossing: study of HeH^+. *J. Phys. B*, 27(24):5943–5953, December 1994.

[158] J. N. Bardsley. Configuration interaction in the continuum states of molecules. *J. Phys. B*, 1(3):349–364, May 1968.

[159] A. Giusti. A multichannel quantum defect approach to dissociative recombination. *J. Phys. B*, 13(19):3867–3894, October 1980.

[160] T. F. O'Malley. Rydberg levels and structure in dissociative recombination cross sections. *J. Phys. B*, 14(7):1229–1238, April 1981.

[161] M. J. Seaton. Quantum defect theory I. General formulation. *Proc. R. Soc. London*, 88 (4):801–814, August 1966.

[162] M. J. Seaton. Quantum defect theory II. Illustrative one-channel and two-channel problems. *Proc. R. Soc. London*, 88(4):815–832, August 1966.

[163] J. Dubau and M. J. Seaton. Quantum defect theory XIII. Radiative transitions. *J. Phys. B*, 17(3):381–403, February 1984.

[164] U. Fano. Quantum defect theory of l uncoupling in H_2 as an example of channel-interaction treatment. *Phys. Rev. A*, 2(2):353–365, August 1970. Erratum in Phys. Rev. A 15, 817 (1977).

[165] A. Giusti-Suzor and U. Fano. Alternative parameters of channel interactions I. Symmetry analysis of the two-channel coupling. *J. Phys. B*, 17(2):215–220, January 1984.

[166] A. Giusti-Suzor and U. Fano. Alternative parameters of channel interactions II. A hamiltonian model. *J. Phys. B*, 17(21):4267–4275, November 1984.

[167] A. Giusti-Suzor and U. Fano. Alternative parameters of channel interactions III. Note on a narrow band in the Ba J=2 spectrum. *J. Phys. B*, 17(21):4277–4283, November 1984.

[168] Ch. Jungen and S. C. Ross. Unified quantum-defect-theory treatment of molecular ionization and dissociation. *Phys. Rev. A*, 55(4):R2503, April 1997.

[169] R. Guerout, M. Jungen, and C. Jungen. Ab initio molecular quantum defect theory: I. Method of artificial well potentials. *J. Phys. B*, 37(15):3043–3055, August 2000.

[170] R. Guerout, M. Jungen, and C. Jungen. Ab initio molecular quantum defect theory: II. Rydberg and continuum states of NO. *J. Phys. B*, 37(15):3057–3073, August 2000.

[171] A. Giusti-Suzor, J. N. Bardsley, and C. Derkits. Dissociative recombination in low-energy e–H_2^+ collisions. *Phys. Rev. A*, 28(2):682–691, August 1983.

[172] H. Takagi. State-specific dissociative recombination at low energy. In A. Wolf, L. Lammich, and P. Schmelcher, editors, *Dissociative Recombination: Theory, Experiment and Applications VI*, pages 155–161, London, 2005. Institute of Physics and IOP Publishing.

[173] S. L. Guberman. New mechanisms for dissociative recombination. In L. J. Dubé, J. B. A. Mitchell, J. W. McComkey, and C. E. Brion, editors, *International Conference on the Physics of Electronic and Atomic Collisions XIX, Book of Invited Papers*, pages 307–316, New York, 1995. American Institute of Physics Press.

[174] S. L. Guberman. The production of $O(^1D)$ from dissociative recombination of O_2^{+*}. *Planet. Space Sci.*, 36(1):47–53, 1988.

[175] B. R. Lewis, J. P. England, S. T. Gibson, M. J. Brunger, and M. Allan. Electron energy-loss spectra of coupled electronic states: Effects of Rydberg-valence interactions in O_2. *Phys. Rev. A*, 63:022707, 2001.

[176] B. R. Lewis, P. M. Dooley, J. P. England, S. T. Gibson, K. G. H. Baldwin, and L. W. Torop. Non-Lorentzian line shapes for interfering rotational resonances in the predissociation of O_2. *Phys. Rev. A*, 55(6):4164–4167, June 1997.

[177] G. C. Groenenboom and D. T. Colbert. Combining the discrete variable representation with the S-matrix Kohn method for quantum reactive scattering. *J. Chem. Phys.*, 99 (12):9681–9696, December 1993.

[178] B. R. Lewis and S. T. Gibson. (private communication) The ascii data of the Σ potential curves of O_2^+ have been supplied to us along with the respective Rydberg-valence and spin-orbit couplings.

[179] R. P. Saxon and B. Liu. *Ab initio* configuration study of the valence states of O_2. *J. Chem. Phys.*, 67(12):5432–5441, December 1977.

[180] W. J. van der Zande, W. Koot, J. Los, and J. R. Peterson. Predissociation of the $d\,^1\Pi_g$ Rydberg state in O_2: Nature of the Rydbergvalence interactions. *J. Chem. Phys.*, 89 (11):6758–6770, December 1988.

Summary

2005
SEPTEMBER

Sun		4	**sUK**	18	25
Mon		5	sNL	19	26
Tue		6	sFR	20	27
Wed		7	Ack	21	28
Thu	1	A	CV	22	29
Fri	2	B	16	23	30
Sat	3	Ref	17	24	

Dissociative recombination of atmospheric ions - towards unravelling the physics behind airglows: what does this mean? Let us start with the first part of the title. Dissociative recombination is a reaction in which an electron and a molecular ion recombine to form a short-lived neutral molecule that subsequently dissociates into neutral fragments. Dissociative recombination takes place in plasmas, and since plasmas exist throughout the universe, it is a ubiquitous reaction. Plasmas are also found in planetary atmospheres, where at high altitudes the atmosphere is continuously bathed by ionising stellar and cosmic radiation. Dissociative recombination of atmospheric ions is of great importance to these ionospheres. The reaction offers three important aspects. First, it provides an efficient means for the removal of ions and slow electrons. In fact, the reaction is the dominant neutralisation process in many types of plasmas. Second, it is a very exothermic reaction and the energetic products can give rise to local heating, non-local thermal equilibrium effects, and even gravitational escape. Third, the reaction produces excited and reactive products. In ionospheric regions, where the particle densities are sufficiently low, these excited products have time to radiatively decay before they meet a collision partner and beautiful geocoronas of light are produced, called **airglows**. This brings us to the second part of the title. Unravelling the dissociative recombination reaction will unravel some of the physics behind airglows. The subject of the research presented in this thesis is about the dissociative recombination of atmospheric ions in the light of airglows.

Chapter 1 provides an introduction to the topics of airglows and dissociative recombination. This introduction revolves around the two goals of the research. The first goal is an investigation of the dissociative recombination of important atmospheric molecular ions in order to provide quantitative results relevant for atmospheric modelling. We carried out experiments to determine the efficiency of the dissociative recombination reaction and to identify and quantify the possible product and internal-state combinations. As dissociative recombination in its appearance in experiments is a rather non-intuitive reaction, this presented us with a second goal for the research. We wanted to gain insight into any possible general dependencies and mechanisms of the reaction. For the above mentioned purposes, experiments were performed on three molecular ions: the two major terrestrial ions, O_2^+ and NO^+, and the dimer ion, $(NO)_2^+$. In addition, a computational study was carried out to look into different dissociation mechanisms and their effects.

Chapter 2 describes the various experimental apparatus and tools used to achieve the stated aims. The experiments were performed at the heavy-ion storage ring, CRYRING. This ring provides a clean reaction-environment and allows for accurate control over the experimental conditions. For each experiment, the selected ions are created in an ion source and stored in the ring for many seconds at a velocity on the order of 1% of the speed of light. An electron beam is merged with this ion beam over a small distance for reactions to occur. The neutral fragments produced in this merged region are allowed to exit the ring via the so-called zero-degree arm in which various detection systems are situated. The high beam

energies make it possible to accurately set the relative velocity of the electrons with respect to the ions, i.e., the electron collision energy, even down to 0 eV. The long storage times allow ions with a permanent dipole moment to cool vibrationally through radiative decay. Mass selection ensures that only the desired ion species enters the ring. Inside the ring, the ions also collide with residual gas molecules, however, the high vacuum and beam energies result in a low background contribution. In the O_2^+ experiments presented here, a new ion source was especially developed to prepare and control the internal-state distributions of the ions. A fast-beam spectroscopy experiment was used to characterise these internal-state distributions using dissociative charge transfer reactions between O_2^+ and Cs. This experiment is described at the end of the chapter.

Chapter 3 covers the analysis of those data obtained from CRYRING. Three different types of data were analysed: the count rate of dissociation events in order to determine cross sections and rate coefficients of the reaction, i.e., the efficiency of the reaction, the count rate of individual products in order to determine the chemical fragmentation in the reaction, and the inter-fragment separations, which reflect the dynamics occurring in the reaction. Several experimental aspects were newly incorporated into the analysis with respect to earlier work. First, the effect of the so-called toroidal regions, where the electron beam is not fully parallel to the ion beam, is now accounted for in the branching behaviour of the dissociative recombination reaction. Second, the trapping of positive ions in the space charge of the electron beam is also treated at low electron energies. Third, the data on the dynamics of the dissociative recombination of NO^+ at different storage times is used to determine the lifetime of the metastable $NO^+(a\,^3\Sigma^+)$ state.

Chapter 4 is dedicated to the dissociative recombination of the O_2^+ ion. This chapter is divided into two parts. **Part one** treats the electron-collision-energy dependence of the reaction. The obtained product-state distributions and quantum yields from the dissociative recombination reaction of O_2^+ in its electronic and vibrational ground state at collision energies between 0 and 300 meV are presented. A water-cooled hollow cathode discharge source was used to produce the cold molecular ions. The collision-energy range is sufficient to allow the determination of temperature-dependent quantum yields and branching fractions for all atmospherically relevant electron temperatures below 1000 K. We find that the branching fractions over the different dissociation limits show distinct oscillations with increasing collision energy, whereas the associated product quantum yields are largely independent of the collision energy above 40 meV. The resonant behaviour observed in the cross section is not accompanied by sudden changes in the branching behaviour. The experimental data reflects a reaction that is isotropic; all relative orientations of the incoming electron with respect to the molecular axis seem equally efficient for dissociative recombination to occur. This isotropic behaviour is in contrast to recent theoretical predictions, a controversy that is not yet resolved. The oscillating branching behaviour and the observed isotropy may point to additional or different neutral states playing a role in the dissociation than those that are usually assumed to participate. **Part two** treats the internal-state dependence of the dissociative recombination reaction of O_2^+ in its electronic ground $X\,^2\Pi_g$ state. The absolute total rate coefficients as a function of collision energy up to 0.4 eV for five different vibrational populations of the ion beam are presented. The partial, i.e., vibrationally resolved, rate coefficients and branching fractions near 0 eV collision energy for the vibrational levels $v = 0$, 1, and 2 are also presented. The different vibrational populations were produced in a modified electron-impact ion source and the source was calibrated using $Cs{-}O_2^+$ dissociative charge

transfer reactions. This technique was developed at SRI International and AMOLF and the experiments were performed at SRI International. Furthermore, the effects of dissociative recombination and super elastic collision reactions, which also occur in the storage ring, on the vibrational populations are discussed. The results show that at low collision energies, the total rate coefficient is weakly dependent on the vibrational excitation, which therefore excludes the possibility of vibration-specific rates that differ by an order of magnitude. The partial rate coefficients, which describe the vibrational-state-dependent rate coefficient, as well as the partial branching fractions, are found to be strongly dependent on the vibrational level. The rate coefficient is the fastest for $v = 0$ and goes down by a factor of two or more for $v = 1$ and 2. The $O(^1S)$ quantum yield, linked to the green airglow, increases strongly upon increasing vibrational excitation. The present results may be extended to higher vibrational levels once the present limitations in the experimental and analytical approaches are overcome.

Chapter 5 covers the dissociative recombination of NO^+ in its ground, $X\,^1\Sigma^+$, and first excited metastable, $a\,^3\Sigma^+$, states. The branching behaviour of the ground state at 0, 1.2, and 5.6 eV collision energies is presented together with the branching behaviour of the metastable state at 0 eV. In addition, these data were compared to a primitive statistical model, revealing surprising results. Finally, the lifetime of the metastable $a\,^3\Sigma^+$ state was determined through the time-dependent signal contribution of its products. We find that the $NO^+(X\,^1\Sigma^+, v = 0)$ ground-state ions dissociate dominantly to the $N(^2D) + O(^3P)$ product limit at 0 and 1.2 eV collision energies, in agreement with previous observations. However, in contrast to earlier reports in which it is observed, the spin-forbidden $N(^4S) + O(^1D)$ channel is negligible at 0 eV. The $O(^1D)$ atom is responsible for the so-called red-line doublet in the atmospheric airglow. At 5.6 eV a new channel, $A'\,^2\Sigma^+$, opens, which leads directly to the production of highly energetic ground-state atoms. Nevertheless, no increase in the production of ground-state product atoms was observed. At each of the investigated collision energies, the observed branching fractions compare very favourably with the predictions from a primitive statistical model. The metastable $a\,^3\Sigma^+$ state is found to dissociate into nearly all of the energetically allowed product pairs. Its determined lifetime is $730(\pm 50)$ ms. Finally, the experimental observations have been complemented with *ab initio* calculations on the different radiative decay processes both for the $X\,^1\Sigma^+$ and $a\,^3\Sigma^+$ states. These calculations show that vibrational relaxation through infrared radiation is faster for $NO^+(a\,^3\Sigma^+, v > 0)$ ions than the electronic decay of the metastable-state ions to the electronic ground state.

Chapter 6 covers the dissociative recombination of the $(NO)_2^+$ dimer ion, a system that is significantly more reactive than its monomer NO^+. The experiments were aimed at looking for clues into why dimer ions have strongly enhanced thermal rates and on the effect of the weak bond on the reaction process. To this end we wanted to determine the dissociation dynamics of the dimer ion, and look for differences and similarities to the behaviour of the monomer. The DR rate reveals that the very large efficiency of the dimer rate with respect to the monomer is limited to electron energies below 0.2 eV. This observation almost certainly suggests an underlying reason for the high rate. The fragmentation products reveal that the break-up into the three-body channel NO + O + N dominates, followed by the break-up into NO + NO. The dominance of three-body fragmentation in the DR of small polyatomic ions has been observed before, and is an active area of continuing investigation. The $(NO)_2^+$ three-body fragmentation leads to electronic and vibrational ground-state products, $NO(v = 0) + O(^3P) + N(^4S)$, in a near majority of the cases. The internal product-state distribution of the

NO fragment shows similarity with the product-state distribution as predicted by the Franck-Condon overlap between a NO-moiety of the dimer ion and a free NO. The dissociation dynamics seem to be independent of any internal energy in the NO fragment. However, the dissociation dynamics do reveal a correlation between the kinetic energy of the NO fragment and the degree of conservation of linear momentum between the O and N product atoms. The observations support a mechanism in which the recoil takes place along one of the NO bonds in the dimer. In systems with equivalent covalent bonds, such as H_2O^+, recoil takes place in more than one coordinate. This forms the first detailed study into the dissociative recombination mechanisms operating in weakly-bound cluster ions.

Chapter 7 introduces model calculations performed on the dissociative recombination of O_2^+. We solve the coupled-channel equations, describing as many as possible of the mechanisms involved as suggested by earlier theoretical papers. Our model calculations focused on the consequences of the large electronic couplings between the n=3 to n=8 Rydberg states and the doubly excited capture state. The model contains the capture, autoionisation, and dissociation mechanisms of the reaction. The rates of these processes can be made independent of each other or, as they would be in nature, dependent on a single parameter. The model allows for the introduction of any number of states, electronic couplings, autoionisation, and spin-orbit couplings. Autoionisation of the electronic dissociative state is introduced through a complex potential. The dissociation and mixing of the involved states is treated exactly, solving the coupled equations for the nuclear motion using a diabatic basis. Although comparison with experiment is only possible on a qualitative level, previously determined branching and cross sections are compared with the simulations involving different capture states. We found that there is an optimum between electron capture and survival towards dissociation due to the influence of Rydberg-valence interactions. These interactions slow down the dissociation and reduce the survival towards dissociation. Our findings agree in general with other theoretical treatments and cannot shed light on the disagreement between theory and experiment.

In conclusion, experimentally, we have approached the limit of what is possible with the presently used tools. More accurate data will require improvements in both the control of the individual quantum states as well as in more precise or newer detection strategies that can fully resolve the reaction products connected to the different fragments or internal states. Further detector development that combines unit detection efficiency with fragment identification or high detection efficiency with arrival-time information could allow further progress in polyatomic and diatomic ions, respectively. We have learned that the dissociative recombination reaction of diatomic ions is highly dependent on the internal state of the ions and not as much on the electron energy. Green airglow production most likely increases upon increasing vibrational excitation of the O_2^+ ions, via the increased production of excited atomic oxygen fragments. The dissociative recombination of NO^+ at low collision energies does not contribute to the red airglow. Though state-selective behaviour is expected from the quantum-chemical point of view, the agreement with a primitive statistical model is surprising. The quantum-chemical approach cannot explain this statistical behaviour, whereas the statistical approach seems to contradict the various quantum-chemical aspects. Despite the apparent simplicity of the DR reaction, it is clear that progress still has to be made in both experiment and theory before we arrive at a complete picture, the ultimate goal being able to make accurate predictions that render laboratory studies superfluous.

In het Licht van Elektron-Ion Recombinatie

2005
SEPTEMBER

Sun		4	sUK	18	25
Mon		5	**sNL**	19	26
Tue		6	sFR	20	27
Wed		7	Ack	21	28
Thu	1	A	CV	22	29
Fri	2	B	16	23	30
Sat	3	Ref	17	24	

Helderheid stelt ons in staat te begrijpen
maar het zijn de mysteries die zorgen dat we het willen

Mijn Onderzoek

Dit proefschrift gaat over een reactie tussen elektronen en kleine molecuulionen, genaamd dissociatieve recombinatie. Dit is een elementaire, echter niet-intuïtieve, reactie met een aantal moeilijk te voorspellen eigenschappen. De reactie is daarom nog steeds omgeven met de nodige mysteries. Ten einde wat licht te werpen op een aantal vragen over dissociatieve recombinatie, hebben wij zowel het gedrag van de reactie bestudeerd als ook een aantal reactiewaarden bepaald. Dit onderzoek staat in het teken van de aëronomie; het onderzoek naar de moleculaire samenstelling en dynamica van de atmosfeer.

Belichting van het Onderzoek

Sinds jaar en dag hebben lichtverschijnselen in onze atmosfeer, zoals regenbogen, het noorderlicht en halo's de mensheid verwonderd en geïntrigeerd. Deze lichtende fenomenen zijn veelvuldig onderwerp geweest van onderzoek. Licht en alle vormen van elektromagnetische straling nemen een belangrijke plaats in bij onderzoek. In onze atmosfeer kan licht niet alleen chemische en fysische processen starten, maar kan het ook een product zijn in een aantal processen. Licht is hierdoor een mogelijke boodschapper van processen en stoffen vanaf moeilijk bereikbare plekken zoals de sterren en ook de grote hoogtes in onze eigen atmosfeer. Om de boodschap die het licht brengt te vertalen, is het noodzakelijk kennis te hebben van de betrokken variabelen en processen. Op dit punt bevinden zich nog de nodige onopgeloste vraagstukken, zo ook voor de interpretatie van de zogeheten airglow. Dit is een globaal en continu aanwezige gloed van een atmosfeer, waarneembaar als een zwakke, desalniettemin prachtige aura rondom een planeet. Elektromagnetische straling vanuit de ruimte, grotendeels in de vorm van zonlicht, is de drijvende kracht achter dit 'planetair fluoresceren'. De energetische straling ioniseert en exciteert de deeltjes in de bovenste lagen van een planeetatmosfeer en creëert daar de zogeheten ionosfeer. De ionosfeer, die zich op Aarde uitstrekt vanaf 60 km (grofweg twee keer zo hoog als de ozonlaag) tot ver daarboven, bevat hierdoor vrije elektronen, ionen, en geëxciteerde deeltjes. De aanwezigheid van vrije elektronen

resulteert in de mogelijkheid radiogolven te weerkaatsen voorbij de horizon. De airglow van de ionosfeer is het gevolg van de extreem ijle lucht op deze hoogtes, waardoor moleculaire botsingstijden kunnen oplopen tot vele seconden en zelfs uren. In afstand uitgedrukt komt dit overeen met vrije weglengtes tussen de moleculen van vele meters tot kilometers. Veel van de geëxciteerde atmosferische gassen hebben dan ook de tijd om te vervallen voordat ze weg reageren. Het zijn deze ionosfeerdeeltjes die de airglow genereren.

Airglow en Dissociatieve Recombinatie

De productie van de geëxciteerde en gloeiende atomen (in tegenstelling tot de moleculen) in de atmosfeer berust vooral op indirecte excitatie, waarbij de door het (zon)licht geïoniseerde deeltjes en geëxciteerde moleculen verder reageren. Een proces van groot belang hierin is de dissociatieve recombinatie reactie tussen de vrije elektronen en de aanwezige molecuulionen. Deze reactie heeft drie bijzondere eigenschappen. Ten eerste is de reactie een zeer efficiënt neutralisatieproces tussen ionen en thermische, laag energetische, elektronen mede vanwege de effectiviteit van de Coulombinteractie. Daarnaast is het 1000 keer zo effectief als de reactie tussen elektronen en atomaire ionen en dat maakt dissociatieve recombinatie zelfs het belangrijkste neutralisatieproces in vrijwel alle plasma's. Ten tweede is het een uitermate exotherme reactie. De resulterende energierijke producten verhitten de omgeving of zorgen lokaal voor niet-thermische effecten door bijvoorbeeld reacties aan te gaan die bij de heersende temperatuur zeer endotherm zijn. De reactieproducten kunnen zoveel kinetische energie hebben dat ze uit het gravitatieveld van een planeet kunnen ontsnappen. Ten derde produceert de reactie elektronisch geëxciteerde en daardoor reactieve producten welke op relatief lage hoogtes (ca. 80 km) een belangrijke rol spelen in de chemie en op grote hoogtes (ca. 150 km) tot de airglow bijdragen. Vermeldenswaardig hierbij zijn de groene en rode lijnemissies afkomstig van geëxciteerde zuurstofatomen. Op Aarde is de dissociatieve recombinatie reactie de hoofdbron van het nachtelijke groene licht. Interessant hieraan is dat er een verband is met de aanwezigheid van zuurstofmoleculen en daarmee een bijzonder aspect vormt van de Aardse atmosfeer, die sterk beïnvloed is door de biosfeer. Waarnemingen van de groene zuurstoflijn zouden wel eens een indicator kunnen vormen voor zuurstofrijke exo-planeten buiten ons zonnestelsel. Overigens zorgen de metingen aan het Aardse groene licht al voor de nodige controverses, mede door het gebrek aan specifieke kennis over de dissociatieve recombinatie reactie.

De Reactie in het Kort

Het dissociatieve recombinatieproces verloopt grofweg in twee stappen: de recombinatie en de dissociatie. Het elektron en het molecuulion recombineren in de eerste stap tot een kortlevend zeer aangeslagen molecuul. Vervolgens moet het aangeslagen molecuul relaxeren; het snelste niet-stralende kanaal is dissociatie in neutrale fragmenten. In de ionosfeer domineren de tweeatomige molecuulionen O_2^+, N_2^+ en NO^+, waarvan de reactieproducten N en O atomen zijn. Er zijn vaak meerdere combinaties van interne toestanden van het geproduceerde atoompaar energetisch mogelijk. Elke combinatie wordt aangeduid als een dissociatielimiet. Voor de aëronomie is het van belang te weten wat de vertakkingpercentages van deze limieten zijn, ofwel hoeveel atomen in welke interne toestand en met welke energie

er worden gemaakt. De omgevingstemperatuur alsmede de interne toestandsverdeling van de molecuulionen kunnen sterk variëren van omgeving tot omgeving. Het in kaart brengen van de afhankelijkheden van de reactie op de temperatuur en de toestandverdeling is dan ook erg gewenst. In een experiment is het echter te verkiezen om de eigenschappen van de dissociative recombinatie reactie direct te meten als functie van de botsingsenergie en de interne toestanden van het ion. Uit deze gegevens kan dan door middeling het gedrag bij elke temperatuur en toestandsverdeling bepaald worden. Een ander voordeel is dat op deze manier ook meer inzicht in de onderliggende dissociatiemechanismen verkregen wordt.

Experimenteren in een Opslagring voor Ionen

Een zware ionen opslagring is een ideaal instrument om dissociatieve recombinatie te bestuderen. Deze faciliteit verschaft namelijk een schone reactieomgeving en een hoge mate van controle over de experimentele condities. De opslagring CRYRING van het Manne Siegbahn Instituut in Stockholm is een indrukwekkend stuk technologie met een omtrek van 56 meter, een vacuüm van interstellaire proporties, opslagtijden van vele seconden en goed gedefinieerde condities. De ionen worden gecreëerd in een te kiezen ionenbron, waarna ze met hoge nauwkeurigheid geselecteerd en in de ring opgeslagen worden. Het hoge controleniveau kan worden toegeschreven aan het extreme vacuüm en de hoge snelheid van de ionenbundel welke in de orde van 1% van de lichtsnelheid is. Elektronen kunnen zeer precies worden samengevoegd met de ionenbundel in één van de rechte secties van de ring. De relatieve snelheid van elektronen en ionen, en dus de botsingsenergie, kan elke waarde van nul tot 100 eV krijgen. De elektronenbundel zelf is 'koud', dat wil zeggen dat de bundel een zeer smalle snelheidsverdeling kent; deze eigenschap maakt het mogelijk om de botsingsenergie met een nauwkeurigheid van ongeveer 2 meV vast te leggen. De lange opslagtijd staat toe dat ionen met een permanent dipoolmoment spontaan kunnen vervallen naar hun elektronische en vibrationele grondtoestand. In totaal leggen de molecuulionen afstanden af die ongeveer gelijk zijn aan die van de Aarde tot de maan.

Ionenbronnen en Metingen

Het meest uitdagende aspect van de experimenten is het produceren en vasthouden van de interne toestandsverdeling van de ionen. Hoewel voor ionen met een permanent dipoolmoment de opslagtijd in de ring de mate van elektronische en vibrationele relaxatie bepaalt, geldt dit niet voor symmetrische ionen, welke juist degenen zijn die veelvuldig voorkomen in planeetatmosferen. Voor deze ionen helpt slechts de keuze van de goede bron. Een belangrijk deel van mijn onderzoek betrof de ontwikkeling van een ionenbron speciaal voor het gecontroleerd wijzigen van vibratieverdelingen. Daarnaast was het vastleggen van de interne toestanden van de reactieproducten een minstens zo grote uitdaging. Deze meting is indirect; de kinetische energie van de neutrale deeltjes wordt bepaald aan de hand van plaatsgevoelige detectie. Elke kinetische energiewaarde is uniek geassocieerd met een dissociatielimiet, ofwel een dissociatiepaar. Het is niet moeilijk te bedenken dat bij bundelsnelheden die overeenkomen met een energie in de orde van MeV, het meten van de dissociatie-energie in de orde van enkele eV niet triviaal is.

Zuurstof

Zuurstof als moleculair ion is het meest voorkomende molecuulion in de atmosferen van de binnenste planeten van ons zonnestelsel. Op Aarde komen deze ionen direct voort uit de ionisatie van zuurstofmoleculen. Op Venus en Mars gebeurt dit indirect via de ionisatie van het overvloedig aanwezige kooldioxide. De interne toestanden van de Aardse ionen verschillen hierdoor sterk van de Martiaanse en Venusiaanse ionen. Daarnaast is de ionosfeer een stuk heter op Aarde vanwege het gebrek aan een efficiënt koelingmechanisme. Dissociatieve recombinatie van O_2^+ is een bron van geëxciteerde $O(^1S)$ en $O(^1D)$ atomen en daarmee een bron van respectievelijk de groene en rode lijnemissies. De reactie produceert snelle atomen met vele eV aan kinetische energie. Op Mars leidt dit tot ontsnapping uit de atmosfeer, waar een minimale snelheid van 5 km/s, ofwel 2 eV voor zuurstofatomen, nodig is om te ontsnappen. Het O_2^+ systeem is vanwege een aantal specifieke kwantummechanische aspecten, naast de aëronomische relevantie, ook een prachtig systeem vanuit het oogpunt van de fysica. De intramoleculaire weg naar het groene licht haalt hieruit zelfs zijn bestaansrecht.

Mijn onderzoek is een eerste stap naar het in kaart brengen van het dissociatiegedrag van zuurstof met variërende botsingsenergieën en interne vibratietoestanden. De energieafhankelijkheid van de reactie is onderzocht met zuurstofionen in hun grondtoestand. De vibratieafhankelijkheid is onderzocht bij 0 eV botsingsenergie. Hieruit zijn meerdere interessante resultaten gekomen. Als eerste is de vibratieafhankelijkheid erg sterk in tegenstelling tot de zwakkere energieafhankelijkheid. Het energiegedrag laat zien dat de vertakkingpercentages naar de dissociatielimieten oscilleren met botsingsenergie; een teken van concurrerende dissociatiewegen. De totale hoeveelheid geproduceerde $O(^3P)$, $O(^1D)$ en $O(^1S)$ over alle dissociatielimieten blijft echter verrassend constant. Bij een toenemend vibratieniveau in het molecuulion neemt de productie van $O(^1S)$ sterk toe. Omdat de efficiëntie van de reactie afneemt blijft er in aëronomische modellen een gering effect over. Verder blijkt de reactiekans ongevoelig voor de oriëntatie van het molecuulion ten opzichte van het inkomende elektron bij alle onderzochte botsingsenergieën. Bovengenoemd gedrag kan nog niet verklaard worden aan de hand van de moleculaire toestanden en dissociatieroutes die traditioneel vanuit de theorie van belang worden geacht.

Stikstofoxide

Op Aarde zijn de concentraties van geladen stikstofmonoxide en zuurstof ongeveer gelijk. Dissociatieve recombinatie van dit stikstofmonoxide kan energetisch resulteren in $O(^1D)$ atomen en is daarmee een mogelijke bijdrager van de rode lijnemissie. De $O(^1D)$ productie is echter verboden vanwege de regels van elektron-spinbehoud en wordt verwacht nul te zijn. De $N(^2D)$ productie, een blauwe lijnstraler en een ook zeer reactief deeltje, is wel toegestaan.

Mijn onderzoek brengt de productverdeling van de dissociatieve recombinatie van NO^+ bij 0, 1 en 5 eV botsingsenergie in kaart. Specifieke aandachtpunten waren het verboden kanaal bij 0 eV, de eventuele hoekafhankelijkheid tussen het inkomende elektron en de molekuulas van het ion bij 1 eV en de productie van grondtoestandatomen bij 5 eV. Dit laatste is verwacht vanwege de vergrote invangkans in de neutrale toestand die direct tot deze producten leidt. Daarnaast hebben we de resultaten vergeleken met een primitieve statistische benadering. De spinverboden limiet bleek inderdaad niet aanwezig te zijn. Dit betekent dat het NO^+ ion niet bijdraagt aan de rode lijnemissie. Bij 1 eV zien we een extra

dissociatielimiet die mogelijk is vanwege de toegevoegde energie. Een opvallende hoekafhankelijkheid is waarneembaar in de dominante dissociatie naar de $N(^2D) + O(^3P)$ limiet. Bij 5 eV blijken zowat alle energetisch mogelijke limieten mee te doen, behalve de grondlimiet $N(^4S) + O(^3P)$. Voor elke botsingsenergie is de productie van het belangrijke $N(^2D)$ atoom dominant. De percentages van de dissociatielimieten tonen een verrassende overeenkomst met de verwachtingen gebaseerd op de statistische benadering bij elke onderzochte botsingsenergie.

Superdissociatieve Recombinatie

In de lage ionosfeer van de Aarde, rond 60-90 km hoogte, nemen vanwege de hogere druk en de verhoogde kans op reacties, complexere ionen toe ten koste van tweeatomige ionen. De belangrijkste ionen zijn de watercluster ionen. In het creatieproces van deze ionen spelen dimeerionen van zuurstof, stikstof en stikstofmonoxide een cruciale rol. De efficiëntie van de dissociative recombinatie van dimeerionen ligt gemiddeld een factor 10 hoger dan dat van hun tegenhangers, de monomeren. De hoge reactiesnelheid bij dimeerionen wordt daarom aangeduid met superdissociatieve recombinatie. Zwakgebonden dimeerionen vormen een aparte groep dimeerionen met een hoge mate van symmetrie. Het $(NO)_2^+$ ion is zo'n dimeerion.

Mijn onderzoek gaat in op de superefficiëntie van de reactie en op de eventuele lokalisatie van het invang- en dissociatieproces. Daarnaast is de fragmentatie van het polyatomig molecuul bepaald. De superdissociatie blijkt gelimiteerd te zijn tot lage botsingsenergieën, dus trage elektronen. De dimeer dissocieert bovenal in drie deeltjes, namelijk NO, O en N, waarbij de fragmenten zich het vaakst in de grondtoestand bevinden. De reactie lijkt gelokaliseerd te zijn in een van de NO deeltjes, waarbij de zwakke binding met het andere NO deeltje het moet begeven.

Modelberekeningen op Zuurstof

Een diepere kijk op de reactie belicht het moeilijk te voorspellen gedrag van de dissociatieve recombinatie reactie. Dit heeft te maken met de vele aspecten die meetellen. Bij recombinatie hangt de invangkans van het elektron af van de initiële relatieve snelheid van het elektron, de oriëntatie van het molecuul ten opzichte van het inkomende elektron, de effectieve grootte van het ion en de aanwezigheid van geschikte neutrale dubbelaangeslagen toestanden van het molecuul. Mocht recombinatie optreden, dan kan auto-ionisatie optreden voordat het molecuul uiteenvalt, waarbij het elektron weer wegvliegt. Tijdens het uiteenvallen kan het molecuul kiezen uit een wirwar van mogelijke toestanden, die elkaar beïnvloeden en naar verschillende dissociatielimieten kunnen leiden. Om alles nog gecompliceerder en meer intrigerend te maken blijken de kans op recombinatie, de efficiëntie van auto-ionisatie en de complicaties in de mogelijke routes naar dissociatie af te hangen van één moleculair aspect. Daarom hebben wij berekeningen uitgevoerd op zuurstofmodellen, waarbij we met deze aspecten konden spelen. In de modelberekeningen laten we zien wat de invloed is van de verschillende deelprocessen. Wij vonden dat een grote recombinatiekans beslist niet garant staat voor een efficiënt dissociatief recombinatieproces; er is een optimum tussen recombinatie, auto-ionisatie en snelle dissociatie. Onze berekeningen komen in grote lijnen

overeen met eerdere theoretische werken en bieden geen uitkomst voor het verschil tussen experiment en de theoretische voorspellingen betreffende O_2^+.

Een Lichtpunt in het Donker

De experimenten en de experimentele ontwikkeling hebben geleid tot kwantitatieve resultaten van belang voor aëronomie, alsmede interessante bevindingen die gebruikt kunnen worden om tot een verder inzicht te komen. Er is een discrepantie tussen de huidige theorie en experimenten die erop wijzen dat de selectie van belangrijke toestanden en koppelingen in berekeningen van het dissociatieproces wel eens anders kon zijn. Daarnaast voorspelt de huidige kwantummechanische benadering de waargenomen vibratieafhankelijkheid en de zwakkere energieafhankelijkheid. Het schiet echter tekort in de precieze tendensen en kwantificering hiervan. Daartegenover staat dat de voorspelde waarden van de statistische benadering verrassende overeenkomsten tonen met de waarnemingen. Deze benaderingwijze schiet echter tekort in het verklaren van de kwantumaspecten zoals de vibratieafhankelijkheid. Het is duidelijk dat zowel experimenteel als in theorie nog grote stappen gezet moeten worden voordat we het ultieme doel bereiken waarin laboratoriumexperimenten overbodig zijn geworden wegens de bereikte voorspellingskracht.

Dans la Lumière de la Recombinaison Électron-Ion

2005
SEPTEMBER

Sun		4	sUK	18	25
Mon		5	sNL	19	26
Tue		6	**sFR**	20	27
Wed		7	Ack	21	28
Thu	1	A	CV	22	29
Fri	2	B	16	23	30
Sat	3	Ref	17	24	

Clarté nous permet de comprendre,
mais ce sont les mystères qui font en sorte qu'on le veuille

Ma Recherche

Cette thèse s'intéresse à la réaction entre des électrons et des petits ions moléculaires, nommée **recombinaison dissociative**. C'est une réaction élémentaire, pourtant non-intuitive, avec des caractéristiques difficiles à prédire. Cette réaction est ainsi toujours entourée de mystères. Afin de clarifier des questions sur la recombinaison dissociative, nous avons non seulement étudié le comportement de la réaction elle-même, mais aussi désigné des valeurs de réaction. Cette recherche est placée sous le signe de l'aéronomie; la recherche sur la composition moléculaire et la dynamique atmosphérique.

Lumière sur la Recherche

Les phénomènes lumineux dans notre atmosphère comme les arcs-en-ciel, la lumière nordique et les halos ont depuis toujours émerveillés et intrigués l'humanité. Ces phénomènes ont souvent été sujets de recherche. La lumière et toutes les formes de radiation électromagnétique prennent des places importantes dans la recherche. Dans notre atmosphère la lumière n'active pas seulement des processus chimiques et physiques, mais elle peut aussi être le produit même d'un ensemble de processus. La lumière fournit ainsi des informations précieuses sur des processus et des compositions chimiques depuis des endroits difficilement accessibles comme les étoiles, mais aussi depuis les altitudes élevées de notre propre atmosphère. Pour traduire les messages que transmet la lumière, il est nécessaire de connaître les variables et processus concernés. Sur ce point il existe toujours des problèmes irrésolus, en particulier pour l'interprétation des '**airglows**', une luminosité continuellement présente et perceptible comme une aura diffuse et magnifique autours d'une planète. L'énergie sous-jacente et responsable de cette fluorescence planétaire est la radiation électromagnétique dans l'espace en grande partie sous forme de lumière solaire. Cette radiation électromagnétique ionise et excite les particules présentes dans les couches supérieures d'une atmosphère planétaire et y crée l'ionosphère. L'ionosphère qui s'étend sur la Terre à partir de 60 km (à peu près deux fois plus haut que la couche d'ozone), jusqu'à des altitudes bien plus élevées, est

constituée d'électrons libres, d'ions et de particules excitées. La présence d'électrons libres rends possible la réflexion des ondes radio au-delà de l'horizon. L'airglow de l'ionosphère est la conséquence d'air extrêmement rare à ces altitudes, ce qui fait que le temps entre les collisions peut augmenter de plusieurs secondes jusqu'à des heures. Traduit en distance ceci correspond avec des distances de plusieurs mètres jusqu'à des kilomètres où les particules excitées ne rencontrent pas d'autres particules. Ces particules excitées ont alors le temps de retomber dans un état d'énergie sous-jacente nommé la relaxation. L'énergie qui est ainsi produite est transmise en tant que lumière. C'est l'ensemble de ces particules qui génèrent l'airglow.

Airglow et Recombinaison Dissociative

La production d'atomes excités et brillants dans l'atmosphère repose surtout sur l'excitation indirecte, où les particules ionisées par la lumière solaire et les molécules excitées continuent de réagir. Un processus essentiel est la recombinaison dissociative entre les électrons libres et les ions moléculaires présents. Cette réaction a trois propriétés particulières. Premièrement, la réaction est un processus de neutralisation très efficace entre des ions et des électrons à basse énergie, entre autres, à cause de l'efficacité de l'interaction de Coulomb. De plus, cette réaction est 1000 fois plus efficace que la réaction entre des électrons et des ions atomiques et cela fait de la recombinaison dissociative même le processus de neutralisation le plus important dans presque tous les plasmas. Deuxièmement, c'est une réaction extrêmement exothermique. L'énergie qui en résulte, soit chauffe le milieu ambiant, soit provoque localement des effets iso-thermiques en activant par exemple des réactions fortement endothermiques à la température ambiante. Les produits de la réaction peuvent avoir une énergie cinétique si importante qu'ils peuvent s'échapper du champ gravitationnel d'une planète. Troisièmement, cette réaction crée des produits excités et par ainsi réactifs qui jouent un rôle important dans la chimie à des altitudes basses (environ 80 km) et qui contribuent à l'airglow à des altitudes élevées (environ 150 km). Il faut mentionner ici que les lignes d'émission vertes et rouges sont issues d'atomes d'oxygène excités. Sur la Terre, la recombinaison dissociative est la source principale de la lumière nocturne verte. Ce qui est remarquable est que la présence de molécules d'oxygène donne un aspect particulier de l'atmosphère terrestre qui est très influencée par la biosphère. Les perceptions de la ligne verte d'oxygène pourraient très bien former une indication de l'existence d'exoplanètes hors de notre système solaire. Par ailleurs, sur la Terre les mesures sur la lumière verte sont déjà controversées, entre autres en raison d'un manque de connaissances spécifiques sur la recombinaison dissociative.

La Réaction en Bref

Le processus de la recombinaison dissociative peut être grossièrement divisé en deux étapes: la recombinaison et la dissociation. L'électron et l'ion moléculaire recombinent dans la première étape en une molécule qui est énergiquement fortement excitée et qui a une vie courte. Ensuite, la molécule excitée doit se relaxer; le chemin non-radiatif le plus rapide est la dissociation en fragments neutres. Dans l'ionosphère les ions moléculaires O_2^+, N_2^+ et NO^+ sont dominants; les produits de ces réactions sont les atomes N et O. Il est énergiquement possible qu'il existe plusieurs combinaisons d'états internes de produits de réaction. Chaque

combinaison définie une limite de dissociation. Pour l'aéronomie il est important de connaître les pourcentages de ramification de ces limites ou bien de savoir la quantité d'états internes des produits de réaction ainsi que leurs énergies cinétiques. Selon l'environnement, la répartition des états internes des ions moléculaires ainsi que leur température peuvent fortement varier. La classification des dépendances de la réaction vis-à-vis de la température et des répartitions d'états est alors souhaitée. Par contre, pendant une expérience il est d'avantage souhaitable de mesurer les propriétés de la recombinaison dissociative directement en fonction de l'énergie de collision et des états internes de l'ion. En analysant ces données on peut déterminer le comportement de cette réaction à toutes les températures et répartitions d'états. Un autre avantage est qu'il est ainsi possible de mieux comprendre les mécanismes sous-jacents de dissociation.

Expériences dans un Anneau de Stockage d'Ions

Un anneau de stockage d'ions lourds est un instrument idéal pour étudier la recombinaison dissociative. Cet immense appareil fournit un environnement de réaction propre et un fort contrôle sur les conditions expérimentales. L'anneau de stockage CRYRING de l'Institut Manne Siegbahn à Stockholm est un ouvrage technologique impressionnant avec une circonférence de 56 mètres, un vide de proportion interstellaire, un temps de stockage de plusieurs secondes et avec des conditions bien définies. Les ions sont créés dans une source d'ions choisie. Ils sont ensuite sélectionnés avec une grande précision et stockés dans l'anneau. Le fort contrôle est obtenu grâce au vide extrême et à la grande vitesse du faisceau d'ions qui est de l'ordre de 1% de la vitesse de la lumière. Les électrons peuvent être joints avec grande précision au faisceau d'ions dans une des sections de l'anneau. La vitesse relative des électrons et des ions, c'est à dire l'énergie de collision, peut varier entre 0 et 100 eV. Le faisceau d'électrons est froid, c'est-à-dire qu'il a une répartition de vitesse très étroite. Cette propriété donne la possibilité de définir l'énergie de collision avec une précision d'environ 2 meV. Le temps long de stockage permet aux ions possédant un moment dipolaire permanent de relaxer spontanément à leur état de base électronique et vibratoire. Au total les ions moléculaires franchissent des distances à peu près identiques à celle qui sépare la Terre de la Lune.

Sources d'Ions et Mesures

Le plus grand défi d'une expérience dans un anneau de stockage est d'obtenir et de garder les états internes des ions moléculaires. Bien que pour des ions ayant un moment dipolaire permanent, le temps de stockage dans l'anneau détermine le degré de relaxation électronique et vibratoire, ceci ne vaut pas pour des ions symétriques qui justement sont ceux qui sont le plus souvent présents dans les atmosphères planétaires. Pour ces ions, seul le choix d'une bonne source peut aider. Un aspect important de ma recherche concernait le développement d'une source d'ions avec laquelle il est possible de contrôler la répartition des états internes. Un autre grand défi est de déterminer les états internes des produits de la recombinaison dissociative. La mesure est indirecte: l'énergie cinétique des particules neutres est définie par une détermination de l'endroit où les particules touchent le détecteur. Chaque valeur d'énergie cinétique est uniquement associée à une limite de dissociation. Il n'est pas dur

d'imaginer qu'avec une vitesse de faisceau de particules qui correspond à une énergie de l'ordre de MeV, une mesure d'énergie cinétique qui est relâchée dans la réaction de l'ordre de quelques eV n'est pas trivial.

Oxygène

L'ion d'oxygène est l'ion moléculaire le plus souvent présent dans les atmosphères des planètes intérieures de notre système solaire. Sur la Terre, ces ions sont le produit direct de l'ionisation des molécules d'oxygène. Sur Vénus et Mars, cela se produit indirectement via l'ionisation du dioxyde de carbone (CO_2) dominant. Les états internes des ions terrestres diffèrent alors fortement de ceux de Mars et de Vénus. De surcroît, l'ionosphère de la Terre est plus chaude car elle est dépourvue d'un système de refroidissement efficace. La recombinaison dissociative de O_2^+ est une source d'atomes $O(^1S)$ et $O(^1D)$ excités et ainsi une source d'émission de lignes vertes et rouges. La réaction produit des atomes rapides avec une énergie cinétique de plusieurs eV. Sur Mars cela conduit à l'échappement des atomes de l'atmosphère; la vitesse d'échappement nécessaire est 5 km/s, ou bien 2 eV pour des atomes d'oxygène. Le système O_2^+ n'est pas seulement d'une importance aéronomique, mais aussi un système fabuleux du point de vue de la physique à cause de certains aspects spécifiques de la mécanique quantique. La production de la lumière verte en tire même son droit d'existence.

Ma recherche est une première étape pour dresser en carte le comportement de dissociation d'oxygène en ce qui concerne l'énergie de collision et l'état interne variable de vibration. La dépendance vis-à-vis de l'énergie de la réaction est examinée avec des ions d'oxygène dans leur état de base. La dépendance vibratoire est examinée avec une énergie de collision d'à peu près 0 eV. Plusieurs résultats intéressants ont ainsi été déduits. Premièrement, la dépendance vibratoire est très élevée par rapport à celle de l'énergie qui est plus faible. Le comportement de l'énergie montre que les pourcentages de ramification vers les limites de dissociation oscillent avec l'énergie de collision; signe de trajets de dissociation concurrents. Ce qui est surprenant est que la quantité totale produite de $O(^3P)$, $O(^1D)$ et $O(^1S)$ sur toutes les limites de dissociation reste constante. Par contre, la production de $O(^1S)$ augmente fortement quand le niveau de vibration s'élève. Parce que l'efficacité de la réaction diminue, les modèles aéronomiques ne prennent en compte qu'un effet moyen. De plus, la probabilité de réaction paraît insensible à l'orientation de l'ion moléculaire par rapport à l'électron entrant pour toutes les énergies de collision étudiées. Le comportement mentionné ci-dessus ne peut pas encore être expliqué à l'aide des états moléculaires et des trajets de dissociation qui sont traditionnellement jugés important par la théorie.

Oxyde d'Azote

Sur la Terre les concentrations de monoxyde d'azote chargé et d'oxygène chargé sont à peu près identiques. La recombinaison dissociative de ce monoxyde d'azote peut énergiquement produire des atomes $O(^1D)$ et par ainsi probablement contribuer à l'émission de lignes rouges. La production de $O(^1D)$ est par contre interdite à cause des règles de conservation du spin de l'électron (la rotation de l'électron sur lui-même) et est supposée nulle. La production de $N(^2D)$, une émettrice de lignes bleues et une particule très réactive, est par contre parfaitement autorisée.

Ma recherche a permis de dresser en carte la ramification des produits de la recombinaison dissociative de NO^+ à des énergies de collision de 0, 1 et 5 eV. Les aspects essentiels dans ma recherche étaient la bande interdite à 0 eV, la dépendance éventuelle de l'angle entre l'électron entrant et l'axe moléculaire de l'ion à 1 eV et en plus, à 5 eV, la production d'atomes dans un état de base. Ce dernier est attendu à cause de la probabilité de capture élevée dans l'état neutre qui mène directement à ces produits. De plus, nous avons comparé les résultats avec une approche statistique simple. La limite de spin interdite semblait effectivement ne pas être présente ce qui signifie que l'ion NO^+ ne contribue pas à l'émission de lignes rouges. À 1 eV on voit une limite de dissociation supplémentaire qui est rendue possible grâce à l'énergie ajoutée. Une dépendance angulaire évidente est perceptible dans la dissociation dominante vers la limite $N(^2D) + O(^3P)$. À 5 eV pratiquement toutes les limites énergiquement possibles semblent participer, sauf la limite de base $N(^4S) + O(^3P)$. Pour chaque énergie de collision la production de l'atome $N(^2D)$ est dominante. Les pourcentages des limites de dissociation montrent une analogie surprenante avec les prévisions basées sur l'approche statistique pour chaque énergie de collision étudiée.

Recombinaison Ultra Dissociative

Dans l'ionosphère basse de la Terre, entre 60-90 km d'altitude, le nombre d'ions complexes augmente au détriment des ions diatomiques à cause d'une pression plus élevée et d'une plus grande possibilité de réactions. Les ions les plus importants sont les clusters d'ions d'eau. Dans le processus de création de ces ions, les ions dimères d'oxygène, d'azote et de monoxyde d'azote, jouent un rôle principal. L'efficacité de la recombinaison dissociative des ions dimères est en moyenne 10 fois plus efficace que celle de ses opposants, les monomères. La grande vitesse de réaction chez les ions dimères est alors indiquée avec **recombinaison ultra dissociative**. Des ions dimères faiblement liés forment un groupe d'ions dimères séparé. L'ion $(NO)_2^+$ est un tel ion dimère.

Ma recherche s'intéresse à l'efficacité élevée de la réaction et à l'éventuelle localisation des processus de capture et de dissociation. De plus, la fragmentation de la molécule poly-atomique en est déduite. L'ultra dissociation semble être limitée à des faibles énergies de collision, autrement dit à des électrons lents. Le dimère se dissocie souvent en trois particules, à savoir NO, O et N, où ces trois fragments se trouvent le plus souvent dans leurs états de base. La réaction paraît être localisée dans une des particules de NO où le lien avec l'autre particule de NO est trop faible pour pouvoir se maintenir.

Calculs de Modèle sur l'Oxygène

Une vue plus approfondie sur ces réactions montre le comportement complexe de la recombinaison dissociative. Ceci a un rapport avec les nombreux aspects qui entrent en jeu. Pendant une recombinaison, la probabilité de capture de l'électron entrant dépend de sa vitesse relative initiale, de l'orientation de la molécule par rapport à cet électron, de la taille effective de l'ion et de la présence d'états neutres et doublement excités des molécules. Si une recombinaison intervient, une auto-ionisation peut se produire avant que la molécule ne se dissocie et donc que l'électron ne s'échappe à nouveau. Pendant la dissociation, la molécule a le choix entre plusieurs états possibles qui s'influencent et qui peuvent mener à

des différentes limites de dissociation. Pour rendre le tout encore plus compliqué et intriguant, la probabilité de recombinaison, l'efficacité de l'auto-ionisation et les complications dans les divers trajets de dissociation dépend d'un simple aspect moléculaire. C'est pour cela que nous avons effectué des calculs de modèle sur l'oxygène, où nous avons pu jouer avec les aspects mentionnés ci-dessus. Dans les calculs on montre l'influence des divers processus individuels. On a trouvé qu'une grande probabilité de recombinaison ne garantit en aucun cas un processus de recombinaison dissociative effectif; il existe un optimum entre recombinaison, auto-ionisation et dissociation rapide. Nos calculs montrent des similarités avec d'autres travaux théorique et n'expliquent pas la différence entre les expériences et les prédictions concernant l'oxygène.

Une Lueur dans l'Obscurité

Les expériences et le développement expérimental ont mené à des résultats quantitatifs importants pour l'aéronomie ainsi qu'à des constatations intéressantes qui peuvent être utilisées pour obtenir une plus grande compréhension des processus de recombinaison dissociative. Il y a une discordance entre la théorie actuelle et les expériences qui montre que la sélection des états moléculaires et leurs associations dans les calculs du processus de la dissociation pourraient très bien être différents. Les calculs effectués depuis le modèle le confirment. De plus, la vue mécanique quantique actuelle prédit les dépendances vibratoires et énergétiques observées dans les expériences, mais ne peut pas prédire les tendances précises et non plus donner une bonne quantification. En contrepartie, la prédiction de vue statistique montre des correspondances surprenantes avec les observations expérimentales, mais est en défaut en ce qui concerne les dépendances. Il est clair qu'au niveau expérimental aussi bien qu'au niveau théorique d'énormes progrès sont encore nécessaires avant de pouvoir atteindre le but ultime où les expériences en laboratoire seront devenues superflues grâce à la force de prédiction obtenue.

Dankwoord

Acknowledgements

Discours de Remerciement

2005
SEPTEMBER

Sun		4	sUK	18	25
Mon		5	sNL	19	26
Tue		6	sFR	20	27
Wed		7	**Ack**	21	28
Thu	1	A	CV	22	29
Fri	2	B	16	23	30
Sat	3	Ref	17	24	

De afgelopen jaren zijn geweldig geweest en ik ben blij deze periode te mogen afronden met het proefschrift wat je hier in handen hebt. Natuurlijk kan ik daarbij niet vergeten mijn dank te betuigen aan de nodige mensen. Mijn onderzoek heeft me langs vele wegen geleid en ik heb dan ook vele indrukwekkende mensen mogen ontmoeten. Het begon eind 2000, toen ik solliciteerde naar een project in de atmosferische foto fysica groep van Wim van der Zande op het FOM Instituut AMOLF te Amsterdam. Hier overdonderde Wim mij met zijn passie voor de wetenschap en voelde ik me al snel op mijn plek. Wim, jij hebt in mij, als pas afgestudeerde in een veld compleet anders dan het jouwe, potentieel gezien en mij de kans gegeven mijn passie te vinden. Je bent een fantastische begeleider, begaan met je studenten, hun werk, de verbreding van kennis, alsmede de sociale aspecten van de werkomgeving. Je nieuwsgierigheid is prikkelend, je enthousiasme is aanstekelijk, je inzicht en wijsheid zijn een beetje intimiderend, maar worden gelukkig gecompenseerd door je bescheidenheid. Je eerlijkheid is, alhoewel confronterend, ontzettend gewaardeerd en je optimisme en inzet zijn verrijkend. Wat ik je graag wil laten weten is dat jij je vertrek naar Nijmegen hebt weten om te zetten in een voor mij positieve ervaring, waarbij we elkaar vaker zijn gaan zien dan daarvoor.

Een vaak bewandelde weg gedurende de afgelopen jaren was die naar Zweden. In Stockholm vond namelijk het overgrote deel van de experimenten plaats. These experiments were carried out with help of Mats Larsson's group, where everyone was ready to assist, even when it concerned the night shifts or providing the meals. Mats Larsson, thank you for your hospitality and help. Richard Thomas, I have gotten to know you both as a colleague and a dear friend. If it is about work or finding a nice place to relax, I can always count on you. Thanks for the 'frelling' good times! Fredrik Hellberg, I got to know you as a friend and as a companion in research with whom (and sometimes from whom) I got to know the tricks of the trade. The rest of you 'Sweeds' (genuine or not), thank you for your discussions and the nice times. To the staff of the Manne Siegbahn Institute, without whom the experiments could not have taken place, I would like to say: thank you for standing by day and night during the experiments as well as for your quick responses to my questions and requests. Anders Källberg, the skating trip with my sister was a great success.

Door de vele samenwerkingen zijn mijn paden gangbaarder geworden en heb ik mijn eindbestemming kunnen bereiken. Phil Cosby, your knowledge, attentiveness, and humour are outstanding. You often gave me food for thoughts by answering with subtle questions. Jim en Lindy Peterson, you made my stay in California unforgettable because of your great hospitality and care. I will never forget the maple syrup pancakes in the garden. Christine and Jessica, thank you for your support and help, which I really appreciated being so far removed from my 'future husband'. Steven Guberman, I enjoyed the critical discussions,

which forced me to think about many aspects of my research. Jan Pettersson and Partik Andersson, I learned a great deal through our experiments. Gerrit Groenenboom, dank je wel voor het beschikbaar stellen van je werk.

Op mijn thuisstation AMOLF heb ik vele kamergenoten en groepsgenoten zien komen en gaan en elke keer wisten zij gezelligheid en kennis met mij te delen. Rüdiger Lang, jij nam altijd de tijd voor me en wist je opgedane ervaring als promovendus goed te besteden aan een beginneling als ik. Hester Volten, onze gesprekken over geschiedenis, taal, filosofie, en menig ander onderwerp waren erg interessant en amusant. Andreas Gürtler, jouw passie en tegelijkertijd jouw nuchterheid hebben mij overdonderd. Juist toen ik het nodig had, was jij er en het is mij een genoegen geweest daar elke keer gebruik van te hebben mogen maken. Anouk Wetzels, dank je wel voor je vrolijkheid en versterking. Afric Meijer, elke keer opnieuw bracht jij een glimlach op mijn gezicht. Laura Dinu, dank je wel voor je wijze raad. Ben Veihelmann, dank je wel voor je nieuwsgierigheid. Jullie allen, natuurlijk ook bedankt voor het geweldige eten en de interessante gesprekken in de lunchgroep, wie wil nou niet weten hoe malt bier gemaakt wordt. Na het vertrek van Wim, hebben Jennifer Herek en haar groep mij opgevangen. Jennifer, zonder jou zouden mijn laatste maanden een stuk zwaarder zijn geweest. Onze gesprekken hebben mij gesterkt en geholpen beslissingen te maken. Dank je wel dat je me hebt laten voelen bij je groep te horen door me te betrekken bij de groepsactiviteiten. Ricardo, Dennis, Peter en vooral Janne, jullie hiervoor ook bedankt. AMOLF zou AMOLF niet zijn, als ik ook niet vele collega's buiten de groep als vrienden heb leren kennen. Wolf, Christian, Arjan, Katrien, Grace, Andrea, Liam, Hinco en ga zo maar door (ik moet ergens stoppen), dankzij jullie heb ik me altijd op mijn plek gevoeld. Verder wil ik ook graag Ad de Snaijer bedanken. Ad, dank je wel voor je hulp, vooral bij het ontwikkelen van de ionenbron. Mijn waardering is groot voor de ondersteunende staf van AMOLF, met name Trees, die ondanks het vele komen en gaan van de wetenschappers, nog steeds de moeite doen om 'ons tijdelijke medewerkers' te leren kennen.

Een omleiding die ik halverwege mijn weg moest nemen, bracht mij in Nijmegen. Hier heb ik een geheel nieuwe groep mogen leren kennen en ook wat vertrouwde gezichten teruggezien. Collega's van Molecuul en Laser Fysica, dank je wel dat jullie mij welkom hebben geheten. Mirjam, dank je voor je werk en moeite om mij als experimentalist te onderwijzen op het theoretisch gebied. Viola, thank you for your care and help with the experiments. Stefan, your different approach was refreshing and I enjoyed your cheerful optimism. Afric, waazzzzuupp? Het was onwijs fijn dat je altijd blij was te weten dat ik weer naar Nijmegen kwam. Mi descritorio es su descritorio.

Aan al mijn collega's en vrienden: ik hoop dat onze wegen elkaar mogen blijven kruisen. To all my friends and colleagues: I hope that our paths will continue to cross.

Avec plaisir, je voudrais aussi remercier ma famille, juste pour être ma famille. Aan mijn zus Mariska, in jouw heb ik een lotgenoot gevonden met hetzelfde enthousiasme en dezelfde nieuwsgierigheid voor de wetenschap en de wereld. Het is fijn mijn thesis te hebben mogen sieren met je gedicht. Aan mijn broer Frederick, jij bent en blijft altijd mijn grote voorbeeld. Ik vond het echt te gek je te mogen introduceren in mijn wereld (om vervolgens je studieboeken te lenen). Aan mijn zus Ericka, jij hielp juist in de zwaarste tijden en maakte het daarnaast mogelijk voor mij om een beetje te ontspannen. Je bent echt mijn grote zus. Aan mijn toekomstige schoonzus Carolijn, ik vond het erg leuk en motiverend om de laatste loodjes van het promoveren met je te hebben kunnen delen. Je spontane beslissing bij mij thuis te komen om samen aan onze promoties te werken, was een geweldige zet. Natuurlijk

wil ik graag mijn moeder, schoonmoeder, mijn onmisbare tweelingbroertje Pieter, mijn broer Mike, Claire, Dimitri, Carly, Anke, Mike, en John danken voor hun begrip en geduld, zeker in de laatste maanden, waarin ze mijn aanwezigheid vaak hebben moeten missen. Merci pour votre compréhension et votre patience.

Zonder enige twijfel is mijn grootste steun en toeverlaat mijn man Werner geweest. Werner, dank je wel voor je oneindige liefde, geweldige zorg (je kookkunsten zijn gewaardeerd) en voor mij nog steeds verbazingwekkende geduld (gelukkig kan je nu niets terugzeggen). Jij hebt het voor elkaar gekregen om de vele rollen te vervullen die ik nodig had. Naast mijn man en vriend, was jij ook mijn publiek, mijn constructieve criticus, mijn persoonlijk ontwerper (je bijdrage aan de opmaak van het proefschrift straalt ervan af) en op het laatst ook nog mijn crisismanager. Ik ben blij samen met jou het volgende avontuur aan te gaan in these brand new days. Je serai toujours ta petite.

Annemieke
xxx

About the Author

2005
SEPTEMBER

Sun		4	sUK	18	25
Mon		5	sNL	19	26
Tue		6	sFR	20	27
Wed		7	Ack	21	28
Thu	1	A	**CV**	22	29
Fri	2	B	16	23	30
Sat	3	Ref	17	24	

After 8 months together with her twin brother, this author was pushed into the world a little too early. It was on a winter-Monday, December 1, 1975. She was small and eager to discover life! That's Annemieke in a nutshell. But almost 30 years have passed since that moment. And a lot has happened. She grew up in Oost-Souburg with two other brothers and two sisters. Already at primary school she was in a hurry and skipped the last grade together with her twin brother. The two of them joined their elder sister and so they became a triplet. A nice clan to terrorise the teachers you would say? Well yes, timid as she was, sometimes Annemieke did make them tremble. She does know when she's right! She cycled through secondary school easily and took on an additional course on top of the obliged ones. Twin brother and newly gained triplet sister copying her neatly done homework feverishly. She actually wanted to take on two additional courses, but the school thought that such a small timid girl shouldn't be hiding behind books all the time. How wrong they were... At the age of seventeen, she moved to Delft to study Applied Physics at the Delft University of Technology. Here, she joined, amongst other, a political youth organisation. Delft is also where she met her true love. After enjoying this picturesque Dutch town for quite a while she graduated in the Pattern Recognition Group on the development of a real-time eye-tracker as part of an augmented-reality system: virtual reality on top of the real world. (It had something to do with slimy pig-eyeballs that had to be freshly picked up from the butchers every day I believe...) She received her M.App.Sc. (Ingenieur) degree in the year 2000. With a thirst for more physics and less development, she searched for a PhD position in fundamental research. On her 25th birthday, December 1 2000, she started her PhD work in Amsterdam at the FOM Institute of Atomic and Molecular Physics in the Atmospheric Photo Physics group of Wim van der Zande. The resulting research is the subject of this thesis.

Mariska